Investigation into the role of DRAM2 on the lysosomal activity of retinal organoids and RPE using patient-specific cell models.

Rozaliya Tsikandelova

A thesis submitted to Newcastle University for the degree of Doctor of Philosophy (PhD)

Student Number ID: 09461396

Biosciences Institute

Faculty of Medical Sciences

Newcastle University

October 2023

Abstract

Biallelic *DRAM2* mutations cause an autosomal recessive cone-rod dystrophy manifesting in the third decade of life. DRAM2 is known to be expressed in the lysosomes of photoreceptors (PRs) and retinal pigment epithelium (RPE), however it remains unclear how this protein contributes to retinal disease. Induced pluripotent stem cells (iPSCs) reprogrammed from somatic tissue are successfully used for disease modelling of retinal dystrophies. Herein, we detail the generation and characterisation of retinal organoids (ROs) and RPE from two patient-specific iPSCs carrying biallelic mutations in *DRAM2.* To control for genetic background variation, we generated isogenic controls using CRISPR-Cas9 and differentiated them to ROs and RPE alongside wild-type controls. Preliminary data showed a fundamental difference in the ability of both iPSC-derived patient ROs to initiate autophagic processes. Complete loss of DRAM2 in ROs resulted in a failure to initiate autophagy, as opposed to minimal DRAM2 expression, which was sufficient to maintain basal levels of autophagic activity. Characterisation of ROs by immunofluorescence did not show a reduction in either rods or cones consistent with an adult-onset of the disease. Patient ROs and RPE, however, presented with a marked accumulation of lipid deposits on electron microscopy suggesting inefficient degradation of cellular waste. A combined proteomics and western blot approach revealed a cytosolic reduction and increased media expression of key lysosomal degradative enzymes in both cell models. A significant decrease in lysosomal enzyme activity corroborated a putative lysosomal deficiency. Altered lipid composition of ROs indicated that aberrant membrane dynamics may exacerbate the vesicular trafficking defect. Co-expression of DRAM2 with AP-1 (Adaptor Related Protein Complex 1) and AP-3 (Adaptor Related Protein Complex 3) provided further evidence for a role in clathrin-mediated transport. Collectively, these data suggest an indispensable role for DRAM2 in the maintenance of PRs and RPE in overseeing the proper transport of lysosomal enzymes.

Acknowledgements

First and foremost, I would like to dedicate this thesis to my mother whose unconditional love and support has been instrumental for me to continue my higher education. Her longstanding encouragement of my passions is at the foundation of why I want to be a scientist and she will always live on in my memory. My love and gratitude also go out to my dad and my sister, Mitko and Desi, whose unwavering financial and emotional support has been absolutely critical for me the past four years. I would like to thank sincerely my main supervisor Linda Lako for giving me the opportunity to work on this special project in the first place. Linda has been a guardian angel and I would like to genuinely thank her for being a continuous source of inspiration, for providing solid emotional support and for being an exceptional mentor over the past four years. Next, I would like to thank my supervisor Marzena for her dear friendship, for being an incredible scientist and for providing outstanding intellectual input throughout the course of this project. I would also like to sincerely acknowledge my other supervisor Birthe for all the help with ICC and retinal organoid work, which has been greatly appreciated. In addition, I would like to thank prof. Phil Whitfield for all the lipidomics work, Dr. Pawel Palmowski for performing the proteomics analysis, Chunbo Yang for his initial supervision, Dr. Martin McKibbin for providing DRAM2 cell lines, Edvinas Cerniaukas and Dean Hallam for their previous work on the DRAM2, Florence Burte for providing help with lipidomics analysis and MRes student Eldo Galo for contributing important RPE data at a difficult time last year. Special thank you goes out to Rodrigo Cerna-Chavez for his friendship and work on DRAM2 RPE, Rob Atkinson and Maria Georgiou for carrying out RPE experiments. Furthermore, I would like to thank my friends Zara Taskova, Corin Nesbit, Milena Balkandzhieva and Matt Colquhoun for their friendship and outstanding emotional support during this time. Last but not least, I would like to thank my partner Jack Laverick for his unconditional belief in me and for always standing by my side. It is only thanks to his love and support that I am able to find joy in the community of scientific practice.

Table of Contents

Table of Figures

Table of Tables

List of Abbreviations	
4-MU	4-Methylumbelliferone
AAV	Adeno-Associated Virus
AQP1	Aquaporin 1
c- Myc	MYC Proto-Oncogene
CC	Connecting Cilium
CLTRN	Collectrin
CRYAB	Crystallin Alpha B
CYBRD1/DCytb	Plasma Membrane Ascorbate-Dependent Reductase
FIP200	Family Interacting Protein of 200 kD
GBA	Glucocerebrosidase
GRN	Progranulin
HESI II	heated electrospray ionization
HIST1H4A	H4 Clustered Histone 1
ILVs	Intraluminal Vesicles
KIF1A	Kinesin-like protein KIF1A
LCA	Leber Congenital Amaurosis 10
LCO	Lipid-Containing Organelles
LMP	Lysosomal Membrane Permeabilization
LXN	Latexin
MEA	Microelectrode Array
MYH11	Myosin Heavy Chain 11
NPC	Niemann-Pick disease type C
OV	Optical Vesicle
pegRNA	Prime Editing RNA
PIP5K1C	Phosphatidylinositol 4-Phosphate 5-Kinase Type-1 Gamma
PMEL	Premelanosome Protein
PSEN1	Presenilin
RAB3A	Ras-related protein Rab-3A
RNP	Ribonucleoprotein
SNAP91	Clathrin coat assembly protein AP180
SREBPs	Sterol Regulatory Element-Binding Proteins
Stx17	Syntaxin 17
TEAB	Triethylammonium bicarbonate
TGN	Trans-Golgi Network
TYRP1	Tyrosinase-Related Protein-1
VAMP2	Vesicle-associated membrane protein 2
2D	Two-dimensional
3D	Three-dimensional
3-MA	3-Methyladenine
ABEs	Adenine-Based Editors
AC	Amacrine Cell
ACN	Acetonitrile
AD	Alzheimer's Disease
ADD	Autosomal Dominant Drusen
AEBP1	AE Binding Protein 1

ALS	Amyotrophic Lateral Sclerosis
AMD	Age-related Macular Degeneration
AMD	Age-Related Macular Degeneration
AMPK	AMP-Activated Protein Kinase
AP-1	Adaptor Related Protein Complex 1
AP-2	Adaptor Related Protein Complex 2
AP2α	Activating Enhancer-Binding Protein 2-Alpha
AP-3	Adaptor Related Protein Complex 3
ARL8	ADP Ribosylation Factor Like GTPase 8
Atg101	Autophagy-related protein 101
Atg13	Autophagy-related protein 13
ATP13A2	ATPase 13A2
ATP6AP2	ATPase H+ transporting accessory protein 2
ATP6V0A2	ATPase H+ transporting VO subunit A2 (V0a2)
ATP6V0A4	ATPase H+ transporting VO subunit A4 (V0a4)
ATP6V1B1	ATPase H+ transporting VI subunit B1 (V1B1)
ATP6V1B2	ATPase H+ transporting VI subunit B2 (VIB2)
AVd	Late-stage Autophagic Vesicles
AVi	Early Autophagic Vesicles
Axin	Axis Inhibition Protein
BC	Bipolar Cell
BECN1	Beclin 1
bFGF	Basic Fibroblast Growth Factor
BIN1	Bridging integrator 1
BLOC	Biogenesis Of Lysosomal Organelles Complex
BMP-4	Bone Morphogenetic Protein 4
BORC	BLOC-1 Related Complex
Brn3	Pou-Domain Transcription Factor
BSA	Bovine Serum Albumin
C90RF72	C90RF72
Cas12a	CRISPR-associated protein 12a
Cas13	CRISPR-associated Protein 13
Cas9	CRISPR-associated protein 9
CBEs	Cytosine Base Editors
CD63	CD63 Antigen (Melanoma 1 Antigen)
CD-M6PR	Cation-Dependent Mannose 6-Phosphate Receptor
CEP290	Centrosomal Protein 290
CI-M6PR	Cation-Independent Mannose 6-Phosphate Receptor
CLCN7	Chloride voltage-gated channel 7 (CLC7)
CLEAR	Coordinated Lysosomal Expression And Regulation
CLs	Curvilinear Lipopigments
CMA	Chaperone-Mediated Autophagy
COG	Component Of Oligomeric Golgi Complex
COL12A1	Collagen Type XII Alpha 1 Chain

COLIV	Collagen IV
COPII	Coat Protein Complex II
CORD21	Cone-Rod Dystrophy 21
CRALBP	Cellular Retinaldehyde-Binding Protein
Crb	Crumbs Cell Polarity Complex Component
CRBP1	Cellular Retinol Binding Protein 1
CRD	Cone-Rod Dystrophy
CRIP2	Cysteine Rich Protein 2
CRISPLD1	Cysteine Rich Secretory Protein LCCL Domain Containing 1
CRISPR	Clustered Regularly Interspaced Short Palindromic Repeats
CRISPRi	CRISPR Interference
crRNA	CRISPR RNA
CRX	Cone Rod Homeobox
CTSA	Protective protein-cathepsin A
CTSB	Cathepsin B
d	Days
DAPI	4',6-diamidino-2-phenylindole
dCas9	Dead Cas9
DCN	Decorin
DCT	Dopachrome Tautomerase
DES1	Dihydroceramide Desaturase 1
DHDDS	Dehydrodolichyl Diphosphate Synthase Subunit
DKK1	The Dickkopf-1
DMBT1	Deleted In Malignant Brain Tumors 1
DMEM/F12	Dulbecco's Modified Eagle Medium: Nutrient Mixture F-12
DMT1	Divalent metal Transporter 1
DNA	Deoxyribonucleic acid
DPP4	Dipeptidyl Peptidase 4
DRAM2	DNA Damage Regulated Autophagy Modulator 2
DRAM2a	DRAM2 Isoform a
DRAM2c	DRAM2 Isoform c
DSB	Double Strand Break
DTT	Dithiothreitol
EARP	Endosome-Associated Recycling Protein
Easi-CRISPR	Efficient additions with ssDNA inserts-CRISPR
EB	Embryoid Bodies
EC23	Retinoic Acid Receptor (RAR) agonist
EIPR1	EARP and GARP complex-interacting protein 1
ELISA	Enzyme-Linked Immunosorbent Assay
ER	Endoplasmic Reticulum
ERG	Electroretinogram
ESCRT	Endosomal Sorting Complexes Required for Transport
EV	Extracellular Vesicle
EXO84	Exocyst Complex Component Exo84

FAF	Fundus Autofluorescence Imaging
FBLN5	Fibulin 5
FBN1	Fibrillin 1
FBS	Foetal Bovine Serum
FGF2	Fibroblast Growth Factor 2
FGF9	Fibroblast Growth Factor 9
FGFR	Fibroblast Growth Factor Receptor
FIG 4	FIG 4
FITC	Fluorescein Isothiocyanate
FN1	Fibronectin 1
FTD	Frontotemporal Dementia
FYCO	FYVE And Coiled-Coil Domain Autophagy Adaptor
GARP	Golgi-Associated Retrograde Protein
GARP	Golgi-Associated Retrograde Protein
GBA	Glucosylceramidase β
GDP	Guanosine Diphosphate
GEF	Guanine Nucleotide Exchange Factor
GFAP	Glial Fibrillary Acidic Protein
GFRA2	GDNF Family Receptor Alpha 2
GLB1	β-Galactosidase
GlcNAc-TV	β-1– 6-N-acetyl glucosaminyl transferase V
GlutaMAX	L-alanyl-L-glutamine
GM130	Golgin A2
GPCRs	G protein-Coupled Receptors
GRN	Progranulin
gRNA	Guide RNA
GROD	Granular Osmiophilic Deposits
GTP	Guanosine Triphosphate
GWAS	Genome-Wide Association Study
HC	Horizontal cell
HDR	Homology Directed Repair
hESC	Human Embryonic Stem Cell
HEXB	β-Hexosaminidase
hiPSC	Human induced Pluripotent Stem Cell
HMGA1	High Mobility Group AT-Hook 1
HOPS	Homotypic Fusion and Vacuole Protein Sorting (HOPS) complex
HPS	Hermansky-Pudlack Syndrome
HSPG2	Heparan Sulfate Proteoglycan 2
IDS	Iduronate 2-sulfatase
IDUA	α-L-iduronidase
IF	Immunofluorescence
IGF-1	Insulin-like Growth Factor 1
IMDM	Iscove's Modified Dulbecco's Media
INCL	Infantile Neuronal Ceroid Liposcinosis

INL	Inner Nuclear Layer
IP3R1	IP3 Receptor, Type 1
IPL	Inner Plexiform Layer
iPSCs	Induced Pluripoten Stem Cells
IRBP	Iron-Responsive Element Binding Protein
IRDs	Inherited Retinal Dystrophies
IS	Inner Segment
IWR-1	Tankyrase Inhibitor
KCL	Potassium Chloride
Klf4	KLF Transcription Factor 4
KOSR	KnockOut™ Serum Replacement-Multi-Species
LAMP1	Lysosomal-associated membrane protein 1
LAMP2	Lysosomal-associated membrane protein 2
LB	Lamellar Body
LC3	Microtubule- Associated Protein Light Chain 3
LC-MS/MS	Liquid Chromatography with Tandem Mass spectrometry
LD	Lipid Droplet
LE	Late Endosome
LIPG	Lipase G, Endothelial Type
LOMETS	Local Meta-Threading Server, version 3
LRRK2	Leucine rich repeat kinase 2
LSD	Lysosomal Storage Disorder
LYSET	Lysosomal Enzyme Trafficking Factor
LYST	Lysosomal trafficking regulator
MAN2B1	Mannosidase Alpha Class 2B Member 1
MAPT	Microtubule associated protein tau
Matrigel	Basement-membrane matrix components
MCA	7-Methoxycoumarin-4-Acetic Acid
MCOLN1	Mucolipin 1 (TRPML1)
MFAT	Multifunction O-Acyltransferase
miRNA	MicroRNA
MITF	Melanocyte inducing transcription factor
ML	Melanolysosome
MLF	Melanolipofuscin
MT-ND5	Mitochondrially Encoded NADH:Ubiquinone Oxidoreductase Core Subunit 5
mTORC1	Mammalian Target of Rapamycin Complex 1
MYOC	Myocilin
NAADP	Nicotinic Acid Adenine Dinucleotide Phosphate
NAGLU	N-α-acetylglucosaminidase
Nanog	Nanog Homeobox
nCas9	Nickase Cas9
NCKX1	Sodium/Potassium/Calcium exchanger 1
NCL	Neurounal Ceroid Lipofuscinosis
NEAA	Non-Essential Amino Acids
NES	Nestin
NFATC4	Nuclear Factor Of Activated T Cells 4

NHEJ	Non-Homologous End-Joining Pathway
NMD	Nonsense-Mediated mRNA Decay
NPC1	Niemann-Pick Cl
NPC2	Niemann-Pick type C2 protein
NR	Neural Retina
Nrf2	Nuclear Factor Erythroid 2–Related Factor 2
NRL	Neural Retina Leucine Zipper
NRVs	Neuroretinal Vesicles
NtBuHA	N-tert-(Butyl)hydroxylamine
NUP210	Nucleoporin 210
OC	Optic Cups
OCT	Optical Coherence Tomography
Oct3/4	Octamer-Binding Transcription Factor3/4
OF	Optic Fibers
OPL	Outer Plexiform Layer
OPN1LW/MW	Opsin 1, Long Wave Sensitive
OS	Outer segment
p62	Sequestosome 1
PAM	Protospacer Adjacent Motif
Par	F2R Like Trypsin Receptor 1
PAS	Phagofore Assembly
Pax2	Paired Box 2
Pax6	Paired Box 6
PBS	Phosphate-Buffered Saline
PD	Parkinson's Disease
PDB	Protein Data Bank
PDE6	Phosphodiesterase
PEDF	Pigment Epithelium-Derived Factor
PI(3,5)P2	Phosphatidylinositol 3,5-bisphosphate
PI3K	Phosphoinositide 3-Kinase
PKC-α	Protein Kinase C α
PM	Plasma Membrane
POS	Photoreceptor Outer Segment
PPP1R1B	Protein Phosphatase 1 Regulatory Inhibitor Subunit 1B
PPT1	Palmitoyl-protein thioesterase 1 (CLN1)
PR	Photoreceptor
PROX1	Prospero Homeobox 1
PRPFs	Pre-mRNA Processing Factor
PRPH	Peripherin
PSEN1	Presenilin 1
PTC	Premature Translation-Termination Codon
PtdIns(3)P	Phosphatidylinositol 3-Phosphate
qPCR	quantitative PCR
RA	Retinoic Acid
RABEP1	Rabaptin, RAB GTPase Binding Effector Protein 1

Rab5	Ras-Related Protein Rab-5
Rab7	Ras-Related Protein Rab-7
RALB	RAS Like Proto-Oncogene B
RCD	Rod-Cone Dystrophy
RCF	Relative Centrifugal Force
RCVRN	Recoverin
RDH12	Retinol Dehydrogenase 12
RDH8	Retinol Dehydrogenase 8
Rheb	Ras Homolog, MTORC1 Binding
RHO	Rhodopsin
RNA	Ribonucleic acid
RO	Retinal Organoid
ROCKi	Rho-associated Coiled-coil protein Kinase inhibitor
RP	Retinitis Pigmentosa
RPE	Retinal Pigment Epithelium
RPE65	Retinoid Isomerohydrolase RPE65
RT	Room Temperature
RUBCN	Rubicon
Rx	Retinal homeobox protein
RXRγ	Retinoid X Receptor Gamma
S100A1	S100 Calcium Binding Protein A1
SAPs	Sphingolipid Activator Proteins
SCARB2	LIMP2, Scavenger Receptor Class B Member 2
SCMAS	Mitochondrial ATP Synthase
SDCBP	Syndecan Binding Protein
SFD	Sorsby Fundus Dystrophy
SFRP5	Secreted Frizzled Related Protein 5
sgRNA	Single Guide RNA
Shh	Sonic hedgehog homolog
siRNA	Small Interfering RNA
SLC38A9	Solute Carrier Family 38 Member 9
SMPD1	Sphingomyelin phosphodiesterase 1
SNAP29	Synaptosomal-Associated Protein 29
SNCA	α-Synuclein
SNCG	Synuclein Gamma
Sox1	SRY-Box Transcription Factor 1
Sox2	SRY-Box Transcription Factor 2
SPG11	Spatacsin
SRC-7	Proto-Oncogene Tyrosine-Protein Kinase Src 7
ssODN	Single-Strand Oligodeoxynucleotide
STGD	Stargardt Disease
STRA6	Signaling Receptor And Transporter Of Retinol STRA6
SYP	Synaptophysin
SYT11	Synaptotagmin 11
TARDBP	TAR DNA binding protein (TDP-43)

TCIRG1	ATPase H+ transporting VO subunit A3 (V0a3)
TEER	Transepithelial Electrical Resistance
TEM	Transmission Electron Microscopy
TFEB	Transcription Factor EB
TGN46	Trans-Golgi Network Protein 2
THBS1	Thrombospondin 1
THY1	Thy-1 Cell Surface Antigen
TMEM106B	Transmembrane protein 106B
TMEM175	Transmembrane protein 175
TOMM20	Translocase of the Outer Mitochondrial Membrane Complex Subunit 20
TPC1	Two Pore Segment Channel 1
TPP1	Tripeptidyl Peptidase 1
tracrRNA	Transactivating crRNA
TRAPPC	Trafficking Protein Particle Complex
TRPML	Transient Receptor Potential Mucolipin Channels
UCHL1	Ubiquitin C-terminal hydrolase L1
ULK1	Unc-51-like Kinase 1
ULK2	Unc-51-like kinase 2
UPR	Unfolded Protein Response
V0a1	ATPase H+ Transporting V0 Subunit A1
VAMP8	Vesicle-Associated Membrane Protein 8
VAT1L	Vesicle Amine Transport 1 Like
vATPase	Vacuolar-type ATPase
VCAN	Versican
VEGF	Vascular Endothelial Growth Factor-A
VPS34	VPS34 Retromer Complex Component
VPS35	VPS35 Retromer Complex Component
VPS35	VPS35 Retromer Complex Component
VPS41	VPS41 Subunit Of HOPS Complex
VPS53	VPS53 Subunit Of GARP Complex
VSX2/Chx10	Visual System Homeobox 2, CEH10 Homeodomain-containing homolog
Vti1b	Vesicle Transport Through Interaction With T-SNAREs 1B
WB	Western Blot
WFS1	Wolframin ER transmembrane glycoprotein
Wnt	Wingless Integration Site
WT	Wild type
XLRS	X-Linked Retinoschisis
Ykt6	YKT6 V-SNARE Homolog
ZFYVE26	Spastizin (SPG15)
ZO-1	Tight Junction Protein 1

Statement

Statistical analyses presented in this PhD thesis have the WT sample excluded from comparisons where patient and isogenic samples are interrogated. Hence, most statistical significance outlined here pertains to pairwise comparisons between patient and isogenic control samples and does not reflect on the presence or absence of such between the WT control and the rest of the samples examined.

Chapter 1: Introduction

1. Introduction.

1.1. The Retina as a central tissue of visual perception

1.1.1. Structural organization of the retina

Eyesight arises from the ability of the eye to convert light from the surrounding environment and translate it into neural impulses that are processed by the brain. Visual perception begins in the anterior cavity of the eye, where the lens, cornea, iris, and the ciliary body refract and focus light onto the retina. The retina is the innermost, sensory component of the eye, which facilitates vision via the transduction of light photons into graded membrane potentials. It is an intricately laminated tissue comprising several layers of highly specialized retinal cells. Electrochemical impulses generated by cones and rods, the two types of photoreceptors, which can be found in the outer nuclear layer (ONL), feed into a circuit of bipolar cells residing in the inner nuclear layer (INL). Communication between photoreceptor presynaptic termini and the postsynaptic processes of bipolar and horizontal cells is established in the outer plexiform layer (OPL), the site of synaptic contact. Second- order interneurons such as horizontal and amacrine cells, also located within the INL, mediate lateral inhibitory responses to fine-tune the excitatory firing of photoreceptors and bipolar cells, respectively. An additional type of retinal cell, known as Müller glia, that can also be found in the INL, provides structural and homeostatic support by enabling neurotransmitter recycling as well as the regulation of extracellular pH and ion concentration. The neurons of the INL relay information of the OPL to the inner plexiform layer (IPL), where bipolar cells synapse with the dendrites of ganglion cells. Synaptic contacts in the IPL are formed between amacrine and bipolar cells, ganglion cells or interneurons. Visual signals subsequently converge on ganglion cells in the ganglion cell layer and are further relayed to the visual cortex of the brain. Separating the overlying receptors from the choroid is a monolayer of retinal pigment epithelium (RPE), which is indispensable for the long-term viability and function of the photoreceptors (Demb and Singer, 2015) (Figure 1).

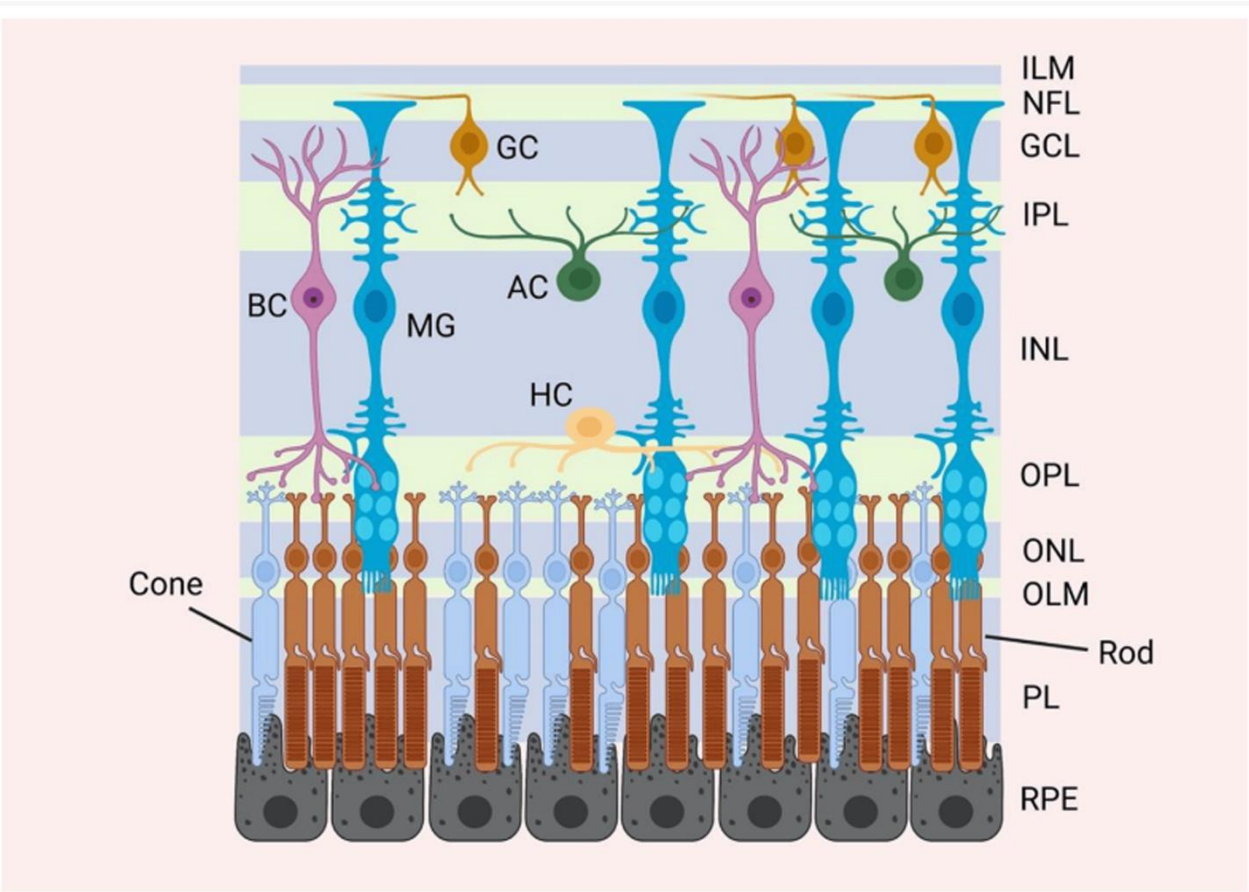

Figure 1 Cellular architecture of the retina. The retina is the innermost light sensitive tissue of the eye which enables the conversion of light into electrical signals that is then forwarded to the brain in the form of visual input. The main cells responsible for detecting light are the photoreceptor cells. Important for the phagocytosis of photoreceptor outer segments and the regeneration of visual pigment is a single postmitotic layer of RPE cells which lies between the sensory part of the retina and the choroid. The mammalian retina is characterized by three main layers - the outer nuclear layer (ONL), the inner nuclear layer (INL), and the ganglion cell layer (GCL), functionally defined by the presence of six types of neurons and one type of glial cells. Rod and cone photoreceptor cell bodies present in the outer nuclear layer (ONL) transmit signals across a variety of interneurons - bipolar (BC), amacrine (AC) and horizontal cells (HC) residing within the inner nuclear layer (INL). Müller glia (MG), which are also native to the INL extend from the outer to the inner limiting membranes (OLM and ILM). The processes of photoreceptor cells synapse with interneurons in the outer plexiform layer (OPL). In turn, interneurons of the INL extend their processes into the inner plexiform layer (IPL) where they establish communication with ganglion cells (GC) of the ganglion cell layer (GCL). Ganglion cells (GC), ultimately feed visual input to the optic nerve across the nerve fiber layer (NFL). Image taken from Salman;McClements and MacLaren (2021). (PL- photoreceptor layer).

1.1.2. Photoreceptors and RPE.

The two primary photoreceptor types in the retina are cones and rods. The latter have evolved different functional characteristics to enable visual perception. Rods are the most prevalent photoreceptor type and enable night- time vision. Rods are located around the periphery of the retina and are heavily distributed within the region surrounding the fovea, an area within the macula, which exhibits the highest visual acuity. The fovea itself is devoid of rods but is highly enriched in cone photoreceptors. Cones are essential for perceiving daylight and color. Cones can singularly contribute to higher levels of visual acuity, whereas rods demonstrate a much higher level of photon sensitivity. Other functional discrepancies between the two main types of photoreceptors pertain to differences in saturation levels as well as recovery response following light exposure (Wang and Kefalov, 2011).

Trichromatic color vision, which is an evolutionary feature of primates, is characterized by allelic diversity of the opsin gene, giving rise to three types of cone pigment, which enable the full discrimination of the color spectrum (Bowmaker and Hunt, 2006). L cones and M cones respond to long -and middle-wavelength light frequencies (λmax~565 nm and λmax~537 nm), respectively, whereas S cones are sensitive to short-wavelengths of the electromagnetic spectrum (λmax~430 nm) (Mustafi;Engel and Palczewski, 2009). Rhodopsin is the rod-specific opsin, which is required for phototransduction of low-light monochromatic vision. Intrinsically photosensitive ganglion cells express a melanopsin pigment, which governs circadian rhythm responses as well as the constriction of the pupil in response to light adaptation (Do, 2019).

Both rods and cones possess a synaptic terminus, a nuclear region, outer (OS) and inner segments (IS) interconnected by a cilium. Photopigments, which endow the retina with the ability to absorb light photons, are retained in the OS of the photoreceptors, which is a specialized type of sensory cilium. The outer segments of rods comprise a mass of rhodopsin -loaded discs enclosed by a ciliary membrane. By contrast, the OSs of cones entail multiple projections in continuation with the OS membrane (Goldberg;Moritz and Williams, 2016). Being exposed to the milieu of the extracellular environment, cone OSs are subject to more rapid bursts of phototransduction (Yau, 1994). Photoreceptor outer segments (POSs) exhibit a high dynamic turnover, so much so that up to 10% of their discs are being synthesized and approximately the same amount is being phagocytosed by the RPE daily (Young and Bok, 1969).

The RPE is a single postmitotic layer of specialized neuroepithelium found between the light-sensory part of neural retina and the choroid. It is a highly polarized structure of hexagonally arranged cells, which assemble into tight junctions. Basolaterally, RPE forms a firm contact with the Bruch's membrane and the adjacently located choriocapillaris while their apical side envelop their microvilli towards the photoreceptor layer (Klettner and Dithmar, 2020). In addition to serving as an outer blood-retinal barrier, the tight monolayer of RPE enables the directed exchange of waste and nutrients, the re-isomerization of visual pigment, the internalization and degradation of POS as well as the release of extracellular factors, which contribute mechanical cohesion to the retina (Klettner and Dithmar, 2020). Failure in the ability of RPE to fully degrade damaged POS by their lysosomes leads to the accumulation of autofluorescent lipofuscin granules in the RPE - a heterogenous mix of oxidized cell debris, lipid, protein and chromophore metabolites (Kennedy;Rakoczy and Constable, 1995). The autofluorescent properties of lipofuscin are largely due to the presence of bisretinoid fluorophores, which are metabolites of vitamin A and other visual related processes.

The high metabolic rates and the abundance of polyunsaturated phospholipids in the membranes of POS contribute acute susceptibility to oxidative stress (Bazan, 2006). Compromised RPE integrity often leads to secondary irreversible damage to the overlying layer of photoreceptors and has been implicated in the development of multiple retinal diseases, including dry and wet age-related macular degeneration (AMD) (Klettner and Dithmar, 2020). Damage to the RPE due to continued metabolic stress has been linked to the natural processes of ageing, dysfunctional autophagy as well as abnormal Nrf2 antioxidant signaling in the RPE (Mitter *et al*., 2014; Handa, 2012). Chronic oxidative stress can therefore lead to the excessive accumulation of oxidized epitopes in the macula leading to the overt induction of innate immunity, which may induce RPE cell apoptosis and the deposition of drusen onto the Bruch's membrane (Handa, 2012).

1.1.3. Initiation of the phototransduction cascade

The conversion of a photon light into electrical signal of the retina is termed phototransduction. The process of phototransduction originates with photon detection by the opsin family of G protein-coupled receptors. The chromophore, 11-cis retinal bound to the opsin, is isomerized by photons to become all-trans retinal. The photoisomerization of retinal causes a conformational change of the opsin protein, which, once activated, initiates a signal transduction cascade. The activated form of the opsin, Meta II, activates the trimeric G protein, transducin. Activation of transducin catalyzes the dissociation of GDP bound to its α-subunit in favor of binding GTP. As GTP is bound, the α-

subunit dissociates from the β- and γ-subunits, this GTP-bound α-subunit then facilitates the activation of phosphodiesterase (PDE6). PDE6 is a tetramer consisting of an α-subunit, a β-subunit, and two γ-subunits. It is one of the γ-subunits of PDE6 that is activated by the GTP-bound complex, inciting the hydrolysis of cGMP into GMP. As the sodium ion (Na^+) channels of the photoreceptor are gated by cGMP, a reduction in intracellular cGMP results in closure of these channels preventing the influx of Na^+. This is what provokes the hyperpolarization of the photoreceptor cell, as potassium ions (K^+) are still transported out of the cell. Hyperpolarization of the photoreceptor cell causes closure of voltage-gated calcium ion (Ca^{2+}) channels decreasing the level of intracellular Ca^{2+}, as the ion is no longer flowing into the cell but is still being extruded from the outer segments by Na^+/Ca^+, K^+ exchangers such as NCKX1 (Tsin;Betts-Obregon and Grigsby, 2018).

1.1.3.1 Visual cycle

Upon light excitation a classical visual cycle cascade is triggered that enables the activation of opsin photoreceptors and the recycling of visual pigment by the RPE. In the meantime, renewed pigment is supplied to both cones and rods in a competitive manner. An additional cone-specific visual phototransduction cascade exists which recycles and provides chromophore specifically to cones in an RPE-independent manner. Both pathways are briefly summarized here (Wang and Kefalov, 2011).

1.1.3.2 Canonical visual cycle and cone-specific visual cycle

The classical visual cycle is initiated by the isomerization of 11-cis retinal to all-trans- retinal upon activation of the opsin GPCR by light photons. This leads to a conformational change of the opsin receptor resulting in hyperpolarization. Retinol dehydrogenases such as RDH8 and RDH12 enable the conversion of all trans-retinal to all-trans-retinol. The latter molecule associates with IRBP protein once it enters the interphotoreceptor matrix and is transported to the RPE in a CRBP1-dependent manner. Once in the RPE, it is modified to all-trans-retinyl ester by the lecithin retinol acyl transferase. RPE65 protein then enables the catalysis of esterified all-trans-retinol to 11-cis-retinol, which is then oxidized to 11-cis-retinal allowing it to be reused by opsins receptors (Tsin;Betts-Obregon and Grigsby, 2018; Wang and Kefalov, 2011) (Figure 2).

The cone visual cycle undergoes analogous stages but is further facilitated by isomerase II, dihydroceramide desaturase 1 (DES1), and multifunction O-acyltransferase (MFAT) proteins within Müller glia cells. Consequent to the reduction of all-trans-retinal to all- trans-retinol by retinol

dehydrogenase, the latter chromophore is delivered to Müller glia cells, where it associates with CRBP to be converted to 11-cis-retinol by Isomerase II (DES1) and to be esterified by MFAT (Kaylor *et al.,* 2013). Subsequently, 11-cis-retinal is returned to the cone outer segments and oxidized to 11-cis-retinal which can then be reused by cone opsins (Tsin;Betts-Obregon and Grigsby; Wang and Kefalov, 2011).

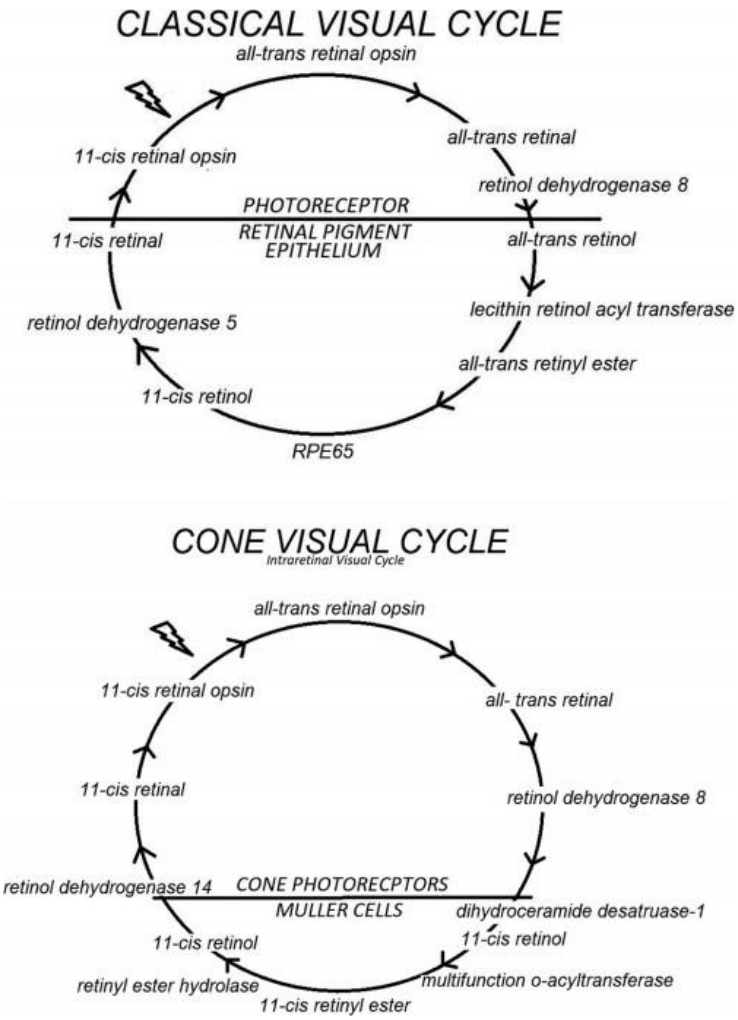

Figure 2 Schematic depiction of the canonical and cone visual cycle pathways. Image taken from Tsin;Brandi and Grigsby, 2018.

1.2 Blindness

A systematic review on the global population has reported that retinal degenerative disorders account for a significant number of visual impairment cases worldwide (Flaxman *et al.,* 2017) (Figure 3). Even though an overall reduction in blindness and visual impairment cases has been reported

globally, the prevalence of preventable visual impairment has continued to increase within the ageing population with the improvement of life expectancy (Flaxman *et al.,* 2017). The current classification of the World Health Organization only takes into record blinding conditions of public health significance, which can be prevented. However, when multiple co-existing conditions are encountered in the same individual, vision loss is ascribed to the 'most readily curable cause', which has been associated with an overestimation of curable vision impairment. This calls for an unbiased approach to determine the prevalence of debilitating eyesight conditions and the development of reliable treatments for diseases leading to the irreversible loss of vision.

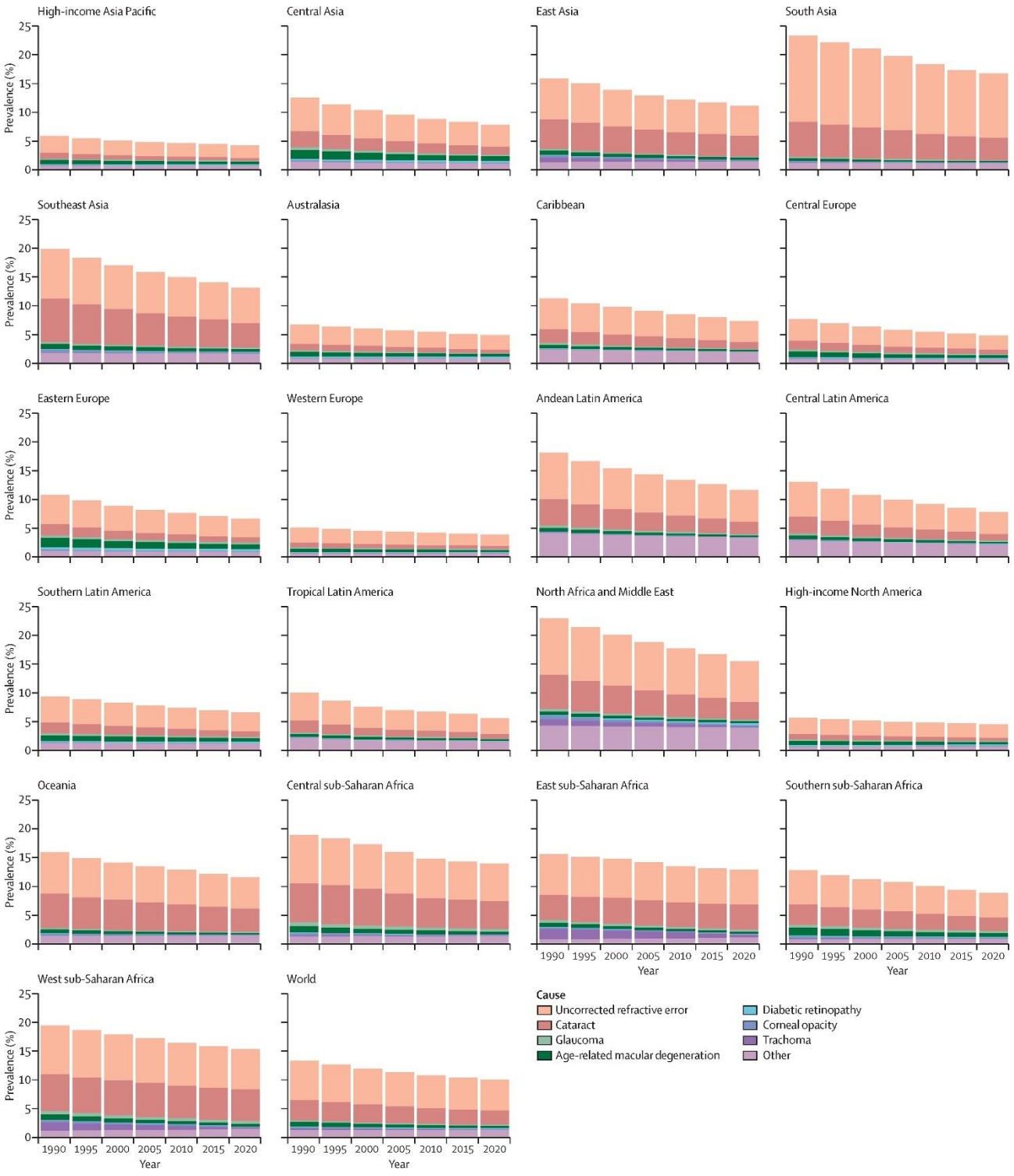

Figure 3. Prevalence of moderate to serious visual impairment ≥ 50 years of age. Data was normalized to age and acquired per world region between 1990 and 2015. Image taken from Flaxman *et al*., (2017).

1.3. Inherited retinal degeneration.

Inherited retinal dystrophies (IRDs) comprise a group of genetically and phenotypically heterogeneous disorders with an overall incidence of 1:2000 (Sohocki *et al*., 2001; Rein *et al*., 2006; Cremers *et al*., 2018). IRDs are characterized by severe visual impairment with disease presentation varying greatly across the age spectrum (Georgiou; Fujinami and Michaelides, 2021). T herapeutic options are limited, however, recent developments in next generation sequencing have prompted the discovery of novel pathogenic variants and causative genes associated with IRDs (Georgiou; Fujinami and Michaelides, 2021). Significant genetic and allelic heterogeneity can be observed but the primary etiology is attributed to dysfunctional photoreceptors and/or RPE with clinical severity being dependent on the affected retinal cell type (Georgiou;Fujinami and Michaelides, 2021). Leber congenital amaurosis, cone- rod/rod-cone dystrophies and retinitis pigmentosa (RP) are some examples of common hereditary retinal degenerative disorders (Scholl *et al*., 2016). Furthermore, progressive atrophy of the macula is associated with the development of Stargardt disease (STGD), Sorsby fundus dystrophy (SFD), X-linked retinoschisis (XLRS), Best disease (BD) and autosomal dominant drusen (ADD) (Rahman *et al*., 2020).

1.4. Contribution of *DRAM2* to retinal degeneration

DRAM2 encodes a 266-amino-acid protein containing six transmembrane domains (Yoon *et al*., 2012; Zeng *et al*., 2014). The protein localizes to lysosomal membranes where it may initiate the lipidation of endogenous LC3-I (microtubule- associated protein light chain 3) to LC3-II during autophagosome formation (Zeng, *et al*., 2014; Kim, *et al.* 2017) Kim, *et al.* (2017) recently demonstrated that DRAM2 is able to physically interact with key autophagy proteins BECN1 and displace RUBCN from the BECN1 complex to initiate phagofore formation in human macrophages. Furthermore, DRAM2 was also shown to bind to both LAMP1 and LAMP2, which may be important for endolysosomal maturation (Kim, *et al.* 2017). Collectively, these data suggests that DRAM2 may have a crucial role in the maintenance of photoreceptor and RPE cells.

Biallelic mutations in the novel lysosome and autophagy regulator DNA Damage Regulated Autophagy Modulator 2 (*DRAM2*) are associated with an autosomal recessive form of retinal dystrophy, affecting both cones and rods (El-Asrag *et al*., 2015; Sergouniotis *et al*., 2015; Kuniyoshi *et al*., 2020; Abad-Morales *et al*., 2019). A recent study reported lower *DRAM2* expression in AMD eyes and the loss of cones in *DRAM2* knockout mice, which supports a primary macular involvement (Jones *et al.*, 2023). Most DRAM2 patients present with macular involvement and loss of cone

photoreceptors by the third decade of life. At advanced stages of the disease, clinical presentation is often also accompanied by peripheral retinal degeneration which undermines one's ability to see in dimly lit conditions (El-Asrag *et al*., 2015; Sergouniotis *et al*., 2015; Kuniyoshi *et al*., 2020; Abad-Morales *et al*., 2019). The classic DRAM2 clinical diagnosis entails central vision loss with early funduscopic findings of a granular macular appearance and white/yellow dots. On fundus autofluorescence (FAF) patients may exhibit regions of hypoautofluorescence pertaining to areas of significant macular cell loss. The presence of hyperautofluorescent rings surrounding these regions of hypoautofluorescence has been associated with sites of photoreceptor loss where RPE is still functional, but likely subjected to a significant lipofuscin burden (Sergouniotis *et al*., 2015; Krasovec *et al.*, 2022). The central atrophic area is seen to enlarge over time, leading to peripheral degeneration and the presence of bone-spicule pigmentation. Consistent with these data, optical coherence tomography (OCT) findings from a pre-symptomatic patient showing the loss of photoreceptor cells appear to suggest a primary photoreceptor etiology (Sergouniotis *et al*., 2015). Studies have shown that the onset and the severity of the disease is largely dependent on the type of *DRAM2* mutation in patients. The two pilot studies on *DRAM2* dystrophy demonstrated that loss-of-function *DRAM2* mutations are associated with an earlier disease onset and a more severe disease progression compared to missense mutations or in-frame deletion variants (Sergouniotis *et al*., 2015; El-Asrag *et al*., 2015). This is in keeping with the observation that certain missense variants may contribute to a significantly delayed disease presentation which could be mistaken for AMD in the sixth decade of life (c.3G > A/, c.737T > C) (Krasovec *et al*., 2022). The slowly progressing macular dysfunction reported in this patient, is likely to be due to the presence of the mild missense c.737T > C variant, which could lead to the retention of some residual DRAM2 function. By contrast, in a homozygous state, the null variant c.3G > A (loss of start codon), presents with a severe CRD at the age of 35, concurrent with intraretinal cysts, an autoimmune response, completely ablated rod, and significantly delayed cone responses.

Further investigation into the clinical impact of homozygous frameshift and alternative splicing variants, revealed that individuals carrying frameshift mutations exhibited a relatively milder phenotype in terms of peripheral retinal degeneration which was also contingent on the level of transcript degradation and the location of the premature termination codon in the genetic sequence of *DRAM2*. By contrast alternative splicing mutations were associated with more pervasive peripheral retinal damage and associated RPE abnormalities (Abad-Morales *et al*., 2019). A comprehensive analysis of all clinical electroretinogram (ERG) data revealed that the majority of

DRAM2 cases have been diagnosed as CRD, 29% as macular dystrophy and 21% pertain to rod-cone dystrophy (RCD) (Krasovec *et al.*, 2022). As becomes evident from clinical data, both cones and rods are affected, however, in spite of ERG findings, RCD never presents as a typical RCD due to the strong macular involvement seen in patients (Kuniyoshi *et al.*, 2020; Krasovec *et al.*, 2022). RCD DRAM2 patients displaying night blindness and dark adaptation difficulties upon presentation, subsequently also develop a significant macular impairment.

Two major isoforms have been reported for *DRAM2* – a ubiquitously expressed isoform (*DRAM2a*) and a retinal-specific one (*DRAM2c*) as inferred by RT PCR analyses in a set of human tissues (Abad-Morales *et al*., 2019). The *DRAM2c* isoform is defined by the skipping of exon 5 and is expected to produce protein half the size of ubiquitously expressed DRAM2a (~30kDa). Hence *DRAM2c* (exons 6-9) represents a shortened version of the *DRAM2a* isoform (exons 3-9) (Abad-Morales *et al*., 2019). The Abad-Morales study has shown that RPE disturbances leading to a more severe disease progression are particularly apparent in the patients carrying alternative splicing mutations which affect the expression of both isoforms (e.g., c.693+2T>A). So far, all literature data derives from a total of 19 *DRAM2* variants associated with the degeneration of both PR and RPE cells, but the contribution of the two major isoforms to the loss of either retinal cell type demands further investigation.

1.5. Lysosomal contribution to neurodegeneration.

The ageing lysosome poses a significant vulnerability to the long-term maintenance of neuronal tissue. Due to being long-lived post-mitotic cells not able to carry exocytosis, a substantial proportion of neuronal cells are subjected to the growing burden of lysosomal clearance during the course of ageing. The specific dependance of neuronal tissue on lysosomal function is demonstrated by the numerous congenital disorders associated with aberrant lysosomal function (Fraldi *et al*., 2016; Llyod-Evans and Haslett, 2016). Common deficits leading to Lysosomal Storage Disorders (LSDs) are linked to reduced lysosomal hydrolase activities due to aberrant lysosomal transport or acidification, the deposition of lipofuscin, oxidative damage to lysosomal components as well as reduced autophagic clearance over time (Colacurcio and Nixon, 2016, Cuervo and Wong, 2014; Nixon, 2016). The list of genes shown in Table 1 are widely associated with lysosomal acidification, the degradative function and trafficking of lysosomal hydrolases, the functioning of lysosomal ion transporters, and vesicular trafficking.

Whether lysosomal dysfunction manifests as a congenital disorder or an age-related condition is dependent on the type and the severity of the mutation. Table 1 provides a comprehensive summary of the different type of LSDs gene mutations associated with neurodegenerative decline. Gene dosage effects are shown by the association of homozygous mutations with severe congenital LSDs, in contrast to LSD gene haploinsufficiency which often leads to the development of late-onset neurodegenerative disease. Such is the case for *Progranulin* (*GRN*) mutations, which could either lead to childhood Neurounal Ceroid Lipofuscinosis (NCL) when biallelic, or to Frontotemporal Dementia when heterozygous (Ward *et al*., 2017). Similarly, *glucocerebrosidase* (*GBA*) mutations can cause congenital Gaucher's disease in the biallelic state and late-onset Parkinson's disease as monoallelic mutations (Riboldi and Di Fonzo, 2019). Furthermore, homozygous *GBA* and compound heterozygous mutations can lead to earlier and more severe Parkinson's presentation (Thaler *et al*., 2017). Gene dosage effects in *presenilin* (*PSEN1*) which affects lysosomal acidification can also modify the onset of Alzheimer's depending on the location of the mutation and its impact on the gene (Bagaria;Bagyinszky and An, 2022).

Lysosomes are the endpoint of convergence for autophagic and endocytic routes of degradation (Nixon;Yang and Lee, 2008) (Figure 4). Autophagy is an umbrella term for a variety of lysosome-dependent degradative processes responsible for the clearance of intracellular waste and the recycling of cellular components. Macroautophagy facilitates the processing of cellular waste and even entire organelles such as mitochondria via the fusion of autophagosomes with lysosomes, whereby hydrolases native to the lysosome carry out waste degradation. Alternatively, chaperone molecules can deliver the cargo directly to the lysosome in a process known as chaperone-mediated autophagy. Indeed, waning chaperone-mediated autophagy (CMA) function due to the loss of LAMP2a has been outlined as a major predicament for age-related neurodegeneration (Cuervo and Dice, 2000), Lysosomes can additionally directly engulf cellular waste by selective or non-selective microautophagy. Last but not least lysosomes can receive endocytosed waste cargo via the stepwise maturation of endosomes (Figure 4). The widely accepted lysosomal definition pertains to a single-membrane degradative structure that exhibits acidic pH (4.5-5) and is highly concentrated in

lysosomal hydrolases and membrane receptors whilst at the same time being devoid of the mannose-6-phosphate receptors (M6PR), that have trafficked them (Saftig and Klumperman, 2009).

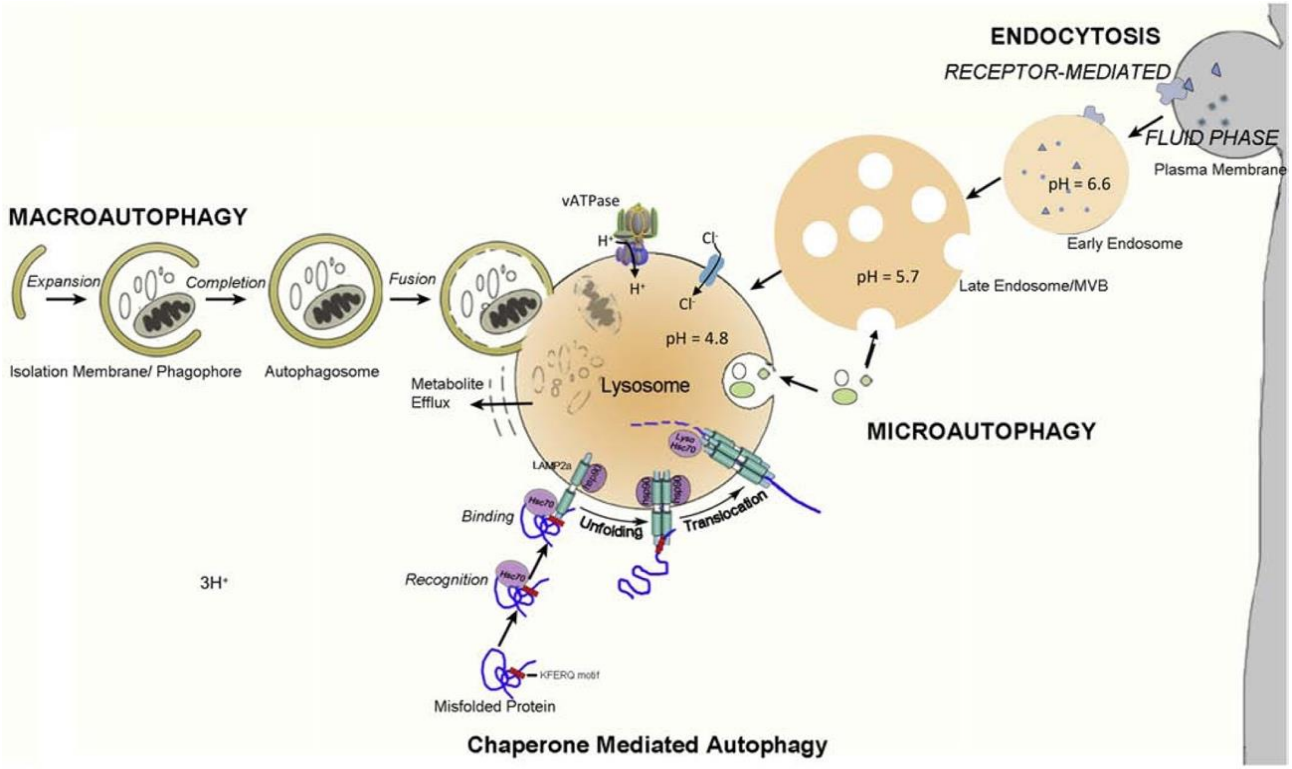

Figure 4. Simplified schematic showing the main routes of lysosomal waste entry. The macroautophagy pathway can deliver lysosomal cargo for degradation by merging double-membrane enclosed autophagosomes with the lysosome. Cellular waste also can be delivered to the lysosome by chaperone molecules via the recognition of the lysosomal LAMP2a receptor. Furthermore, endocytosed cargo can be sequestered to the lysosome by the sequential maturation of early endosomes following endosomal sorting. Finally, small cargo can be directly taken up by lysosomes and degraded in the lysosomal lumen during selective or non-selective microphagy. Image taken from Nixon, 2020.

Table 1. List of genes associated with Lysosomal Storage Disorders. Adapted from Lie and Nixon, 2019.

Gene	Protein	Known/proposed role in lysosomal function	Associated disease (s)	References
Lysosomal hydrolases and their delivery				
CTSD	Cathepsin D	Proteolysis	NCL, INCL, AD	(Vidoni *et al*., 2016)
CTSA	Protective protein-cathepsin A	Proteolysis	Galactosialidosis	(Caciotti *et al*., 2013
IDUA	α-L-iduronidase	Glycosaminoglycan metabolism	Mucopolysaccharidosis type I	(Campos and Monaga, 2012)
IDS	Iduronate 2-sulfatase	Glycosaminoglycan metabolism	Mucopolysaccharidosis type II	(Kosuga *et al*., 2016)
NAGLU	N-α-acetylglucosaminidase	Glycosaminoglycan metabolism	Mucopolysaccharidosis type III, PD	(Ohmi et al., 2009; Winder Rhodes et al., 2012)
SMPD1	Sphingomyelin phosphodiesterase 1	Sphingolipid metabolism	Niemann-Pick disease type A, PD	(Gan-Or *et al.*, 2015
GBA	Glucosylceramidase β	Glycolipid metabolism	PD, Gaucher's disease	(Westbroek *et al.*, 2011)
GLB1	β-Galactosidase	Ganglioside metabolism	GM1 - gangliosidosis	(Sandhoff and Harzer, 2013)
HEXB	β-Hexosaminidase	Ganglioside metabolism	GM2-gangliosidosis	(Sandhoff and Harzer, 2013)
VPS35	VPS35	Hydrolase receptor sorting	PD	(Vilarino-Guell *et al.*, 2011)
SCARB2	LIMP2	Receptor for GBA	Diffuse Lewy body disease, PD	(Bras *et al.*, 2014; Michelakakis *et al*.,
LYSET	Lysosomal trafficking factor	Golgi retention of GNPTAB	Skeletal dysplasia	(Pechincha *et al*., 2022; Richards *et al*., 2022; Zhang *et al*., 2022; Qiao *et*
Lysosomal acidification				
ATP6V1B1	ATPase H+ transporting VI subunit B1 (V1B1)	vATPase subunit	Renal tubular acidosis	(Karet *et al*., 1999)
ATP6V1B2	ATPase H+ transporting VI subunit B2 (VIB2)	vATPase subunit	Dominant deafness-onychodystrophy syndrome, Zimmermann-Laband syndrome	(Kortum *et al*., 2015; Yuan *et al*., 2014)
ATP6V0A2	ATPase H+ transporting VO subunit A2 (V0a2)	vATPase subunit	Autosomal recessive cutis laxa type II	(Kornak *et al.*, 2008)
TCIRG1	ATPase H+ transporting VO subunit A3 (V0a3)	vATPase subunit	Autosomal recessive osteopetrosis with neurodegeneration	(Kornak *et al.*, 2000)
ATP6V0A4	ATPase H+ transporting VO subunit A4 (V0a4)	vATPase subunit	Renal tubular acidosis	(Stover *et al*., 2002)
ATP6AP2	ATPase H+ transporting accessory protein 2	Coordination of vATPase assembly	PD	(Korvatska *et al*., 2013)
ATP13A2	ATPase 13A2	Heavy metal transport; lipid flippase	PD, NCL	(Bras *et al.*, 2012; Ramirez *et al.*,
PSEN1	Presenilin 1	Chaperone for delivery of vATPase VOal subunit to lysosomes	AD	(Lee *et al*., 2010)
PPT1	Palmitoyl-protein thioesterase 1 (CLN1)	Palmitoylation of vATPase VOal subunit for delivery to	INCL	(Bagh *et al*., 2017)
WFS1	Wolframin ER transmembrane glycoprotein	Stabilization of vATPase VIA s	Wolfram syndrome	(Gharanei *et al*., 2013)
Lysosomal ion channels or transporters				
MCOLN1	Mucolipin 1 (TRPML1)	Lysosomal Ca+channel	Mucolipidosis type IV	(Bargal *et al*., 2000)
TMEM175	Transmembrane protein 175	Lysosomal K+channel	PD	(Jinn *et al*., 2017)
CLCN7	Chloride voltage-gated channel 7 (CLC7)	Lysosomal Cl−channel	Osteopetrosis	(Kasper *et al.*, 2005)
NPC1	Niemann-Pick Cl	Cholesterol export	Niemann-Pick disease type C	(Vanier, 2010)
NPC2	Niemann-Pick type C2 protein	Cholesterol export	Niemann-Pick disease type C	(Vanier, 2010)

Other functions				
LYST	Lysosomal trafficking regulator	Lysosomal fission; secretory lysosome exocytosis	Chediak-Higashi syndrome, PD	(Durchfort *et al.*, 2012; Sepulveda *et al.*, 2015; Weisfeld-Adams *et al*., 2013)
ZFYVE26	Spastizin (SPG15)	Autophagic lysosome reformation	Hereditary spastic paraplegia	(Chang *et al*., 2014)
SPG11	Spatacsin	Autophagic lysosome reformation	Hereditary spastic paraplegia	(Chang *et al*., 2014)
TARDBP	TAR DNA binding protein (TDP-43)	Regulation of TFEB translocation and dynactin expression	ALS, FTD	(Xia *et al.*, 2016)
C90RF72	C90RF72	Regulation of mTORC1 signaling	ALS, FTD	(Amick *et al*., 2016)
FIG 4	FIG 4	Regulation of phosphoinositide signaling	ALS, Charcot-Marie-Tooth disease type 4J	(Chow *et al*., 2009; Chow *et al.*, 2007)
GRN	Progranulin	Unclear; enhances lysosome acidification	FTD, NCL	(Tanaka *et al.*, 2017)
SYT11	Synaptotagmin 11	Unclear; required for proper lysosomal acidification	PD	(Bento *et al*., 2016)
TMEM106B	Transmembrane protein 106B	Unclear; upregulation induces lysosome enlargement	FTD	(Brady *et al*., 2013; Van Deerlin *et al*., 2010)
Lysosomal substrates				
MAPT	Microtubule associated protein tau	CMA substrate; mutants block CMA	PD, FTD	(Wang *et al*., 2009)
SNCA	α-Synuclein	CMA substrate; mutants block CMA	PD, FTD	(Bougea *et al*., 2017; Cuervo *et al.*,
LRRK2	Leucine rich repeat kinase 2	CMA substrate; mutants block CMA	PD, FTD	(Dachsel *et al*., 2007; Orenstein *et*
UCHL1	Ubiquitin C-terminal hydrolase L1	CMA substrate; mutants block CMA	PD	(Kabuta *et al*., 2008)

Legend: AD (Alzheimer's disease), ALS (Amyotrophic Lateral Sclerosis), FTD (Frontotemporal Dementia), iNCL (infantile Neuronal Ceroid Lipofuscinosis); NCL (infantile Neuronal Ceroid Lipofuscinosis).PD (Parkinson's disease).

1.6. Macroautophagy pathway

The maintenance of cellular homeostasis is critical for cellular survival and is achieved through the continuous recycling and degradation of damaged cellular components. Autophagy is a major catabolic process, which facilitates the intracellular degradation in a lysosome-dependent manner (Levine and Klionsky, 2004). Furthermore, autophagy also enables the adaptation to metabolic stress, the clearance of pathogens and provides the only cellular mechanism for the disposal of entire organelles. This section is going to focus on the most thoroughly characterized pathway, macroautophagy, commonly known as autophagy. The latter is often referred to as a non-selective process, however more specialized forms of macroautophagy have been described based on the cargo that is being targeted (Lamb;Yoshimori and Tooze, 2013). Macroautophagy can be distinguished from other modes of autophagy by the assembly of specialized cytosolic vesicles

known as autophagosomes, which enable cargo transport to lysosomes over the course of 5 stages - initiation, nucleation, elongation, fusion, and degradation (Figure 5) (Feng *et al*., 2014). The process is initiated as cytoplasmic material begins to be enveloped by the double membrane of the phagophore. The membrane sac then stretches to accommodate damaged debris and upon sealing an autophagosome is formed. The autophagosome merges with lysosomes to give rise to an autolysosome, whereby cytoplasmic cargo is hydrolyzed by lysosomal proteases, and released into the cytoplasm (Lamb;Yoshimori and Tooze, 2013). Autophagosome formation is initiated in response to signals of nutrient deprivation or stress, whereby the Ser/Thr kinases ULK1 and ULK2 are released from the inhibitory action of mTORC1. The following occurs following the activation of the RALB GTPase, which induces the recruitment of an EXO84- vesicle complex (Bodemann *et al*., 2011). The EXO84- vesicle complex sequesters mTORC1, bringing ULK1 and the PI3K complex closer to each other and to the site of phagofore assembly (PAS), the omegasome (Lamb;Yoshimori and Tooze, 2013).

The omegasome is an extension of the endoplasmic reticulum (ER) marked by the presence of PtdIns(3)P-binding protein DFCP1 (Axe *et al*., 2008). At the omegasome ULK1 and ULK2 attach to the membrane via their conserved C- terminal domains to facilitate the recruitment and phosphorylation of Atg13, FIP200 and Atg101, comprising the ULK1 complex (Chan *et al*., 2009). A crucial step for the nucleation of the autophagosome is the activation of the phosphatidylinositol 3-OH kinase (PI3K) complex via the phosphorylation of Beclin1 at Ser15 and the lipid kinase VPS34 at Ser249 by ULK1 (Egan *et al*., 2015; Russell *et al*., 2013). Activation of VPS34 enables PtdIns(3)P synthesis at the isolation membrane of the autophagosome (Dooley *et al*., 2014) and promotes further autophagosome maturation by mobilizing WIPI and the Atg12-Atg5-Atg16 complex. WIPI facilitates the recruitment of ATG16 (Fujita *et al*., 2008) and the subsequent assembly of the ATG5/12/16L1 complex (Dooley *et al*., 2014). The latter carries out lipidation and attachment of microtubule-associated protein 1A/1B-light chain 3 (LC3) to the autophagosomal membrane, which is a major prerequisite for the elongation of the autophagosome (Tanida;Ueno and Kominami, 2008; Kabeya et al., 2004). The process of lipidation entails the conjugation of cytosolic LC3 (LC3-I) to phosphatidylethanolamine (PE) (Sou *et al*., 2006; Ohsumi, 2001) which is catalyzed by the E1 enzyme Atg7 and subsequently converted to LC3II via the E2 enzyme Atg3 (fig.4) (Tanida *et al*., 2001; Tanida *et al*., 2002; Tanida;Ueno and Kominami, 2004). Atg5–Atg12/Atg16 has been reported to bind to the isolation membrane and mediate a more efficient recruitment of Atg3 to autophagosomes, ultimately accelerating LC3 conjugation to PE (Romanov *et al*., 2012). Furthermore, the highly conserved Atg9 core autophagy protein has been implicated in the transport of Atg proteins as well

as the delivery of membrane constituents (Suzuki *et al*., 2001; Reggiori *et al*., 2004; Reggiori and Klionsky, 2006; Yen *et al*., 2007). Once the isolation membrane has fully enclosed around cellular cargo, the autophagosome can be trafficked to lysosomes. Atg proteins disengage from the mature autophagosome and LC3II can interact with p62 inside the autophagosome to facilitate the degradation of ubiquitinated cargo (Pankiv *et al*., 2007; Rogov *et al*., 2014). As a result, p62 is continuously degraded (Klionsky *et al*., 2008). The localization of SNARE protein syntaxin 17 (Stx17) to the outer membrane of the autophagosome marks the completion of autophagosome maturation. Of note, the interaction of Stx17 with Synaptosomal-associated protein 29 (SNAP29) and Vesicle-associated membrane protein 8 (VAMP8) on lysosomes is considered to be critical for autophagosome-lysosomal fusion to occur (Itakura; Kishi-Itakura and Mizushima, 2012). Finally, autolysosomal cargo is degraded by lysosomal proteases (Figure 5).

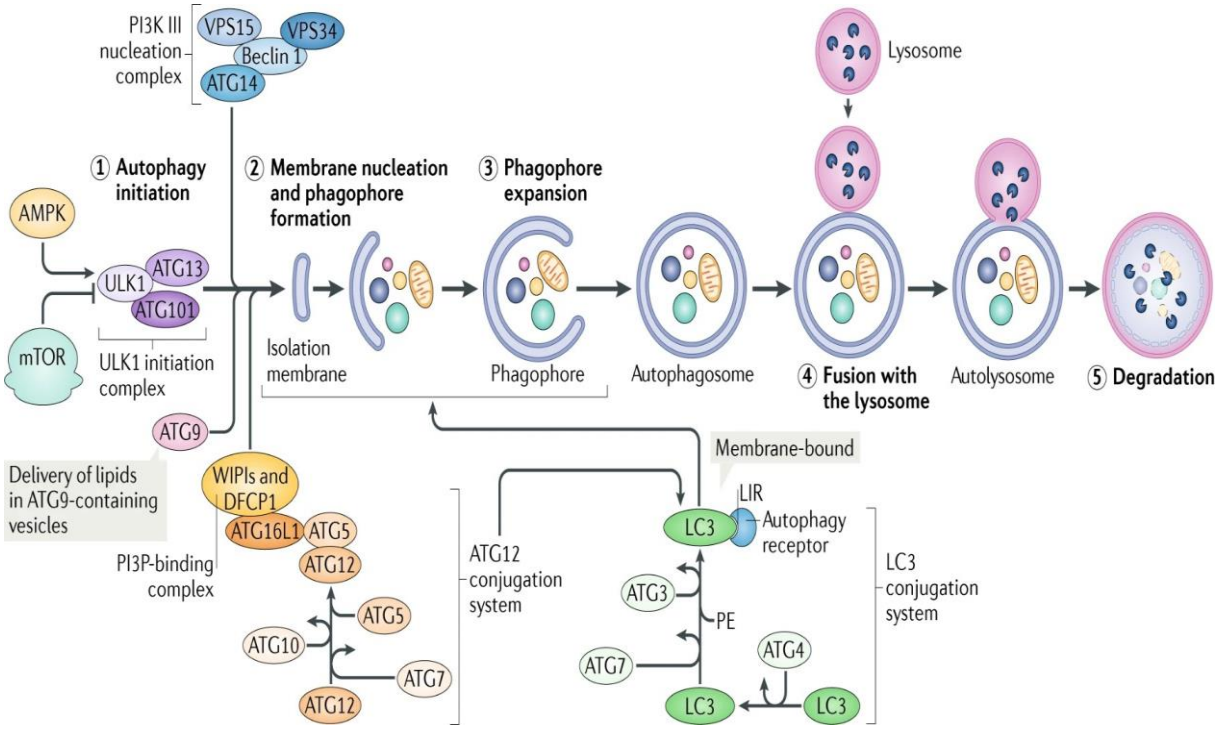

Figure 5. Macroautophagy process. Autophagosome formation is initiated at the site of phagofore assembly following inhibition of mTOR and the consequent activation of the ULK1 complex, which activates PI3K synthesis. The PI3K complex encompasses proteins such as BECN1, VPS34, VPS15 and Atg14. Recruitment of WIPI and assembly of the Atg5-Atg12/Atg16 complex sets the scene for phagofore nucleation and double membrane expansion of the nascent autophagosome. Elongation of the isolation membrane is facilitated by consecutive ubiquitin-like reactions mediated by Atg4 and Atg3. The function of Atg4 and Atg3 enable the conjugation of LC3 to PE and conversion to LC3II, respectively. The maturing autophagosome then fuses with the lysosome to form an autolysosome. Within the autolysosome, cargo is degraded and recycled constituents are made available for the cell to reuse. Image is taken from Hansen *et al*. 2018.

1.7 Lysosomes as key effectors of metabolic adaptation.

Apart from carrying out an indispensable role in cellular degradation, lysosomes act as crucial responders to environmental stress. Recent evidence suggests that lysosomes are able to integrate key signals regarding nutrient abundance and instigate an appropriate metabolic response which is orchestrated by the continuous cellular repositioning of lysosomes. During anabolic conditions when nutrients are replete, the transcription factor EB (TFEB) remains cytosolic due to phosphorylation by mTORC1 present on the lysosomal surface. By contrast, conditions of nutrient starvation result in the inactivation of mTORC1 leading to TFEB dephosphorylation and its localization to the nucleus where it can induce the expression of CLEAR genes (Coordinated Lysosomal Expression And Regulation) to initiate autophagy and upregulate lysosomal biogenesis (Napolitano and Ballabio, 2016) (Figure 6).

The vATPase-SLC38A9-Ragulator-Rag complex enables the sensing of nutrients and relays information regarding nutrient availability. The vATPase pump is a lysosomal protein which carries out lysosomal acidification but also enables the activation of mTORC1 based on a mechanism of amino acid detection in the lysosomal lumen (Zoncu *et al*., 2011). Similarly, the transmembrane lysosomal protein SLC38A9 allows for the detection of amino acids and cholesterol in addition to also carrying out roles as an amino acid transporter (Wang *et al*., 2015a; Castellano *et al*., 2017). Together, these two protein nutrient sensors stimulate Ragulator GEF activity towards Raga proteins to promote the lysosomal anchoring of mTORC1 and its activation by Rheb during anabolic growth (Bar-Peled *et al*., 2012; Long *et al*., 2005). This culminates in the cytosolic sequestration of TFEB. Conversely, nutrient deprivation triggers a catabolic switch leading to the disassociation of mTORC1 from the lysosomal membrane, the dephosphorylation of TFEB and TFEB nuclear translocation (Zoncu *et al*., 2011; Castellano *et al*., 2017; Wang *et al*., 2015a). A crucial step leading to the displacement of mTORC1 from the lysosomal membrane is deemed to be the coupling of vATPase and Ragulator with Axin resulting in AMPK activation (Zhang *et al*., 2014).

The lysosomal response to nutrient availability and metabolic stress also encompasses a change in the lysosome Ca^{++} (Figure 6). Lysosomes are now being increasingly recognized as prominent stores of Ca^{++} which could pertain to the frequent ion exchange between lysosomes and the ER (Waller-Evans and Lloyd-Evans, 2015). Indeed, studies have shown that aberrant Ca^{++} lysosomal levels are important contributing factors to the development of Niemann-Pick disease type C, juvenile Neuronal Ceroid Lipofuscinosis (*CLN3*), Alzheimer's and Parkinson's disease and

Frontotemporal dementia (FTD) (Waller-Evans and Lloyd-Evans, 2015). Emerging lysosomal regulators of calcium efflux appear to be the TRPML and TPC Ca^{++} pore receptors which can be rendered active by PI (3,5) P_2 (phosphatidylinositol 3,5-bisphosphate). Furthermore, the activity of TPC can be induced by NAADP (nicotinic acid adenine dinucleotide phosphate) (Morgan *et al*., 2011; Patel and Cai, 2015; Waller-Evans and Lloyd-Evans, 2015). Upon nutrient starvation (Medina *et al*., 2015) or elevated lysosomal pH (Raychowdhury *et al*., 2004), Ca^{++} release by TRPML may cause lysosomes to localize perinuclearly, TFEB to translocate and to initiate gene transcription in the nucleus. Closer proximity to the nucleus is also associated with the higher incidence of autophagy due to the enhanced fusogenic potential of lysosomes following lysosomal Ca^{++} release (Medina *et al*., 2015; Li *et al*., 2016) (Figure 6). The TPC1 receptor has also been implicated in trafficking of endolysosomal material however there is an ongoing debate as to what ion selectivity and mode of activation is truly characteristic of this ion pore channel (Cang *et al*., 2013; Morgan *et al*., 2011).

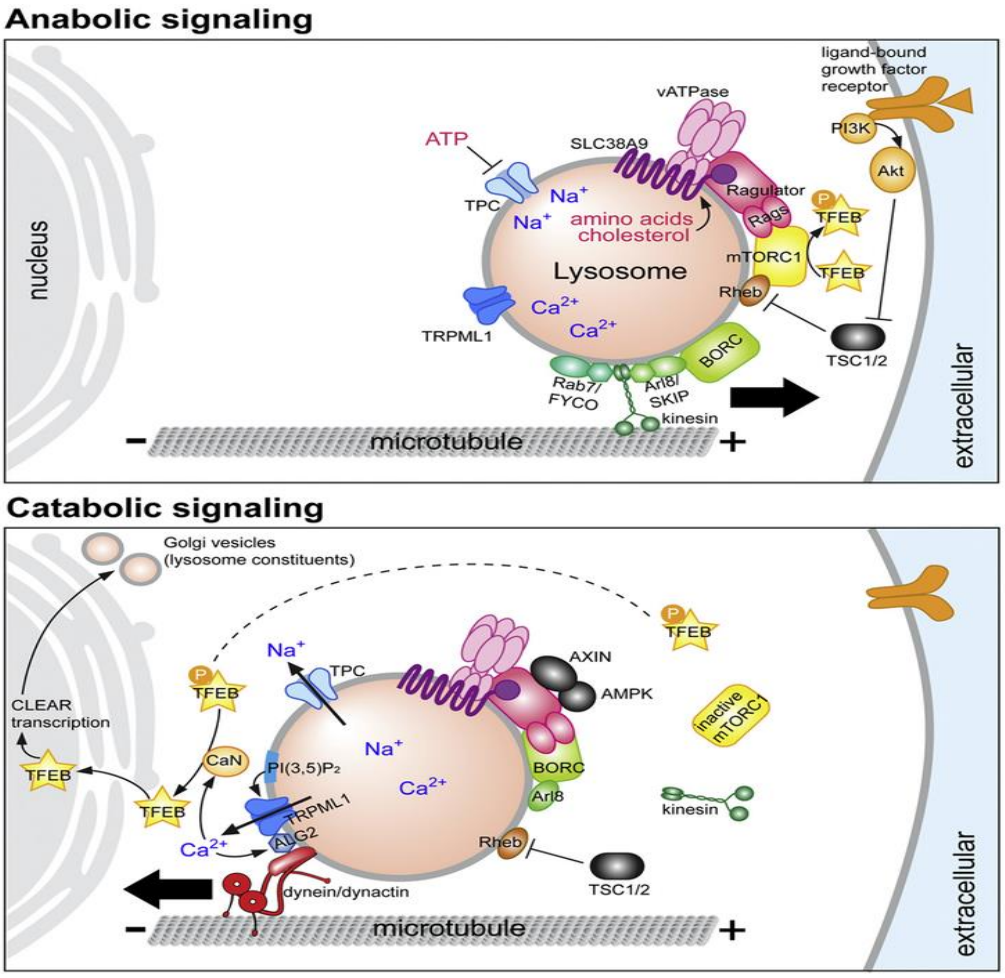

Figure 6. Lysosome signaling during anabolic and catabolic metabolic states. Top panel shows that during growth favorable conditions, mTORC1 is retained at lysosomal surface by the Rheb GTPase following initial recruitment by the vATPase-SLC38A9-Ragulator-Rag GTPase complex. This results in the phosphorylation of TFEB by active mTORC1 and its retention at the cytosol. In the meantime, BORC is free to interact with Arl8/SKIP to facilitate kinesin-mediated positioning of the lysosome in the cellular periphery where it can respond to growth factor signaling. Furthermore, when nutrient conditions are replete, Ca^{++} and Na^{+} lysosomal release from the TRPML1 and TPC lysosomal receptors is blocked, respectively. Bottom panel depicts the dynein-mediated lysosomal movement toward the nucleus following mTORC1 and Rheb inactivation in the absence of nutrient signaling. As a result, TFEB is dephosphorylated by the release of lysosomal Ca^{++} and Na^{+} and is relocated to the nucleus where it can initiate the transcription of autophagy and lysosomal genes of the CLEAR pathway. The efflux of lysosomal Ca^{++} further stimulates dynein-associated microtubule movement by ALG2, to enable relative lysosomal proximity to both the cell nucleus and incoming vesicles from the Golgi. Na^{+} lysosomal release, on the other hand, contributes to the function of the vATPase and may promote lysosomal fusogenic potential. (Wang *et al*., 2012) Image taken from Lie and Nixon, 2019.

As outline in Figure 6, the change in lysosomal positioning can have a significant impact on lysosomal function (Pu *et al*., 2016). Lysosome motility along the plus and minus poles of microtubules is facilitated by kinesin (perinuclear) (Hollenbeck and Swanson, 1990) and dynein (cell periphery) (Harada *et al*., 1998). The perinuclear localization of lysosomes, which can be induced by starvation (Korolchuk *et al*., 2011). increases the probability of autophagic clearance due to the higher concentration of endosomes and early autophagic vesicles in this cellular location (Jongsma *et al*., 2016; Willett *et al*., 2017). This may also result in the higher efficiency of endosome acidification due to the more straightforward transport of newly synthesized lysosomal hydrolases from the Golgi (Johnson *et al*., 2016). By contrast, lysosomal movement towards the cell periphery during anabolism is promoted by the association of BORC and ARL8 with kinesin microtubules (Filipek *et al*., 2017; Pu;Keren-Kaplan and Bonifacino, 2017), as well as the interaction with ER-derived kinesin via FYCO and protrudin 1 (Hong *et al*., 2017) (Figure 6). The repositioning of lysosomes towards the cell periphery ultimately facilitates an encounter between lysosomal mTORC1 and PM-associated growth factor receptors which provide instructions for anabolic growth (Korolchuk *et al*., 2011) (Figure 6).

As mentioned previously, post-mitotic neurons are highly susceptible to cell death due to an overburdening of the lysosomal system with ageing. An important disease factor is neuronal asymmetry i.e., the long distances degradative vesicles must travel in neurons to carry out efficient waste clearance. Fully acidified lysosomes are only located in the cell body of neuronal cells (Overly *et al*., 1995) and the stepwise maturation of endocytic vesicles along the retrograde axonal transport

follows a decreasing pH gradient (Overly and Hollenbeck, 1996). Studies have shown that autophagosomes starting out from the distal axon begin to merge with late endosomes via syntaxin 17 forming amphisomes as evident by the acquisition of LAMP1 and Rab7. The presence of these late endosomal proteins on the surface of newly formed amphisomes enables movement along microtubules thereby facilitating long-distance transport (Lee;Sato and Nixon, 2011; Cheng *at al*., 2015). Analogously, access to long-range means of transportation is rendered to early endosomes following the replacement of Rab5 with late endosomal marker Rab7 (Deinhardt *et al*., 2006). Along the retrograde axonal transport pathway, amphisomes and late endosomes are subjected to increasingly more acidic pH prior to finally fusing with fully acidified lysosomes of the neuronal cell body (Cheng *et al*., 2015; Lee;Sato and Nixon, 2011; Maday;Wallace and Holzbaur, 2012; Overly *et al*., 1995) (Figure 7).

Their delivery to the cell body is facilitated by the activity of microtubule motor, dynein, and an interaction with a cargo adaptor and the dynein multiunit co-factor dynactin (McKenney *et al*., 2014). The challenges posed by long-range transport are hence emerging as a significant caveat to the maintenance of neuronal tissue. Further research in favor of impaired axonal retrograde trafficking has demonstrated a close relationship between aberrant microtubule function and the development of Alzheimer's disease (Vicario-Orri;Opazo and Munoz, 2015; Iqbal *et al*., 2010). Moreover, Gowrishankar *et al*., (2015) have reported an endolysosomal trafficking defect associated with a protease deficiency due to the stalling of immature degradative structures in the axons of mice suffering from Alzheimer's disease. These studies provide evidence in support of the underappreciated role of tubular transport in neurodegeneration.

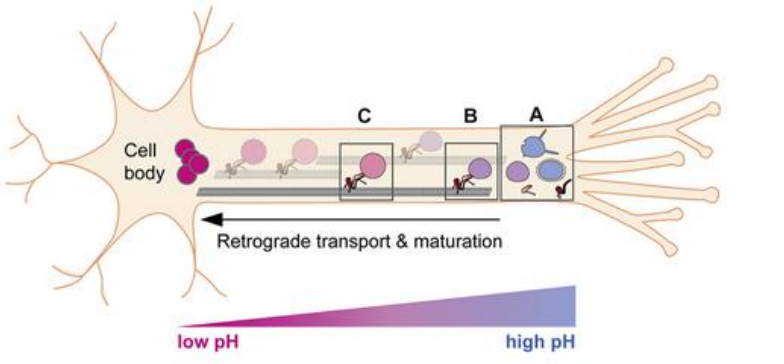

Figure 7. Retrograde transport of maturing degradative vesicles is enabled by microtubule-transport along a decreasing pH gradient. Image taken from Lie and Nixon, 2019.

Lysosomes are also important for the maintenance of neuronal synapses. Studies have shown that aberrant lysosomal activity can have profound effects on synaptic connectivity as demonstrated by the increased proteasomal clearance of the presynaptic cysteine string protein α (Sambri *et al*., 2017). Importantly, Presenilin-1 (PSEN1) and Palmitoyl-protein thioesterase 1 (PPT1) which regulate lysosomal acidification via the lysosomal targeting of vATPase (Lee *et al*., 2010; Bagh *et al*., 2017), have been shown to be essential for neurotransmitter release and the effective turnover of synaptic vesicles (Kim *et al*., 2008; Zhang *et al*., 2009). Lysosomal degradation in response to synaptic activity appears to also be important for the maintenance of dendritic spines (Goo *et al*., 2017). Further to this, enhanced synaptic activity has been shown to ameliorate Alzheimer's and FTD pathology by inducing increased autophagic clearance of pathological tau oligomers (Akwa *et al*., 2018). Collectively, these data underscore the importance of lysosomal function in the dynamic maintenance of synaptic termini and neuronal connectivity.

1.8. Stem cells.

Stem cells are unique in that they can give rise to mature cells of multiple cell lineages whilst also retaining their capacity to self-renew. They represent undifferentiated cell types whose differentiation potential can be broadly characterized based on their degree of cell fate commitment or the stage of embryonic development (Zakrzewski *et al.*, 2019). A totipotent stem cell, such as the zygote, can give rise to cells of the three germ layers as well as extra-embryonic tissue. Embryonic stem cells, derived from the inner cell mass of the blastocyst, can differentiate into all three germ layers as well as give rise to extra-embryonic tissues of the trophoectoderm (Nosi *et al.*, 2017). Multipotent stem cells represent a specialized type of niche stem cell able to give rise to multiple cell types of the same tissue. Unipotent stem cells are most restricted due to their ability to differentiate into a single cell type (Zakrzewski *et al.*, 2019).

The long-term replenishment of cycling adult stem cells in any one tissue is governed by dynamic stochastic cell fate decisions. These underlie the ability of stem cells to divide in a symmetric or asymmetric fashion. Symmetric division is proposed to be regulated at the level of the cell population via achieving a type of 'population asymmetry'. Conversely, asymmetric stem cell division, which is essential for maintaining the balance between differentiated and stem cells, may be controlled at the level of the single cell (Klein and Simons, 2011). The delicate balance between asymmetric and symmetric stem cell division is of utmost importance to the maintenance of stem cell niches in the body.

1.8.1. Induced Pluripotent stem cells.

A breakthrough discovery by Takahashi and Yamanaka in 2006 (Takahashi and Yamanaka, 2006) demonstrated that mouse embryonic and adult fibroblasts can be reprogrammed to an ESC-like state via the introduction of four transcription factors - Oct3/4, Sox2, c- Myc, and Klf4. A year later, an analogous experiment was carried out, showing that induced pluripotent stem cells (iPSCs), resembling the gene expression of embryonic cells, can be derived from reprogrammed human dermal fibroblasts (Takahashi *et al*., 2007). This milestone discovery in the stem cell field was preceded by major scientific developments in somatic cell transfer, such as the generation of viable tadpoles using the nuclei of intestinal epithelium cells (Gurdon, 1962), and the cloning of the Dolly the sheep from adult mammary gland cells (Wilmut *et al*., 1997).

1.8.1.1. Retinal differentiation from pluripotent stem cells.

The permanent loss of photoreceptors is a common feature of debilitating retinal conditions. Transplantation of photoreceptor precursors has led to the restoration of vision in murine models (Garita-Hernandez *et al.*, 2019), however, a similar approach in humans has been hindered by ethical concerns with regards to the derivation and the culturing of fetal retinal explants (Zheng, 2016). The inability of mouse retinal models to fully recapitulate retinal function is largely due to evolutionary differences in photoreceptor development between humans and mice. These differences pertain to the fact that mice lack a strictly defined ‘macula’ - the differences between the central retina and the peripheral retina are less pronounced in the mouse, despite the increased thinness of the Bruch’s membrane of the central murine retina and enhanced phagocytic load due to the higher concentration of photoreceptors in this region (Volland *et al.*, 2015). This calls into question the applicability of murine models for the study of diseases which occur as a result of an insult to the macula such as AMD. The advent of iPSC technology has successfully mitigated issues associated with the use of animal cell models by facilitating the generation of patient-derived 2D and 3D retinal models, which are more representative of human retinal biology (Bellapianta *et al*., 2022).

1.8.1.1.2. 2D Retinal differentiation.

Initial attempts at generating retinal cells were carried out using human embryonic stem cells (ESCs) in adherent conditions (Osakada *et al.*, 2009; Osakada *et al.*, 2008; Lamba *et al.*, 2006). Application of WNT and BMP inhibitors in conjunction with insulin-like growth factor-1 (IGF-1) could direct ESCs

into becoming $Pax6^+$ and $Chx10^+$ retinal progenitors (Lamba *et al.*, 2006). Furthermore, the combined use of retinoic acid (RA) and taurine in the presence of NOTCH inhibitor led to the enrichment of photoreceptor-like cells (Osakada *et al.*, 2008). Heparin and N2 supplementation further induced the formation of neurospheres under adherent conditions (Meyer *et al.*, 2009). Collectively, the outcome of these protocols did not enable the efficient derivation of photoreceptors cells highlighting the need for methods that would more faithfully recapitulate the endogenous mechanisms of photoreceptor differentiation. Although studies based on the generation of photoreceptors in 2D conditions have been successful in restoring some visual function upon transplantation in animals, these were met with considerably low rates of host engraftment, suggesting that proper retinal specification may require additional cues from the three-dimensional environment (Lund *et al*., 2006; Lamba;Gust and Reh, 2009).

1.8.1.1.3. 3D Retinal Organoids.

Morphogenesis of the retina follows the emergence of an optic vesicle from induced neural epithelium, which develops into the optic cup by invagination. The outer lining of the optic cup is further specified into RPE, whereas the inner part gives rise to the neural retina. The neural retina and the RPE thus derive from the same neuroepithelial progenitors expressing *Pax2*, *Pax6* and *Mitf* (Baumer *et al.*, 2003). Pioneering research by the Sasai group set the scene for retinal differentiation following the generation of neuronal cells from mouse ESC cells (Eiraku *et al.*, 2008; Watanabe *et al.*, 2005). Two subsequent studies on mouse and human ESCs (Eiraku *et al*., 2011; Nakano *et al.*, 2012) served as the basis for future 3D retinal organoid (RO) differentiation (Zhong *et al.*, 2014; Wahlin *et al.*, 2017; Wang *et al.*, 2015; Zhou *et al.*, 2015).The Sasai mouse ESC protocol entailed the self-organization of an optic-cup followed by the step-wise specification and invagination of the $Rx^+/Sox1^-$ neuroepithelium possessing basal-apical polarity. A crucial step for the self-autonomous organization of the optic cup and the subsequent derivation of stratified neural retina was the use of non-adherent 3D suspension culture and Matrigel (Eiraku *et al*., 2011). These ROs were consistent with the expression of all retinal cell types (photoreceptors ($Rhodopsin^+$, $Recoverin^+$), bipolar ($Chx10^+Pax6^-$), horizontal ($Calbindin^+$, $Calretinin^-$), amacrine ($Pax6^+$, $calretinin^+$) and Müller glia cells ($CRALBP^+$), ganglion cells ($Brn3^+Pax6^+Calretinin^+$), RPE ($Rx^+Pax6^+Mitf^+$)) and the presence of inner and outer nuclear layers. The improved Nakano *et al.* (2012) protocol using human ESCs was based on the combined use of WNT inhibition, Matrigel, FBS supplementation and Hedgehog activation for the differentiation of neural retina. Major differences between the mouse and the human study were the thicker neuroepithelium and apically convex curvature of the neural retina in human ROs

(Nakano *et al.*, 2012). It was observed that the derivation of rod (NRL^+) and cone ($RXR\gamma^+$) precursors could be improved upon Notch inhibition. Furthermore, the photoreceptor layer contained primitive connecting cilia but no POS. This study was able to demonstrate for the first time the *in vitro* generation of human neural retina and RPE (Table 2).

***Table 2. Key developments in the differentiation of 3D Retinal Organoids*:** Table taken from Bellapianta *et al*., 2022. Main protocol differences are outlined in bold.

Study	Cell Source	Culture	Culture Diff.	Prot. Length	Tissues Produced	Notes
Lamba *et al* ., 2006	hiPSCs	Matrigel-coated dishes. **noggin, DKK1, IGF1** for 3 w.	Cells cultured in N2/B27 medium	60 d	NR by d2; OC by d25; Rods PRs and OF by 6 w	First 2D retinal cells from ESCs
Nakano *et al* ., 2012	hESCs	Matrigel KSR medium + **IWR-1e,**	FBS, SAG for 6 d, DMEM/F12+N2 medium	126 d	Bi-layered OC of NR and RPE PRs d126	3D method improvement
Phillips *et al* ., 2012	Blood-derived hiPSCs	Cell aggregates in KSR for 4 d. N2 + **heparin** for 2d	Aggregates on 10 d. d16, neural clusters in B27 medium. d20, OVs maintained in adherent culture.	50 d	OVs by d20; NR or RPE d40; NR rosettes d50	
Zhong *et al* ., 2014	hiPSCs	Cell aggregates in mTeSR1 medium with **blebbistatin.** Medium gradually transitioned into N2 + heparin.	d16, B27 medium. w4, aggregates detached. d42, medium with FBS, **taurine**. Addition of **RA** for PR maturation.	21 w	NR; 3D retinal cups on d21–28; rhodopsin+ PRs by w21.	First 3D/2D method to describe mature and light-responding PRs
Reichman *et al* ., 2014	hiPSCs	Confluent culture without FGF2 for 2 d, Medium transitioned into N2.	d14, neural clusters floating in N2 + **FGF2**; pigmented patches isolated on gelatin. FGF2 removed at d21	30 d	Rapid diff. of NR and RPE; NR rosettes d42	First 2D/3D method; NRV excision
Zhou *et al* ., 2015	hESCs hiPSCs	EBs cultured in KSR + B27, **noggin**, **DKK1**, **IGF1** for 3 d.	Adherent culture in N2/B27 + noggin, DKK1, IGF1, **COCO**, **FGF2** 4 w.	5 w	Cones PR d35; polarized cone PRs + CC + OS d60	
Singh *et al* ., 2015	hESCs	Dense colonies in mTeSR1 + FGF2. Medium changed to FGF2-free Neurobasal medium + **noggin.** d3, N2/B27 added.	2 w + FGF2, 4 w **DKK1**+ **IGF1** for 1 w. Neurobasal medium + **noggin, FGF2, FGF9** for 12 w.	12 w	Four retina layers: RPE, early PRs, INL and RGCs	
Lowe *et al* ., 2016	hESCs hiPSCs	Cell gelling for 30 min Floating	d12–17, detach adherent cultures;	25–30 d	NR, ciliary margin, and	Spontaneous formationof NR
Völkner *et al* ., 2016	hESCs	ROs in KSR + **ROCKi** + **IWR1e** 12 d, + Matrigel + FBS + SAG	ROs cut into 5 parts in N2 + FBS + **EC23** 41 d.	41 d	cone or rod PRs.	
Hunt *et al* ., 2017	hESCs hiPSCs	EBs in mTeSR1 + **ROCKi**.	d3, KSR + **IGF1** + B27; d5–9, + FBS d12, EBs	45 d	NR and RPE	
Capowski *et al* ., 2019	hESCs hiPSCs	hPSCs in mTeSR1 +	d6, + **BMP4**, d16, B27 + FBS	175 d	Highly developed	staging system of ROs. BMP4
Kaya *et al* ., 2019	hESCs hiPSCs	Cells in E8 + Matrigel. EBs lifted and weaned in N2 + Heparin 16 d.	d16, B27 + FBS; d42, + **taurine**; d63, + **9-cis retinal**; d92, half conc. + N2.	200 d	NR and cone, rod PRs	9-cis retinal enhance rod PRs
Zerti *et al* ., 2021	hESCs	Cells in mTESR + Matrigel + ROCKi KOSR + B27 + IGF-1 18d	d18, + **RA** + **IGF-1** + **T3** + **Taurine**; d37, N2/B27 + IGF-1	90 d	NR, RPE, lens and cornea; PRs by d90	IGF-1 increases the formation of laminated NRVs.

Legend: hiPSC (human induced pluripotent stem cells); ESCs (embryonic stem cells); PR (photoreceptors); NR (neural retina); NRVs (neuroretinal vesicles); EB (embryoid bodies); KSR (knock-out serum replacement); CC (connecting cilium); OV (optical vesicle); OC (optic cups); OF (optic fibers); d (days); w (weeks); m (months).

1.8.1.1.4. 2D/3D Retinal Differentiation.

The first 3D to 2D protocol to report the generation of light responsive organoids was described by Zhong *et al*. (2014). This was achieved by building on the observations made by Meyer *et al*., (2009). that retinal cells can arise under 3D conditions without the need for extrinsic signaling factors. Crucial for the generation of photoreceptor cells was the timely exposure of RA which was deemed to promote photoreceptor outer segment maturation. The reverse approach of initially culturing neuroepithelial structures under adherent conditions and transitioning them to suspension culture following excision was also demonstrated (Reichman *et al.*, 2014). Despite being able to produce photoreceptor cells, this protocol failed in generating neural retina lamination characteristic of protocols based on the initial formation of embryoid bodies (Reichman *et al.*, 2014). An adapted 2D/3D protocol by Gonzalez-Cordero *et al.*, (2017), succeeded in generating photoreceptors with primitive outer segments in the presence of neural supplementation (N2, B27, taurine, FBS and RA). The generation of somewhat mature photoreceptors was also demonstrated by the formation of epithelial cysts from floating hESC culture (Lowe *et al.*, 2016).

1.8.1.1.5. Further protocol development.

Research by various groups over time revealed stepwise optimization steps by which RO derivation could be improved. For instance, the application of ROCKi (Rho-associated kinase) inhibitor can significantly enhance the survival of pluripotent stem cells in protocols relying on the initial dissociation and subsequent aggregation of the starting pluripotent cells (Osakada *et al.*, 2009; Shirai *et al.*, 2016; Compagnucci *et al.*, 2015). Implementation of BMP4 was proven to have a neuroepithelial induction effect as demonstrated by the reproducible derivation of 3D ROs leading to a significant reduction of the inconsistencies associated with retinal differentiation (Capowski *et al.*, 2019; Kuwahara *et al*., 2015). The combined approach of a Bmp4- neuroepithelium induction and an induction-reversal by FGFR inhibition resulted in the generation of ROs of a higher neuroepithelial integrity (Kuwahara *et al*., 2015). The formation of a stem cell niche at the neural retina - RPE boundary reported in this study greatly facilitated the specification and expansion of the neural retina. Moreover, research conducted by the Lako group, has shown that the application of IGF-1 significantly improves RO lamination and supports photoreceptor development (Mellough

et al., 2019; Zerti *et al.*, 2021). An adaptation of the Kuwahara protocol by the Lako group was able to generate light-responsive ROs from hiPSCs and additionally show that the induction of neuroepithelium by BMP4 and IGF-1 is cell line specific (Hallam *et al*., 2018). The application of 9-cis-retinal and thyroid hormone by different groups promoted for the development of rods and cones, respectively (Eldred *et al.*, 2018; Kaya *et al.*, 2019). Further methods employing Matrigel embryoid body encapsulation and agarose supported the maintenance of retinal ganglion cells and the overall efficiency of the differentiation procedure (Wagstaff *et al.*, 2021; Cowan *et al.*, 2020). More recently, a paper by West *et al*., (2022) reported that the use of antioxidants and BSA-bound fatty acids dramatically improves the formation of photoreceptor outer segments and disc formation in both cones and rods. Major problems encountered with 3D RO culture still are the high levels of batch-to-batch variability (Volkner *et al*., 2016), the differential differentiation capacity of iPSC lines (Hallam *et al*., 2018), the inaccurate representation of neurons residing in the inner nuclear layer (Llonch; Carido and Ader, 2018). Future work using automated platforms may hold promise for reducing some of variability seen with 3D RO generation (Kegeles;Perepelkina and Baranov, 2020).

1.8.1.1.6. RPE differentiation

RPE represents a single postmitotic layer of pigmented cells responsible for the recycling of photoreceptor outer segments. RPE-differentiated cells exhibit visible pigmentation, a hexagonal morphology, the polarized secretion of VEGF and PEDF as well as the ability to phagocytose photoreceptor OS *in vitro* (Idelson *et al.*, 2009; Rowland *et al*., 2013; Buchholz *et al*., 2013). In view of the significant health repercussions associated with visual decline, efforts have been directed towards the derivation of transplantable RPE tissue.

Observations made by the pioneering work of the Sasai group suggested that pluripotent stem cells may exhibit an inherent propensity for retinal differentiation as their 'default' developmental programme in the absence of additional stimuli (Eiraku *et al*., 2011; Nakano *et al*., 2012). Indeed, one of the very first accounts of RPE generation was following the spontaneous *in vitro* differentiation of hESCs (Klimanskaya *et al*., 2004). Early protocols for RPE differentiation entailed the use of morphogens during early neuroectoderm specification as well as the late stages of RPE differentiation (Rowland; Buchholz and Clegg, 2012; Meyer *et al*., 2011; Zahabi *et al*., 2012). Considerable improvement of the RPE yield was observed upon introduction of nicotinamide to suspension culture which was further augmented by Activin A (Idelson *et al.*, 2009). RPE

differentiation with more than 50% percent of *Mitf* positive cells after two-months of differentiation was reported following the sequential addition of noggin, bFGF, RA, and Shh (Zahabi *et al*., 2012). A significant increase in pigmented cells (80%) was demonstrated through the combined use of IGF1, Noggin, Dkk1, bFGF, nicotinamide, Activin A, SU5402, and VIP (Buchholz *et al*., 2013). An even higher efficiency of RPE derivation from mouse iPSCs was observed following activation of Wnt by CHIR99021 in combination with MERK/ERK (SU5402) and ROCK inhibitors (Y27632). This led to acquisition of apical-basal polarity, the expression of tight junction markers as well as the ability of these RPE cells to phagocytose outer segments (Iwasaki *et al*., 2016). An adaptation of this protocol led to the rapid derivation of RPE cells in two weeks (Foltz and Clegg, 2017).

Despite the significant success in differentiating RPE cells from iPSCs, considerable effort is still being directed at generating RPE in a high-throughput manner. Similarly, to what has been observed with RO differentiation, the efficiency of the procedure is largely influenced by ESC and iPSC line variability (Rowland *et al*., 2013; Zhu *et al*., 2013). Moreover, most of the protocols relied on the manual excision of pigmented differentiated cells from non-pigmented cells. Choudhary *et al.* (2017) first published a protocol, which describes efficient RPE monolayer differentiation in xeno-free conditions, without the need for manual dissection and re-plating of the RPE patches. More recently, a 'directed differentiation protocol' has been devised based on the sequential application of Nicotinamide, Activin A and Chir99021. This method allowed for a significant improvement in RPE yield over the course of two months, leading to the efficient derivation of a highly enriched RPE population. The study was based on an automated robot system allowing for large-scale RPE cell production which circumvented the need for manual cell enrichment. (Regent *et al*., 2019). Future continued effort in the high-throughput production of RPE cells will significantly increase the translational value of RPE research (Truong *et al.*, 2021; Matsumoto *et al.*, 2019).

1.9. CRISPR-Cas genome editing.

The CRISPR-Cas9 system is a genome editing technique that has gained increasing popularity for its ease of manipulation and high target specificity. A CRISPR endonuclease Cas9 derived from *Streptococcus pyogenes* and a single-guide RNA (sgRNA) can be utilized to form a ribonucleoprotein (RNP) complex, which can be targeted to genomic DNA (Ran *et al*., 2013). The targeting specificity of the Cas9 complex is defined by the 20 nucleotides of base pairing between the crRNA region of the gRNA and the target DNA strand. Once targeted to the site of genomic interest via sequence complementarity of the gRNA, wild-type Cas9 can cleave the DNA target by recognizing a conserved

NGG PAM (protospacer-adjacent motif) motif. This in turn, leads to the activation of the double strand break (DSB) repair machinery (Figure 8). Once formed in genomic DNA, DSBs can either be repaired by the error-prone Non-Homologous End Joining (NHEJ) pathway, leading to the introduction of insertions and/or deletions (indels), or the homology-directed repair (HDR) pathway which allows for more precise gene editing (knock-in). Although CRISPR/Cas9 can be used to produce gene knockouts by employing NHEJ with relative ease (Cong *et al*., 2013; Dow *et al*., 2015; Platt *et al*., 2014; Wang *et al*., 2013), introduction of single nucleotide corrections by HDR remains relatively inefficient and can be corrupted by the presence of additional indels (Inui, *et al*., 2014). A downside to HDR is its limitation to the S/G2 cycle, hence its efficiency is often negligible compared to NHEJ (Heyer; Ehmsen and Liu, 2010; Lin *et al.*, 2014; Cong *et al.*, 2013; Mali *et al.*, 2013). Recent studies in the field have successfully demonstrated that the delivery of Cas9 as an RNP molecule, the design of the gRNA and donor DNA template as well as the use of a DNA ligase IV inhibitor can significantly improve HDR efficiency in human cells. (Maruyama *et al*., 2015; Liang *et al*., 2017; Liu *et al.*, 2019; Paquet *et al*., 2016; Richardson *et al*., 2016; Okamoto *et al*., 2019). A publication by Quadros *et al*., (2017) further described the generation of *Easi*-CRISPR (*E*fficient *a*dditions with *s*sDNA *i*nserts-CRISPR) which enables the manipulation of conditional insertions using a long ssDNA template.

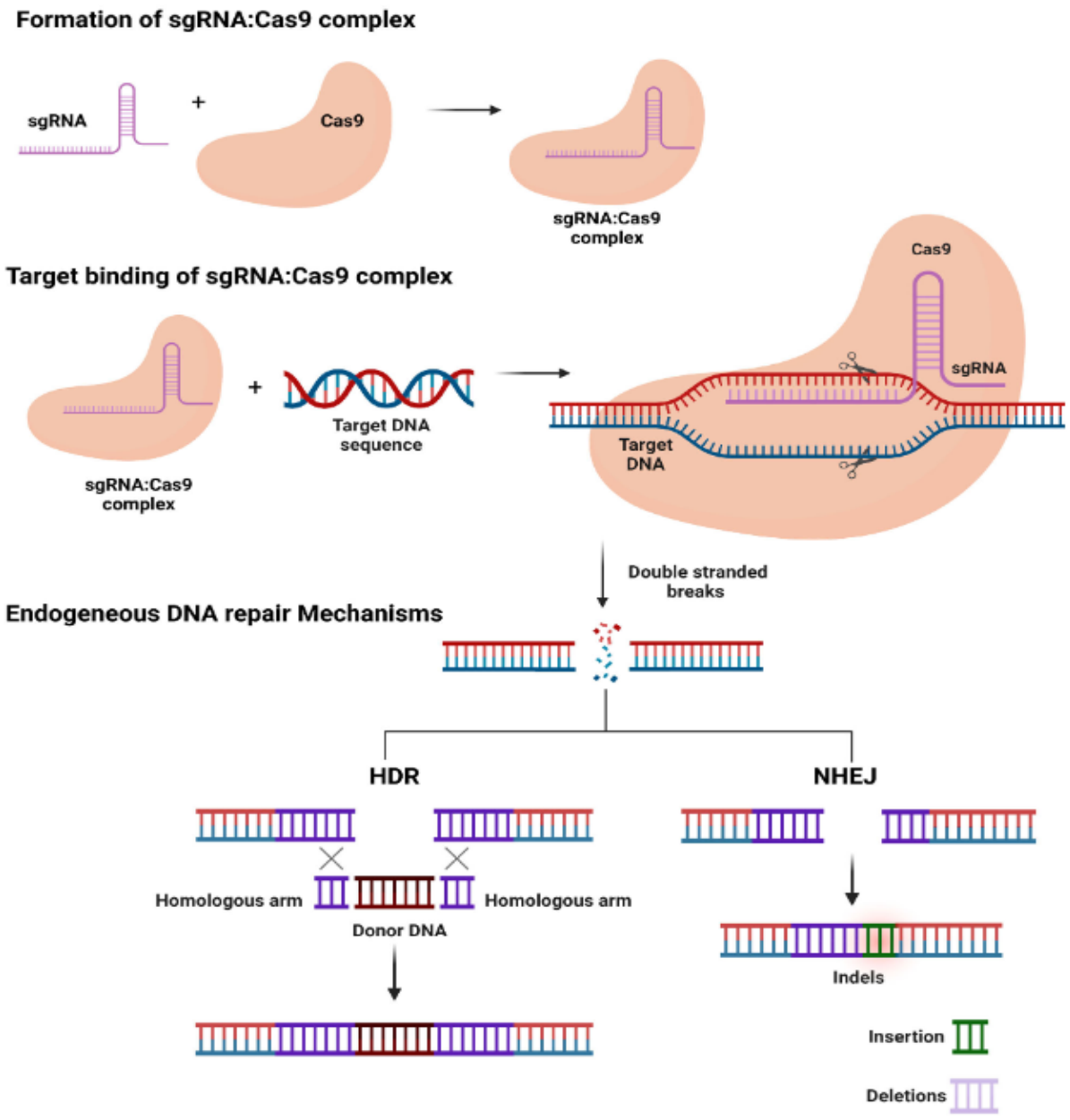

Figure 8. CRISPR-Cas9 mechanism of gene editing. sgRNA forms a complex with Cas9 protein and targets genomic DNA via sequence complementarity of the sgRNA. Cas9-mediated cleavage can occur 3 nucleotides upstream of the PAM motif in genomic DNA. This results in the generation of double strand breaks which can be resolved through the Non-Homologous End Joining pathway which often results in insertions or deletions. Alternatively, double strand breaks can be repaired at a single nucleotide by the high-fidelity Homology Directed Repair pathway by using a donor DNA template. Image taken from Sundaresan *et al*., 2023.

Despite the ongoing adaptations of the standard CRISPR-Cas9 system, gene editing still posed challenges associated with low editing efficiency, precision, and high off-targeting rates. This prompted the scientific community to devise novel ways of optimizing and diversifying the already available CRISPR editing toolbox, starting off with the type of CRISPR-Cas enzyme being used. Other

than Cas9 the most commonly used Cas enzyme is Cas12a, which is endogenous to *Acidaminococcus* and *Lachnospiraceae* bacteria. Cas12a is a gRNA-dependent endonuclease which recognizes T-rich PAM sequences (Zetsche *et al*., 2015). Furthermore, a modified 'dead' Cas9 (dCas9), which is devoid of cleavage activity has been used for targeted gene disruption. This method is known as CRISPR interference (CRISPRi) and has been particularly useful for the silencing of DNA transcription (Qi *et al*., 2013). By contrast, Cas13 enzyme represents an alternative to siRNA knockdown which can be used to block the mRNA translation (Abudayyeh *et al*., 2017). Further to the development of dCas9 and nCas9 (single strand cleavage activity, 'nickase'), which avoid the introduction of DSBs and therefore the high risk of unwanted indels, inversions or translocations, CRISPR base editing has facilitated the implementation of single base-pair corrections in the absence of template donor DNA in both dividing and non-dividing cells (Gaudelli *et al*., 2017; Komor *et al*., 2016; Porto *et al.*, 2020; Anzalone;Koblan and Liu, 2020). Between cytosine base editors (CBEs) and adenine based editors (ABEs), four base pair conversions are possible (C to T, T to C, A to G, G to A), however, some prominent shortcomings of this method are the constraints of the editing window, off-target deamination of cytosine to uracil and the occurrence of bystander mutations (Jeong;Song and Bae, 2020). A state-of-the-art CRISPR Prime Editing technique holds great promise for enabling the next generation of CRISPR-Cas editing. Prime Editing entails the use of a nCas9, murine leukemia virus reverse transcriptase and a prime editing RNA (pegRNA) and can carry out all 12 possible base pair conversions. This promising technique can be manipulated for a larger scope of genetic manipulations with higher precision (no DSBs or exogenous template needed) and fewer off-targeting effects (Sen;Sarkar and Mukhopadhyay, 2023; Huang and Liu, 2023).

1.9.1. CRISPR-Cas application for the treatment of visual impairment.

A decade since its original inception as a genetic engineering tool, CRISPR can now be used for a range of applications including single-nucleotide gene corrections, DNA transcriptional and RNA translational modifications (Li *et al.*, 2023). Despite many of the challenges associated with CRISPR techniques, significant progress has been made towards their application for the treatment of visual impairment (Sundaresan *et al.*, 2023). Due to representing an isolated immune-privileged location which has an easy access and requires minimal injection volumes for therapeutics, the eye represents an ideal experimental target for CRISPR-Cas9. Jain *et al*. (2017) was the first study to demonstrate the reversal of ocular phenotype using CRISPR-Cas in an *ex vivo* cultured human model. In this study they were able to show the targeted disruption of the dominant-negative *MYOC* gene associated with glaucoma both *in vitro* and *in vivo*. A combined AAV and CRISPR-Cas9 approach

knocking out *aquaporin 1* (*AQP1*) also led to the amelioration of glaucoma related phenotype (Wu *et al.*, 2020). Further studies have demonstrated the successful targeting of *VEGFA using* Cas9 ribonucleoproteins in an AMD mouse model (Kim *et al.*, 2017). A *CEP290* cryptic splice site which is associated with Leber Congenital Amaurosis 10 (LCA) was successfully targeted by SpCas9 in an *in vitro* proof-of-principal cellular model (Ruan *et al.*, 2017). The authors of the study went on to also delete this pathogenic intronic variant in mice by using a dual AAV approach. Considering the success of CRISPR in the removal of mutant alternatively spliced *CEP290* variants, a pioneering clinical trial enabled the restoration of vision in LCA patients carrying the pathogenic intronic variant using a similar approach (NCT03872479). This success demonstrated that CRISPR-Cas editing can be particularly useful for the treatment of dominant negative traits and can be superior to AAV in the case of large genes such as *CEP290* (Hernandez-Juarez;Rodriguez-Uribe and Borooah, 2021). Analogously, the targeting of dominant retinitis pigmentosa (RP)-associated variants has also been reported in murine models (Giannelli *et al.*, 2018; Patrizi *et al.*, 2021). CRISPR-Cas9 has furthermore been used to restore the WT expression of *RPE65* in the RPE of an LCA *rd12* mice model (Jo *et al.*, 2019). As *RPE65* mutations affect cone expression, adenine base editing (ABE) in mice was able to significantly improve LCA cone-related phenotype (Choi *et al.*, 2022). Furthermore, HDR-based approaches have also been successfully demonstrated for the treatment of RP in animal models (Cai *et al.*, 2019; Wu *et al.*, 2016). Collectively, these recent developments have uncovered the great potential of CRISPR-Cas for the treatment of deleterious eye conditions. Consistent improvements in the field affecting the precision of CRISPR-Cas editing will facilitate more clinical trials in the not so distant future.

1.10. Aims and objectives.

It was the aim of this study to gain an in-depth understanding of how *DRAM2* mutations may contribute to disease mechanisms in patient-derived 3D Retinal Organoids and RPE. Key objectives included:

- ✓ The generation of isogenic CORD21 iPSC controls and their characterization for pluripotency, genomic stability, Sendai virus clearance and off-target sequencing. This entailed the characterization of CORD21-P1c and the generation of CORD21-P2c (**Chapter 3: CRISPR-Cas9 correction of the CORD21-P2 line).**

- ✓ The differentiation of patient-derived iPSCs alongside isogenic and wild-type controls to 3D Retinal Organoids and RPE. To this end we have successfully generated Retinal

Organoids and RPE from two patient (CORD21-P1 and -P2) and two isogenic (CORD21-P1c and -P2c) iPSC lines alongside a WT control (**Chapter 4: Assessment of lysosomal activity in CORD21 Retinal Organoids).**

- ✓ To understand the impact of *DRAM2* mutations on retinal tissues using a combination of molecular assays. For the purposes of DRAM2 antibody validation we have conducted siRNA knockdown, qPCR, Immunofluorescence and Western blot analyses. To characterize the mechanisms of CORD21 disease in Retinal Organoids and RPE we have performed a combination of experimental approaches including Autophagy flux, Immunofluorescence, TEM, TEER, ELISA, Western Blot, Enzymatic activity, Proteomics and Lipidomics analyses (**Chapter 5: Assessment of lysosomal activity in CORD21 Retinal Pigment Epithelial cells).**

Chapter 2: Materials and Methods

2. Materials and methods.

2.1. iPSC culture.

iPSCs were maintained under standard incubator conditions at 37°C, 95% humidity and 5% $C0_2$. Routine cell maintenance was carried out in a laminar flow hood cabinet using an aseptic technique. All patient-derived iPSCs (Table 3) were grown and expanded on 6-well Matrigel-coated plates (Corning, USA) using mTeSR™ Plus cell culture media (STEMCELL Technologies) supplemented with 1% penicillin-streptomycin (Thermo Fisher Scientific, UK). Cells were passaged at a 1: 6 ratio once every 4-5 days using 0.02% Versene- EDTA (Lonza, UK).

2.1.1. Preparation of Matrigel-coated cultureware.

Patient-derived iPSCs were routinely maintained and expanded on 6-well plates coated with Corning® Matrigel® Growth Factor Reduced (GFR) Basement Membrane Matrix (cat No. 354230, Corning USA). Preparation of Matrigel- coated plates entailed the dissolution of a frozen 1mg aliquot stock of Matrigel in 24 mL pre-chilled DMEMF12 (cat. No 11320033, Thermo Fisher Scientific, USA). Plates were coated with cold Matrigel at 4.33-4.39 $\mu g/cm^2$ and allowed to set for 1 hour at room temperature (RT) or overnight at 4 ° C. Cultureware was sealed with parafilm and stored at 4 ° C for up to one week.

2.1.2. Preparation of iPSC culture media.

iPSC media was prepared by adding 100mL mTeSR Plus 5x supplement (cat. No 05827, STEMCELL Technologies) to 400mL mTeSR Plus Basal media supplemented with 5mL of Penicillin-Streptomycin (5,000 U/mL) (cat. No 15070063, Thermo Fisher Scientific, USA). Prior to seeding with iPSCs, Matrigel on plates was replaced with 1mL/well mTeSR plus.

2.1.3. Passaging of iPSCs.

iPSCs colonies were split upon reaching approximately 80% confluency. To passage colonies, cells were briefly washed with 2 mL Versene/EDTA (cat. No 15040066, Thermo Fisher Scientific) and incubated for 3-5 min at RT. Following incubation, the Versene was aspirated and 6mL of mTeSR plus was added to each well. To allow gentle detachment of the colonies, care was taken to not break up the colonies too much by pipetting excessively. As mentioned above, iPSCs were seeded in a 1:6 ratio onto 6-well Matrigel-coated plates. iPSC lines were cryopreserved in 10% DMSO – 90% Foetal Bovine Serum (FBS) supplemented with 10 μM Rock inhibitor (cat. No CD0141, Y-27632,

Chemdea, Fischer scientific, Hampton, New Hampshire, USA) using cryovials tubes (cat. No 11787939, Thermo Fisher Scientific).

2.2. Mycoplasma detection.

All human iPSC as well as retinal organoid and retinal pigment epithelium cell cultures were routinely tested for the presence of mycoplasma infection. The following was carried by a monthly service available at the Institute of Biosciences at Newcastle University by using a MycoAlert® Mycoplasma Detection Kit (cat. No., LT07-118 Lonza) following the manufacturer's instructions.

2.3. CORD21 cell lines used in the project.

Dermal skin fibroblasts were obtained in collaboration with Mr. Martin MCkibbin and Dr. Jacqueline Bond (Leeds Teaching Hospital NHS Trust). The fibroblasts were converted to iPSCs using a non-integrative RNA- based Sendai virus by Dr. Dean Hallam. The mutation and clinical phenotype of the patient-derived iPSC lines are outlined in (Table 3). Heterozygous correction of the CORD21-P1 (045-016 c6) cell line, which is homozygous for the c.140delG deletion, was successfully carried out using CRISPR/Cas9 by the MRes student Edvinas Cerniauskas. Analogously, CRISPR-Cas9 editing of the CORD21-P2 iPSC line was carried out as described in Chapter 3. Assessment of Sendai virus clearance, pluripotency and genomic stability was performed by a combined RT PCR, qPCR and Pluritest (Thermo Fisher Scientific) approaches by undergraduate students Gabrielle Chai Jia Min and Sam Steel under the supervision of Mr. Cerniauskas. Full characterization of the WT1 (Ad2) and WT3 (Ad4) cell lines for Sendai virus clearance, expression of pluripotency markers, chromosome integrity and fibroblast parent identity were completed by Dr. Adriana Buskin [297]. The patient-derived cell lines will hereafter be referred to as CORD21-P1, CORD21-P1c, CORD21-P2 and CORD21-P2c, in line with the DRAM2 disease nomenclature of CORD21, whereby 'c' delineates the respective CRISPR/Cas9 isogenic control. Throughout this thesis both WT1 and WT3 were used as wild-type controls, so wild-type controls will hereafter be collectively referred to as 'WT'.

Table 3 iPSC lines used during the PhD project.

Abbrev.	iPSCs Cell line	Gene mutation	Mutation status	Predicted effect on DRAM2	Phenotype	Disorder	DOB/sex	Sendai virus clearance	Pluripotency Assessment	Genomic stability
WT1	WT1 (Ad2)	Wild-type	no	NA	Unaffected	NA	51 male	✓	✓	✓
WT3	WT3 (Ad4)	Wild-type	no	NA	Unaffected	NA	68 male	✓	✓	✓
CORD21-P1	045-016	DRAM2, c.140delG	Homozygous	NMD or PTC	Progressive loss of visual acuity, retinal dystrophy	Inherited macular dystrophy	1/24/91 male	✓	✓	✓
CORD21-P1c	045c-016	DRAM2, c.140delG	Heterozygous	NMD or PTC for mutated c.140delG allele	No phenotype expected	NA	1/24/91 male	✓	✓	✓
CORD21-P2	17-07610T	DRAM2, c.131G>A, c.494 G>A	Compound heterozygous	missense change/NMD or PTC	Blurred vision, progressive loss of visual acuity, maculopathy	Inherited macular dystrophy	12/24/67 female	✓	✓	✓
CORD21-P2c	72-07610T	DRAM2, c.494 G>A	Heterozygous	NMD or PTC for c.494G>A allele	No phenotype expected	NA	12/24/67 female	✗	✓	✓

**NMD – non-sense mediated decay; PTC –premature truncation of protein.*

2.4. Modelling of DRAM2 structure.

The amino acid sequence of DRAM2 was submitted into the Zhang lab online platform L-Tasser software for the modelling of protein structure. 3D modelling of protein structure is facilitated by alignment of the AA sequence to existing super-secondary structures available within the PDB (Protein Data Bank) database using a LOMETS algorithm approach. In subsequent steps of the analysis, residue fragments are amassed into full-length models and further refined for low-energy conformations and spatial constraints by running a clustering SPICKER algorithm as well as structural alignments using TM-Align. In addition, assessment of structural identity between the protein of interest and existing libraries enabled comprehensive insight into protein function via the assignment of GO terms and ligand-binding sites. Analysis returned a .pdb file format which was finally annotated using PyMOL software (Python, Schrödinger, Inc.).

2.5. CRISPR/Cas9 genome editing in iPSCs.

The experiment aimed to create an isogenic control for CORD21-P2, a compound heterozygous patient-derived cell line with inherited macular dystrophy (Table 3). Previous success in correcting the c.140delG mutation on the CORD21-P1 patient prompted the need for a similar approach in CORD21-P2 (131G>A [p. Ser44Asn], c.494G>A [p. Trp165*]) using an optimised method of CRISPR/Cas9 genome editing. The aim was to introduce a single nucleotide correction at the c. 131A site utilizing CRISPR/Cas9-mediated homology directed repair (HDR). To achieve this, a target gRNA sequence was designed using the Benchling CRISPR tool (https://www.benchling.com/crispr). The selection of the gRNA was based on the following criteria: proximity of the PAM to mutation site, ability to abrogate the PAM (Protospacer adjacent motif) without disrupting the reading frame, GC% content as well as on-and off-target scoring (Table 4 and Table 5).

A suitable gRNA was identified which has its cut site 15 nucleotides away from the mutation site (Figure 9 and Figure 10). This was the only gRNA design that could have its PAM recognition site changed post-modification, with a cut site in sufficient proximity, considering the significant limitations posed by distance relative to PAM. The gRNA also showed satisfactory values for GC% content (~40%), on- target efficiency and off-target specificity

(above >60) (Table 4). After establishing the CRISPR-Cas9 blueprint for gRNA and ssODN design, the experiment progressed through various stages, including gRNA synthesis and purification, *in vitro* validation of gRNA activity, nucleofection of CORD21-P2 iPSCs, and screening for positive *Alu I* clones by PCR and restriction digest analysis. Selected clones were then further sequenced to assess mutation status.

Figure 9. Schematic showing annotated gRNA (A) and ssODN sequences (B). Design of gRNA on mutant DNA of the compound heterozygous CORD21-P2 cell line.

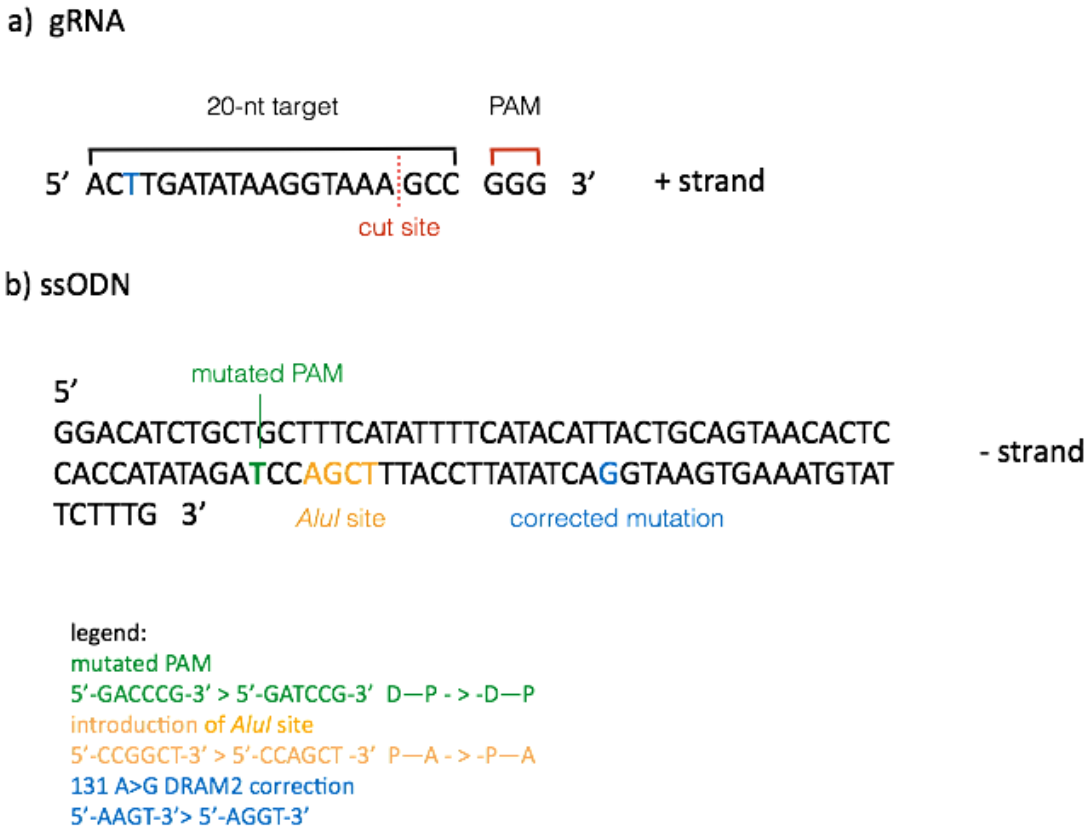

Table 4. List of all gRNAs spanning 130bp of the DRAM2 mutation site in mutant CORD21-P2 DNA. Outlined in bold is the gRNA design used in the project, including PAM site, on- and off-target scores, absolute position, and strand coordinates. High-scoring gRNAs exhibit GC% content between 40-80%, on-and off-target values above >60 and >50, respectively.

Position	Strand	gRNA sequence	PAM	GC%	Efficiency (on- target score)	Specificity (off-target score)
111131403	-	GTGAAATGTATTCTTTGTAT	AGG	25	42.9	45.1
111131429	+	CATTTCACTTACTTGATATA	AGG	25	44.3	59.9
111131438	+	TACTTGATATAAGGTAAAGC	CGG	30	56.4	68.9
111131439	**+**	**ACTTGATATAAGGTAAAGCC**	**GGG**	**35**	**60.9**	**72.2**
111131446	-	AACACTCCACCATATAGACC	CGG	45	66.3	76.9
111131448	+	AAGGTAAAGCCGGGTCTATA	TGG	45	39.8	90.9
111131451	+	GTAAAGCCGGGTCTATATGG	TGG	64	64.6	91.4

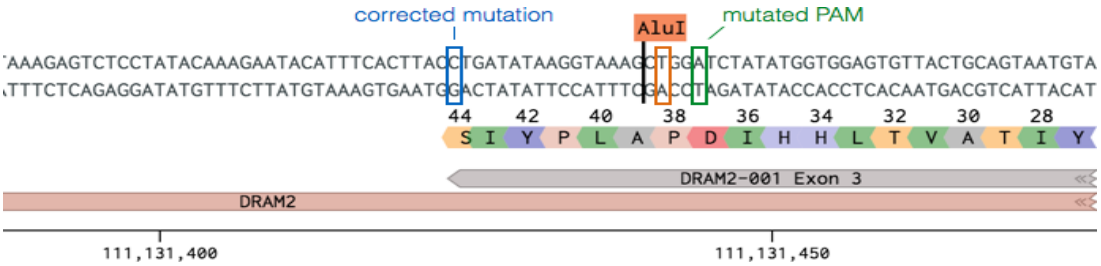

Figure 10. Graphic shows DNA sequence following hypothetical recombination of ssODN template into CORD21-P2 genomic DNA via CRISPR/Cas9-mediated editing. Outlined in blue, orange, and green, respectively, are the corrected mutation c.131 A>G, introduced Alu I restriction site (G>A) and PAM mutation (C>T). Following ssODN-facilitated HDR, a single Alu I site is present within the region of interest. Subsequent digestion with Alu I of amplified region would generate PCR fragments of about 216 and 192 base pairs.

Table 5. Sequence summary of gRNA DNA template, gRNA target, target-specific gRNA primers and ssODN used to edit the c.131G>A mutation in CORD21-P2 cells. ssODN design outlined in the last column details the corrected site (blue) alongside the two additional synonymous mutations marking abrogated PAM (green) and Alu I site introduction (orange).

gRNA DNA template	gRNA target sequence	Target-specific gRNA primers	ssODN sequence
(+ strand) 5'TAATACGACTCACTATA G**ACTTGATATAAGGTAAA/ /GCC**GTTTTAGAGCTAGAA ATAGCAAGTTAAAATAAG GCTAGTCCGTTATCAACTT GAAAAAGTGGCACCGAGT CGGTGCTTTT 3'	(+ strand) 5'**ACTTGATATAAGGTAAA //GCC** 3' **//** denotes cut site	**Forward primer** 5'TAATACGACTCACTATAG ACTTGATATAAGGTAA3' **Reverse primer** 5'TTCTAGCTCTAAAACGGCT TTACCTTATATCAAG 3'	(- strand) 5'TGGACATCTGCTGCTTTCATATTTTCATACATT ACTGCAGTAACACTCCACCATATAGATCCAGCT TTACCTTATATCAGGTAAGTGAAATGTATTCTTT G 3' *** Mutated PAM** **5'-GAC-3' > 5'-GAT-3'** **D- > D** ***Introduction of *AluI* site** **5'-CCG-3' > 5'-CCA-3'** **P - > P** *** 131 A>G DRAM2 correction** **5'-AAGT-3'> 5'-AGGT-3'**

2.5.1 gRNA synthesis

gRNA DNA template was assembled under sterile conditions using the GeneArt™ Precision gRNA Synthesis Kit (cat. No A29377, Thermo Fisher Scientific, USA). Detailed explanation of gRNA DNA assembly is provided below (Figure 11). In brief, gRNA DNA containing a T7 promoter and a crRNA/tracr RNA fragment is generated by PCR using a combination of

custom-made oligonucleotides overlapping the sequence of interest and a pair of universal primers (T7 primer mix and Tracr Fragment). The assembled DNA template is used for the *in vitro* transcription of a functional gRNA composed of target-specific and auxiliary trans-activating crRNA (tracrRNA) domains.

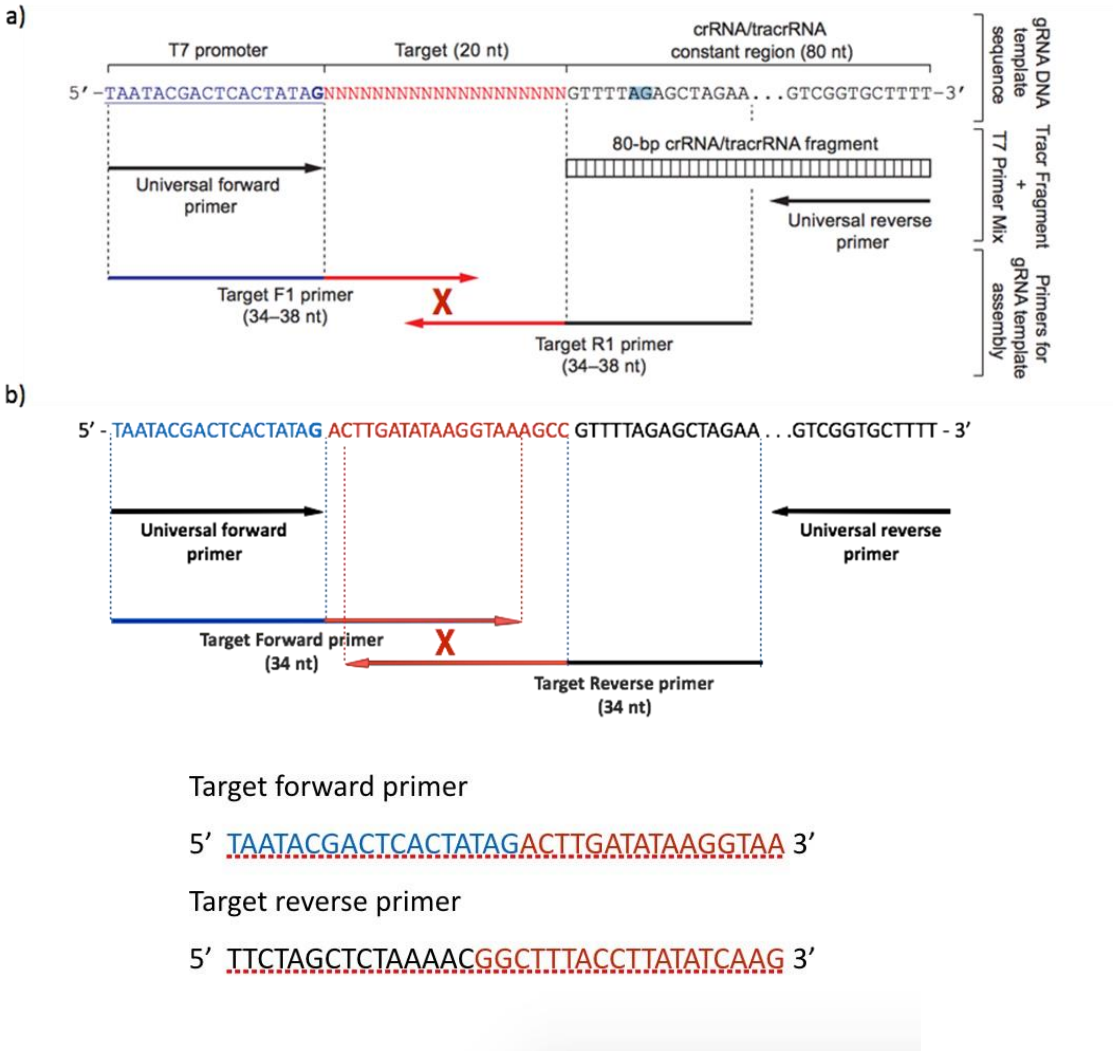

Target forward primer

5′ TAATACGACTCACTATAGACTTGATATAAGGTAA 3′

Target reverse primer

5′ TTCTAGCTCTAAAACGGCTTTACCTTATATCAAG 3′

Figure 11. Schematic illustrates the principles of gRNA DNA assembly. *(*A) gRNA DNA was synthesized using target-specific and universal primers according to the template described in the GeneArt ™ Precision gRNA Synthesis Kit (image is adapted from the handbook manual). gRNA DNA contains a T7 promoter sequence, the target gRNA sequence, and an 80bp crRNA/Tracr RNA fragment. (B) Image shows sequence of 34 nucleotides- long forward and reverse target-specific primers, overlapping the DNA target. Target-specific sequence to be transcribed from gRNA DNA template is coloured in red. Image taken from the GeneArt™ Precision gRNA Synthesis Kit manual.

For the purposes of the procedure, RNAase free tubes were pre- treated under UV light for 30 minutes under a laminar flow hood. 0.3M Target oligonucleotide mix was prepared for forward and reverse primers (forward primer 5' - TAATACGACTCACTATAGACTTGATATAAGGTAA-3'; reverse primer 5' - TTCTAGCTCTAAAACGGCTTTACCTTATATCAAG- 3') and the gRNA DNA template was assembled in the following PCR reaction:

Phusion High-Fidelity PCR mix (2x)	12.5 µL
Tracr Fragment + T7 Primer Mix	1 µL
0.3M Target F1/R1 oligonucleotide mix	1 µL
Nuclease- Free Water	10.5 µL

Initial denaturation	98° C	10sec	1x
Denaturation	98° C	5 sec	32x
Annealing	55° C	15 sec	
Extension	72° C	60 sec	
Final extension	72° C	3 min	
Hold	4° C	∞	

gRNA was transcribed at 37° C for 4h in the following reaction mix:

NTP mix	8 µL
gRNA DNA template	6 µL
5X TranscriptAid™ Reaction Buffer	4 µL
TranscriptAid™ Enzyme Mix	2 µL

The resulting mix was then incubated with 1µL of *DNAse I* mix for an additional 15 min at 37° C to degrade any residual DNA contamination. A gRNA purification procedure was performed according to the manufacturer's instructions.

2.5.2. Nucleic acid concentration measurement

Concentration of the synthesized gRNA was determined using the protocol outlined for the Qubit® RNA BR (Broad range) Assay Kit (cat No. Q10210, Molecular Probes, Thermo Fisher Scientific, USA) by following the manufacturer's instructions. An analogous procedure was performed when measuring DNA concentration using the Qubit™ dsDNA BR Assay Kit (cat. No Q32850, Thermo Fisher Scientific). DNA quality ratios for A_{260}/A_{280} falling within ranges of 1.5-2.0 were considered acceptable following re-measurement on Nanodrop.

2.5.3. Genomic cleavage detection.

Following gRNA synthesis, the ability of the gRNAs to direct Cas9 cutting on mutant CORD21-P2 DNA was evaluated by performing an *in vitro* digest in the presence of a Cas9/RNP complex (Figure 12).

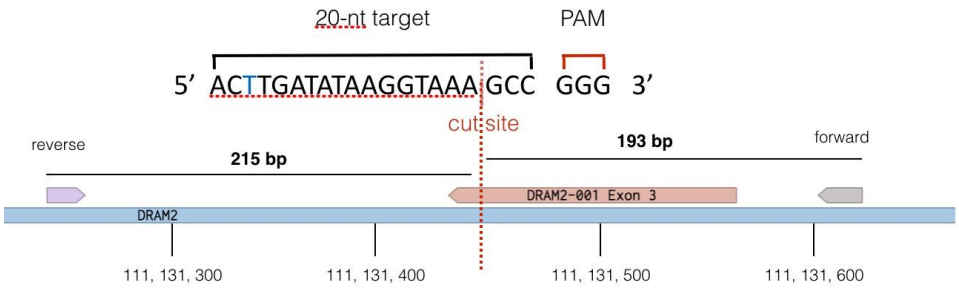

Figure 12. Diagram shows theoretical Cas9-mediated cleavage of 408 bp DNA fragment produced by PCR amplification. gRNA complementarity guides Cas9 to cut DNA 3 nucleotides upstream of PAM recognition site (outlined in red). This results in the formation of two fragments of similar size - one of 215 bp and another one of 193 bp. Primers used are summarized in Table 2.6.5.1.

Table 6. Primers used for genomic cleavage detection for the CORD21-P2 iPSC line.

Gene	Forward primer	Reverse Primer	PCR product (bp)
DRAM2	5'GGCTAAAGTAGGATGAGGAAAC3'	5' ACTGAATCTTATTGGGCTG 3'	408bp

Mutant DNA template was first amplified by PCR using primers shown in Table 6. *In vitro* digestion was then carried out in a total volume of 30 µL following the schematic below:

NFW	20 µL
NEBuffer3.1	3 µL
300 nM sgRNA	3 µL (30 nM final)
1 µM Cas9 Nuclease, S. pyogenes (M0386S)	1 µL (~30 nM final)
10 min at 25°C	
30 nM DNA	3 µl (3 nM final)
37° C for 1 hour	

Following digestion, samples were treated with 1 µL Proteinase K (cat. No P8107S, NEB) for an additional 10 min prior to analysis by gel electrophoresis.

2.5.4. Gel electrophoresis.

Digests were run on a 2% agarose gel (Melford Laboratories, UK) at 100V for 1h. Gel images were visualized on a GelDoc-it Imaging system (Analytik Jena AG, Jena, Germany).

2.5.5. Nucleofection.

The patient-derived CORD21-P2 iPSC line was propagated in culture for at least 4 passages prior to nucleofection. The procedure was performed using P3 Primary Cell 4D-NucleofectorTM X Kit according to the manual's instructions (cat. No V4XP-3024, Lonza, Basel, Switzerland). To boost the efficiency of HDR recombination ~ 1 million cells were treated with 10 µM of NHEJ inhibitor SRC-7 (cat. No SML1546, Sigma Aldrich, St. Louis, Missouri, USA) approximately 8 hours prior to nucleofection. 200pM gRNA and 100pM TrueCut™ Cas9 Protein v2 enzyme (cat. No A36497, Invitrogen, Thermo Fisher Scientific) were incubated together at RT for 10 min to allow for the formation of ribonucleoprotein complexes (RNPs). In the meantime, iPSCs were detached using 1mL Accutase for 5min at 37° C (cat. No 07922, STEMCELL Technologies, Vancouver, Canada). The single-cell suspension of iPSCs was centrifµged in the presence of 10µM Rock inhibitor at 1000 rpm for 2 min (cat. No CD0141, Y-27632, Chemdea, Fischer scientific, Hampton, New Hampshire, USA). Cells were reconstituted in 100 µL of 4D nucleofector solution P3 supplemented with 10µM Rock inhibitor. A premixed solution containing gRNA and Cas9 was added to the single-cell suspension alongside 200pM ssODN and transferred to a nucleofection cuvette using a Pasteur pipette. The nucleofection reaction was performed on a 4D-Nucleofector™ system at the following settings x->A2, hES9, CB150 (Lonza, Basel, Switzerland). Matrigel-coated 10mm

Petri dishes were individually seeded with 0.1 mL, 0.2 mL, 0.3 mL and 0.4 mL of nucleofected solution in the presence of 10µM SRC-7 and 10µM Rock inhibitor. Rock inhibitor was removed 24h post-nucleofection and the mTeSR media was replenished every two days. Colony growth from single cells was allowed to ensue over the course of 10 days, whereby cluster growth was monitored daily.

2.5.6. Colony picking and maintenance of single cell derived iPSCs colonies following nucleofection.

Upon single colony expansion, 96 clones were picked from Petri-dishes containing 0.1 mL and 0.2 mL of the nucleofected solution. Clones were seeded on 24 well-plates in the presence of 10 µM Rock inhibitor for a period of 24h. Within approximately 10 days, most single colonies were ready to be passaged. The expanded colonies were again re-plated on new Matrigel-coated 24 well plates in the presence of 10µM Rock inhibitor. After 24 hours Rock inhibitor was removed by changing the media. Subsequent passaging of colonies was enabled via routine detachment with 1x Versene/EDTA, whereby 50 µL was used to continue the passaging of individual colonies. The remainder of cells was pelleted and stored at -80 ° C until at least 96 clone pellets were available for DNA extraction.

2.5.7. DNA extraction of nucleofected cells.

DNA extraction for a total of 107 colonies was performed using the Wizard® SV 96 Genomic DNA Purification System (cat. No A2371, Madison, Wisconsin, USA). In brief, pellets were lysed and loaded onto a binding plate, which was positioned inside on a vacuum manifold provided with the kit. DNA was bound onto 96 individual columns and washed with ethanol-enriched column wash buffer twice under vacuum pressure. Vacuum pressure was applied for an additional 15 minutes to enable complete flow- through of buffer. The binding plate was dried by repeatedly tapping it against a clean, dry roll paper. DNA was eluted in 100 µL of NFW (nuclease-free water) and DNA concentration was determined using a NanoDrop™ 2000 spectrophotometer (cat. No ND- 2000, Thermo Fisher Scientific). A brief schematic outlining the procedure is available below (Figure 13):

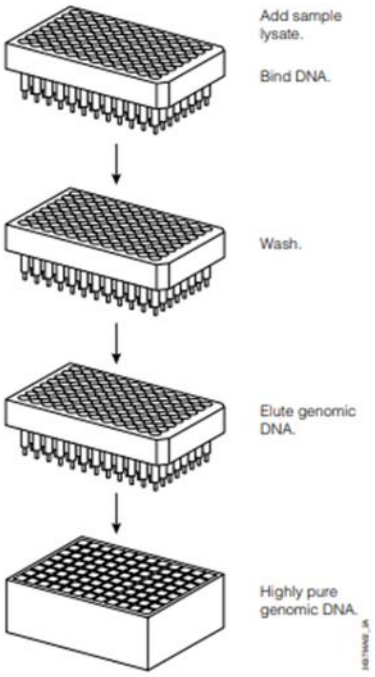

Figure 13. Schematic illustrates the principle of DNA extraction using the Wizard® SV 96 Genomic DNA Purification System. Pellets are lysed and applied to binding column, washed twice, and eluted with the help of a vacuum manifold. Image is adapted from the user manual of the kit. Image taken from the manual of the kit.

2.5.8. PCR amplification of CRISPR clones

PCR amplification was performed on a PCR thermocycler (Geneflow, UK) using the same primer pair used in the genome cleavage assay (5' GGCTAAAGTAGGATGAGGAAAC 3' and 5' ACTGAATCTTATTGGGCTG 3'). For every clone at least 150ng of DNA template was amplified:

Reagent	Total volume 25 µl
dNTPs 10mM	0.5 µL
Forward primer 10 µM	0.5 µL
Reverse primer 10 µM	0.5 µL
GoTaq Reaction buffer (5x)	5 µL
GoTaq G2 DNA polymerase	0.125 µL
Template DNA	variable
Nuclease-Free water	up to 20 µL

The reaction was performed using the following PCR conditions:

Initial denaturation	95° C	2:00 min	1x
Denaturation	95° C	15 sec	35x
Annealing	60° C	30 sec	
Extension	72° C	60 sec	
Final extension	72° C	5:00 min	1x
Hold	4° C	∞	

2.5.9. Restriction digest

A total of 17.5 µL of PCR product was incubated for an hour with 0.5 µL of *Alu I* restriction enzyme (cat. No R0137S, NEB) and 2 µL CutSmart® Buffer (10x) (cat. No B7204S, NEB) at 37° C. The digestion products were analyzed by gel electrophoresis.

2.5.10. DNA extraction, PCR amplification and sample preparation for Sanger sequencing.

The QIAamp DNA Mini Kit was used to obtain high-quality DNA from *Alu I* positive clones (cat. No 51304, QIAGEN, Hilden, Germany). The procedure was in accordance with the guidance manual. To prevent ethanol contamination, shortly prior to DNA elution, columns were centrifuged an additional three times at full speed (20 000 x g) and transferred to new collection tubes. DNA was finally eluted in 40 µL AE buffer at 6000 x g for 60 sec. 36 µL of DNA was amplified for each clone in a 50 µL PCR reaction by using the same pair of primers outlined in the genome cleavage and CRISPR screening assays (Table 6). In the PCR reaction, Colourless GoTaq buffer was used to generate dye-free product. PCR products were subjected to a clean-up procedure using the QIAquick PCR purification kit according to the manufacturer's instructions (cat. No 28104, QIAGEN). DNA concentration was determined using the Qubit™ dsDNA BR Assay Kit. Sequencing samples reactions were prepared by adding 1 µL of 10µM forward or reverse primers to 15 µL of DNA (5-100ng/µL) extract. Sanger sequencing was performed in-house by the Joris Veltman group using BigDye Terminator v3.1 Cycle Sequencing and BigDye XTerminator™ Purification Kits or by a commercial sequencing platform (www.eurofinsgenomics.eu).

2.5.11. CRISPR-Cas9 Off-target analyses.

The online platform http://www.rgenome.net/cas-offinder/ was used to identify genomic regions bearing high sequence homology to the sites of CRISPR/Cas9 correction. Query sequences were allowed a maximum of up to three mismatches. Top 10 sequences with

highest homology were selected and primers were designed for the desired genomic regions. Primers used for off-target sequencing of CORD21-P1c and P2c iPSCs are shown in Table 7.DNA was isolated from CORD21-P1c and CORD21-P2c iPSCs using a QIAamp DNA Mini Kit. DNA concentration was measured by the Qubit™ dsDNA BR. Subsequently, DNA was PCR amplified (GoTaq® G2 DNA Polymerase) and cleaned up using a QIAquick Gel Extraction Kit. Samples for sequencing were prepared as per above (see section 2.5.10) and processed by the Veltman group. Sequencing reads were aligned to a reference human genome to corroborate the absence of unwanted genetic alterations (Appendix B). Off-target sequencing for the CORD21-P1c iPSC line was carried out under supervision with the help of MRes student Eldo Galo.

Table 7. Primers used for the CRISPR-Cas9 off-targeting analysis of the CORD21-P1c and CORD21-P2c iPSC lines.

iPSC line	Target Sequence	Locus	Gene	Forward Primer	Reverse Primer
CORD21-P1c	TGGGGCAATGCTAAATATTGCGG	chr1:-111126239	*DRAM2*	5' GATAAGAGGTTTGAATTAACTCCTG 3'	5' TACTGTAGCAATTTGGCTATTATC 3'
CORD21-P1c	AGTGGCAATGCTAAATACTGGGG	chr4:+98112904	*STPG2*	5' AGTCGTCTGCTATGTCCAAGT 3'	5' CGCAAACCCAGTTGACAGAA 3'
CORD21-P1c	TGGCAATGCTAAATACTGGG	chr21:+14242055	*ABCC13*	5' GCCCTAACATTCTGTCAGAGC 3'	5' GCTAATAGGACGCTCATGAATCT 3'
CORD21-P1c	GCAATGCTAAATACTGGGG	chr13:23518575	*ENSG00000289688*	5' TGACATGTTTCTGTAAGCGTTCA 3'	5' TAATACCGCGCTGCCAGATA 3'
CORD21-P1c	TAGGGAAATGCTAGATATTGGGG	chr17:+10978967	NA	5' TGGTTTGGGATTGGCAATGG 3'	5' TGTATTGCTGCTCTCTGGCT 3'
CORD21-P1c	TGGGGCAGCTCTAAATATTGAGG	chr9:-109805627	*PALM2AKAP2*	5' TGCTCACCATCCCATGAAGT 3'	5' TCCCCGAAATTCCAGTCTGA 3'
CORD21-P1c	TGTGGCAATGCAGAATATTGGGG	chr6:-20328875	*ENSG00000286590*	5' CACCCAGGAGAGAGGAGAAA 3'	5' GCACTGTCTCACACCCCTAT 3'
CORD21-P1c	GCAATGCAGAATATTGGG	chr3:+197784824	*FYTTD1*	5' GGCGGGAGAATTGCTTGAAT 3'	5' CCACATGCAAGTCTTGAAAACA 3'
CORD21-P1c	TCCGGCAATGCTAAATATGGAGG	chr11:+134742411	*LINC02714*	5' GTTGTGTAGCCAGCAGTGAG 3'	5' GCATGTGGTAAGGCTGTGAG 3'
CORD21-P1c	TGGGTGAATGCTCAATAATGGGG	chr3:+47891747	*MAP4*	5' CTCATGGACTGATTATGGACAGGAC 3'	5' GCAGGTCAGCAAAGAACTTATAGCC 3'
CORD21-P2c	ACCTGATATAAGGTAAAGCC	chr1:+111131421	*DRAM2*	5' GGCTAAAGTAGGATGAGGAAAC 3'	5' ACTGAATCTTATTGGGCTG 3'
CORD21-P2c	ATTTGATATAGGGTAAAGCC	chr1:-184362081	NA	5' CCAGGATACCTAACTTGGTGCT 3'	5' TAGCCAGACTGGACCCACAA 3'
CORD21-P2c	AATTGGTATAAGGTAAAGTC	chr20: -4407165	NA	5' TAGCTGCTAGGATGCAGGACT 3'	5' AAGTGGTAGCAAGGGAAGAGG 3'
CORD21-P2c	GCCTAGATATAATGTAAAGCC	chr8:-110241689	NA	5' GCACTACAAAATACGGTGGTGG 3'	5' GATGAGCAGACCTTCTCAGCAT 3'
CORD21-P2c	ACCTGATAGAAGGTAAAGGC	chr7:+137551003	*DGKI*	5' CAGCAAACCCTTGGTCCATT 3'	5' GGTGGCACATGTTGGTTGAG 3'
CORD21-P2c	CACTAGTCATAAGGTAAAGCC	chr5:-74308619	*LINC01335, LINC01331*	5' ATCCAGGCAGCTGGTACAAAT 3'	5' TCCCCCTACCCCACACAGAT 3'
CORD21-P2c	TCTTAATATGAGGTAAAGCC	chr2:-12850715	*ENSG00000225649*	5' TGTAACTGGAGTTAAAAGGGGCT 3'	5' TCTGAAGCCTTTTGTGACATGA 3'
CORD21-P2c	TTTTGATATAAGGTAAAGCA	chr3:+139919673	NA	5' TCCAATTATCCCAGCACAATT 3'	5' TGACTAGAGATACCAAGTTA 3'
CORD21-P2c	ACTTGAAATAAGGTAAAACA	chr1:+15332224	*FHAD1-AS1, FHAD1*	5' CCTCCAGAGAGCCTGCATCA 3'	5' AGGGGACAGTGCACACGTA 3'

2.6. Generation of Retinal Organoids (ROs).

Patient-derived iPSCs were differentiated to ROs following a protocol outlined by Kuwahara *et al*. (2015) with minor modifications by the Lako group (Hallam *et al*. 2018) (Figure 14, Table 8). Briefly, iPSCs were washed with PBS and dissociated into a single cell suspension by Accutase (Gibco, Thermo Fisher Scientific) and plated at 7000 cells/well density onto U-bottom Lipidure pre-coated 96-well plates (AMSbio, UK). iPSCs were seeded using a multichannel pipette and grown in mTeSR ™ PLUS in the presence of 10 µM Y-27632 ROCK inhibitor (Chemdea, USA) for the first 48 hours. Upon formation of spheroids the latter were fed by half-media changes (100 µL mTeSR per well) every other day. On day 6 of differentiation, the medium was supplemented once with 2.25nM BMP4. Half-media changes were undertaken every three days until day 18. From day 18 onwards, organoids were grown in maintenance media until the end of the differentiation procedure (d220), whereby retinoic acid (RA) was added fresh at 0.5 µM to organoids until d120 of the differentiation procedure. Development of the organoids was monitored for the emergence of a transparent bright phase neuroepithelium layer, which is a reliable sign of the differentiating retinal tissue. Organoids presenting with a thick neuroepithelial layer were thus collected for western blot, immunofluorescence, proteomics, lipidomics and enzymatic activity analyses at d150 and d220.

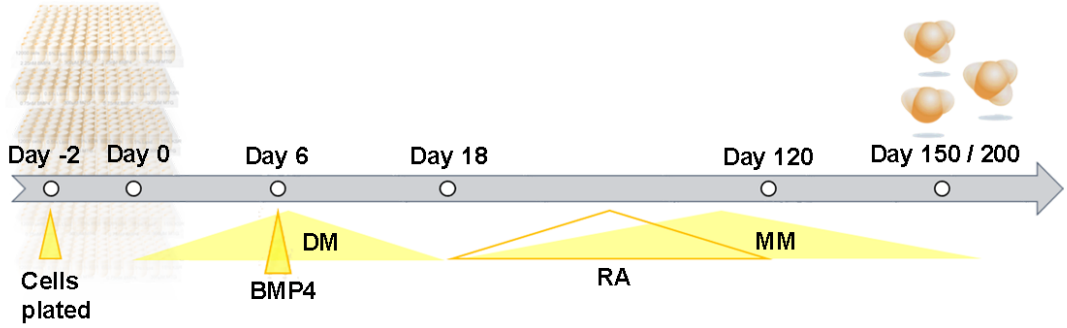

Figure 14. Schematic shows a simplified timeline of the optimized Sasai method used for RO differentiations. iPSCs were plated on 96-well lipidure coated plates in mTeSR media. From d0 to d18, ROs were cultured in Differentiation media, whereby the emergence of retinal neuroepithelium was induced by the key addition of BMP4 at d6. From d18 onwards, ROs were grown in Maintenance media in the presence of freshly added retinoic acid. Retinoic acid was later withdrawn at d120, and samples were collected at d150 and d220. Image was taken from Dorgau *et al*., 2022.

Table 8. Timeline of differentiation and media composition.

Media	Time-span of differentiation	Media composition
1. Differentiation media	Add 200 µL per well on d0 and grow newly formed spheroids in differentiation media until d6. Media is changed every two days (100 µL per well d2 onwards).	41% IMDM, 41% HAM's F12, 15% KOSR, 1% Glutamax, 1% Chemically defined lipid concentrate, 1% Penicillin/Streptomycin, 225 µM 1-Thioglycerol
2. BMP4 addition	Feed on d6 and change media every three days until d18	2.25 nM BMP4 in Differentiation media
3.Maintenance media	On d18 change to maintenance media and feed every two days. 0.5 µM retinoic acid is added fresh until d120. Differentiation procedure is maintained until d220 when samples are collected.	DMEM/F12 with L-Glutamine, 10% FBS, 1% Glutamax, 1% N2, 0.1mM Taurine, 1% Penicillin/Streptomycin, 0.25 µg/mL fungizone and freshly thawed 0.5 µM retinoic acid

2.6.1. Embedding and cryosectioning of ROs.

ROs were transferred one by one from a 96-lipidure coated well plate to a 1.5 mL Eppendorf tube and carefully washed with PBS (Thermo Fisher Scientific). The organoid material was first fixed for 30 min with 4% PFA (Paraformaldehyde, Santa Cruz Biotechnology, USA). To preserve their structural integrity, ROs were immersed in sucrose solutions of increasing concentrations. Dehydration by sucrose exposure enables a stronger preservation of outer segment structure upon cryopreservation. This was followed by successive 1-hour incubations in sucrose solutions of 6.25% and 12.5% at 4°C, respectively. The material was then incubated overnight at 4°C in a 25% sucrose solution. 24hrs later, ROs were gently transferred to a 10mm petri dish containing OCT embedding matrix (CellPath, UK) and any remaining sucrose was washed off by swirling the dish. Finally, the organoids were embedded in OCT (CellPath, UK) onto plastic DISPOMOLD containers (10x10xx5mm, CellPath) through a brief incubation on dry ice and then frozen at -20°C. The embedded samples were cut into sections of 10-20 µm thickness and collected onto SuperFrost glass slides (Menzel, USA) using a Leica Biosystems cryostat system (CM1860, Germany). Until further processing by immunofluorescence, slides were stored long term at - 20°C.

2.6.2. Immunofluorescence analysis (IF) of ROs.

The organoid sections were left to dry at RT for an hour. Afterward, they were washed 3x5 min with PBS (Thermo Fisher Scientific) to remove any remaining OCT. Typically, a set of six sections was partitioned two by two using a liquid repellent pen (Super PAP pen, Thermo Fisher Scientific). To minimize non-specific binding, sections were blocked for 1 hour at RT

with a solution of PBS containing 10% goat serum and 0.3% Triton-X100. Sections were then double stained overnight at 4 °C in a humidifier chamber using primary antibodies diluted in AD (Antibody diluent) buffer (0.001% BSA-PBS and 0.3% Triton-X, Sigma Aldrich, USA) (Table 9). Following incubation overnight, RO sections were washed 3x 10 minutes with AD buffer. Secondary antibodies diluted in PBS (1:1000) (Table 9) were applied to the sections and incubated for 2 hours at RT. Finally, the sections were washed three times with PBS for 15 min. Nuclei were counterstained with a 1:1000 dilution of Hoechst (cat. No. 33342, Thermo Fisher Scientific) in Vectashield (cat. No. H-1000-10, Vector Laboratories, CA). The slides were then covered with 24x60 mm coverslips, sealed on each side with nail polish, and stored at 4 °C in the short term. For quality control, sections stained only with a secondary antibody were analysed for each staining to ensure the specificity of the fluorescent antibody signal.

Table 9. Primary and secondary antibodies used for the characterization of WT and DRAM2-patient retinal organoids by IF.

Antibody	Species	Catalogue number	Supplier	Concentration	Type
AP1γ	Mouse	610385	BD Biosciences	1 in 50	primary Ab
AP2a	Mouse	SC-12726	Santa Cruz Biotechnology	1 in 200	primary Ab
AP3δ	Mouse	SC- 136277	Santa Cruz Biotechnology	1 in 50	primary Ab
CERAMIDE	Mouse	ALX-804-196-T050	Enzo Life Sciences	1 in 10	primary Ab
CLATHRIN	Mouse	ab2731	Abcam	1 in 50	primary Ab
CRX	Mouse	H00001406-M02	Abnova	1 in 200	primary Ab
DRAM2	Rabbit	15701651	Fisher Scientific	1 in 50	primary Ab
GM130	Mouse	NA	gift from Wenke Seifert	1 in 500	primary Ab
GM130	Rabbit	AB52649	Abcam	1 in 100	primary Ab
OPN1L/MW	Rabbit	AB5405	Millipore	1 in 200	primary Ab
OPN1SW	Rabbit	AB5407	Millipore	1 in 200	primary Ab
PROX1	Rabbit	AB5475	Millipore	1 in 1500	primary Ab
Recoverin	Rabbit	AB5585	Millipore	1 in 1000	primary Ab
Rhodopsin	Mouse	MAB5356	Millipore	1 in 200	primary Ab
SNCG	Mouse	H00006623-M01A	Abnova	1 in 500	primary Ab
TOMM20	Mouse	AB56783	Abcam	1 in 100	primary Ab
Vimentin	Rabbit	AB92547	Abcam	1 in 400	primary Ab
anti-Rabbit Cy3	Goat	111-165-003-JIR	Jackson Immuno Research	1 in 800	secondary Ab
anti-Mouse 488	Goat	115-545-146-JIR	Jackson Immuno Research	1 in 1000	secondary Ab

2.6.3. Microscopy and image analysis.

Images were obtained using an Axio Imager fluorescence microscope (Zeiss, Germany). High-resolution Z-stack imaging was facilitated through Apotome optical sectioning, whereby Z stacks was between 10 to 15 µm thick. For each staining, 5-10 representative images were captured at either the 20x objective or at 63x and subsequently processed as maximum intensity projections. To correct for background signal, LUT values were adjusted across the whole dataset based on the LUT values of the secondary antibody only control (per staining). Subsequently, the maximum projection images were adjusted for brightness and contrast using Adobe Photoshop software (San Hose, California). Quantification of retinal cell marker expression was conducted using MATLAB software (Mathworks, MA) based on a previously established protocol developed by the Lako research group (Dorgau *et al*., 2019). The MATLAB algorithm enabled the quantification of retinal marker expression relative to the total number of Hoechst-stained nuclei normalised to the cell surface area. Documentation of ROs development entailed brightfield imaging at various time-points of RO development using AxioVert (Zeiss, Germany). Measurement of neuroepithelial thickness was performed using ImageJ software, as described in a previous study (Felemban *et al*., 2018). Statistical analysis was carried out using Prism software (GraphPad, USA).

2.7. Generation of Retinal pigment epithelium (RPE) cells.

RPE cells were differentiated from iPSC cell lines using a directed differentiation protocol outlined by Regent et al. (2019). The protocol allows for scaling up of the process of efficient and rapid RPE differentiation within the course of two months (Table 10). The differentiation procedure is commenced upon iPSCs reaching 80% confluency. During the initial 7 days (D0-D7), the cells are cultured in a medium containing DMEM/F12 + GLUTAMAXTM (cat. No. 10565018, ThermoFisher Scientific), β-mercaptoethanol (cat. No. M3148, Sigma-Aldrich), MEM NEAA (cat. No. 11140068, Thermo Fisher Scientific), KnockOut Serum Replacement (KOSR, cat. No 10828028, ThermoFisher Scientific) and nicotinamide (cat. No. N0636, Sigma-Aldrich). From day 7 to day 14 (D7-D14), nicotinamide is replaced by Activin A (cat. No. 12014E-250UG, Preprotech). Between the second week up until day 42 (D14-D42), Activin A is substituted by the CHIR99021 compound (cat. No SML1046, Sigma-Aldrich) which allows for further maturation of RPE and development by pigmentation. By D42 nascent patches are

excised with a stainless-steel surgical scalpel (Thermo Fisher Scientific) and passed through a 40 µm cell strainer (Thermo Fisher Scientific). The RPE cells were then either propagated for an additional passage as a pure pigmented population at $4.5x10^5$ per cm^2 or directly seeded onto Matrigel-coated 12-well or 24-well plate (cat. No. 665640; 665641; 662641; 662640 12-well and 24-well translucent and transparent Thincerts™ 0.4 µm pore, Greiner Bio-One, Austria) transwell inserts at 200 000 or 400 000/per well, respectively. At this stage of the differentiation procedure, (D42-84), CHIR99021 supplementation was withdrawn and maturing RPE cultures were maintained in the basal media at a reduced KOSR (4%) concentration. Medium was replaced by carrying out partial media changes (2/3 of the volume removed twice a week).

Table 10. Detailed summary of media used during the sequential stages of RPE directed cell differentiation.

Media	Component	Concentration/Volume
D0-D7 Media	DMEM/F12 Glutamax + 1% penicillin-streptomycin	388.435 mL
	50 µM β-mercaptoethanol	0.455 mL of 55 mM
	1 x MEM NEAA	5 mL of 100x
	20% KOSR	100 mL
	10 mM Nicotinamide	6.11 mL of 818.9 mM
D7-D14 Media	DMEM/F12 Glutamax + 1% penicillin-streptomycin	394.045 mL
	50 µM β-mercaptoethanol	0.455 mL of 55 mM
	1 x MEM NEAA	5 mL of 100x
	20% KOSR	100 mL
	100 ng/ml Activin A	0.5 mL of 100 µg/mL
D14-D42 Media	DMEM/F12 Glutamax + 1% penicillin-streptomycin	394.196 mL
	50 µM β-mercaptoethanol	0.455 mL of 55 mM
	1 x MEM NEAA	5 mL of 100x
	20% KOSR	100 mL
	3 µM CHIR99021	0.349 mL of 4.298 mM
D42-D84 Media	DMEM/F12 Glutamax + 1% penicillin-streptomycin	474.545 mL
	50 µM β-mercaptoethanol	0.455 mL of 55 mM
	1 x MEM NEAA	5 mL of 100x
	4% KOSR	20 mL

The derivation of RPE cells was also performed from RPE spheres growing on retinal organoids (ca~ d90). Briefly, RPE spheres were excised from retinal organoids lacking neural epithelium and transferred onto Matrigel-coated 24-well plates. The culture media combined the use of Advanced RPMI 1640 Medium (cat. No. 12633012, Thermo Fisher Scientific), B-27™ supplement (50x) (cat. No. 17504001, Thermo Fisher Scientific), KOSR, GlutaMAX™ (cat. No. 35050061, Thermo Fisher Scientific) and penicillin-streptomycin. Following approximately two months of RPE maturation in the presence of B27™, RPE cells were seeded onto 12- or 24-transwell inserts (Greiner Bio-One) and maintained in the same media. Detailed media composition can be seen in Table 11.

Table 11. Media composition of RO-derived RPE cells.

Media component
86% Advanced RPMI 1640 Medium
10% KOSR
2% B-27™ Supplement
1% GlutaMAX
1% Pen/Strep

2.7.1. Dissociation of Retinal pigment epithelial cells for passaging.

RPE cells were washed with PBS to remove residual media and incubated with TrypLE™ Select Enzyme (10x) for no more than 20 min at 37° C to allow cells to dissociate. Cells were detached by pipetting and passed through a 100 µm cell strainer. TrypLE™ solution was then deactivated by adding media to the suspension of sieved RPE cells and spun down at 1000 rpm for 5 min. The cells were washed with 1x PBS and either pelleted (stored at -80°C) or seeded onto Matrigel-coated 12- or 24 hanging inserts (Greiner Bio-One) at a density of 200,000 or 400 000 cells per well, respectively.

2.7.2. Immunofluorescence staining of RPE cells.

IF analyses of RPE cells were performed as qualitative experiments (n=3) by Dr. Rodrigo Cerna-Chavez and Dr. Maria Georgiou. In short, transwells were rinsed in PBS and incubated with 4% PFA for 30 min. The tissue was subsequently washed 3x5 min with PBS and flat RPE sheets

were cut into multiple pieces. Additional fixation by methanol was performed at 4°C for 20 min when staining for tight junctions (ZO-1) and Collagen IV. To remove melanin pigment from the RPE a bleaching procedure was carried out using a Melanin Bleach kit (cat. No 24883, Polysciences), following the manufacturer's instructions. To minimize non-specific binding, RPE were then blocked and permeabilized simultaneously for 1h in PBS containing 10% Donkey Serum (cat. No. 7332100-LAM, Stratech) and 0.3% Triton-X-100. Primary antibodies were diluted in PBS containing 0.1% Triton-X-100 and 1% Donkey Serum-PBS and applied at 4°C overnight. The tissue was subsequently rinsed with PBS (3x5 min). Secondary antibodies diluted in PBS were incubated for 1h at RT. RPE sections were washed 3x5 min in PBS and counterstained for nuclei using Hoechst (1:1000 in PBS) for approximately 20 min. After an additional PBS wash, RPE sections were mounted on slides using Vectashield®. A secondary antibody only control was included in each set of experiments. For all antibody details used in RPE IF please refer to Table 12 below.

Table 12. List of all primary and secondary antibodies used for RPE IF analyses.

Antibody	Species	Catalogue number	Supplier	Concentration	Type
Collagen IV	Rabbit	AB65586	Abcam	1 in 200	primary Ab
Ezrin	Mouse	E8897-100UL	Sigma-Aldrich	1 in 100	primary Ab
ZO-1	Goat	STJ140055	John's Laboratory Ltd	1 in 50	primary Ab
Anti-Goat Alexa Fluor 488	Rabbit	A11078	Life Technologies	1 in 1000	secondary Ab
Anti-Mouse Alexa Fluor 488	Goat	115-545-146-JIR	Jackson Immuno Research	1 in 1000	secondary Ab
Anti-Rabbit Cy3	Goat	111-165-003-JIR	Jackson Immuno Research	2 in 1000	secondary Ab

2.7.3. Transepithelial Electrical Resistance measurement of RPE cells.

Transepithelial electrical resistance measurement (TEER) informs on the integrity and barrier function characteristic of epithelial tissues. The RPE cells were first equilibrated to RT and the electrode was sterilized for 15 min in 70% ethanol. The use of a volt-ohm meter (cat. No. MERS00002, Millipore) used in this experiment allows for electrodes to be placed on either side of the transwell membrane. Measurement of transepithelial resistance is facilitated by an electrical current applied to the transwell inserts (Resistance = Voltage/Current). To determine unit area resistance (Ω · cm2), blank values from inserts not seeded with cells containing RPE media alone were subtracted from the sample readings. Obtained values were further multiplied by the surface area of the insert (0.33 cm^2 for a 24-well plate inserts). RPE

culture was deemed mature at TEER > 250 Ω cm^2. Measurements were taken in triplicates and routinely conducted with the supervised assistance of MRes student Eldo Galo.

2.7.4. Phagocytosis assay.

2.7.4.1. Labelling of photoreceptor outer segments (POS) with fluorescein isothiocyanate.

Bovine rod POSs (cat. No. 98740, InVision BioResources, Seattle United States) were treated with 0.4mg/mL fluorescein isothiocyanate (FITC, cat. No. F7367, Sigma Aldrich). POSs were spun down at 3000 RCF for 5 min and diluted in 10 mL of D42-D84 RPE medium. The light-sensitive POS solution was placed on a shaking incubator for 1h at RT shielded from light. This was followed by an additional centrifμgation step and 3x5 min washes with PBS. POSs were counted using a haemocytometer. The POS concentration was adjusted to a previously established desired concentration of 10^6 POSs/mL and the Axio Imager fluorescent microscope was used to corroborate POS labelling. For long term storage POSs were resuspended and maintained at - 80°C in a PBS solution containing 73mM sucrose (cat. No. S0389 Sigma Aldrich).

2.7.4.2. Flow cytometry analysis of phagocytic activity.

Thawed POS-FITC were resuspended in RPE media containing 10% FBS. Each transwell was treated with a 75 µL FITC enriched POS suspension at 37°C for 4 h (including a control sample kept at 4°C). Following incubation with FITC-labelled POS, RPE cells were rinsed with PBS and dissociated into a single-cell suspension using TrypLE™ Select Enzyme (10X). Upon removal of the TrypLE™ enzyme DRAQ5™ (cat. No. ab108410, Abcam) was diluted at 1:40 in 200 µL of flow buffer (2% FBS in PBS) and added to the dissociated cells, which were then transferred to a 1.5 mL Eppendorf tube. The DRAQ5™ dye was incubated with the cells for 10 mins at 37°C to enable the staining of live cells. To quench residual FITC fluorescence 0.2% Trypan Blue (cat. No. 93595, Sigma Aldrich) was added to the cells for an additional 10 min. Samples were centrifμged and rinsed with 2% FBS- PBS to remove all traces of Trypan Blue. Flow cytometry analysis was conducted using a BD™ LSR II flow cytometer (BD Biosciences; Franklin Lakes, United States) with 10,000 events acquired for each sample. All phagocytosis work was performed by MRes student Eldo Galo with the assistance of my supervision.

2.7.5. POS treatment of RPE.

RPE were fed 20 POS per cell every day for a period of 2 weeks and sent for transmission electron microscopy analysis. An untreated control was included in the analysis for each group.

2.7.6. ELISA Detection of VEGF and PEDF secretion by RPE cells.

The levels of VEGF in the basal compartment of RPE cells were determined using a Human VEGF DuoSet ELISA kit (cat. No. DY293B, Biotechne) following the manufacturer's instructions. In short, the procedure entailed a preparation step by coating a 96-well microplate with diluted Capture Antibody overnight. Unbound antibodies were removed by washing and plate was blocked for non-specific binding using Reagent Diluent at RT. Following a round of washing, 100 µL of basal RPE media samples and standards were applied to the wells and incubated at RT for another 2 h. Following another wash, the wells are treated with 100 µL Streptavidin-HRP is for 20 min at RT in the dark. The plate was rinsed further to remove unbound HRP molecules. To facilitate detection substrate solution was added to the samples for approximately 20 min. Upon termination of the reaction with the addition of a Stop Solution and the optical density was measured at 450 nm using a Varioskan LUX Multimode Microplate ELISA reader (Thermo Fisher Scientific). An analogous procedure was carried to determine levels of PEDF secretion in the apical compartment of RPE cells (insert media) using a Human Serpin F1/PEDF DuoSet ELISA kit (cat.No. DY1177-05, Biotechne) in accordance with the guidance manual. All ELISA work on VEGF and PEDF was carried by Dr. Rob Atkinson.

2.8. PCR

2.8.1. RNA extraction.

RNA extraction from pellets was performed under sterile and RNase-free conditions in a laminal flow hood. The hood was UV sterilized and decontaminated from RNA nucleases using RNaseZap™ (cat. No AM9780, Thermo Fisher Scientific). RNA was extracted using the ReliaPrep™ RNA Cell Miniprep System (cat. No Z6012, Promega), following the manual instructions. A detailed outline of the procedure can be found below:

Component	Description
Prepare 32.5µL 1-Thioglycerol (TG) in 3.25mL BL buffer	≤ 10 samples
Add 250 µL TG+ BL mix to cell pellet	5 × 105 - 2 × 106 cells
Mix and add 85 µL100% isopropanol	Vortex
Apply to Reliaprep minicolumns	Spin at 14 000 x g at RT for 30 sec
Add 500 µL RNA Wash solution	Spin at 14 000 x g at RT for 30 sec
Add 30 µL DNAase I solution to column (24 µL Yellow core buffer, 3 µL 0.09M MnCl2, 3 µL DNAse I enzyme)	Incubate at RT for 15 min
Add 200 µL ethanol- enriched Column wash	Centrifuge at 14 000 x g for 15 sec
Add 500 µL RNA Wash solution	Spin at 14 000 x g at RT for 30 sec
300 µL RNA Wash solution in new collection tube	Centrifuge at 14 000 x g for 2 min
Elute 30 µL NFW in 1.5 mL tube	Centrifuge at 14 000 x g for 1 min
	Store at -80 ° C

2.8.2. cDNA synthesis.

For conversion of total RNA to cDNA, the GoScript™ Reverse Transcription System was used (cat. No. A5001, Promega). First strand cDNA synthesis was initiated by preparing a 5µL total volume reaction containing the maximum amount of RNA present in the sample of the lowest RNA concentration (up to 5 µg of RNA/per reaction), primer Oligo$(dT)_{15}$ and Nuclease-Free Water (NFW). Samples were placed onto a pre-heated block at 70°C for 5 min and subsequently pre-chilled at 4°C for another 5 min. Each of the samples was briefly centrifµged to remove lid condensation and stored on ice. A reverse transcriptase mix was prepared using GoScript™ 5X Reaction buffer, $MgCl_2$, dNTPs, RNasin Ribonuclease Inhibitor and GoScript Reverse Transcriptase in accordance with the guidance manual. 5µL RNA and 15µL of the mix were then carefully mixed and the RNA was converted to cDNA at the following thermocycler conditions:

Annealing	25° C	5 min
Extension	42° C	60 min
Reverse transcriptase	70° C	15 min

Samples were then processed by PCR.

2.8.3. RT PCR

Pluripotency assessment and Sendai virus clearance were performed by undergraduate students Gabrielle Chai Jia Min and Sam Steel by carrying out a standard PCR procedure using

cDNA template. Primers used for *GAPDH,* and *Klf4*, *C-myc*, *SeV*, (Sendai clearance) and *Oct4*, *Sox2*, *Nanog* (pluripotency assessment) are shown in Table 13.

Table 13. Summary of primers used RT-PCR for Sendai virus clearance, pluripotency analysis.

Target Gene	Forward Primer	Reverse Primer	PCR fragment size
OCT4	5' CTTGAATCCCGAATGGAAAGGG 3'	5' GTGTATATCCCAGGGTGATCCTC 3'	164 bp
SOX2	5' GGCAGCTACAGCATGATGCAGGAGC 3'	5' CTGGTCATGGAGTTGTACTGCAGG 3'	131 bp
KLF4	5' GCGCTGCTCCCATCTTTCT 3'	5' TGCTTGACGCAGTGTCTTCTC 3'	69 bp
NANOG	5' AGAAGGCCTCAGCACCTAC 3'	5' GGCCTGATTGTTCCAGGATT 3'	206 bp
GAPDH	5' TGCACCACCAACTGCTTAGC 3'	5' GGCATGGACTGTGGTCATGAG 3'	87 bp
KLF4	5' TTCCTGCATGCCAGAGGAGCCC 3'	5' AATGTATCGAAGGTGCTCAA 3'	410 bp
KOS	5' ATGCACCGCTACGACGTGAGCGC 3'	5' ACCTTGACAATCCTGATGTGG 3'	528 bp
SeV	5' GGATCACTAGGTGATATCGAGC 3'	5' ACCAGACAAGAGTTTAAGAGATATGTATC 3'	181 bp
c-Myc	5' GAGAAGAGGATGGCTACAGAGA 3'	5' GACGTGCAACTGTGCTATC 3'	237 bp

2.8.4. qRT-PCR.

To determine *DRAM2a* isoform expression by RT-qPCR, RNA was cleared from DNA contamination using a TURBO DNA-free™ kit (cat. No. AM1907, Thermo Fisher Scientific). Briefly, 0.3X TURBO™ DNase buffer and 3µL of DNase were added to the RNA and incubated at 37 ° C for 30 minutes before adding 3µL of inactivation reagent. Following cDNA conversion, the following reaction was set up on a 384-well plate using a GoTaq qPCR Master mix kit (cat. No. A6002, Promega), whereby equal amounts of cDNA were used from each sample:

Reagent	Volume
cDNA Template	1 µL
COX reference dye	0.1 µL
Nuclease free water	0.9 µL
GoTaq qPCR master mix	5 µL
Forward and Reverse primer mix	3 µL
Final volume	10 µL

qPCR was performed on the Quantstudio™ 7 Flex Real-time instrument (Applied Biosystems). Data were normalized to the expression of the housekeeping gene *GAPDH*. Gene expression was calculated using the $2^{(-\Delta\Delta C_T)}$ method. Samples were run in triplicates and all data was presented as means ± SEM. Statistical analysis was carried using GraphPad Prism version 9.5.0

(GraphPad Software, USA). qRT-PCR for *DRAM2a* knockdown were optimized by me and finalized by MRes student Eldo Galo under supervision. Table 14 below shows the primers used for *DRAM2a* isoform expression.

Table 14. Primer pair used for the detection of DRAM2a (isoform a) by qRT PCR.

Target Gene	Forward Primer	Reverse Primer	PCR fragment size
DRAM2a (isoform a)	5'TATTGTGGCAAACTTCCAGAAAACA 3'	5'ACCAAAGGTAAGCACAGCTCC 3'	70 bp

2.9. DRAM2a siRNA knockdown

Due to the low siRNA uptake efficiency, d230 WT ROs were dissected and grown onto Matrigel, and poly-L-ornithine (10µg/mL) (cat. No. A-004-C, Sigma Aldrich) coated 24-well plates. Following successful plate adherence, RO cells were allowed to proliferate until reaching 80% confluency. siRNA transfection was facilitated using a Lipofectamine™ RNAiMAX Transfection reagent (cat. No. 13778030, Thermo Fisher Scientific) at about 50% confluence in accordance with the guidance manual. A crucial optimization step was the use of antibiotic and serum-free RO media. *DRAM2* Silencer Select siRNA (4392420, Assay ID: s43281) and a scrambled control (cat. No. 4390849, Thermo Fisher Scientific) were incubated at 20µM with the RO cells for a period of 72h. Successful knockdown of *DRAM2* isoform a (*DRAM2a*) was confirmed by both qRT-PCR using primers shown in Table 14 as well as Western blot analysis using methods outlined in section 2.10. The siRNA knockdown procedure was optimized by me and finalized under supervision by the MRes student Eldo Galo.

2.10. Western blot.

2.10.1. BCA protein assay.

Cell pellets were maintained at -80 ° C for long-term storage. Once thawed, samples were initially incubated at RT for 5 min with PhosphoSafe™ extraction buffer (cat. No 71296, Merck Millipore) and supplemented with a 14X protease inhibitor cocktail (cat. No 04693159001, Roche, Switzerland) (25µL per 5 RO or 1 transwell of a 24 well plate of RPE). Lysis by rigorous pipetting was alternated with vortexing and resting on ice for 20 min until complete lysis.

Samples were spun at 4° C for 10 min at 1000xg, and protein concentration of the supernatant was determined using a Pierce™ BCA Protein Assay Kit (cat No. 23225, Thermo Fisher Scientific). Briefly, protein supernatant (2.5µL) diluted with 10X diluted (22.5µL) PhosphoSafe™ buffer was applied to a 96-well plate in duplicates. A standard curve was prepared using known concentrations of BSA (cat No. 23209, Pierce™ Bovine Serum Albumin Standard Ampules, 2mg/mL, Thermo Fisher Scientific) protein. WR solution (200µL) provided by the kit was added to each well (50:1 Reagent A: Reagent B) and the plate was incubated on a shaker at 37 ° C for 30 min under minimal light exposure. Absorbance was measured at 562 nm on a Varioskan LUX Multimode Microplate Reader (Thermo Fisher Scientific). Protein samples were stored at -80 ° C.

2.10.2. SDS-PAGE.

Western blot (WB) was used to determine protein expression of autophagy, lysosomal and vesicular trafficking markers in d220 RO, RPE for both cell lysates and cell media. Typically, 10 µg of total protein lysate was diluted in 4X NuPAGE™ LDS Sample Buffer (cat. No NP0007, Thermo Fisher Scientific), reduced with a NUPAGE reducing agent and heated at 70° C for 10 min (cat. No NP0004, NuPAGE™ Sample reducing agent, Thermo Fisher Scientific). For separation of small (<70kDa) to big (>70kDa) molecular targets, NuPAGE™ MES SDS Running Buffer 20X (cat. No NP0002) and MOPS SDS Running Buffer (20X) were used, respectively (cat. No NP0001, Thermo Fisher Scientific). Samples were loaded onto precast 4-12% gradient polyacrylamide Bis-Tris gels (cat. No NP0321PK2, WG1403BOX, Thermo Fisher Scientific) and electrophoresed at 180V for 40 min using a Mini Gel Tank system (cat. No A25977, Thermo Fisher Scientific). A size standard PageRuler™ Plus Prestained Protein Ladder 10 to 250kDa (cat No 26619, Thermo Fisher Scientific) or a SeeBlue™ Plus2 Prestained Protein standard (cat. No LC5925, Thermo Fisher Scientific) were used for molecular weight reference. Please refer to Table 15 and Table 16 for a full description of WB conditions of individual protein markers. For autophagy markers such as LC3-II, samples were boiled, reduced, and processed by WB on the same day to minimize the de-lipidation of LC3-II upon freeze-thaw cycles.

2.10.3. Gel transfer.

Following electrophoresis, the gel was carefully removed from its cast. After being briefly rinsed in ultrapure ddH_20, it was transferred onto Blot™ 2 Transfer PVDF Stacks (cat. No IB24002 and IB24001, Thermo Fisher Scientific). A sandwich was assembled according to the manual's instructions and dry transfer was performed at standard conditions on an iBlot 2 Dry Blotting system over three consecutive steps - 20V for 1min, 23V for 4 min and 25V for 2min (Thermo Fisher Scientific). For autophagy markers, as well as DRAM2 protein detection, transfer was carried out at 10V for 7 min.

2.10.4. Reversible total protein staining.

Reversible total protein staining was performed on all membranes to confirm the equal loading of protein using the Pierce™ Reversible Protein Stain Kit for PVDF Membranes (Cat. No 24585, Thermo Fisher Scientific). Briefly, the PVDF membrane was washed with ultrapure ddH_20 and incubated with Memcode™ Sensitizer for 2 min under shaking conditions. Subsequently, the membrane was stained with a total protein stain for 1 min and rinsed three times with Memcode™ Destain. Rigorous washing was carried out on a shaker by adding a 1:1 Methanol/Destain solution, followed by an additional brief five washes with ultrapure ddH_20 to minimize background staining. Membranes were then imaged colorimetrically using Amersham Imager 600 (GE Healthcare, Boston, Massachussetts, USA). Finally, staining was erased using an Eraser/Methanol solution (1:1) (10-20 minutes) and membranes were briefly washed with ultrapure ddH_20.

2.10.5. Membrane blocking and antibody incubation.

Membranes were blocked for non-specific binding with 5% milk TBST (Tris-buffered saline with 0.1% Tween®20 detergent) at RT for 1 h. Incubation with primary antibodies was carried out in 5% milk TBST on a rotating platform overnight at 4° C (Table 15 for all primary antibody conditions). On the following day, membranes were washed 3x 5 min with TBST at RT. Secondary antibodies were incubated at 1:1000 for 1h at RT (Table 16) and washed 3x 5 min with TBST. To enable visualization, chemiluminescence substrate was prepared using the SuperSignal™ West Pico PLUS Chemiluminescent Substrate kit (cat. No 34579, Thermo Fisher

Scientific). Reagents were mixed in a 1:1 ratio and the chemiluminescent solution was incubated with the membranes for 5 min with minimal exposure to light. Image acquisition was carried out on an Amersham Imager 600 (GE Healthcare). Band intensity quantitation analysis was performed on Image J. Protein expression was normalized to the WT sample within each blot and total protein stain was used to corroborate equal loading.

Table 15. Summary of primary antibodies and conditions used for the WB analysis of d220 RO and RPE lysate samples.

Antibody	Species	Catalogue number	Supplier	Concentration	Protein	Incubation time	Gel condition	Running buffer
AP1γ	rabbit	PA1-18306	Fisher Scientific	1 in 1000	10 µg	overnight at 4°C	reducing	MOPS
AP2α	mouse	610502	BD Biosciences	1 in 500	10 µg	overnight at 4°C	reducing	MOPS
AP3β1	rabbit	13384-1-AP	Proteintech	1 in 500	10 ug	overnight at 4°C	reducing	MOPS
CD63	rabbit	ab134045	Abcam	1 in 1000	10 µg	overnight at 4°C	reducing	MES
CD81	mouse	ab79559	Abcam	1 in 1000	10 µg	overnight at 4°C	non-reducing	MES
CDM6PR	rabbit	EPR7691	Abcam	1 in 250	10 µg	overnight at 4°C	reducing	MES
CIM6PR	rabbit	AV43519	Sigma	1 in 10 000	10 µg	overnight at 4°C	non-reducing	MES
CTSB	rabbit	31718	Cell Signaling	1 in 5000	10 µg	overnight at 4°C	reducing	MES
CTSD	mouse	C0715	Merck	1 in 10 000	10 ug	1h at RT	reducing	MES
DRAM2	rabbit	HPA018036	Sigma	1 in 250	30 µg	overnight at 4°C	non-reducing, boiled	MES
GBA	rabbit	G404G	Sigma	1 in 1000	10 ug	overnight at 4°C	reducing	MES
LAMP1	mouse	H4A3	DSHB	1 in 500	10 ug	overnight at 4°C	reducing	MES
LAMP2	mouse	A86605	Antibodies.com	1 in 500	10 µg	overnight at 4°C	reducing	MES
LC3	rabbit	3868S	Cell Signaling	1 in 500	10 µg	overnight at 4°C	reducing	MES
LIMP2	rabbit	HPA018014	Sigma	1 in 2000	10 ug	overnight at 4°C	reducing	MES
NPC2	rabbit	HPA000835	Sigma	1 in 750	10 ug	overnight at 4°C	reducing	MES
p62	mouse	610832	BD UK Ltd	1 in 500	10 µg	overnight at 4°C	reducing	MES
PPT1	mouse	MA5-26471	ThermoFischer	1 in 2000	10 ug	overnight at 4°C	reducing	MES
ps6	rabbit	2211S	Cell Signaling	1 in 500	10 ug	overnight at 4°C	reducing	MES
rab5	rabbit	ab218624	Abcam	1 in 500	10 ug	overnight at 4°C	reducing	MES
rab7	rabbit	ab137029	Abcam	1 in 500	10 ug	overnight at 4°C	reducing	MES
sortilin	rabbit	20681	Cell Signaling	1 in 500	10 ug	overnight at 4°C	reducing	MES
VPS35	rabbit	814533	Cell Signaling	1 in 1000	10 ug	overnight at 4°C	reducing	MES
VPS53	rabbit	12878722	Fisher Scientific	1 in 3000	10 ug	overnight at 4°C	reducing	MES

Table 16. Summary of secondary antibodies used for the WB analysis of d220 RO and RPE lysates.

Antibody	Species	Cat. No.	Supplier	Concentration	Incubation period
Secondary anti-mouse	goat	P0447	Agilent Dako	1 in 2000	1h at RT
Secondary anti-rabbit	swine	P0399	Agilent Dako	1 in 1000	1h at RT

2.10.6. Detection of low abundance protein.

For detection of less abundant protein such as lysate DRAM2 as well as PPT1 and NPC2 secreted in the media of RO and RPE, membranes were washed with ultrapure ddH_20 briefly and pre-treated with an antigen pretreatment solution for 10 min at RT (cat. No 46640,

SuperSignal™ Western Blot Enhancer). After blocking for non-specific binding with 5% milk TBST, membranes were rinsed in TBST for an additional 5 min and incubated with primary antibody in antibody diluent overnight at 4°C (SuperSignal™ Western Blot Enhancer). Following 3 washes with TBST (3x 20 min), secondary antibodies were incubated for 1h at RT at 1:20 000- 1:100 000 (Table 16). For optimized signal detection membranes were rigorously washed in TBST for an additional 1h prior to being visualized using Femto-ECL substrate (cat. No 34094, SuperSignal™ West Femto Maximum Sensitivity Substrate kit, Thermo Fisher Scientific). Please refer to Table 17. for a comprehensive description of WB conditions of individual markers.

Table 17. WB conditions used for the detection of low abundance protein in d220 RO/RPE lysate and media samples.

Marker	Species	Catalogue number	Supplier	Sample type	Primary	Secondary	Protein
CTSD	mouse	C0715	Merck	media	1 in 500	1 in 50 000	50 µg
DRAM2	rabbit	HPA018036	Sigma	lysate	1 in 250	1 in 20 000	30 µg
NPC2	rabbit	HPA000835	Sigma	media	1 in 500	1 in 100 000	50 µg
PPT1	mouse	MA5-26471	ThermoFischer	media	1 in 500	1 in 100 000	50 µg

2.11. Lysosomal activity assays.

2.11.1 CTSD kinetic activity assay.

Cathepsin D activity in d220 RO and RPE samples was determined using an in-house kinetic assay developed by Dr. Marzena Kurzawa-Akanbi. The samples were lysed gently in native buffer to preserve enzymatic activity (0.2M Triethylammonium bicarbonate buffer, cat. No T7408, Sigma Aldrich supplemented with protease inhibitors, cat. No 04693159001, Roche, Switzerland). Protein concentration was measured using a Pierce™ BCA Protein Assay Kit. 50 µM MCA (7-Methoxycoumarin-4-acetic acid) diluted in assay buffer was used to generate a standard curve (0-25 µM) (cat. No 265301, Thermo Fisher Scientific). The kinetic assay was performed on black clear bottom 96-well plates (Thermo Fisher Scientific) in a total volume of 100µL assay buffer. In short, 5 µg protein lysate was diluted in 50mM sodium acetate assay buffer pH 4.0 (cat. No AM9740, Thermo Fisher Scientific). Protein lysate treated with 0.2mg/mL pepstatin inhibitor (Enzo Life Sciences) served as a negative control. Immediately prior to the initiation of the kinetic assay, Cathepsin D & E substrate (Enzo Life Sciences) was applied at a final concentration of 80µM. Fluorescence signal kinetics were recorded every 5

min over the course of 20 min upon addition of the substrate. Measurements were taken at 320nm/400nm excitation/emission spectra using Varioskan LUX Multimode Microplate Reader (Thermo Fisher Scientific).

2.11.2. Glucosylceramidase and Alpha-mannosidase activity assays.

Glucosylceramidase activity in d220 RO and RPE lysate and media samples was established using a commercially available Glucosylceramidase activity kit (cat. No. 273339, Abcam). The assay was conducted in a total volume of 160µL. 20µM 4-Methylumbelliferone Standard (4-MU) prepared in Assay Buffer was used to generate a standard curve (0-20µM). The samples were gently lysed using the provided Assay Buffer and concentration was measured using a Pierce™ BCA Protein Assay Kit. 20x diluted substrate was added to 30 µg of protein lysate diluted in Assay Buffer. Samples were incubated on a white flat bottomed 96-well plate (cat. No SS246, Sero-Wel 96-Well Plates, Sterilin, Appleton Woods Ltd) at 37°C degrees for 30 minutes under minimal light exposure. Following incubation, 100µL Glucosylceramidase Stop buffer was added to terminate the reaction including all samples, a Glucosylceramidase positive control, negative background control and standards. Fluorescence intensity was measured at 360nm/445nm excitation/emission spectra at 37°C in end-point mode. Alpha-mannosidase activity in the samples was determined in an analogous fashion using a fluorometric end-point mode Alpha-mannosidase activity assay (cat. No 282917, Abcam).

2.12. Proteomic analysis of Retinal organoid and Retinal pigment epithelial cells.

2.12.1. Protein digestion.

10 µg of total RO protein (5µL) (n=3) was digested using S-Trap micro spin columns (Protifi, NY, USA). Each biological replicate was denatured in 25µL 5% SDS 50mM Triethylammonium bicarbonate (TEAB) (pH 8.5). The proteins were then reduced with 20mM DTT at 65°C for 30 min and alkylated with 40mM iodoacetamide at RT in the dark for 30 min. Acidification was achieved by adding 27.5% phosphoric acid to a final concentration of 2.5% (v/v). Protein sample was subsequently bound onto the micro spin columns in 6 volumes of loading buffer (90% methanol 100mM TEAB pH 8.0) and spun at 4000xg for 30s. Columns were rinsed 3x with loading buffer and flow through was discarded. Protein digestion with trypsin

(Worthington) occurred overnight at 37°C in 50mM TEAB pH 8.5, at a ratio of 10:1 protein to trypsin. Peptide elution was carried out over three consecutive washes: first 50 µL 50mM TEAB, second 50 µL 0.2% formic acid and third 50 µL 50% acetonitrile with 0.2% formic acid. The solution was subsequently frozen, desiccated in a vacuum concentrator and reconstituted in 0.2% formic acid.

The digestion of RPE cell lysates followed a similar protocol with some modifications. 15 µg total protein RPE sample (n=7) were adjusted to 23 µL and equal volumes of 2x concentrated S-trap lysis buffer was added (10% SDS in 100mM Triethylammonium bicarbonate (TEAB) pH 8.5). The samples were prepared using the same general steps of reduction, alkylation, and acidification. Following application and washing onto the S-Trap micro spin columns with loading buffer, digestion with trypsin was carried out for 1.5h at 47°C. Peptides were eluted following the procedure outlined above. Digestion of protein was carried out by Dr. Pawel Palmowski at the Proteomics Unit at the University of Newcastle.

2.12.2 Data Acquisition analysis.

For RO and RPE cell samples two different modes of acquisition were used – data dependent for RO and data independent for RPE, respectively Table 18. LCMS analysis for RO and RPE cells was conducted on an Exploris 480 Quadrupole-Orbitrap Mass Spectrometer (Thermo Fisher Scientific, Waltham, MA, U.S.A.) and a Orbitrap Fusion™ Lumos™ Tribrid™ Mass Spectrometer (Thermo Fisher Scientific, Waltham, MA, U.S.A.), respectively. For RO LCMS, equivalents of 1 µg of each peptide were loaded onto an Acclaim PepMap100 C18 LC Column (Thermo Fisher Scientific) and separated on a 75µmx25cm C18 column (Thermo Fisher Scientific). For the loading of 1 µg RPE a 300µm x 5mm C18 PepMap C18 trap cartridge (Thermo Fisher Scientific) was utilized and a 75µm x 50cm C18 column for separation (Thermo Fisher Scientific). Although the same flow rate was used for sample loading (10 µL min−1) on columns with close to identical parameters, different columns and flow rates were applied for peptide separation (400 nL min^{-1} for ROs, as opposed to 250 nL min^{-1} for RPE). Further differences in experimental conditions shown in Table 18 pertain to differential use of mass spectrometry instruments, gradient time, LCMS run time and ultimately mode of acquisition, which necessitated the use of different experimental conditions. Data acquisition analyses in

both cases was performed by Dr. Pawel Palmowski at the Proteomics Unit at the University of Newcastle.

Table 18. Detailed summary of RO and RPE data modes outlining some key differences in experimental conditions for LCMS analysis.

	RO LCMS	RPE LCMS
Column	Sample loaded onto Acclaim PepMap100 C18 LC Column (5 mm Å~ 0.3 mm i.d., 5 µm, 100 Å, Thermo Fisher Scientific) and separated on 75µmx25cm C18 column (Thermo EasySpray -C18 2 µm)	Sample loaded onto 300µm x 5mm C18 PepMap C18 trap cartridge (Thermo Fisher Scientific) and separated on 75µm x 50cm C18 column (Thermo EasySpray -C18 2 µm)
Flow Rate	10 µL min−1 for both sample loading and 400 nL min−1 for separation	10 µL min−1 for sample loading and 250 nL min−1 for separation
Gradient	60-minute gradient from 97% A (0.1% FA in 3% DMSO) and 3% B (0.1% FA in 80% ACN 3% DMSO) to 35% B	110-minute gradient from 97% A (0.1% FA in 3% DMSO) and 3% B (0.1% FA in 80% ACN 3% DMSO) to 35% B
Mass Spectrometer	Exploris 480 Quadrupole-Orbitrap Mass Spectrometer (Thermo Fisher Scientific, Waltham, MA, U.S.A.)	Orbitrap Fusion™ Lumos™ Tribrid™ Mass Spectrometer (Thermo Fisher Scientific, Waltham, MA, U.S.A.)
LCMS Run Time	90 minutes	150 minutes
Acquisition Mode	Data-dependent (DDA) acquisition	Data-independent (DIA) acquisition
MS Resolution	Orbitrap full scan resolution of 60,000	MS resolution full scan mode of 60,000
Collision Energy	HCD collision energy of 30% for ddMS2 scans	Normalized collision energy level of 33% for DIA MSMS

2.12.3. Data processing.

The obtained DDA and DIA data was queried against the protein sequence database available on (https://www.uniprot.org/uniprot/?query=proteome:UP000005640) using MaxQuant (for RO) v2.0.3.0, and Spectronaut v16.1 (Biognosys) (for RPE). This was done using default settings such as cysteine alkylation: iodoacetamide, digestion enzyme: trypsin, Variable modifications: Oxidation (M), Acetyl (Protein N-term). A confidence cut-off threshold representative to FDR<0.01 was applied to the search file on both the peptide and protein level. Protein information was extracted using an in-house R script, which was further processed in Perseus https://maxquant.net/perseus/. Recorded peak intensities were log2

transformed. An option for "width adjustment" was applied in the Perseus software to normalise for putative discrepancies in loading and peak intensity distribution. Furthermore, any missing values were excluded from the analysis. Statistically significant changes in relative protein abundance were identified using modified ANOVA (FDR<0.05, S0=0.1) followed by Tuckey's post hoc test (FDR<0.05). Comprehensive data analysis was carried out with the supervised assistance of MRes student Eldo Galo and Dr. Pawel Palmowski.

2.13. Lipidomic analysis of RO cells.

Lipidomic analysis is a quantitative method which entails the comprehensive profiling of lipid species present in biological samples. Lipid identification and quantification was conducted by Prof. Phil Whitfield's group at the University of Glasgow. The isolation procedure followed the method of Folch (Folch et al., 1957). Briefly, samples were extracted in chloroform/methanol (2/1, v/v) and centrifuged at 1700 x *g* for 10 minutes. Phase partitioning was facilitated by the addition of 0.1 M KCL, whereby the lower organic phase containing lipids was retained. The lipid-enriched phase was subsequently dried in the presence of nitrogen gas prior to being reconstituted in methanol containing 5 mM ammonium formate. Lipidomic analysis was carried out under positive and negative ion modes over the mass to charge (*m/z*) range 250-2000 at a resolution of 100,000 using a Thermo Exactive Orbitrap mass spectrometer equipped with a heated electrospray ionization (HESI II) probe coupled to a Thermo Fisher Scientific ultimate 3000 RSLC system. Separation of lipids by column chromatography was performed using a Thermo Hypersil Gold C18 column (1.9µm; 2.1 mm × 100 mm) maintained at 50°C. Mobile phase A comprised an aqueous solution containing 10 mM ammonium formate and 0.1% (v/v) formic acid. Mobile phase B was made up of 90:10 isopropanol/acetonitrile (ACN) containing 10 mM ammonium formate and 0.1% (v/v) formic acid. The initial gradient conditions were 65%A/35%B. An increase the gradient of phase B was applied from 35% to 65% over 4 min, followed by 65%-100% over 15 min, with a hold for 2 min before re-equilibration to the starting conditions over 6 min. The gradient flow occurred at a rate of 400µL/min. Raw data were analyzed using Progenesis QI software version 2.1 (Nonlinear Dynamics). Lipid species were further assigned via cross-referencing with LIPID MAPS (www.lipidmaps.org/) and HMDB (http://www.hmdb.ca/) databases.

2.14. Transmission electron microscopy.

D220 RO and mature RPE cells cultured on 12- and 24-well inserts were fixed in 2% glutaraldehyde 0,1 M sodium cacodylate and further processed by Tracey Davey (Electron Microscopy Research Services, Newcastle University). At the TEM facility, the samples were subjected to an additional fixation by 2% osmium tetroxide. They were then dehydrated using a gradual increase in acetone concentration. Once the dehydration process was complete, samples were embedded in epoxy resin and allowed to polymerize at 60°C for 36 hours. Blocks of epoxy resin were then ultra-sectioned into slices of 70 nm thickness and collected on copper grids, stained with uranyl acetate and lead citrate. TEM images were captured using a Philips CM100 TEM 16 microscope. Each set of analyses entailed the blindfold selection of 8-10 images per group to allow for the unbiased evaluation of morphology findings. Quantification of lipid-containing organelles, mitochondria, melanin-containing structures, and lamellar bodies in RPE was carried out by MRes student Eldo Galo under supervision.

2.15. Statistical Analysis.

Data was tested for normality using a Shapiro-Wilk's test. Assuming normal distribution, the data points across different groups were compared using a parametric One-Way ANOVA test (Šídák's multiple comparisons test). When the data did not meet the normality criteria, a non-parametric Kruskal-Wallis test was applied. Due to the presence of 5 or more groups in most of the datasets, comparisons were typically performed in pre-selected pairs (CORD21-P1vsP1c and CORD21-P2vsP2c), whereby the WT control in each case was excluded from the analysis. Statistical analysis was carried out using GraphPad Prism version 9.5.0. All data was presented as mean ± SEM values and statistical significance was assumed when $p \leq 0.05$ (*$p \leq 0.05$, **$p \leq 0.01$, ***$p \leq 0.001$, ****$p \leq 0.0001$).

Chapter 3: CRISPR-Cas9 correction of the CORD21-P2 line

3. Introduction

CORD21 retinal disease is a rare, highly debilitating form of cone-rod dystrophy with adult onset leading to the progressive loss of visual acuity. It is an autosomal recessive condition which typically presents with macular involvement followed by peripheral degeneration of the retina associated with night blindness and light sensitivity (Chapter 1, 1.4).

Dermal skin fibroblasts were obtained from two individuals with DRAM2 macular dystrophy by Dr. Martin McKibbin's group and subsequently reprogrammed into iPSCs by Dr. Dean Hallam and Rachel Wilson. These iPSC lines are hereby known as CORD21-P1 and CORD21-P2. The CORD21-P1 iPSC line is homozygous for a loss-of-function variant at c.140delG [p. Gly47Valfs*3], leading to transcript degradation by nonsense mediated decay, whereas CORD21-P2 is a compound heterozygote for an intron-exon missense change c.131G>A [p. Ser44Asn] and a nonsense frameshift variant c.494G>A [p. Trp165*]. The iPSC lines were characterised for pluripotency, genetic stability, and Sendai virus clearance. Elucidation of DRAM2 function in patient-derived *in vitro* retinal models, necessitated the generation of isogeneic controls, in which one of the patients' mutations is reversed to a heterozygous state on the same genetic background using CRISPR-Cas9 technology. Previous work by MRes student Edvinas Cerniauskas enabled the generation of the CORD21-P1c iPSC line by conducting a heterozygous correction of the c.140delG allele. This chapter outlines the homology-directed repair (HDR) of the c.131G>A [p. Ser44Asn] mutation in CORD21-P2 using CRISPR-Cas9 and the subsequent off-target sequencing analyses in both CORD21-P1c and P2c to corroborate the absence of undesired genetic alterations in regions highly homologous to the sites of CRISPR correction in both patient iPSC lines.

Hence the generation of the CORD21-P1c and CORD21-P2c iPSC lines using CRISPR-Cas9 enabled us to evaluate the impact of CORD21-P1 and -P2 *DRAM2* mutations on the lysosomal activity of iPSC-derived patient models. In summary, data outlined here, delineates prerequisite steps to the generation of valuable *in vitro* retinal models for the study of DRAM2 function in the context of the retina.

3.1 Results

3.1.1 The generation of the CORD21-P2c line: CRISPR-Cas9 correction of the 131G>A allele in CORD21-P2.

3.1.1.1 gRNA and ssODN design

CRISPR-Cas9 genome editing was used to create an isogeneic control, here referred to as CORD21-P2c. This would be done by introducing a single nucleotide A>G correction at c.131 in the compound heterozygous CORD21-P2 iPSC line. The CRISPR-Cas9 technology allows for precise knock-in corrections by homology-directed repair (HDR) (the change of a single-nucleotide within the genomic sequence) by utilising the ability of guide RNAs (gRNA) to target Cas9 enzyme to genomic sites of interest (Figure 15).

Following a thorough analysis of the *DRAM2* exon 3 boundary (111131424-111131424), where the c.131G>A mutation is located, an obvious candidate emerged as the only gRNA capable of targeting the c. 131 site within a 15-nucleotide radius (Figure 16) (Paquet *et al.*, 2016). This gRNA sequence had previously been used in a failed attempt at 131G>A correction by Dr. Chunbo Yang. Dr. Chunbo Yang used a PCR screening method based on mutation- and wild-type specific primers. The latter approach proved inefficient in identifying genuinely corrected iPSC clones. To optimize the efficiency of the screening procedure, a short asymmetric ssODN (single-stranded oligo DNA nucleotides) template was designed (101 bps) (Richardson *et al.*, 2016). The ssODN carried the wild-type c.131G sequence, a restriction site (*Alu I*) to enable the easy identification of corrected clones and a mutated PAM sequence to prevent the re-cutting of genomic DNA following CRISPR-Cas9 editing. The *Alu I* restriction site and the mutation of the PAM sequence acted as silent, reading frame non-perturbing mutations (Figure 16). To further minimise the probability of cleavage post edit, we delivered the Cas9 enzyme as a Cas9/sgRNA ribonucleoprotein (RNP) complex (Okamoto *et al.*, 2019). A non-homologous end joining (NHEJ) inhibitor known as SRC-7 was also applied during nucleofection to increase the efficiency of HDR in iPSCs (Maruyama *et al.*, 2015). Please refer to the Appendix A for a detailed summary of all relevant DNA sequences to the CRISPR-Cas9 experiment.

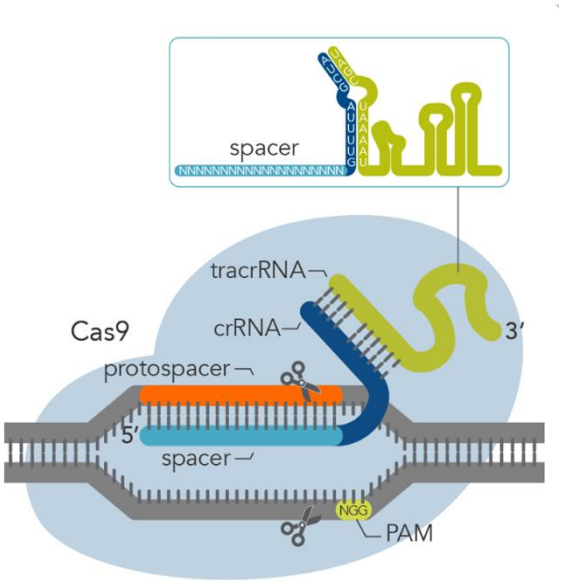

Figure 15. Cas9-targeting is enabled by guide RNA complementarity to the genomic site of interest. The guide RNA is composed of spacer, crRNA (CRISPR RNA) and tracrRNA (trans-activating CRISPR RNA) domains. crRNA and tracrRNA form a complex with the Cas9 enzyme. Cas9 is guided to the region of interest via sequence complementarity of the spacer gRNA. Cas9 then cleaves the target DNA 3 nucleotides upstream of the PAM recognition motif. The resultant DNA double breakage can be resolved either by NHEJ or by cells utilising the more precise genome editing mechanism known as HDR. Image was taken from the integrated DNA technologies website.

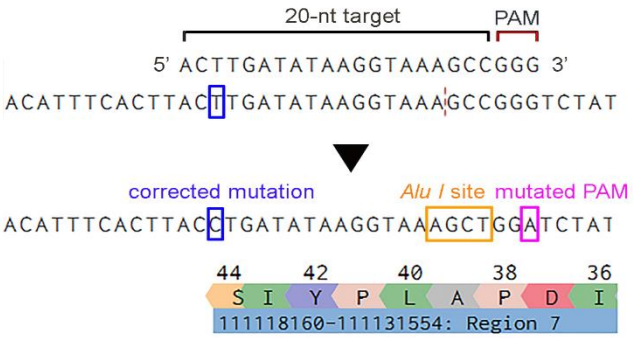

Figure 16. Design of the gRNA and ssODN sequences used in the CRISPR-Cas9 experiment. Top panel shows gRNA complementarity to genomic DNA. The gRNA carries the c.131G>A mutation (blue box). The Cas9 cleavage site is shown as an interrupted red line 3 nucleotides upstream of PAM. Bottom panel shows the ssODN template carrying the wild-type c.131 sequence (blue), the *Alu I* restriction site (orange) and the mutated PAM sequence (pink). Both the restriction site and the mutated PAM are introduced on the ssODN as synonymous changes not affecting the reading frame of *DRAM2*.

3.1.1.2 Validation of selected gRNA in vitro

The selected gRNA (Figure 16) was assessed for its ability to direct Cas9 to the c.131G>A site on PCR amplified CORD21-P2 fragments (Chapter 2). The gel electrophoresis image below demonstrates the successful Cas9 digestion of mutant CORD21-P2 DNA mediated by the gRNA *in vitro* (Figure 17). The cleavage generated DNA bands of expected size validating the gRNA batch for further use in iPSCs nucleofection experiments (Figure 17).

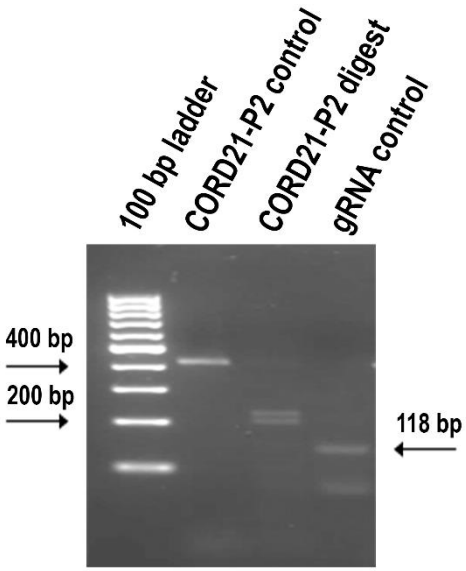

Figure 17. Cas9-mediated in vitro digestion of CORD21-P2 DNA guided by gRNA. Lane 1) 100 bp ladder. 2) Control CORD21-P2 PCR- amplified DNA fragment (408 bp). 3) Two band sizes of 215 bp and 193 bp were observed for the digested CORD21-P2 DNA, respectively. DNA cleavage occurred following incubation with 300nM gRNA for 1h. 4) gRNA control in the absence of Cas9 enzyme and CORD21-P2 DNA shows the presence of a 118 bp band corresponding to the expected length of the gRNA and potential primer dimers left from the gRNA synthesis reaction can be seen in this lane.

3.1.1.3 Screening for corrected CORD21-P2c iPSC clones

Following the nucleofection of CORD21-P2 iPSCs, 96 single -cell iPSC colonies were picked. Out of those, only 48 colonies survived. This prompted the re-picking of another 59 single-cell colonies, which were allowed sufficient time to expand. During expansion, an additional 8 clones were lost. Restriction digests were performed on all 99 clones for which DNA extraction

was successful. This entailed the PCR amplification of clones, followed by digestion of PCR products with an *Alu I* restriction enzyme. Out of a total of 99 clones, PCR reactions failed for 8 clones as evident from restriction digest screens. Investigation into surviving clones (n=91) revealed that 57% of the clones showed positive digestion with the *Alu I* restriction enzyme, whereby only 31% produced correct DNA band patterns. A representative gel example is shown in Figure 18. The generation of DNA bands of 216 and 192 bp sizes following *Alu I* cleavage suggested the integration of the ssODN sequence into the genomic DNA of iPSC clones. The correct incorporation of the ssODN sequence was evident from the introduction of a single *Alu* I site inside the region amplified by the screening primers (Figure 18). Clones showing further bands to the ones outlined above, were not sequenced due to the potential integration of NHEJ-related indels in their genomic sequence (n=19%).

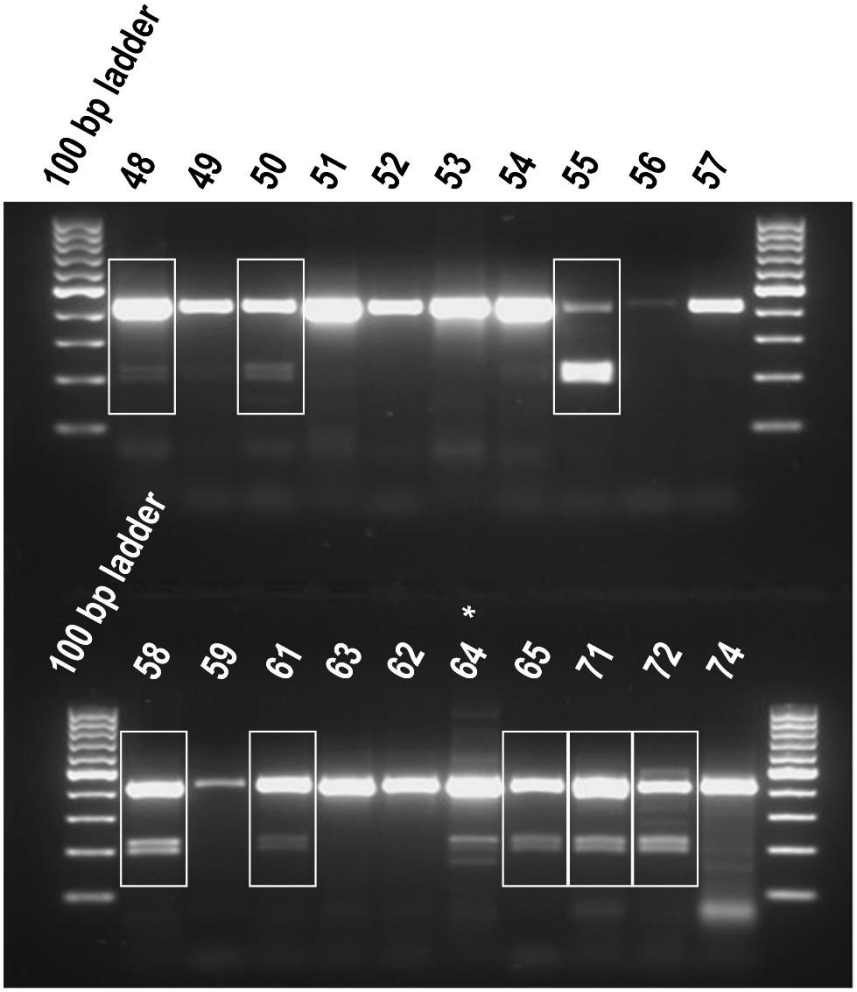

Figure 18. Representative restriction digest image of CRISPR-edited CORD1-P2 clones. Clones 48, 50, 55, 58, 61, 65, 71 and 72 were selected as primary targets for Sanger sequencing due being digestible in the presence of *Alu I* enzyme, as inferred by the presence of two bands of 216 and 192 bp, respectively.

**Clones containing additional bands were not examined due to the presence of potential NHEJ-related indels.*

Based on sequencing data, 63% of all successfully sequenced samples carried indels associated with NHEJ and only 2% of clones were found to be corrected at c.131 by CRISPR-Cas9. These were iPSC clone numbers 13 and 72. Closer examination of their DNA chromatograms, however, revealed that only clone 72 presented with no additional genomic alterations in the immediate vicinity of the site of the correction (Figure 19, A). All Sanger sequencing experiments were conducted by Dr. Bilal Alobaidi from Prof. Joris Veltman's group at Newcastle University.

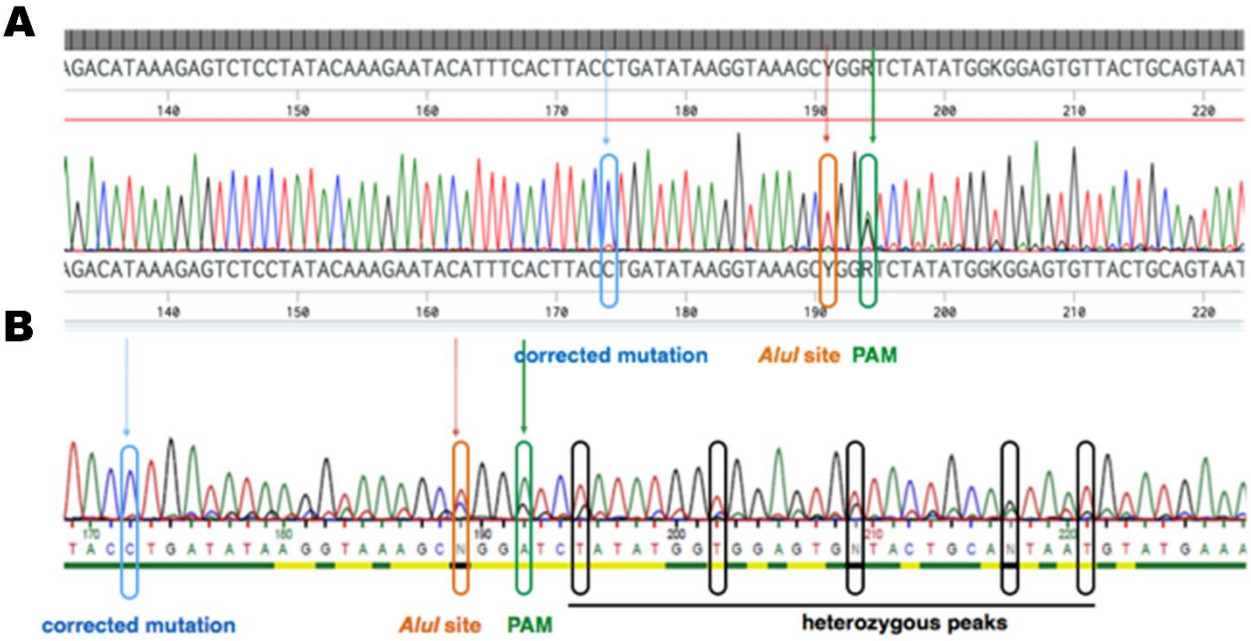

Figure 19. Sanger sequencing output from the CRISPR-Cas9 corrected clones 13 and 72. DNA chromatograms for CORD21-P2c iPSC clones 72 (A) and 13 (B) demonstrated the successful CRISPR-Cas9 correction of the c. 131 site as evident from the presence of a single cytosine peaks marked in blue. Furthermore, heterozygous knock-ins were observed for the two silent ssODN mutations in both clones. One of these synonymous changes is the incorporation of an *Alu I* site (orange), and the other one pertains to the abrogation of the PAM site (green) originating from the ssODN. Sanger sequencing was performed using the reverse primer ACTGAATCTTATTGGGCTG. Peak heterozygosity upstream (underlined in black) of the disrupted PAM in clone 13 (B) indicated the presence of unintended indels following CRISPR-

Cas9 correction.

As it's made evident from the DNA chromatogram of CORD21-P2 clone 13, peak ambiguity is apparent upstream of the disrupted PAM (green) in exon 3 (Figure 19, B). This suggests that clone 13 may carry additional genomic alterations within the coding sequence of *DRAM2*, which was suggestive of repeated Cas9 cutting following ssODN integration. For these reasons, clone 13 was discarded from further use in iPSC differentiation. Additional Sanger sequencing revealed the presence of indels and/or lack of c.131G>A correction in iPSC clones 18, 22, 48, 50, 55, 58, 61, 77, 91, 98, 100, 104 and 105 (Figure 20). One interesting example was presented by clone 55. Despite the fact this clone was found to be homozygously corrected for the two synonymous ssODN changes (Figure 20, C), the ssODN recombination did not extend to the site of the actual mutation (c. 131). Interestingly, the partial homozygous incorporation of the ssODN including the sequence of the *Alu I* restriction site was also reflected in the ability of *Alu I* to cut a significant amount of this clone's PCR fragment (Figure 18, top panel). Sanger sequencing of the remainder of the iPSC clones (3, 10, 16, 20, 23, 28, 44, 45, 47, 50, 60, 61, 65, 71, 78, 82, 87, 92 and 97) was confounded due to failed sequencing reactions and/or low quality of the reads.

Results obtained from the CRISPR correction of the c.131G>A mutation in CORD21-P2 iPSCs showed 2% success rate. Our CRISPR-Cas9 experiment resulted in the identification of one clone (clone 72) suitable for further use in retinal differentiation. Clone 72 would hereafter be referred to as the CORD21-P2c line.

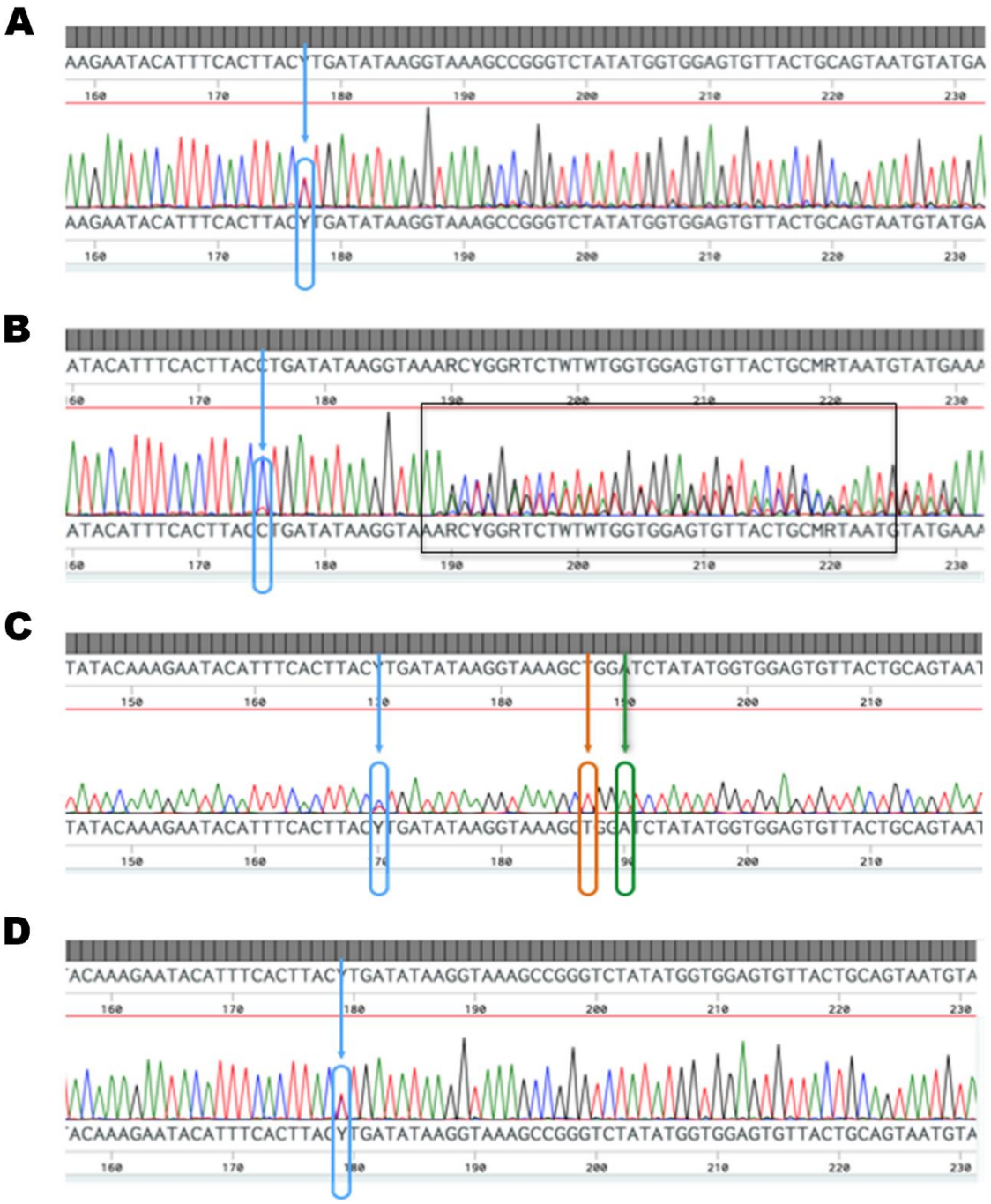

Figure 20. Sanger sequencing reads from clones 18, 50, 55 and 91. (A) DNA chromatogram for clone 18, which appears to still carry the c.131G>A mutation (blue). (B) c. 131A>G correction is evident for clone 50 (blue), however, upstream exon *DRAM2* sequence shows the considerable presence of indels (black box). (C) Clone 55 is homozygously corrected for the presence of an *Alu I* restriction site (orange) as well as the mutated PAM (green) but is still heterozygous for the c.131G>A mutation. (D) Sequencing read for clone 91 shows relatively clean sequence in the absence of a c.131A>G correction (blue).

3.1.1.4. Characterization of DRAM2 iPSC lines for pluripotency, genomic stability, and Sendai virus clearance.

Following establishment, the CORD21-P1 and -P2 lines exhibited typical iPSC morphology on bright field microscopy resembling a colony-like appearance (Figure 21, A). Sanger sequencing confirmed the successful heterozygous correction of the c.140delG and c.131G>A mutations by CRISPR-Cas9 in the CORD21-P1c and -P2c isogenic iPSC controls, respectively (Figure 21, B). As can be seen from the RT PCR analysis, patient iPSCs were cleared of exogenous viral transgenes associated with the Sendai virus reprogramming (Figure 21, C). RT PCR expression of master pluripotency genes *OCT4*, *SOX2* and *NANOG* furthermore confirmed that CORD21-P1 and -P2 iPSCs are pluripotent (Figure 21, D). Pluritest^{TM} assessment of all iPSC lines, supplemented this analysis by corroborating the pluripotency status of CORD21-P1c and -P2c (Figure 21, E and F). The absence of chromosomal abnormalities in CORD21-P1 and -P1c has been reported previously following qPCR karyotype analysis conducted by undergraduate students (data not shown as figure includes data for additional cell lines but can be provided). Subsequently, CORD21-P2 and -P2c were also free of genomic abnormalities as evident from the Karyostat^{TM} analysis, corroborating the absence of chromosomal copy number aberrations on the whole genome view of CORD21-P2 and -P2c (Figure 21, G).

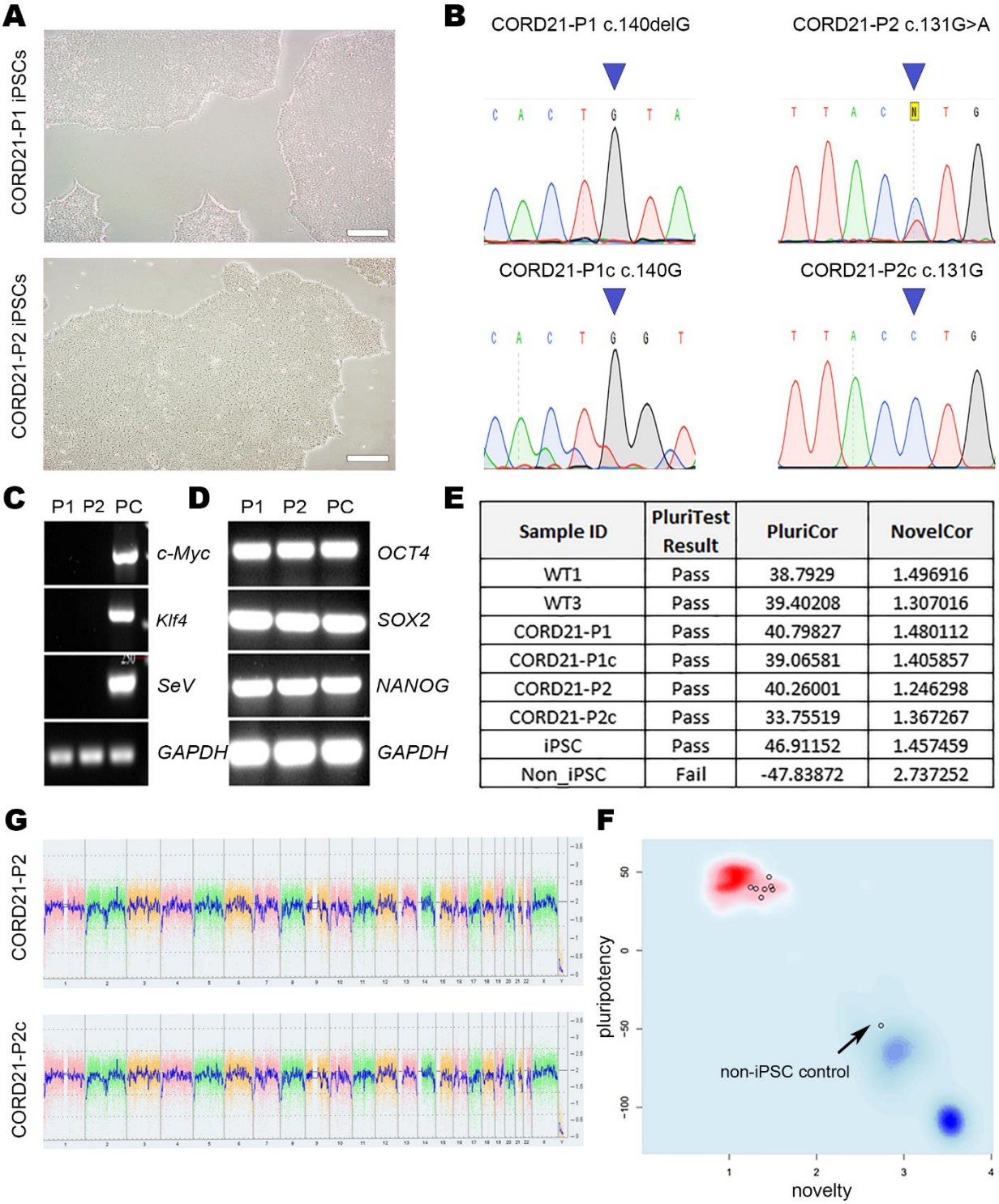

Sample ID	PluriTest Result	PluriCor	NovelCor
WT1	Pass	38.7929	1.496916
WT3	Pass	39.40208	1.307016
CORD21-P1	Pass	40.79827	1.480112
CORD21-P1c	Pass	39.06581	1.405857
CORD21-P2	Pass	40.26001	1.246298
CORD21-P2c	Pass	33.75519	1.367267
iPSC	Pass	46.91152	1.457459
Non_iPSC	Fail	-47.83872	2.737252

Figure 21. Characterization of DRAM2 iPSC for pluripotency, Sendai virus clearance and genomic stability. (A) Brightfield images from the CORD21-P1 and -P2 lines demonstrate a colony-like morphology characteristic of pluripotent iPSCs (Scale bars=200 µm). (B) DNA chromatograms show the absence of a guanine base at c.140 in CORD21-P1 and its respective presence in CORD21-P1c upon CRISPR-Cas9 correction. The heterozygous c.131G>A mutation present in CORD21-P2 is restored to the wild-type state in the CORD21-P2c isogenic control. (C) RT PCR shows clearance of Sendai virus-associated transgenes in CORD21-P1 and -P2 relative to positive control (PC) following iPSC reprogramming. (D) RT PCR demonstrates the pluripotent status of CORD21-P1 and -P2 as evident from the expression of *OCT4*, *SOX2* and *NANOG* genes relative to PC sample. *GAPDH* was used as a control. (E) Pluritest^{TM} Table shows high pluripotency scores (PluriCor) for iPSC lines used in this study. (F) The pluripotency test plot is a visual representation of the samples based on pluripotency (y-axis) and the novelty score (x-axis) listed in the PluriTable (E). The x/y scatter plot shows the relative distribution of pluripotent (red) and non-pluripotent samples (blue) in the reference dataset. A non-iPSC sample indicated by arrow served as a negative control. (G) Whole genome view shows no chromosomal copy number abnormalities for somatic and sex chromosomes in CORD21-P2 and -P2c iPSCs. The smooth signal plot (y-axis) represents log2 ratios of microarray signal intensities, whereby a deviation from the normal chromosome copy number (CN=2) would indicate chromosomal copy number aberrations. Colours pertain to the raw chromosomal signal, whereby blue represents the normalized copy number signal.

3.1.1.5. Off-target sequencing for CORD21-P1c and CORD21-P2c iPSC lines.

After the establishment of CORD21-P1c and -P2c iPSC lines by CRISPR-Cas9 we carried out additional off-target analysis using Cas-OFFinder for the presence of undesirable genomic DNA alterations at sites highly homologous to the sites of CRISPR-Cas9 correction in CORD21-P1c and -P2c. The sequences surrounding the potential CRISPR/Cas9 target sites were amplified by PCR. Sanger sequencing chromatograms for the top genomic targets for each iPSC line (Figure 22) corroborate the absence of point mutations or indels in the shown genes (n=9-10). Of note one sequencing reaction failed for CORD21-P2c and would need to be repeated in the future. Off-targeting analysis for CORD21-P1c was conducted under supervision with the help of MRes student Eldo Galo. Supplementary off-target *blastn* data is shown in Appendix B.

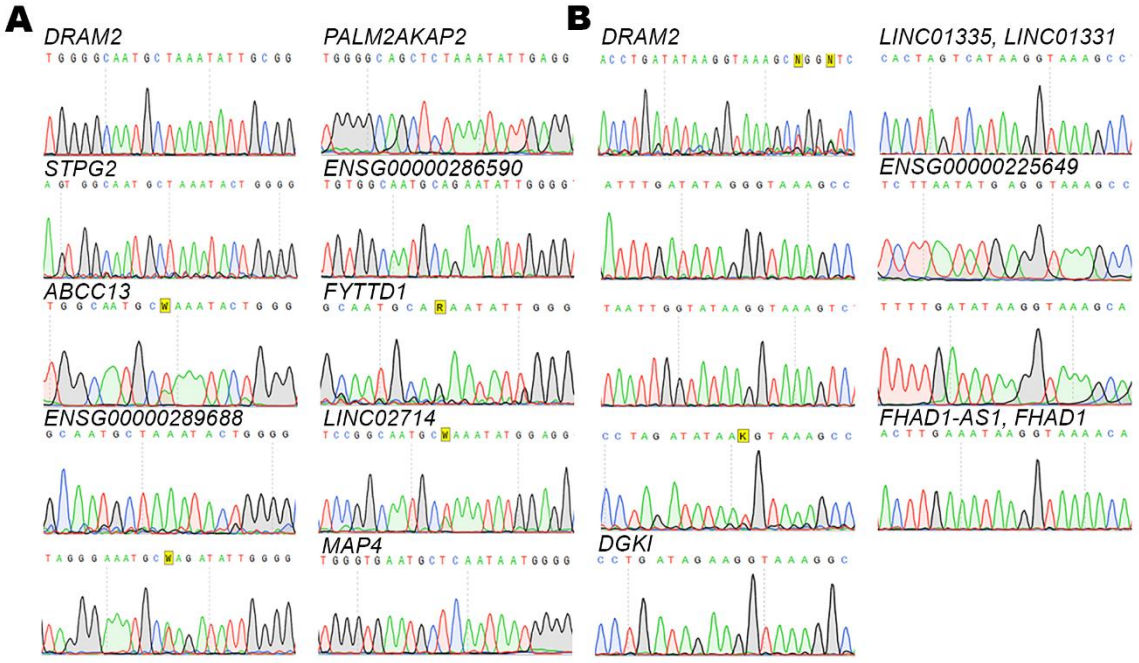

Figure 22*. *Cas-OFFinder off-target analysis for CORD21-P1c and -P2c. Sanger DNA chromatograms confirm the absence of genomic alterations at sites homologous to the targeted genomic sequence as a result of the CRISPR-Cas9 editing of CORD21-P1c (n=10) (A) and CORD21-P2c iPSCs (n=9) (B). The name of genes covering these sequences can be seen in the top left corner of each chromatogram. Sites of homology were identified using the Cas-OFFinder platform by allowing a maximum of three-mismatches in their sequence.

3.1.1.6 Discussion

Previous members of the Lako lab, have been able to reprogram iPSCs from the dermal fibroblasts of patients carrying biallelic mutations in the *DRAM2* gene (Dr. Dean Hallam and Rachel Wilson). These iPSC lines, known as CORD21-P1 and -P2, have been characterized for pluripotency, genomic stability, and Sendai virus clearance by the MRes student Edvinas Cerniauskas and undergraduate students Gabrielle Chai Jia Min and Sam Steel. Previously, the CORD21-P1 iPSC line which has a homozygous deletion (c.140delG) was corrected to a heterozygous state by Edvinas Cerniauskas. The main objective of this chapter was to analogously generate an isogeneic control for the second patient-derived iPSC line- CORD21-P2 and to fully characterise the P1c and P2c corrected iPSCs for use in chapters 4-5.

In line with literature reports demonstrating that CORD21 cone-rod dystrophy only manifests in the presence of biallelic *DRAM2* mutations (El-Asrag *et al.*, 2015; Sergouniotis *et al.*, 2015; Abad-Morales *et al.*, 2019; Krasovec *et al.*, 2022), correcting one allele on the compound heterozygote CORD21-P2 line (c.131G>A (p.Ser44Asn), c.494G>A (p.Trp165*)) would be sufficient to restore the wild-type retinal phenotype. To this end, we corrected the c.131G>A mutation on the CORD21-P2 line to a homozygous state using CRISPR-Cas9 technology. The newly established isogenic control was named CORD21-P2c. The experimental design of the CRISPR-Cas9 correction involved the use of a short asymmetric ssODN (101 bps) complementary to the gRNA strand (Richardson *et al.*, 2016). The ssODN carried a restriction site for the easy identification of corrected clones as well as an abrogated PAM sequence to prevent recutting upon integration of the ssODN (Paquet *et al.*, 2016). To further improve the efficiency of HDR and minimise the risk of recutting we used a NHEJ inhibitor (Maruyama *et al.*, 2015) in addition to also delivering Cas9 as an RNP molecule during the nucleofection procedure (Okamoto *et al.*, 2019).

This combined approach proved successful in overcoming difficulties associated with single-nucleotide correction at more than 10 nucleotides from the Cas9 cut site. Paquet *et al*., (2016) have demonstrated that cut-to-mutation site distance is a critical determinant for the successful introduction of single nucleotides using CRISPR-Cas9, as a distance of > 10 nucleotides from the cut site can greatly diminish HDR rates (<50%). The gRNA used here presented the only design within relative proximity to the mutation site whose PAM sequence

could be changed without introducing a non-synonymous *DRAM2* mutation. Even though the *de facto* distance from the cut site was approximately ~15 nucleotides, the optimised approach described here was sufficient to overcome challenges associated with probabilistic correction at this distance. Furthermore, the CRISPR-Cas9 c.131A>G edit was also unimpeded by the 'GCC' motif present in the highly sensitive crRNA target region (1+ to 4+ position) of our gRNA, previously associated with reduced efficiency of gRNA sequences (Graf *et al.*, 2019). A major improvement to the current design, however, was the implementation of a restriction site (*Alu I*) on the donor ssODN which appeared to facilitate the adequate identification of the CORD21-P2c clones, as compared to previous PCR-based approaches solely relying on the use of mutation-specific primers.

Results showed that CRISPR-Cas9 HDR efficiency remained considerably low (2%). Conversely, a significant amount of CRISPR-related genomic changes was associated with NHEJ (63% of sequenced clones) that could have also led to the random incorporation of *Alu I* restriction sites in some of the sequenced clones. An ideal future design would allow for the use of an ssODN that introduces a restriction site close to the Cas9 site in genomic DNA (within 1-5 nucleotides of the Cas9 cut site). If possible, the Cas9-cut site would be closely located to both the newly introduced restriction site as well as the actual site of the mutation. As seen with some of the clones (55), long distance of the mutation to the cut site (>10 nucleotides) can lead to partial recombination of the ssODN, so future efforts in designing gRNA and ssODN features should allow for the immediate proximity of the targeted region to the cut site. In this way the rate of HDR and the efficiency of clone identification would be much higher. As only clone 72 presented with the complete incorporation of the ssODN sequence and the absence of additional changes to genomic DNA, this was named CORD21-P2c. As it can be seen from the DNA chromatogram for clone 13, repeated cutting near the PAM site may have led to the incorporation of indels for which this clone appears to be heterozygous. Therefore, clone 13 might need to be sub-cloned to avoid future issues of clone heterogeneity that might have arisen during picking and expansion of the colony that gave rise to this particular clone.

A defining feature of iPSCs is the maintenance of a pluripotent status i.e., the ability of iPSCs to give rise to tissues of all the three main germ cell layers. After the establishment of the CORD21-P2c line by CRISPR-Cas9, the pluripotency status of all our iPSC lines was

confirmed using a commercially available service provided by Thermo Fisher Scientific, known as PluriTest™. A functional evaluation of pluripotency can also entail the injection of iPSCs into immunocompromised mice. Provided the cells are pluripotent, they are going to spontaneously differentiate to teratomas giving rise to cells of all the three germ layers. Lack of assay standardisation, accuracy and ethical concerns regarding teratoma use, however, (Montilla-Rojo *et al.*, 2023), have prompted the development of experimental alternatives such as the PluriTest™ used in this study. Furthermore, assessment of genomic integrity is an essential prerequisite to determining the non-malignant capacity of cells with potential for clonal expansion. The genomic stability of CORD21-P1 and -P1c was previously confirmed by qPCR karyotype analysis by undergraduate students Gabrielle Chai Jia Min and Sam Steel corroborating the absence of chromosomal abnormalities. The same was established for CORD21-P2 and -P2c following Karyostat™ analysis performed as a Thermo Fisher Scientific service. Furthermore, patient iPSC lines were assessed for Sendai virus clearance via RT PCR by the same students. CRISPR-corrected isogenic controls were furthermore examined for additional genomic changes at sites highly homologous to the sites of CRISPR-Cas9 correction with the supervised assistance of MRes student Eldo Galo. This entailed off-target sequencing for CORD21-P1c and -P2c to corroborate the absence of undesired genomic changes following CRISPR-Cas9 editing. Further to the generation of an isogenic control (CORD21-P2c), work performed as a part of this chapter demonstrates the maintenance of pluripotency, genomic stability, and Sendai virus clearance for CORD21 iPSC lines, as well as the off-target sequencing of CRISPR-Cas9 corrected iPSCs. Following chapters will detail the generation and the characterisation of patient-derived *in vitro* models using these CORD21 iPSC lines.

Chapter 4: Assessment of lysosomal activity in CORD21 Retinal Organoids

4. Introduction and aims.

DRAM2 encodes a 266-amino-acid transmembrane protein shown in literature to be localised to lysosomal membranes. DRAM2 expression has been reported in the inner segment of the photoreceptors and the apical side of retinal pigment epithelium cells (RPE) in the murine retina (El-Asrag *et al.*, 2015). Existing literature suggests a role for DRAM2 in the conversion of LC3-I to LC3-II during autophagosome formation (Yoon *et al.*, 2012; Zeng *et al.*, 2014) as well as the binding of lysosomal membrane proteins LAMP1 and LAMP2 in the formation of autolysosomes (Kim *et al.*, 2017). This provides evidence towards a function for DRAM2 in the maintenance of postmitotic photoreceptors (PRs) and RPE by enabling autophagy as well as all mechanisms of lysosomal degradation as the lysosome is the major point of convergence for cellular catabolism.

DRAM2 disease presents as an autosomal recessive cone-rod dystrophy (CORD21) typically manifesting by the third decade of life (El-Asrag *et al.*, 2015; Sergouniotis *et al.*, 2015; Abad-Morales *et al.*, 2019). The early loss of photoreceptors in pre-symptomatic patients supports a primary photoreceptor aetiology (Sergouniotis *et al.*, 2015). Clinical data suggest that both rods and cones are affected with loss-of-function variants leading to earlier onset and more severe disease progression compared to missense mutations (Sergouniotis *et al.*, 2015). Alternatively spliced variants were also correlated with extensive peripheral involvement and rod-cone dysfunction (Abad-Morales *et al.*, 2019) The loss of visual acuity experienced as an initial symptom correlates with the degeneration of the macula, often followed by peripheral degeneration and light sensitivity as the disease progresses (El-Asrag *et al.*, 2015; Sergouniotis *et al.*, 2015; Abad-Morales *et al.*, 2019).

The aim of this chapter was to uncover the DRAM2 disease pathomechanism using a patient-specific retinal organoid (RO) model. The impact of c.140delG and c.131G>A *DRAM2* mutations was assessed *in silico* and the three-dimensional DRAM2 structure was studied to gain insight into protein function. The effect of *DRAM2* mutations were examined in day 220 (d220) CORD21-P1 and -P2 patient-derived ROs alongside their CRISPR isogenic controls. To determine DRAM2 expression in ROs, we validated a DRAM2 antibody by knockdown as confirmed by qPCR and Western blot (WB). Here, for the first time we established the expression of DRAM2 in human ROs by both WB and immunofluorescence (IF). To gain more

insight into the early features of DRAM2 disease, d220 ROs were characterized for the expression of retinal markers by IF, autophagy flux and transmission electron microscopy (TEM). A thorough proteomics analysis at d220 revealed key lysosomal protein downregulation in DRAM2 patient ROs. Further, assessment of lysosomal markers by WB and enzymatic activity assays were carried out to enhance our knowledge of affected lysosomal trafficking pathways. Ultimately, lipidomic and IF experiments were carried out to ascertain global lipid changes in DRAM2 ROs.

4.1 Genetic background of CORD21-P1 and CORD21-P2 patients leads to a differential outcome in *DRAM2* expression.

4.1.1. Analysis of DRAM2 mutations and their effect on isoform expression

Individuals diagnosed with inherited *DRAM2* macular dystrophy usually present with acute decline in visual acuity by the third decade of life. Previous literature reports indicate that the disease only manifests clinically in probands carrying biallelic *DRAM2* mutations, which renders DRAM2 dystrophy a recessive condition. Furthermore, the protein exists in two major isoforms - isoform 'a' (*DRAM2a*), which is expressed ubiquitously, and isoform 'c' (*DRAM2c*), which is specific to the retina (Abad Morales *et al*., 2019) (Figure 23). iPSC lines obtained from both affected patients in this study are detailed in Table 19 below. The iPSC lines have previously been characterised for Sendai virus clearance, pluripotency, genomic stability, and off-target sequencing (see chapter 3).

The first patient, here referred to as CORD21- P1, is homozygous for a deletion at c.140delG. According to the online prediction tool http://www.mutationtaster.org/ this is expected to lead to either a severely truncated version of the protein amounting to approximately 5 kDa and/or to non-sense mediated decay (NMD) (Table 19). In the case of the second patient, a compound heterozygote (CORD21-P2), at least some amount of full-length protein may be produced. One allele (c.494 G>A, p. Trp165*) is expected to produce truncated protein (17 kDa) and/or NMD. The second allele on CORD21-P2 is mutated at a conserved serine residue (c. 131G>A, p. Ser44Asn), which could hypothetically result in some amount of full-length protein, however, this may still entail significant implications for DRAM2 function. The conserved serine residue is found at an intron/exon boundary where mutations

are very likely to affect the splicing of the protein (Table 19). A likely outcome would be the acquisition of differential protein conformation and the inability of the protein to interact with the cytoplasmic milieu, assuming that DRAM2 is embedded in the lysosomal membrane. The effect of patient mutations on both cell lines is briefly summarised in Table 19. According to the prediction analysis, two out of three of the studied mutations affect the ubiquitously expressed *DRAM2a* isoform (29.73 kDa). Conversely, the retinal-specific *DRAM2c* isoform (15.73 kDa) is affected only by c.494 G>A present in CORD21-P2. This concludes that the majority of the DRAM2 phenotype can be attributed to a dysfunctional *DRAM2a* isoform.

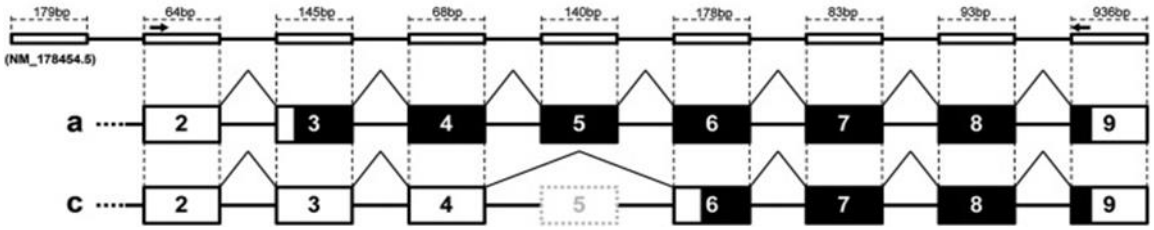

Figure 23. Structure of DRAM2 isoforms taken from Abad-Morales et al. (2019).

Table 19. Effect of mutation on DRAM2a and DRAM2c isoform expression.

DRAM2 Mutation	iPSCs cell line	Age at present/sex	Predicted effect on isoform a	Predicted effect on isoform c	Location within isoform a	Location within isoform c
c.140delG	CORD21-P1	31, male	~5 kDa DRAM2 NMD and/or PTC	Not part of sequence	MWWFQQGLSF LPSALVI WTS AAFIFSYITA VTLHHI DPALPYISDTGTVAPEKCLF GAMLNIAAVLCIATIYVRY KQVHALSPEENVIIKLNKA GLVLGILSCLGLSIVANFQK TTLFAAHVSGAVLTFGMG SLYMFVQTILSYQMQPKIH GKQVFWIRLLLVIWCGVSA LSMLTCSSVLHSGNFGTDL EQKLHWNPEDKGYVLHMI TTAAEWSMSFSFFGFFLTY IRDFQKISLRVEANLHGLTL YDTAPCPINNERTRLLSRD I	Not part of sequence
c.131G>A	CORD21-P2	31, male	dysfunctional protein, splice site alteration	Not part of sequence	MWWFQQGLSFLPSALVIW TSAAFIFSYITAVTLHHIDP ALPYISDTGTVAPEKCLFGA MLNIAAVLCIATIYVRYKQ VHALSPEENVIIKLNKAGL VLGILSCLGLSIVANFQKTT LFAAHVSGAVLTFGMGSLY MFVQTILSYQMQPKIHGK QVFWIRLLLVIWCGVSALS MLTCSSVLHSGNFGTDLEQ KLHWNPEDKGYVLHMITT AAEWSMSFSFFGFFLTYIR DFQKISLRVEANLHGLTLY DTA PCPINNERTR LLSRDI	Not part of sequence
c.494 G>A	CORD21-P2	56, female	18.2 kDa protein and/or NMD; potential splice site changes	~5 kDa protein and/or NMD	MWWFQQGLSFLPSALVIW TSAAFIFSYITAVTLHHIDP ALPYISDTGTVAPEKCLFG AMLNIAAVLCIATIYVRYK QVHALSPEENVIIKLNKAG LVLGILSCLGLSIVANFQKT TLFAAHVSGAVLTFGMGSL YMFVQTILSYQMQPKIHG KQVFWIRLLLVIWCGVSALS MLTCSSVLHSGNFGTDLEQ KLHWNPEDKGYVLHMITT AAEWSMSFSFFGFFLTYIR DFQKISLRVEANLHGLTLY DTA PCPINNERTR LLSRDI	MGSLYMFVQT ILSYQMQPKI HGKQVFWIRL LL**VIW**CGVSA LSMLTCSSVL HSGNFGTDLE QKLHWNPEDK GYVLHMITTA AEWSMSFSFF GFFLTYIRDF QKISLRVEAN LHGLTLYDTA PCPINNERTR LLSRDI

4.2 DRAM2 protein resembles a transmembrane protein.

DRAM2 is a 266-amino acid lysosomal transmembrane protein found to be expressed in the inner segments (IS) of murine photoreceptors and RPE (El-Asrag *et al*. 2015). Despite previous studies on DRAM2 retinopathy, detailed knowledge of DRAM2 function in the context of autophagy remains elusive. To gain insight into the structure of the protein and ascribe functional roles, DRAM2 amino acid sequence was submitted into the Zhang lab I-Tasser platform (https://zhanglab.dcmb.med.umich.edu/ITASSER/). A program database file (.pdb) generated by the I-Tasser online tool was subsequently visualised and annotated in PyMoL software. A putative 3D structure of the main *DRAM2a* isoform is shown in Figure 24 Image shows that DRAM2 protein is likely composed of 6 transmembrane domains connected by alpha helices. As can be seen, the c.131 G>A mutation referring to a highly conserved residue

is located on the outer rim of a helical interface domain linking two major transmembrane regions, likely exposed to the binding of ligands/proteins interacting with the lysosomal membrane (Figure 24). The nonsense mutation c.140delG is located close to c.131 G>A, whereas c.494G>A can be seen deep within domain number 5 (Figure 24).

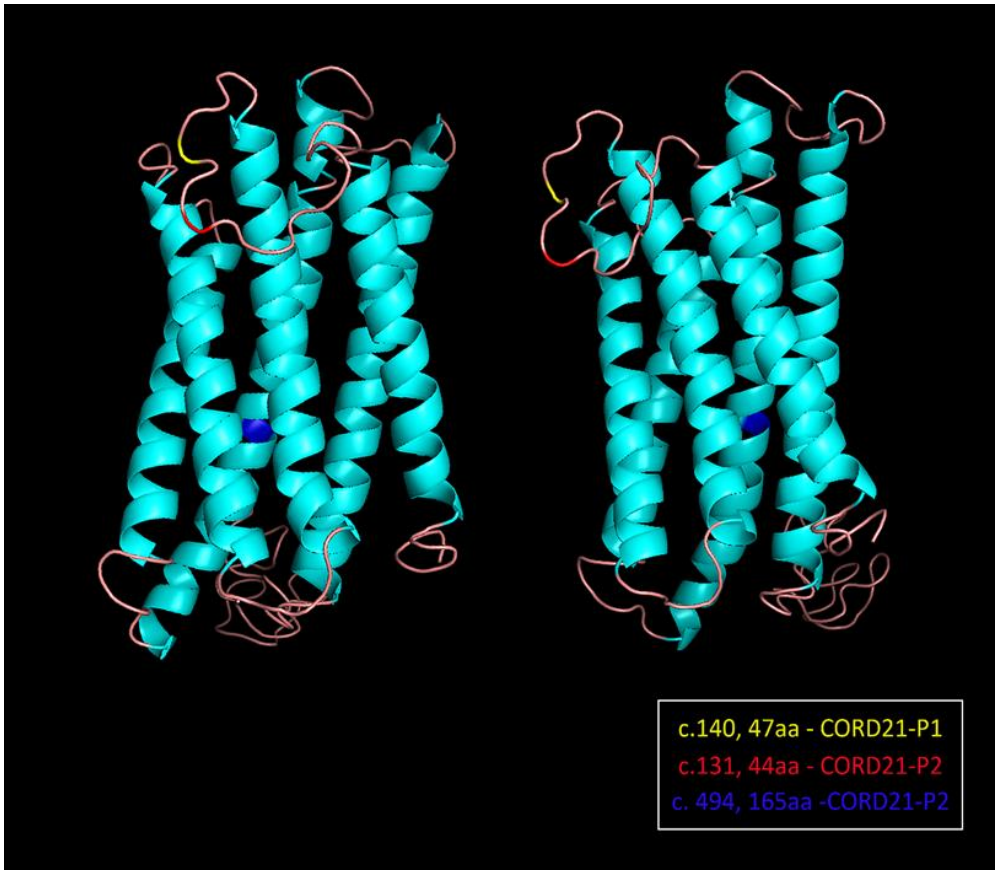

Figure 24. Predicted 3D structure of DRAM2a isoform by I-Tasser. Alternating helix, sheet loop motifs shown in teal and brown, respectively. Mutated sequence present in CORD21-P1 outlined in yellow denotes c.140delG (DT**G**); Site of CRISPR corrected mutation c.131G>A on CORD21-P2 iPSC line is marked in red (YI**S)**. c. 494G>A nonsense mutation in CORD21-P2 is depicted in blue (VI**W**). C-score - 2.93, estimated TM-score=0.38±0.13, estimated RMSD = 12.9±4.2Å. Image generated in PyMoL.

Table 20. List of structural modes generated as .pdb files by I-Tasser. The highest-ranking model 1 (c-score, -2.93) was used for analysis of DRAM2 structure. The typical range for c-score is [-5,2], whereby higher confidence is relayed by a higher value.

Name	C-score	Experimental TM score	Experimental RMSD	No. of decoys	Cluster density
Model 1	-2.93	0.38+-0.13	12.9+-4.2	2143	0.0559
Model 2	3.59			1228	0.029
Model 3	2.68			684	0.072
Model 4	-3.43			640	0.0339
Model 5	3.84			850	0.0225

Table 21. List of top ten structural homologues to query structure identified by structural alignment using TM - align.

Rank	PDB Hit	Protein structure	Species	TM -score	RMSD	IDEN	Coverage
1	5ZLE	Plasma membrane ascorbate-dependent reductase (CYBRD1)	*H. sapiens*	0.726	2.24	0.069	0.804
2	4O6Y	Cytochromeb561	*A. thaliana*	0.716	1.7	0.078	0.767
3	4A01	H-Translocating Pyrophosphatase	*V. radiata*	0.583	4.47	0.045	0.808
4	6QD6	Mb-CHopQ-Nb207	*H. pylori*	0.532	4.41	0.045	0.729
5	5DOQ	bd oxidase	*G. thermodenitrificans*	0.53	4.5	0.087	0.729
6	3RKO	Membrane domain of respiratory complex I	*E. coli*	0.519	4.8	0.053	0.744
7	6QTI	Structure of ovine transhydrogenase	*O. aries*	0.519	4.66	0.067	0.729
8	6RKO	Cytochrome bd-I oxidase	*E. coli*	0.518	4.91	0.066	0.748
9	6HCY	Metalloreductase (STEAP4)	*H. sapiens*	0.512	4.79	0.117	0.737
10	6CFW	Respiratory membrane-bound hydrogenase	*P. furiosus*	0.509	4.57	0.097	0.722

Table 22. List of GO terms identified for top ten functional templates. GO-score is a measure of accuracy of GO-term prediction [0-1].

Consensus prediction of GO terms					
Molecular function	G0:0009055; electron transfer activity	G0:0004129; cytochrome-c oxidase activity	G0:0020037; Heme binding		
GO-score	0.46	0.46	0.46		
Biological process	G0:0006818; proton transmembrane transport	G0:0015672; inorganic cation transmembrane transport	G0:0009060; aerobic respiration	G0:0022900; electron transport chain	
GO-score	0.48	0.48	0.46	0.37	
Cellular component	G0:0071944; cell periphery	G0:0016021; membrane	G0:0070469; respirasome	G0:0019866; organelle inner membrane	G0:0031966; mitochondrial membrane
GO-score	0.48	0.46	0.37	0.34	0.33

The software returned five structural models, and the one with the highest confidence C-score (-2.93), amongst all 5 was selected for protein annotation using PyMoL (Table 20). The c- score is a reliable measure of confidence in modelling prediction based on threading alignment and structure assembly. TM-score and RMSD are measures of global and local structural similarity between query and template protein. The putative model was further probed by structural alignment using TM - align revealing top ten structural homologues with crystallised conformation available on the PDB (Protein data bank) database (Table 21). As high-ranking proteins emerged the plasma membrane ascorbate-dependent reductase (CYBRD1) (5ZLE) (Table 21) and an orthologue from Arabidopsis thaliana, known as cytochromeb561 (4O6Y) (Table 21). Both proteins are classified as oxidoreductases. Amongst further identified hits were H-Translocating Pyrophosphatase (4A01, Vigna radiata) and other membrane proteins which function in electron transport such as Mb-cHopQ-Nb207 (6QD6, Helicobacter pylori), membrane domains of respiratory complex I (3RKO, Escherichia coli), ovine transhydrogenase (6QTI, Ovis aries), cytochrome bd-I oxidase (6RKO, Escherichia coli), STEAP4 (6HCY, Homo sapiens) and respiratory membrane-bound hydrogenase (6CFW, Pyrococcus furiosus) (Table 21).

Functional insight was rendered by the consensus GO term analysis of molecular function, biological process, and cellular component for the top structural homologues by COFACTOR algorithm on the I-TASSER platform (Table 22). GO term annotation for molecular function and cellular component indicated that the homologous proteins were associated with the transmembrane transport of ions and heme- binding but may also possess intrinsic cytochrome c oxidase activity. The latter proteins are integral membrane components, further reiterating a role for DRAM2 as a membrane transporter and potential involvement in mitochondrial membrane homeostasis. Clustal alignment between DRAM2, (CYBRD1/DCytb) and LCytb (Figure 25) showed functional conservation of one Zn^{2+}-ascorbate binding site (black arrow) and two cytoplasmic ascorbate binding sites (magenta arrows) between all three proteins. One of the two cytoplasmic ascorbic sites is in relative proximity to c.131G>A and c.140delG mutations present in CORD21-P1 and -P2.

Figure 25. Clustal alignment of DRAM2, DCytb and LCytb

Colour	Property
RED	Small (small+ hydrophobic (incl.aromatic -Y))
BLUE	Acidic
MAGENTA	Basic - H
GREEN	Hydroxyl + sulfhydryl + amine + G
Grey	Unusual amino/imino acids etc

Legend: (*) Shows a single conserved residue. (:) Indicates conservation between groups of strongly similar properties > 0.5 in the Gonnet PAM 250 matrix. (.) Indicates conservation between groups of weakly similar properties =< 0.5 and > 0 in the Gonnet PAM 250 matrix. ***Blue arrow*** *designates histidine ligand,* ***magenta arrow*** *– cytoplasmic ascorbate binding site,* ***green arrow*** *- through space electron transfer,* ***black arrow*** *-Zn^{2+}-ascorbate binding site;* ***red square*** *shows c.131G>A, 44aa mutation,* ***yellow square*** *denotes c.140delG, 47aa,* ***blue square*** *– c.494G>A, 165aa,* ***black square*** *– functionally conserved domains.*

4.3.1 DRAM2 protein detection by western blot

To validate a DRAM2 antibody for protein detection by western blot (WB) (cat. No HPA018036, Sigma-Aldrich**)**, a 72h siRNA knockdown experiment was performed on d230 WT retinal organoids, whereby ROs were plated as monolayers to increase the efficiency of the procedure. Successful knockdown by at least 50% was confirmed by both qPCR and WB (Figure 26, B and D; see chapter 2). d220 RO lysates were then analysed by WB using the aforementioned antibody, revealing a band of approximately 26 kDa in both wild-type and isogenic controls (Figure 26, C). The blot showed a downregulation of DRAM2 in both patients. Protein was completely absent in CORD21-P1, consistent with NMD transcript degradation. Conversely, a minimal amount of DRAM2 protein was detected in the sample of CORD21-P2 (Figure 26, C).

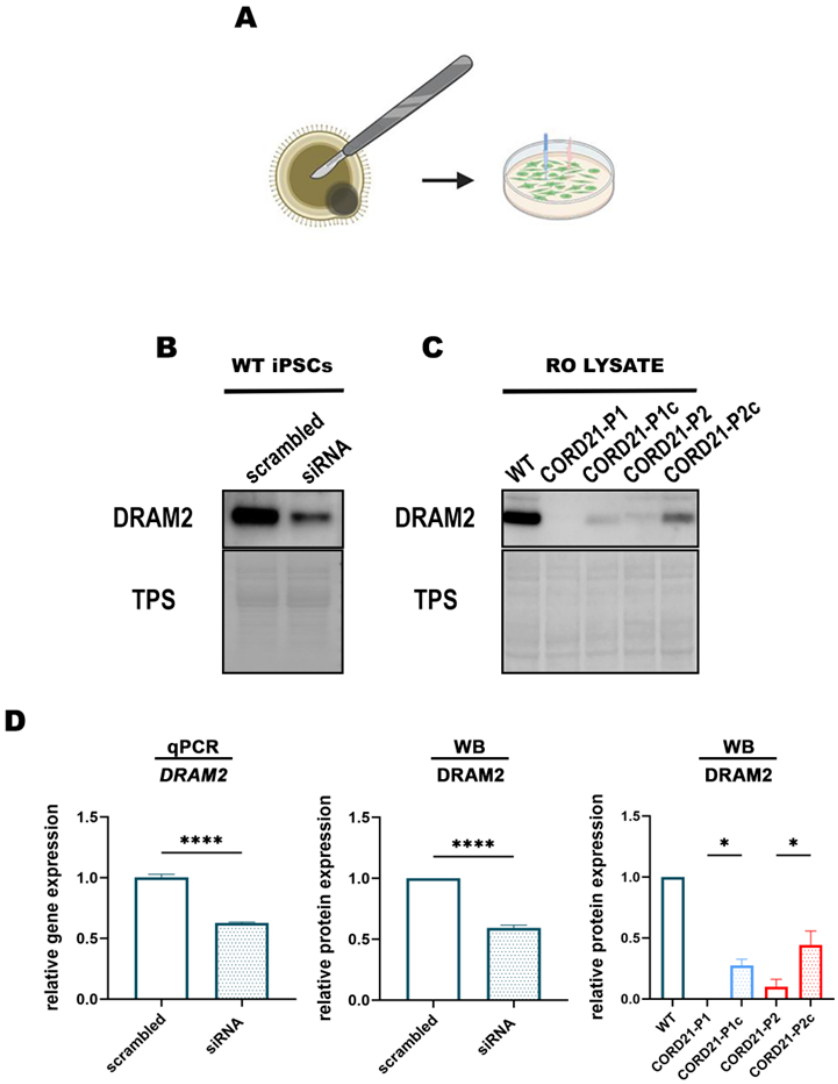

Figure 26. DRAM2 antibody validation and protein detection by western blot. (A) WT d230 retinal organoids were diced and expanded on 24-well plates on Matrigel and poly-L-ornithine. Treatment with 20μM *DRAM2* and scrambled siRNA was carried out for a period of 72h. (B) DRAM2 protein detection in scrambled and siRNA treated WT ROs. (C) DRAM2 protein detection in d220 patient and control retinal organoids. TPS stands for total protein stain showing equal loading of sample. (C) Quantification plots to the left confirming 50% knockdown efficiency by both qPCR (unpaired t-test) and WB in d230 WT ROs (unpaired t-test) (data normalised to scrambled control). Plot to the right shows relative protein expression of DRAM2 in d220 retinal organoids normalised to the wild-type control (ANOVA). All data is presented as means + SEM (n=3).

*Knockdown comparisons show scrambled control vs siRNA treatment (qPCR and WB) and CORD21-P1vs -P1c and CORD21-P2vs-P2c (DRAM2 WB) whereby statistical significance is denoted by * P<.05,**P<.01,***P<.001, ****P<0.0001. The WT sample was excluded from the d220 RO DRAM2 WB analysis.*

4.3.2 DRAM2 protein expression by immunofluorescence is absent in patient derived ROs.

According to clinical findings (El-Asrag *et al*., 2015; Sergouniotis *et al*., 2015) the disease phenotype could be reversed by restoring *DRAM2* mutation status to a heterozygous state. Patient lines CORD21-P1 and -P2 have been corrected by CRISPR/Cas9 to generate CORD21-P1c and -P2c isogenic control cell lines, respectively (chapter 3). Punctate DRAM2 expression is seen at the lower part of inner segments (IS) in WT and isogenic controls, co-localising with inner segment marker TOMM20, which is highly enriched in mitochondria (Figure 27). Immunofluorescence experiment shown below demonstrates that DRAM2 protein expression is absent in the IS of patient cell lines (Figure 27). These data are consistent with a significant reduction in protein expression being associated with DRAM2 retinal phenotype.

4.4 DRAM2 patient derived ROs do not show changes in retinal marker expression.

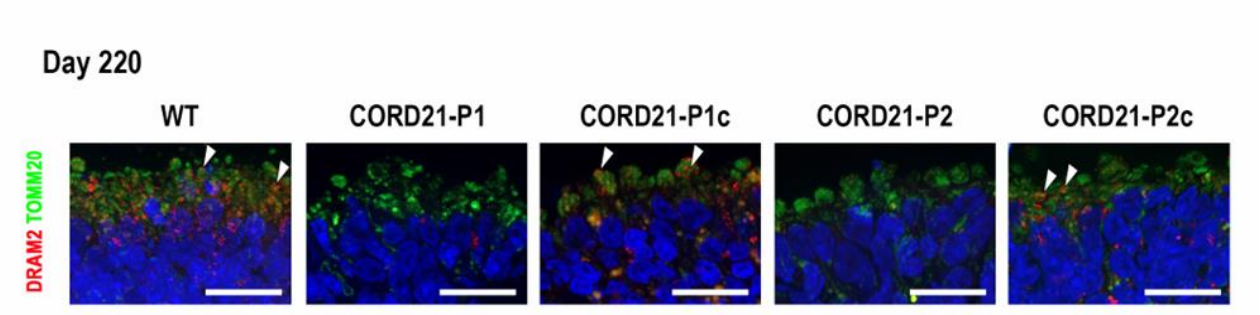

Figure 27. DRAM2 protein detection in d220 ROs by immunofluorescence. IF corroborates the absence of DRAM2 protein in patient ROs. By contrast, DRAM2 is detected at the IS of d220 aged WT, CORD21 -P1c and -P2c ROs (white arrow heads). Scale shows 20μm (n=3).

To assess the impact of DRAM2 mutations on RO development, a comprehensive immunofluorescence analysis (IF) was conducted to ascertain d220 retinal marker expression over the course of multiple RO differentiations (n=3). IF analysis corroborated that patient RO development closely recapitulated the formation of an outer nuclear layer (ONL) marked by the expression of photoreceptor marker Recoverin (RCVRN) (Figure 28, A). Recoverin^{+} cells were mainly distributed along the apical edge of the ROs. Consistent with normal retinal development, retinal ganglion cells were present in all the examined cell lines. This was shown by SNCG expression which amounted to ≤ 5% for all patient derived cell lines (Figure 28, A). SNCG^{+} cells were positioned basally congruent with the knowledge that retinal ganglion cells are the main point of convergence for primary and secondary neurons in the retina (Figure 28, A). Rod bipolar PKCα^{+} cells localised to the inner nuclear layer in WT and CORD21-P1/P1c ROs, whereas a more scattered expression was observed for the CORD21-P2 and -P2c cell lines. Due to the limited abundance of PKCα^{+} cells ≤ 1%, expression data was not quantified (Figure 28, B). Furthermore, horizontal (PROX1) and amacrine cell (AP2α) markers revealed a considerable level of layer stratification in all lines apart from CORD21-P2 and -P2c, which exhibited a lower level of structural lamination (Figure 28, C). PROX1^{+} horizontal cells can be seen to delineate the inner nuclear layer (INL), nested immediately below that of the photoreceptors. By contrast amacrine (AP2α^{+}) cells were seen more basally in line with AP2α also being expressed in a subset of retinal ganglion cells (Figure 28, C). Furthermore, ubiquitous staining was observed for Müller glia marker vimentin in ROs (Figure 28, E, not quantified). All cell lines showed expression of rods (Rhodopsin) and cones (OPN1LW/MW), whereby no significant changes were observed between patients and isogenic controls. Interestingly, OPN1LW/MW^{+} cells could be seen on the inside of CORD21-P1 and -P1c ROs, whereas CORD21-P2 and -P2c ROs showed the lowest levels of OPN1LW/MW expression, which appeared to be cell line-specific.

In summary, although IF analysis did not show any statistical differences in retinal marker expression (Figure 28, F), it corroborated the ability of patient cell lines to differentiate to ROs and concluded the presence of all major retinal cell types (Figure 28, A-F).

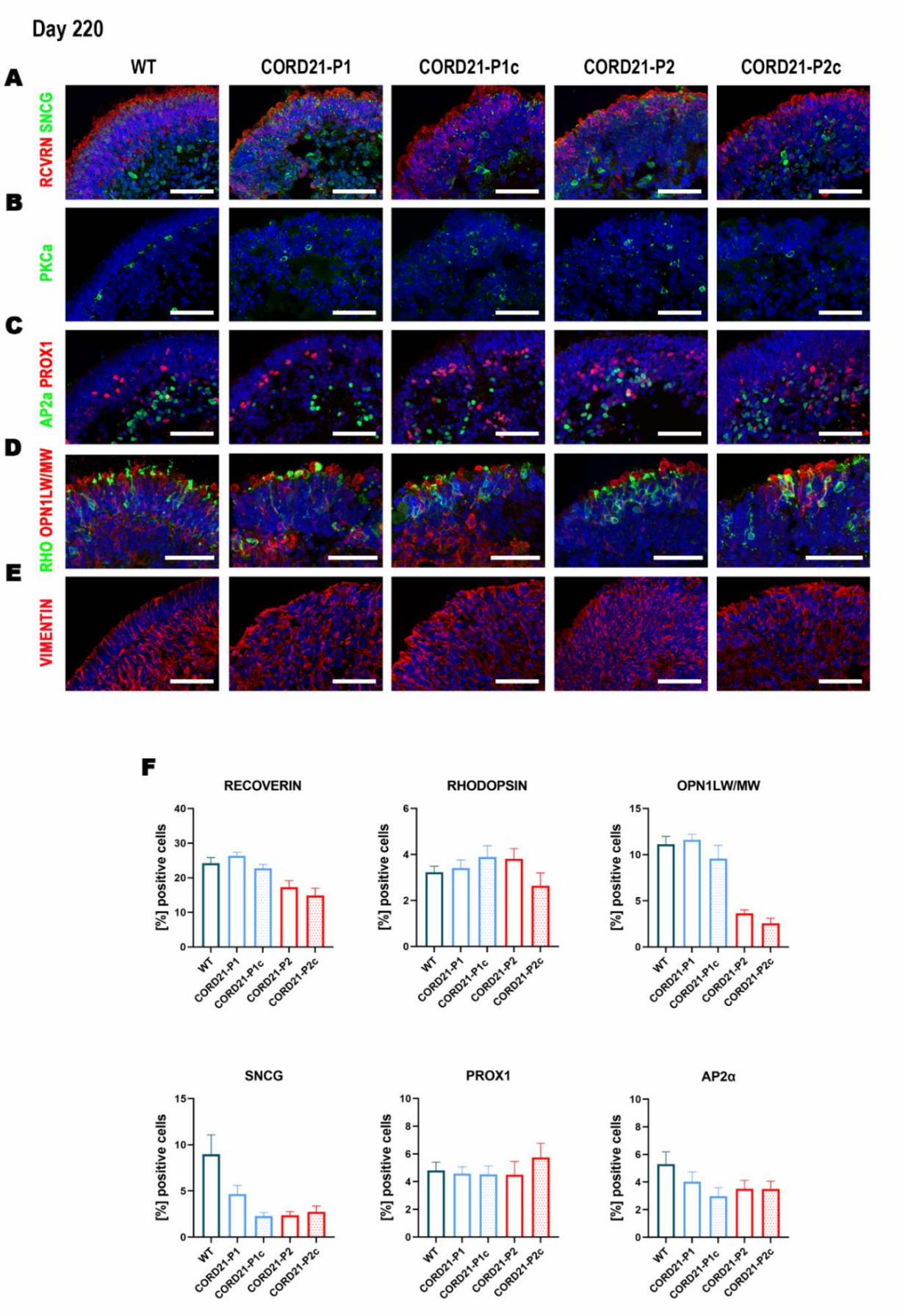
Day 220
WT
CORD21-P1
CORD21-P1c
CORD21-P2
CORD21-P2c
A
RCVRN SNCG
B
PKCa
C
AP2a PROX1
D
RHO OPN1LW/MW
E
VIMENTIN
F
RECOVERIN
RHODOPSIN
OPN1LW/MW
SNCG
PROX1
AP2α
[%] positive cells
WT
CORD21-P1
CORD21-P1c
CORD21-P2
CORD21-P2c

Figure 28. Characterisation of d220 DRAM2-patient derived ROs by IF. IF experiment demonstrates the expression of major retinal cell types such as photoreceptor (A) (Recoverin, red) and ganglion cells (SNCG, green), (B) rod bipolar cells (PKCα, green), (C) horizontal (PROX1, red) and amacrine (AP2α, green) cells, (D) mature red/green cones (OPN1LW/MW, red) and rod photoreceptors (RHO, green) as well as (E) Müller glia (vimentin, red), (G). Nuclei are counterstained with Hoechst (blue). Scale bars show 50µm for RCVRN/SNCG, PKCα, PROX1/AP2α and vimentin, and 20µm for RHO/OPN1LW/MW. (F) Quantification plots show % positive cells corresponding to the expression of each marker relative to the total number of cells (RCVRN, Kruskal-Wallis; Rhodopsin, Kruskal-Wallis; OPN1LW/MW, ANOVA; SNCG, Kruskal-Wallis; PROX1, Kruskal-Wallis; AP2α, Kruskal-Wallis). No significant differences can be seen in the expression of retinal markers between DRAM2-patient and control organoids at d220. Data were presented as means + SEM (n=5-30).

*Comparisons are shown in the following order CORD21-P1vsP1c and CORD21-P2vsP2c, whereby statistical significance is denoted by * P<.05, **P<.01, ***P<.001, ****P<0.0001. The WT sample was omitted from the statistical analysis.*

4.5 Autophagy flux is impaired in CORD21-P1 ROs.

To evaluate the effect of DRAM2 mutations on the state of autophagy flux in mature d150 RO, LC3 expression was evaluated following the sequential addition of 500nM rapamycin (24h) and 100nM bafilomycin over the course of the last 4h. A brief schematic in Figure 29, A explains the function of both drugs with regards to the activation or blockage of autophagy-

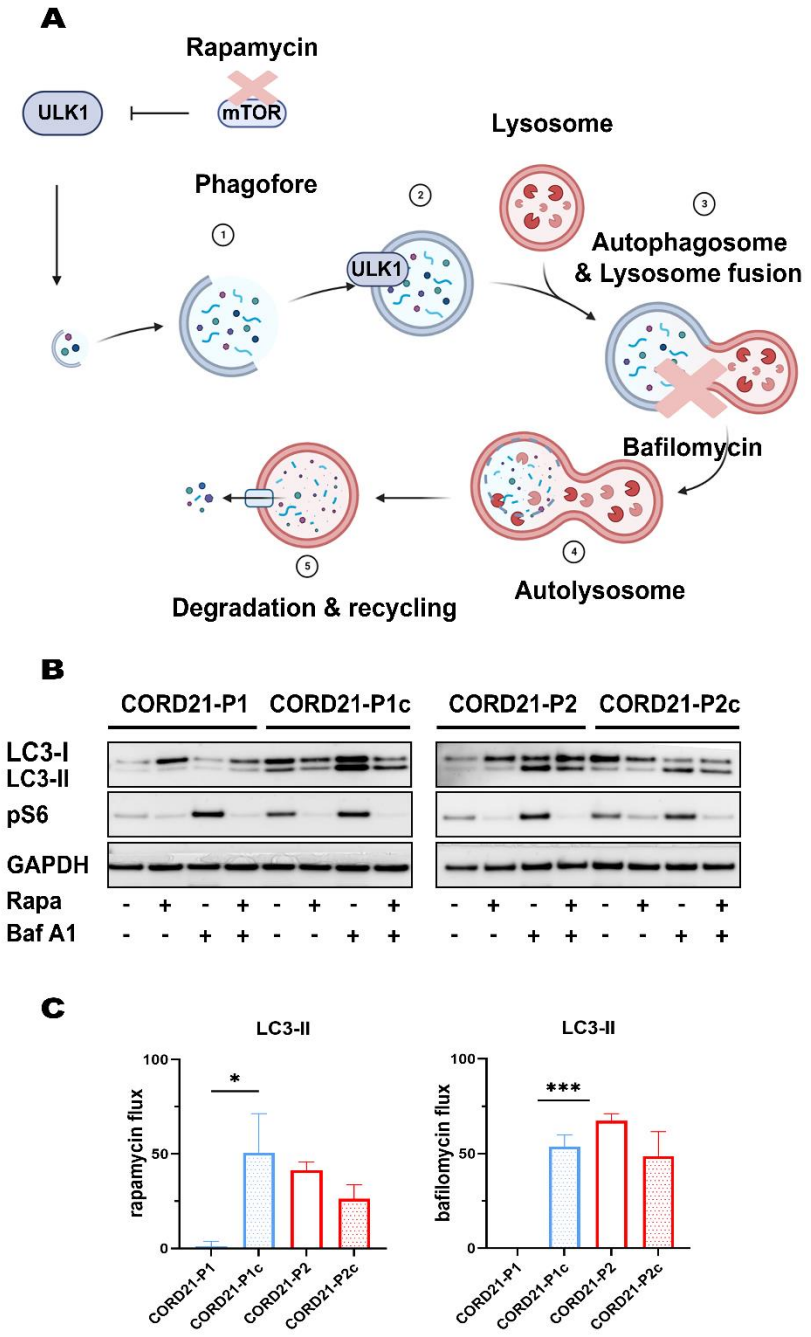

Figure 29. CORD21-P1 d150 ROs show reduced rates of autophagic flux compared to isogenic control by WB. (A) Rapamycin, an mTOR inhibitor, relieves ULK1 from inhibition by mTOR. This leads to the assembly of phagofore double membrane around autophagic cargo and its subsequent maturation to a nascent autophagosome. Bafilomycin blocks the fusion of autophagosomes with lysosomes thereby preventing the formation of autolysosomes. LC3-II is attached to the double membrane of the autophagosome and serves as a reliable marker for autophagosome turnover and degradation. Schematic was generated using BioRender. (B) Increased accumulation of LC3-II protein by WB following single bafilomycin treatment in CORD21-P1 resembles untreated control, whereas CORD21-P2 presents with LC3-II protein accumulation which is suggestive of autophagy induction. (C) Plots show that both rapamycin (ANOVA) and bafilomycin (ANOVA) LC3-II flux rates are increased for CORD21-P1c compared to -P1, whereas no change in flux rates is seen between CORD21-P2 and CORD21-P2c. Rapamycin flux is calculated by subtracting the LC3-II band rates for double treatment from the single rapamycin treatment for each cell line. Bafilomycin flux is generated by subtracting the single bafilomycin treatment from the basal untreated state. Data were normalized to GAPDH expression and presented as means + SEM (n=3). (C) Data were presented as means + SEM (n=3).

*Statistical comparisons for CORD21-P1vs -P1c and CORD21-P2vs-P2c are denoted by * P<.05,**P<.01,***P<.001, ****P<0.0001. The WT sample was excluded from the statistical analysis.*

related degradation. Patient CORD21-P1 and -P2 ROs showed reduced conversion of LC3-I to LC3-II as demonstrated by the retention of LC3 mainly in the form of LC3-I in the basal untreated state as compared to the untreated state of the isogenic controls (Figure 29, B). (Figure 29, B). An increase in pS6 levels suggested an active mTOR pathway, which is associated with the inhibition of autophagy. This confirmed that autophagy flux is suppressed following the addition of bafilomycin. Upon single treatment with bafilomycin, CORD21-P1 failed to respond, whereas CORD21-P2 showed a dramatic increase in LC3-II conversion levels which was a strong indication for a complete loss of flux in the CORD21-P1 compared to the stark presence of such in CORD21-P2 (Figure 29, B and C). Similarly, both rapamycin and bafilomycin flux were significantly increased in the CORD21-P1c cell line relative to their patient counterpart (Figure 29, C). Interestingly, a combined drug treatment leads to partial LC3-II clearance instead of further LC3-II accumulation compared to the -/+ condition. This could indicate that a longer bafilomycin treatment is needed to observe the steady build-up of LC3-II without the rate of LC3-II clearance exceeding that of its degradation (Figure 29, B).

4.6 DRAM2 d220 ROs exhibit curvinuclear lipopigments associated with lipid accumulation on transmission electron microscopy.

Analysis of ultrastructural findings on transmission electron microscopy revealed a significant increase in aberrant lysosomal-like structures in the PRs of patient RO samples (Figure 30, A, B, C). The hallmark TEM features were recognised as curvilinear lipopigments (CLs) due to bearing visual resemblance to structures laden with undigested lipid in Neuronal Ceroid Lipofuscinoses (Anderson *et al*. 2012). Patient and isogenic controls additionally showed no change in the number of lysosomes observed (Figure 30, B, C). Furthermore, no significant changes were apparent for early (AVi) and late autophagic vehicles (AVd) between the groups.

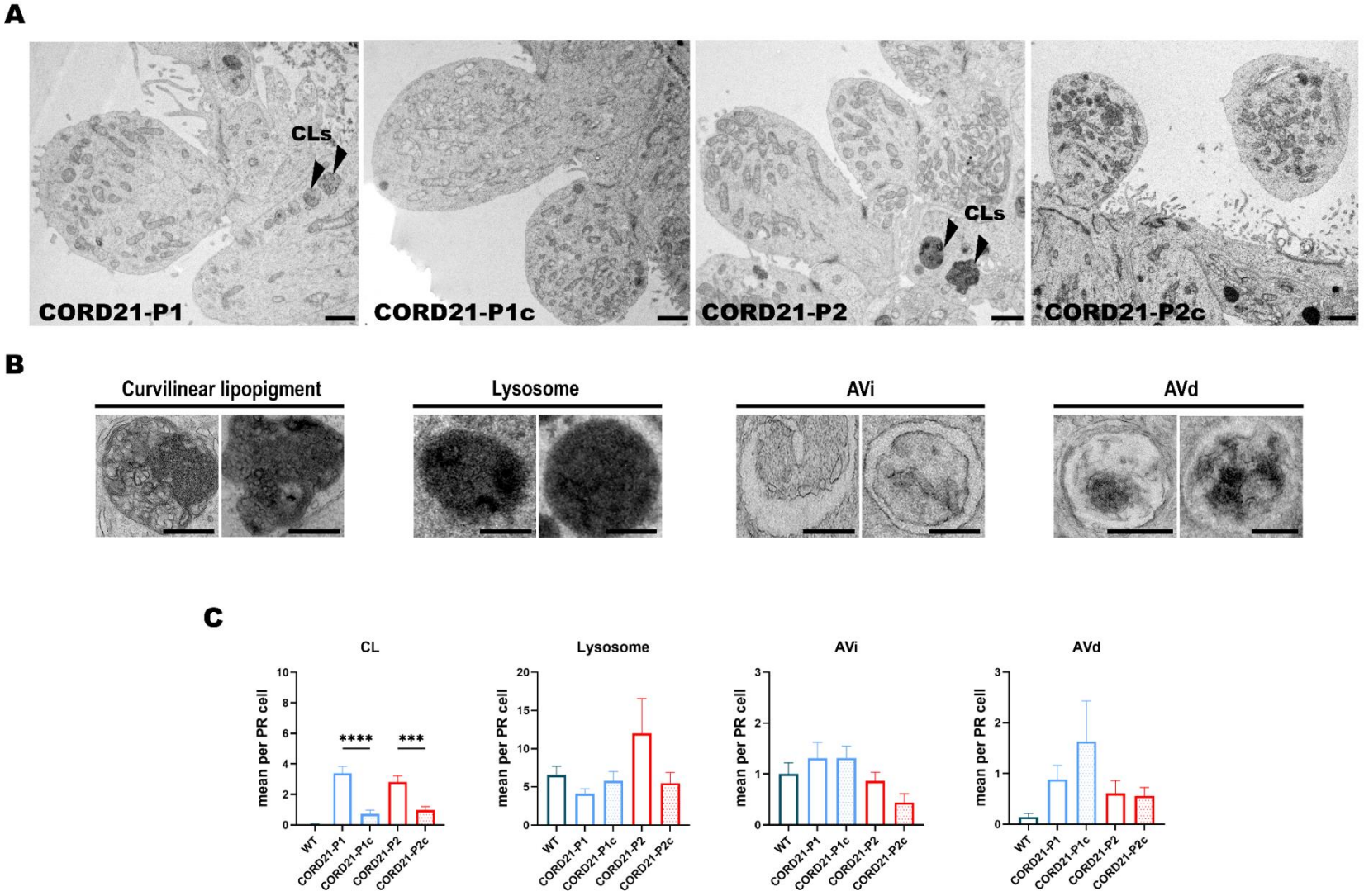
A
CLs
CORD21-P1
CORD21-P1c
CLs
CORD21-P2
CORD21-P2c
B
Curvilinear lipopigment
Lysosome
AVi
AVd
C
CL
Lysosome
AVi
AVd
mean per PR cell
****
***
WT
CORD21-P1
CORD21-P1c
CORD21-P2
CORD21-P2c

Figure 30. Patient organoid samples show increased numbers of curvilinear profiles. (A) Image shows an aberrant accumulation of curvilinear lipopigments in CORD21-P1 and CORD21-P2 (CLs black arrow heads). By contrast no such features were present in isogenic controls. Scale bar=1 μm (B) Magnified images of quantified cellular structures (CL, scale bar=500nm; Lysosomes, scale bar=125nm; AVi, scale bar=1.5 μm; 250nm; AVd, scale bar=500nm, 250nm). (C) Plots show an increase in CLs per cell in patient organoids. Lysosomes as well as early (AVi) and late autophagic vehicles (AVd) do not differ in their number per cell. All data was plotted as means + SEM, tested for normality and analysed by a non-parametric Kruskal-Wallis test (n=10). Image segmentation and processing was conducted using the open-source Microscopy Image Browser software (Belevich *et al.*, 2016). Segmentation accounted for the presence of cellular features in both the cell body and the inner segment of ROs.

*Statistical comparisons for CORD21-P1vs -P1c and CORD21-P2vs-P2c are denoted by * P<.05, **P<.01, ***P<.001, ****P<0.0001. The WT sample was excluded from the statistical analysis.*

4.7 Increased mitochondrial branching is observed in d220 CORD21-P1 ROs.

To assess the state of mitochondrial health in DRAM2 ROs, d220 samples from each cell line (n=10) were examined as a part of a blind analysis of mitochondrial count per cell, shape, and level of mitochondrial branching. The shape of mitochondria was determined as a ratio between the centreline length and width of individual mitochondrial organelles (Major/Minor

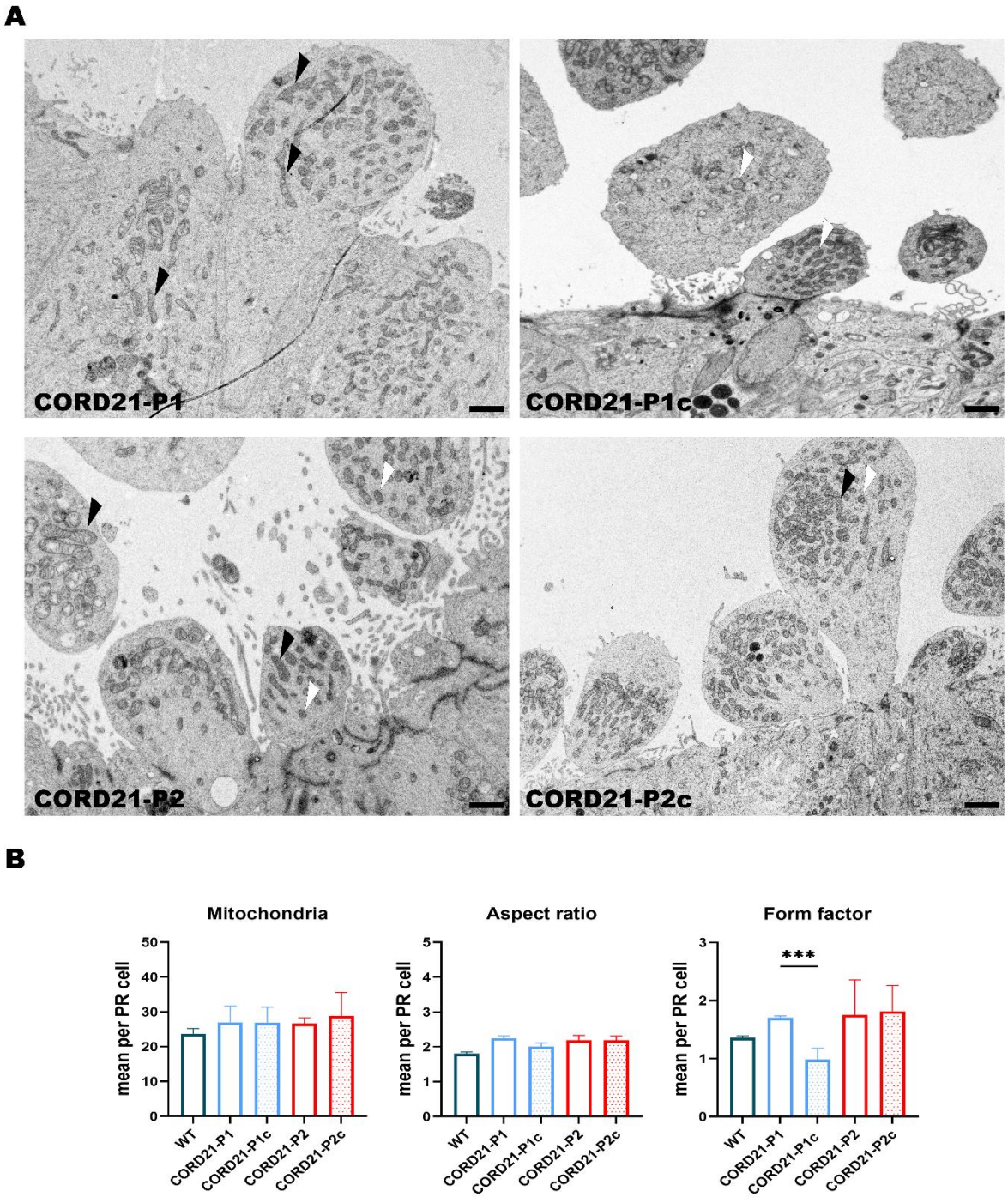

Figure 31. CORD21-P1 patient ROs show increased number of elongated mitochondria relative to isogenic control. (A) CORD21-P1 image indicates the abundance of more elongated mitochondria in photoreceptor cell bodies, and inner segments as opposed to CORD21-P1c where less mitochondrial branching is apparent. Images from CORD21-P2 and CORD21-P2c demonstrate high levels of mitochondrial diversity, whereby both smaller and more elongated mitochondria are apparent in the photoreceptor cell bodies/inner segment. (B) Graphs show no difference in mitochondrial cell count per cell (Kruskal-Wallis) and aspect ratio (ANOVA). Significant differences are observed for form factor which served as mitochondrial branching output between CORD21-P1 and CORD21-P1c (Kruskal-Wallis). Elongated mitochondria are shown by black arrow heads and rounded mitochondria by white arrow heads, respectively. Data were presented as means + SEM. Mitochondrial segmentation analysis was carried out using the Microscopy Image Browser software (n=10).

*Statistical comparisons for CORD21-P1vs -P1c and CORD21-P2vs-P2c are denoted by * P<.05, **P<.01, ***P<.001, ****P<0.0001. The WT sample was excluded from the statistical analysis.*

axis length), whereas branching was inferred by dividing the squared perimeter of mitochondria 4π by the mitochondrial area (i.e., Form factor). Data analyses revealed that no differences were observed in the number of mitochondria per cell and that no gross alterations were evident in terms of mitochondrial shape between patient and control groups (Figure 31, A and B). However, the form factor was shown to be significantly higher in CORD21-P1 compared to CORD21-P1c, suggesting the presence of more elongated mitochondria in the CORD21-P1 patient (Figure 31, A and B).

4.8 Key lysosomal deficiency in CTSD, NPC2 and PPT1 enzymes suggests lysosomal content accumulation in DRAM2 patient ROs.

4.8.1 Proteomic analysis reveals vesicle-mediated response as affected biological process.

10 μg of total protein lysate from each sample was subjected to LC-MS/MS peptide detection and processed for MaxQuant protein identification. WT sample was excluded from the analysis to improve statistical power between selected group pairs - CORD21-P1/CORD21P1c and CORD21-P2/CORD21-P2c (n=3). Principal component analysis showed a clear separation between isogenic control and patient samples (Figure 32, A). Most of the variation between the samples could be explained by Component 1 (45.9%). A total of 3321 proteins were identified using modified ANOVA (FDR<0.05) and a follow-up Tuckey's post hoc t-test (FDR<0.05), revealing 101 proteins to be commonly changed between the two groups (Figure

32, B) (Appendix C). Out of these, 19 followed the same tendency for up-or downregulation (Table 23). Metascape enrichment analysis (n=19) further revealed vesicle-mediated response, protein processing in the endoplasmic reticulum, cellular responses to stress, visual perception, negative regulation of cellular component organisation, cellular homeostasis, and the cone pathway as the major affected biological processes in the patient samples (Figure 32, D). Nearly half of the tandemly changed proteins fell well below the cut-off threshold for logged fold change (FC>2) as indicated by the volcano scatterplots (logged p value <0.05) (Figure 32, E). Amongst significantly downregulated targets for both patients were CTSD, PPT1, TPP1, NPC2, PMEL, SDCBP, CRYAB, HMGA1, DCT, CRIP2, HIST1H4A, NUP210 and VAT1L (p value<0.05). Of particular interest were CTSD, PPT1 and NPC2 as downregulation of these proteins could explain a putative lysosomal deficiency in the retina.

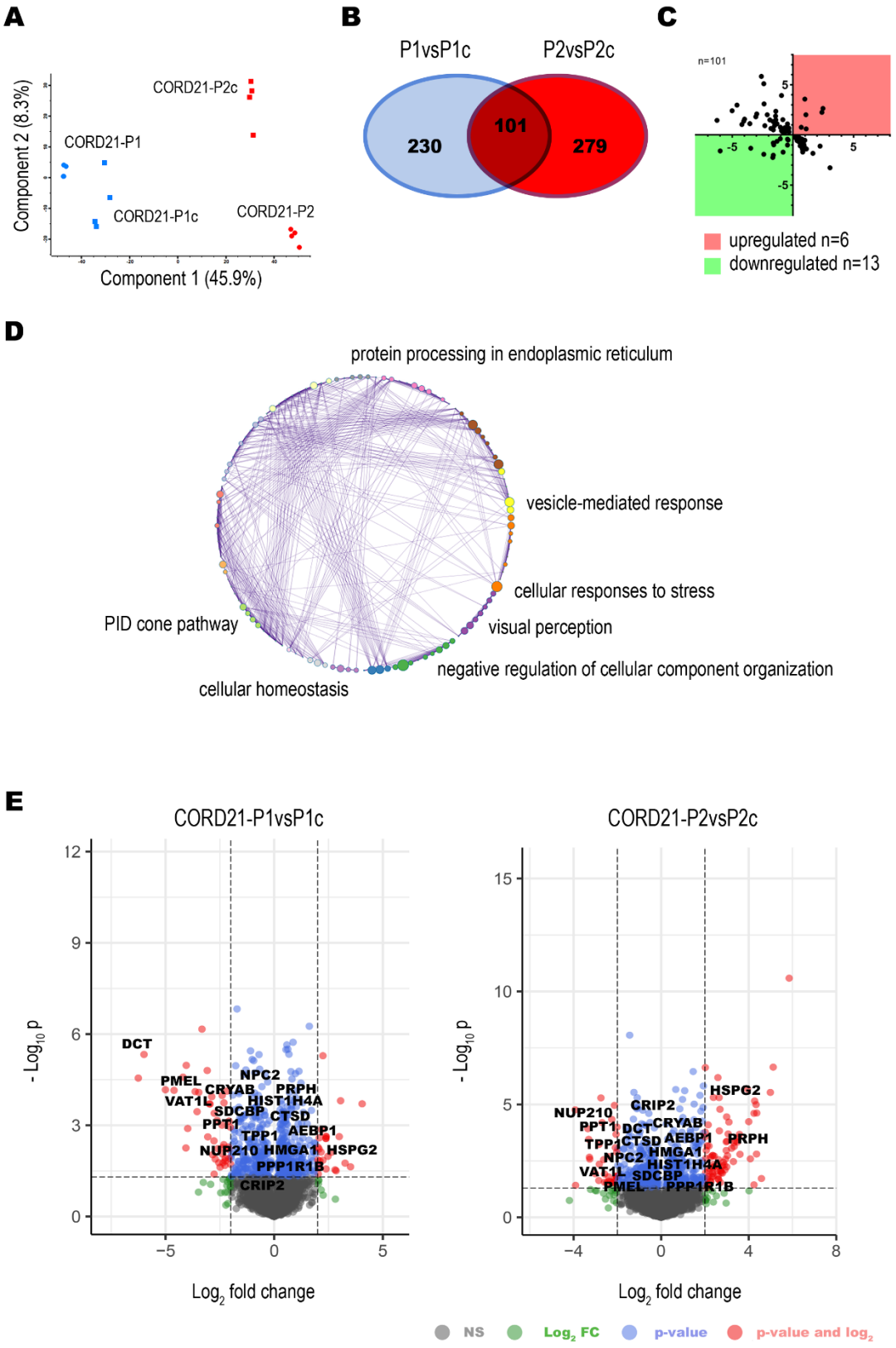

Figure 32. Differential protein analysis identifies vesicle-mediated response as a key biological process. (A) Principal Component Analysis reveals clear separation between

CORD21-P1/P1c (outlined in blue) and CORD21-P2/P2c samples (red). The WT sample was excluded from the proteome analysis. (B) Venn diagram shows an overlap of 101 commonly changed protein following Tuckey's post hoc (FDR<0.05, n=3). (C) Dot plot highlighting commonly upregulated (red) and downregulated (green) proteins (n=19). (D) GO Term enrichment of significantly changed proteins following the same trend by Metascape revealed major affected biological processes (n=19). (E) Volcano plots enable visual identification of tandemly changed proteins with logged fold change cut-off >2 that are also statistically significant (logged p<0.05) (n=19). For CORD21-P1/P1c these are DCT, PMEL, CRYAB, VAT1L and HSPG2, whereas for CORD21-P2/P2c these include NUP210, PPT1, VAT1L, HSPG2 and

Table 23. List of all commonly changed proteins following differential protein analysis in retinal organoids. Same trend downregulated proteins are outlined in green whereas upregulated ones are highlighted in red.

PRPH.

Protein IDs	Full protein name	Protein abbreviation	Location	Known function	Log P1/P1C	Log P2/P2C
F8W787;A0A1B0GW44;A0A1B0GVD5;A0A1B0GWE8;P07339;A0A1B0GVP3;A0A1B0GV23;C9JH19;A0A1B0GU92;A0A1B0GU03;H7C469;F8WD96;A0A1B0GVF1	Cathepsin D;Cathepsin D light chain;Cathepsin D heavy chain	CTSD	Lysosome, endosome, membrane raft	Major acid protease involved in lysosomal degradation; APP processing and degradation (Letronne *et al*., 2016).	-0.4488	-1.00551
A0A2C9F2P4;A0A286YFF7;P50897;Q5T0S4;A0A286YFE3;A0A286YFL8;A0A286YFL6;E9PSE5;E9PK48;E9PIA8	Palmitoyl-protein thioesterase 1	PPT1	Lysosome, exosome, membrane raft, Golgi apparatus	Thioesterase involved in the lysosomal degradation of lipid-modified protein (Lu;Verkruyse and Hofmann, 1996).	-1.61603	-2.0135
A0A2R8YGD1;A0A2R8YD45;O14773;A0A2R8Y7U1;A0A2R8YDY1;A0A2R8Y7I4	Tripeptidyl-peptidase 1	TPP1	Lysosome, exosome, melanosome, membrane raft, recycling endosome, Golgi apparatus	Serine protease involved in lysosomal degradation; non-specific lysosomal peptidase (Lin; Sohar and Lobel, 2001).	-0.81063	-1.70905
A0A590UJZ9;A0A590UJ76;Q9UGM3;A0A590UIX5;A0A590UJF8;A0A590UK99	Deleted in malignant brain tumors 1 protein	DMBT1	Cytoplasm, exosome, extracellular matrix, extracellular space, phagocytic vesicle membrane	Tumour supressor function in brain, lung, colorectal, esophageal and gastric cancer (Mollenhauer *et al*., 1997; Mollenhauer *et al*., 2001). Opsonin receptor for SFTPD and SPAR in macrophage tissues (Deng *et al*., 2019).	1.071564	2.016714
A0A7I2V2R5;A0A7I2V2X8;P27487;A0A7I2V5R8;A0A7I2V2I2;A0A7I2V3F5;F8WBB6;F8WE17	Dipeptidyl peptidase 4;Dipeptidyl peptidase 4 membrane form;Dipeptidyl peptidase 4 soluble form	DPP4	Plasma membrane, cell surface, invadopodium membrane, lamellopodium membrane, endocytic vesicle, exosome, membrane raft	Cell surface glycoprotein receptor supporting the function of T cell receptor during T-cell activation (Durinx *et al*., 2003). Positively regulates T-cell activation by binding ADA, CAV1, IGF2R and PTPRC (Durinx et al., 2003; Ikushima *et al*., 2000; Gines *et al*., 2002; Aertgeerts *et al*., 2004). Regulates T-cell proliferation, NF-kappa-B activation and lymphocyte-epithelial cell adhesion (Ohnuma *et al*., 2007; Gines *et al*., 2002). Involved in the pericellular proteolysis of the extracellular matrix (ECM), the migration and invasion of endothelial cells into the ECM (Ghersi *et al*., 2006, Park *et al*., 1999). Serine exopeptidase with a dipeptidyl peptidase activity that regulates various physiological processes by cleaving peptides in the circulation, including chemokines, mitogenic growth factors and neuropeptides (Brandt *et al*., 2006; Abbott *et al*., 1999).	2.383215	2.263017

J3KMY5;G3V3E8;E7EMS2;G3V3D1;P61916;G3V2V8;H0YIZ1	Epididymal secretory protein E1	NPC2	Lysosome, ER, exosome, extracellular space	Faciliates cholesterol egress from lysosomes with the help of NPC1 (Liou *et al*., 2006; Naureckiene *et al*., 2000; Infante *et al*., 2008; Berzina *et al*., 2018; Chikh *et al*., 2005). May bind and mobilize cholesterol that is associated with membranes (Xu *et al*., 2008). Sequesters sterols such as lathosterol, desmosterol, stigmasterol and beta-sitosterol (Liou et al., 2006). Extracellular NCP2 regulates biliary cholesterol secretion (Yamanashi *et al*., 2011).	-1.30511	-0.63899
F8W1D1;H0YIJ2;P40967;F8VUB1;F8VZC6;F8VXH8	Melanocyte protein PMEL;M-alpha;M-beta	PMEL	ER membrane, Golgi apparatus, cis-Golgi network membrane, endosome, melanosome, extracellular vesicle	Involved in amyloid formation hence a central role in melanosome morphogenesis and pigmentation. Protects from pigmentation-associated toxicity by sequestering toxic eumelanin reaction intermediates (Berson *et al*., 2001; van Niel *et al*., 2015; Hee *et al*., 2017; Graham *et al*., 2019).	-3.47141	-1.33188
O00560;B4DHN5;E9PBU7	Syntenin-1	SDCBP	Cell junction, focal adhesion; adherens junction; ER membrane, melanosome, nucleus, exosome, cell membrane	Roles in vesicular trafficking, regulation of the early secretory pathway, the transport of transmembrane proteins, tumorogenesis, neuro and immunomodulation and exosome biogenesis (Philley;Kannan and Dasgupta, 2016; Zimmerman *et al*., 2001;Fernandez-Larrea *et al*., 1999).	-1.58042	-0.98449
P02511;E9PJL7;E9PRA8;E9PNH7;A0A024R3B9;E9PS12	Alpha-crystallin B chain	CRYAB	Cytoplasm, nucleus, lysosome, extracellular space	Involved in lens homeostasis. Acts like a chaperon during conditions of stress and is involved in the stabilisation of lysosome pH acidity regulator ATP6V1A (Cui *et al*., 2019).	-1.61522	-0.7958
P17096	High mobility group protein HMG-I/HMG-Y	HMGA1	Nucleus	AT-rich DNA-binding protein implicated in the regulation of gene transcription, retroviral DNA integration and the acquitisition of metastatic potential in cancer cells (Wang *et al*., 2019; Dragan *et al*., 2003).	-0.4482	-0.42401
P40126;A0A0A0MTD3	L-dopachrome tautomerase	DCT	Cytosol, melanosome, plasma membrane	Role in melanin biosynthesis (Pennamen *et al*., 2021).	-5.99067	-1.58859
P41219;H7C5W5;F8W835	Peripherin	PRPH	Axon, neuronal cell body, cytoskeleton	Neuronal intermediate filament protein involved in the organisation of a filamentous network (Leung *et al*., 2004; Gros-Louis *et al*., 2004).	0.97705	3.577267
P52943;H0YFA4;H0YHD8	Cysteine-rich protein 2	CRIP2	Cell cortex	Transcription factor involved in the differentiation of smooth muscle (Chang *et al*., 2007).	-0.39638	-0.50636
P62805	Histone H4	HIST1H4A	Nucleus	Nucleosome core component involved in higher order chromatin organisation (Megee; Morgan and Smith, 1995).	-1.03219	-0.38149
P98160;A0A3B3IT11	Basement membrane-specific heparan sulfate proteoglycan core protein;Endorepellin;LG3 peptide	HSPG2	Extracellular space, ECM, basement membrane	Component of basement membranes and glomerular basement membranes (GBM). Role in the maintenance of negative membrane charge, as well as the establishment of a barrier which is both size- and charge-selective (Murdoch *et al*., 1992; 1730768; Nicole *et al*., 2000; Heremans *et al*., 1989).	2.472854	2.646933
Q8IUX7;H7C0W8;H7C4B5;H7C391;H7C1J5;H7C3D7;Q8N436	Adipocyte enhancer-binding protein 1	AEBP1	Extracellular space	Enhances collagen fibriollogenesis (Blackburn *et al*., 2018).	1.094172	0.607201

Q8TEM1	Nuclear pore membrane glycoprotein 210	NUP210	Nucleus, Nucleus membrane, ER membrane	Role in nuclear pore assembly, spacing and structural integrity (Cohen *et al*., 2003).	-1.6546	-2.25228
Q9HCJ6	Synaptic vesicle membrane protein VAT-1 homolog-like	VAT1L	NA	Protein with putative oxidoreductase and zinc ion binding activities (Nagase *et al*., 2000).	-2.39406	-1.92959
Q9UD71;J3KSJ8;J3KT77	Protein phosphatase 1 regulatory subunit 1B	PPP1R1B	Cytoplasm	Protein-phosphatase 1 inhibitor (Yang;Hurley and DePaoli-Roach, 2000).	0.686484	0.760977

4.8.2. PPT1 and NPC2 lysosomal deficiency associates with hypersecretion to RO media.

Following differential protein analysis by LC-MS/MS, PPT1 and NPC2 were identified as protein targets that could directly contribute to retinal lysosomal phenotype. Detection of PPT1 and NPC2 protein abundance by WB corroborated a significant downregulation of these proteins in the lysates of patient d220 RO samples (Figure 33, A and B). To determine whether the deficiency in these lysosomal enzymes could be due to an abrogated delivery to lysosomes, concentrated media samples from d220 aged RO were subjected to WB analysis. The results confirmed that PPT1 and NPC2 can indeed be found to accumulate in the media of age-matched patient ROs (Figure 33, A and B). Further analysis revealed that patient lysates presented with reduced enzymatic activities for CTSD, Glucocerebrosidase as well as α-Mannosidase, all being crucial lysosomal enzymes (Figure 33, C).

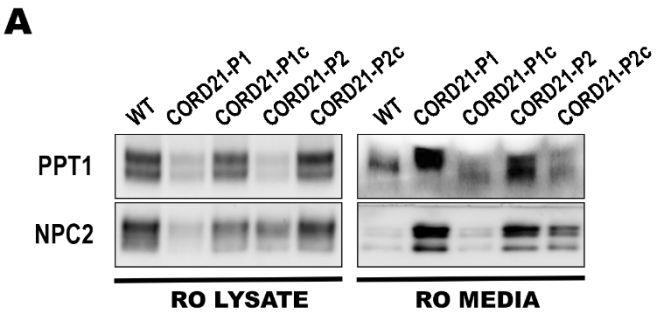
A
WT
CORD21-P1
CORD21-P1c
CORD21-P2
CORD21-P2c
WT
CORD21-P1
CORD21-P1c
CORD21-P2
CORD21-P2c
PPT1
NPC2
RO LYSATE
RO MEDIA

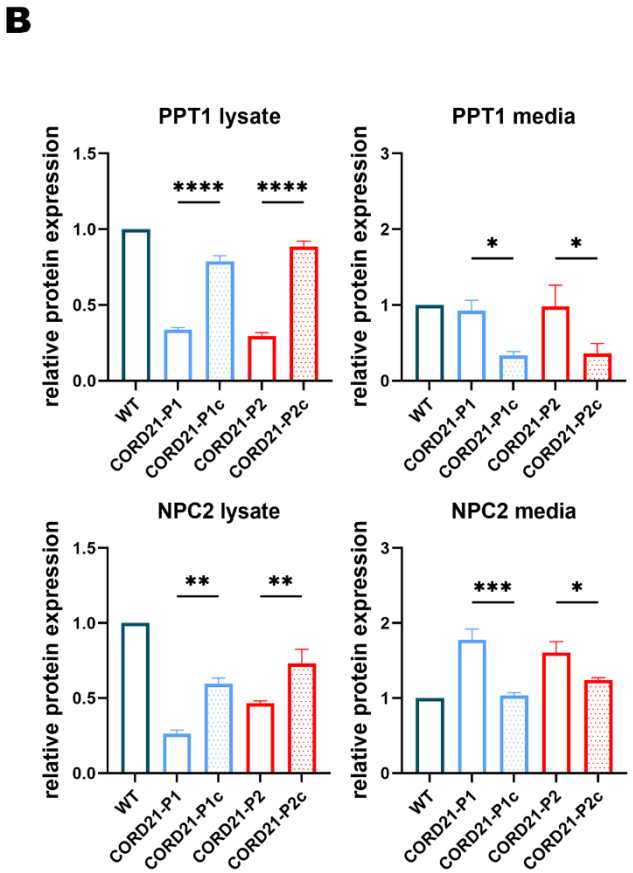
B
PPT1 lysate
PPT1 media
NPC2 lysate
NPC2 media
relative protein expression
****
*
**
***
WT
CORD21-P1
CORD21-P1c
CORD21-P2
CORD21-P2c

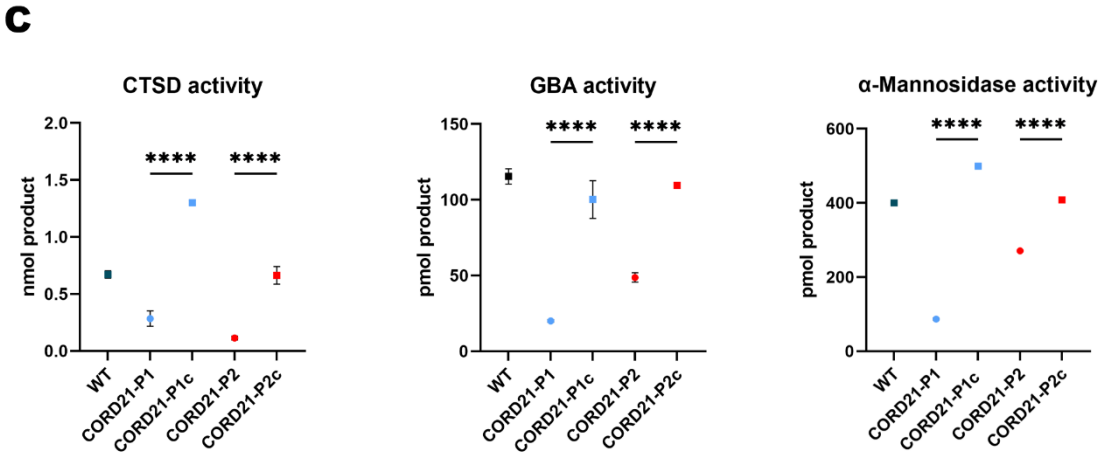
C
CTSD activity
GBA activity
α-Mannosidase activity
nmol product
pmol product
pmol product
****
WT
CORD21-P1
CORD21-P1c
CORD21-P2
CORD21-P2c

Figure 33. PPT1 and NPC2 enzymes are present in the extracellular media of patient ROs. (A) PPT1 and NPC2 enzymes are severely deficient in the lysates of CORD21-P1 and CORD21-P2 ROs relative to isogenic controls. Conversely, the latter proteins can be detected in the media of age-matched patient samples. (B) Western blot plots show a significant decrease in the abundance of PPT1 (ANOVA) and NPC2 (ANOVA) in the lysates of d220 RO patients. This is followed by a concomitant increase of these enzymes in the media of age-matched samples (PPT1, ANOVA and NPC2, ANOVA). A total protein stain was used to confirm equal protein loading and normalisation was carried out to the WT sample. Data were presented as means + SEM, (n=3). (C) Kinetic assay for the activity of CTSD shows reduced enzymatic activity in patient lysates relative to isogenic control (ANOVA). Endpoint ELISA assays for GBA (ANOVA) and α-Mannosidase (ANOVA) demonstrated a similar reduction in patient enzymatic activities in d220 RO lysates. Data were shown as means + SEM (n=3).

*Statistical comparisons for CORD21-P1vs -P1c and CORD21-P2vs-P2c are denoted by * P<.05, **P<.01, ***P<.001, ****P<0.0001. The WT sample was excluded from the statistical analysis.*

4.8.3 Western blot characterisation of DRAM2 ROs reveals a downregulation of lysosomal and transport proteins.

4.8.3.1. Patient ROs show downregulation in CTSD, GBA and CD63 protein levels as well as altered LAMP2 glycosylation status.

Proteomic and TEM analyses converged on an underlying lysosomal deficiency in both DRAM2 patients. To further elaborate on the nature of the lysosomal defect and whether it originates from the faulty delivery of lysosomal targets, we conducted extensive western blot screening for lysosomal markers, their transport receptors as well as clathrin-adaptor proteins across the d220 sample set.

The scarcity of CTSD protein in patient lysates suggested by LC-MS/MS was corroborated by WB. The latter showed a significant downregulation of CTSD heavy chain in CORD21-P1 and -P2 d220 RO (Figure 34, A). Interestingly, CTSD active intermediate was significantly downregulated in the CORD21-P1 patient sample in conjunction with a tendency for a reduction of pro-CTSD in patients. By comparison, no changes were observed in the main CTSD forms secreted in retinal organoid media (Figure 34, C and D).

Patient samples presented with altered glycosylation patterns for lysosomal receptor LAMP2, which appeared to be hypo- and hyperglycosylated in CORD21-P1 and CORD21-P2

relative to isogenic controls, respectively. A complete lack of endosomal sorting protein CD63 correlated with the absence of DRAM2 in the CORD21-P1 patient. GBA protein which is integral to sphingolipid degradation was also markedly reduced in CORD21-P2 compared to the isogenic control. Further investigation by WB rendered no changes in the expression of early and late endosomal markers RAB5 and RAB7, as well as lysosomal enzyme CTSB (Figure 34, A and B).

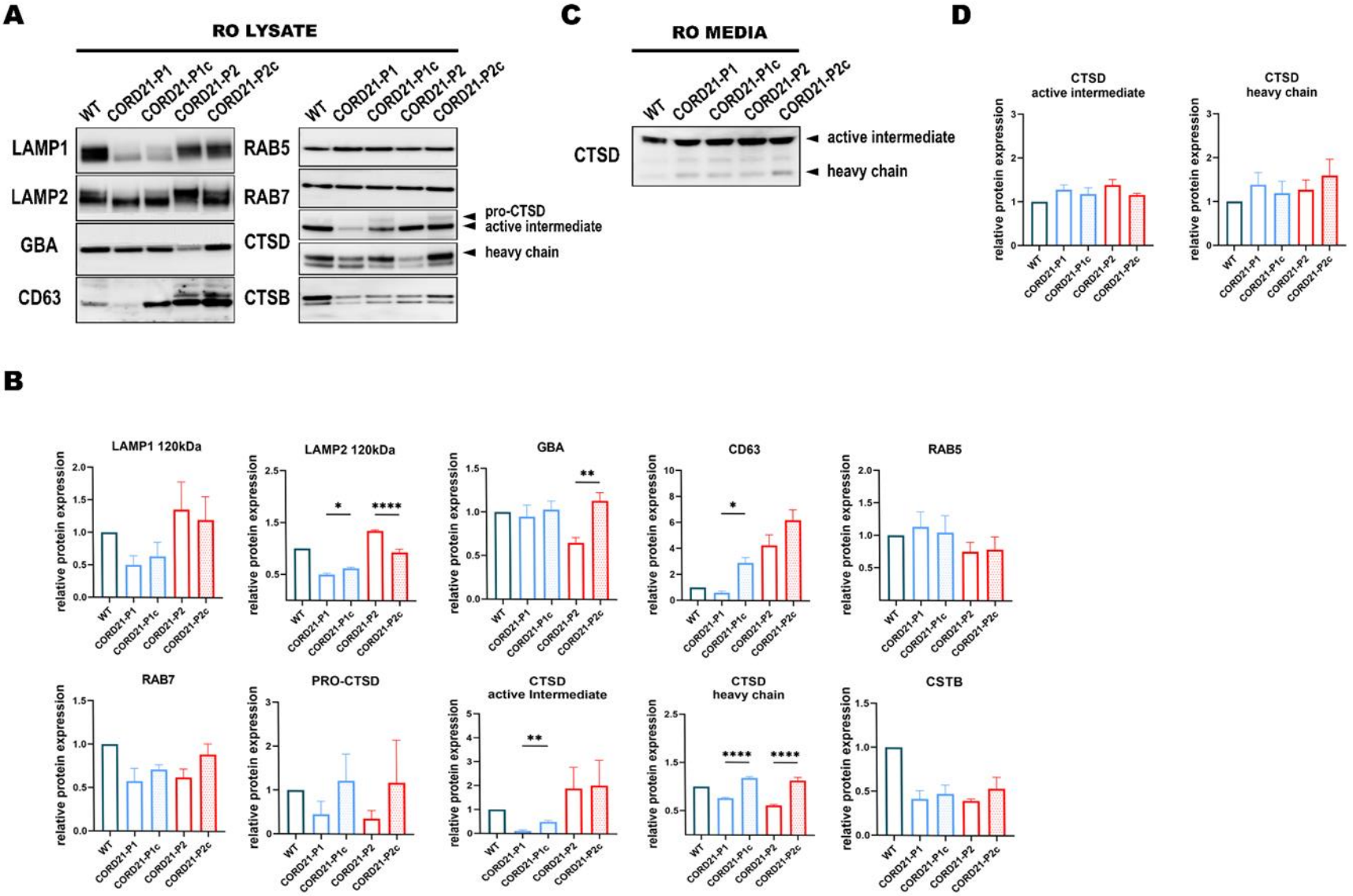
A
RO LYSATE
WT
CORD21-P1
CORD21-P1c
CORD21-P2
CORD21-P2c
LAMP1
LAMP2
GBA
CD63
RAB5
RAB7
CTSD
CTSB
pro-CTSD
active intermediate
heavy chain
C
RO MEDIA
CTSD
active intermediate
heavy chain
D
CTSD
active intermediate
CTSD
heavy chain
relative protein expression
B
LAMP1 120kDa
LAMP2 120kDa
GBA
CD63
RAB5
RAB7
PRO-CTSD
CTSD
active Intermediate
CTSD
heavy chain
CSTB

Figure 34. CTSD, GBA and CD63 are reduced in DRAM2 d220 RO lysates. (A) WB panel shows a significant CTSD heavy chain deficiency in CORD21-P1 and -P2 d220 lysates (ANOVA). CD63 and GBA are significantly downregulated in CORD21-P1 and -P2, respectively (ANOVA). Lysosomal receptor LAMP2 showed opposing trends of glycosylation in both patients relative to isogenic control (ANOVA). No statistically significant changes are seen for RAB5 (ANOVA), RAB7 (ANOVA) and CTSB (ANOVA). (B) ANOVA quantification plots generated by Prism 9.5.0 showing statistically significant differences in protein expression for 120-kDA LAMP2, GBA, CD63, CTSD heavy chain and active intermediate (n=3). (C-D) Secreted CTSD heavy chain and active intermediate present no changes in RO media on WB (ANOVA). All data were presented as means + SEM and normalised to the WT sample (n=3-5).

*Statistical comparisons for CORD21-P1vs -P1c and CORD21-P2vs-P2c are denoted by * P<.05, **P<.01, ***P<.001, ****P<0.0001. The WT sample was excluded from the statistical analysis.*

4.8.3.2 A reduction in LIMP2, VPS53 and AP-1γ transport proteins is observed in DRAM2 d220 ROs.

To gain more insight into the varying degree of lysosomal perturbation amongst patients, we assessed the expression of proteins that regulate distinct modes of endolysosomal transport by WB.

A notable decline in the GBA receptor LIMP2 was a consistent finding in both patients at d220 (Figure 35). The trafficking of M6P- tagged enzymes was unaffected as CI-M6PR (cation-independent mannose 6-phosphate receptor) and CD-M6PR (cation-dependent mannose 6-phosphate receptor) displayed cell line-specific patterns of expression. M6PR-independent transport facilitated by the sortilin receptor was also not impacted (Figure 35, A and B). Furthermore, VPS35, a known retromer component, remained unchanged amongst pre-selected group pairs.

Interestingly however, the GARP (Golgi-associated retrograde protein) complex component VPS53 was specifically downregulated in the CORD21-P2 patient. Out of the three main clathrin adaptors examined, AP-1γ was consistently downregulated in the DRAM2-deficient CORD21-P1 sample (Figure 35, A and B).

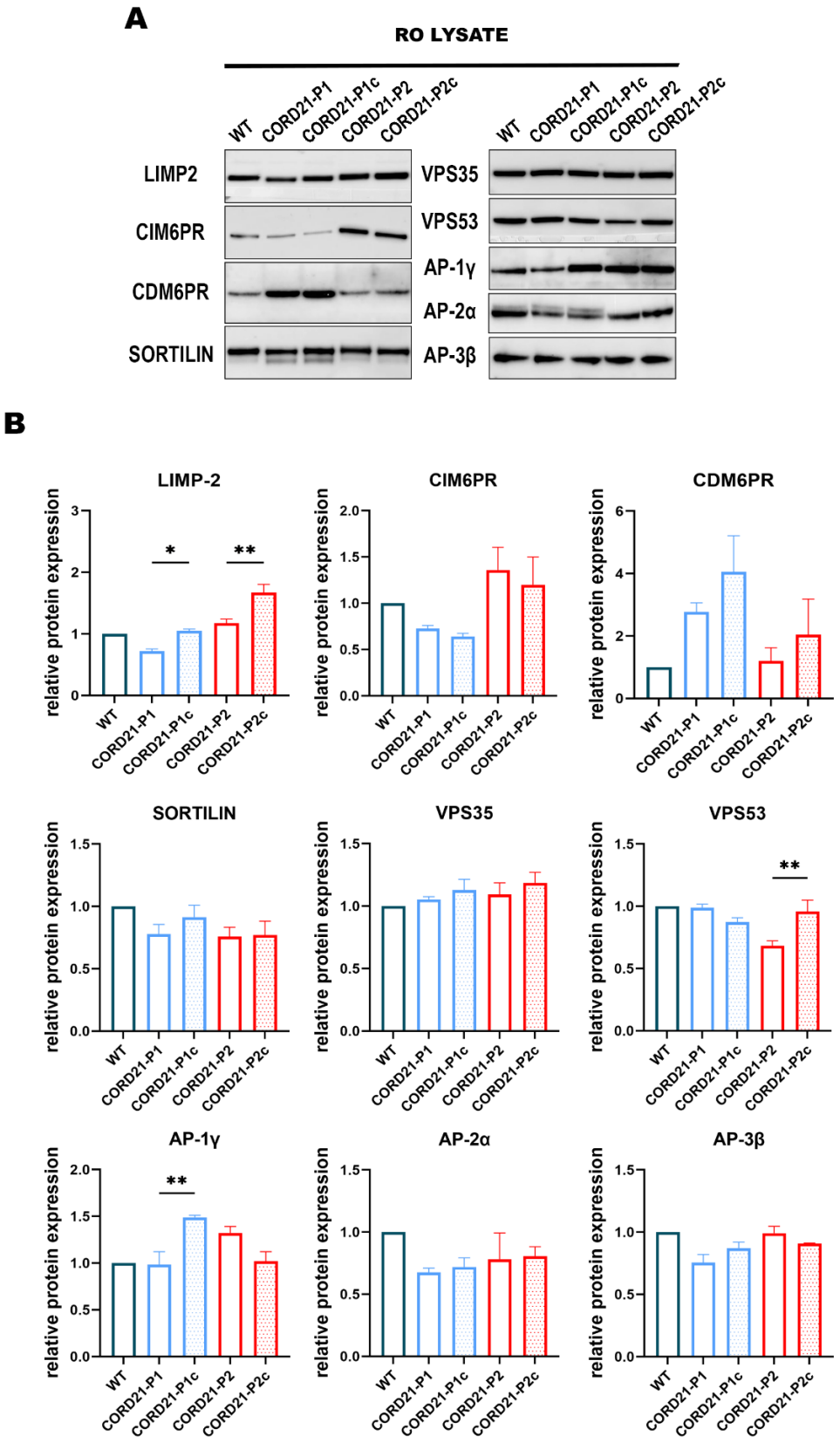
A
RO LYSATE
WT
CORD21-P1
CORD21-P1c
CORD21-P2
CORD21-P2c
LIMP2
CIM6PR
CDM6PR
SORTILIN
VPS35
VPS53
AP-1γ
AP-2α
AP-3β
B
LIMP-2
CIM6PR
CDM6PR
SORTILIN
VPS35
VPS53
AP-1γ
AP-2α
AP-3β
relative protein expression
*
**

Figure 35. Additional screening of transport proteins suggests cellular transport malfunction as indicated by the depletion of specific lysosomal receptors and clathrin adaptor proteins. (A-B) d220 RO lysate analysis by WB reveals a consistent downregulation in GBA receptor LIMP2 for both patients (ANOVA). A significant reduction in protein expression was observed for GARP component VPS53 (ANOVA) and AP-1γ (ANOVA) for CORD21-P2 and -P1, respectively. Conversely, no significant differences were established for the expression of CIM6PR (ANOVA), CDM6PR (Kruskal-Wallis), VPS35 (ANOVA), AP-2α (ANOVA) and AP-3β (ANOVA). Data were presented as means + SEM and normalised to the WT sample (n=3).

*Statistical comparisons for CORD21-P1vs -P1c and CORD21-P2vs-P2c are denoted by * P<.05, **P<.01, ***P<.001, ****P<0.0001. The WT sample was excluded from the statistical analysis.*

4.9 Differential lipidomic analysis corroborates a defect in membrane-lipid composition as well as the accumulation of toxic lipid intermediates.

To ascertain whether a lipid imbalance accompanied a potential vesicular trafficking defect, 220 patient and control ROs were subjected to quantitative lipidomics analysis. Lipid profiling under both positive and negative ion modes revealed an enrichment of ceramide species in patient samples (HexCer 38.1, HexCer 40.1, 41.1-2, HexCer 42.1-2 as well as Cer 34.2) (Figure 36, B). A build-up of ceramide in patient ROs was further corroborated by a qualitative IF experiment as shown in Figure 37.

An interesting hallmark feature of disease also appeared to be the significant depletion of an array of glycerophospholipids (PE, PS, PC, PI, PG) compared to the controls (Figure 36, A and B). Patients further presented with an upregulation in GM3 ganglioside glycosphingolipids (GM3 40.1, 41.1 and 42.1-2) and the isoprenoid alcohol dolichol (Dolichol.19-20) which was a specific finding under positive ion mode analysis (Figure 36, A and B). All lipidomics work was conducted by Professor Phil Whitfield and his team at the University of Glasgow.

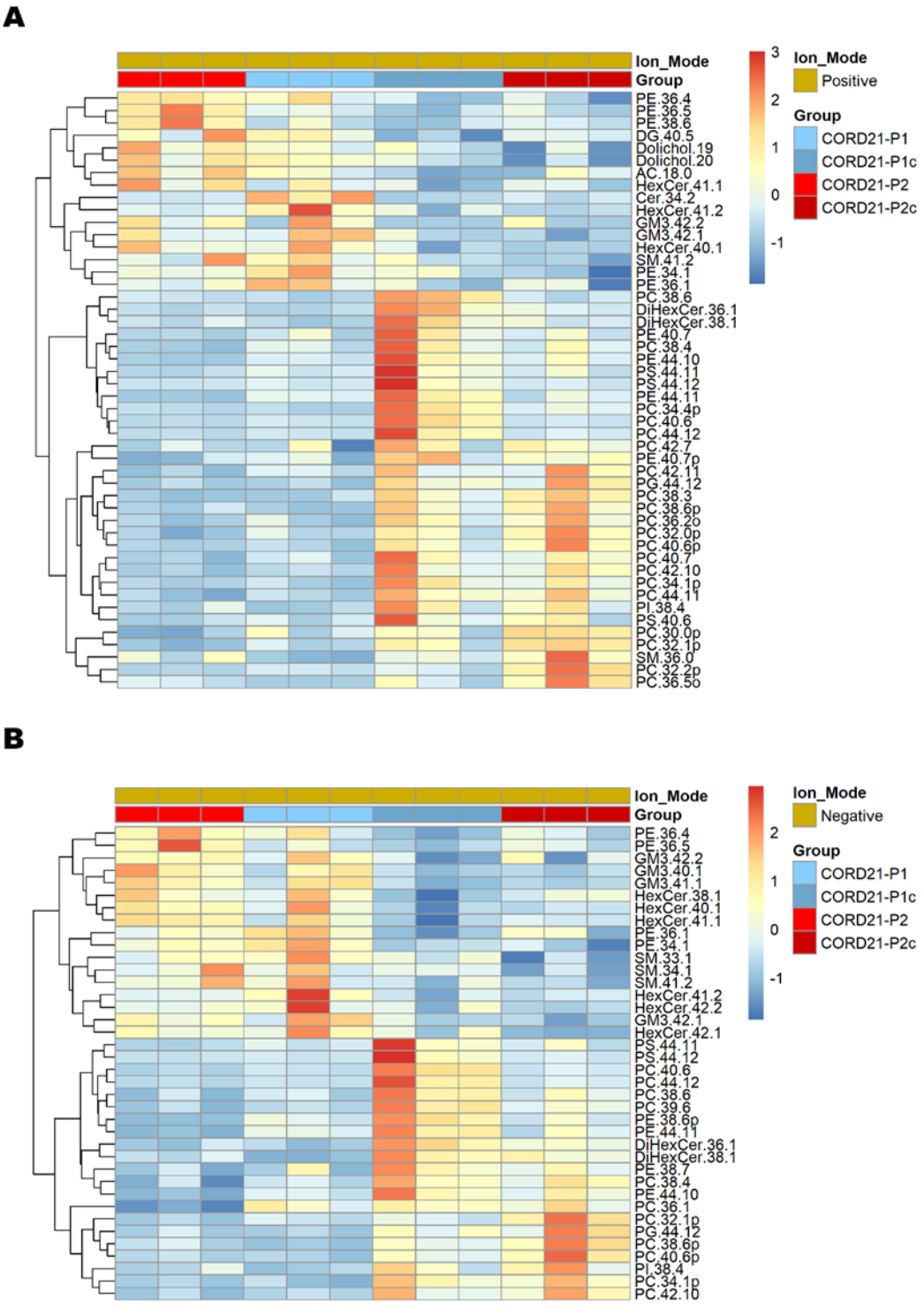

Figure 36. Lipidomic analysis of d220 DRAM2 and control ROs. Heatmaps reveal significant changes in lipid species under positive (A) and negative ion modes (B) of data acquisition based on t-test and p value <0.05 cut-off (n=3). Heatmaps were generated by Dr. Florence Burte. CORD21-P1 is shown in light blue, CORD21-P1c in dark blue, CORD21-P2 and CORD21-P2c in red, left and right, respectively. The WT sample was not subjected to lipidomics analysis.

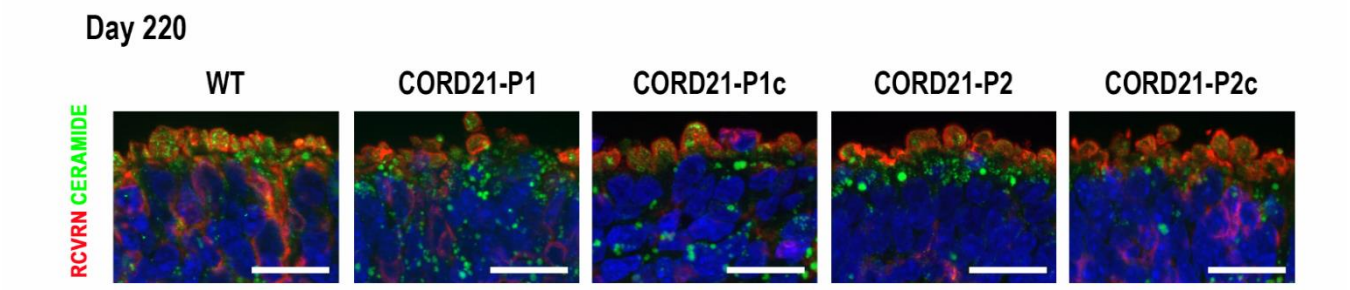

Figure 37. RCVRN and Ceramide double staining in d220 ROs shows ceramide accumulation basally to photoreceptor inner segments. In WT and isogenic controls ceramide expression is mostly limited to the inner segment of the photoreceptor layer indicated by RCVRN staining. By contrast, in patient organoids ceramide accumulation extends beyond the inner segment into the photoreceptor cell bodies, and further basally into the reaches of secondary neurons at the apical edge. IF staining was conducted as a qualitative experiment. Scale bars represent 20µm (n=3).

4.10 DRAM2 co-localises with key inner segment and membrane transport markers.

To qualitatively assess the location of DRAM2 expression within ROs, WT RO sections were probed by IF in combination with known cellular markers. As shown in Figure 38, A, DRAM2 protein expression pattern broadly pertains to the area of the inner segment (IS) of photoreceptors which is marked by the mitochondrial marker TOMM20. Limited and a very punctate DRAM2 expression can also be seen at the apical portion of the IS (Figure 38, A, left image). Relative to TOMM20, the cis-Golgi protein GM130 localises more so within the basal body and Golgi apparatus part of the IS (Figure 38, A, middle image). Interestingly. DRAM2's co-localisation with GM130 is only partial at the IS (Figure 38, A, image to the right). This is in line with DRAM2 supporting protein trafficking activities to and from the organelle.

Following on from results presented previously, DRAM2 stains positively for co-localisation with coating membrane vesicle marker clathrin (Figure 38, B, left image). Further to lipidomics data, the precise location of ceramide accumulation in WT ROs was of particular interest to this project. Interestingly, the polar lipid species ceramide almost exclusively localises to the IS in RO photoreceptors and DRAM2 can be seen to co-stain with it (Figure 38, B, middle image). Moreover, ceramide is only present at the apical region of ROs as seen by the co-expression with the photoreceptor marker RCVRN (Figure 38, B, right image). Importantly, DRAM2 expression partially overlaps with that of lysosomal membrane marker LAMP2 (Figure 38, C, left image).

To gain a more thorough insight into the potential role of DRAM2 in membrane-mediated trafficking, DRAM2 was also tested in conjunction with clathrin adaptor markers AP-1 and AP-3. Interestingly, DRAM2's partial co-localisation with AP-1 is organised around vesicle—like structures dispersed alongside the perimeter of the IS (Figure 38, C middle). Further support for a role of DRAM2 in vesicle mediated trafficking is rendered by the strong co-localization with lysosome transport adaptor AP-3 (Figure 38, C image to the right).

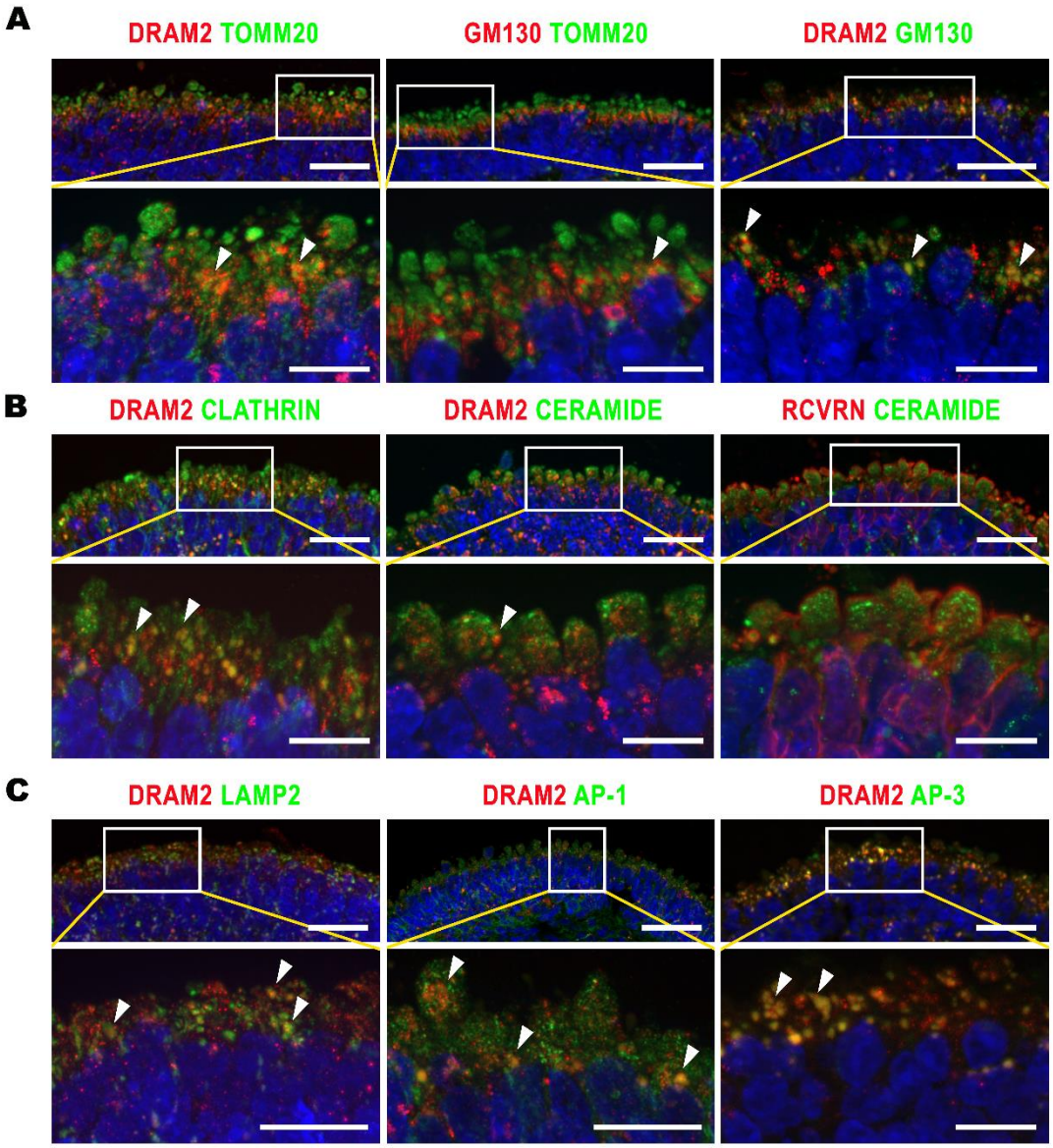

Figure 38. DRAM2 expression in WT d220 ROs is observed broadly within the area of the inner segment (IS) and associates with clathrin vesicle adaptors AP-1 and AP-3. (A) DRAM2 expression in WT RO as marked by DRAM2 antibody (red). Co-localisation with mitochondria

can be seen at the IS as marked by TOMM20 expression (green, left image). GM130 is seen in the cell bodies of the photoreceptors, near the Golgi apparatus at the basal bottom side of the IS (middle image). DRAM2 (red) only partially localises at the cis-Golgi compartment of IS of the photoreceptor layer (GM130, green, right image) (n=3). (B) Clathrin (green) is detected in a punctate-like pattern across the entirety of the IS and can be seen to only partially co-stain with DRAM2 (red, left image). Ceramide expression (green) pertains to the $RCVRN^{+}$ photoreceptor layer (red, right image) and is co-expressed together with DRAM2 within the IS region of the RO (red, middle image) (n=3). (C) DRAM2 (red) co-staining with LAMP2 (green, left). DRAM2 expression (red) strongly overlaps with that of transport vesicle proteins AP-1 (green, middle) and AP-3 (green, right) at the IS of ROs. Hoechst (blue) counterstains nuclei. Scale bars in the top panels represent 20µm and 10µm in the bottom magnified panels, respectively (n=3).

4.11. Discussion

4.11.1 DRAM2a isoform structure and functional implications

Experimental work outlined here was aimed at elucidating the effect of *DRAM2* mutations on the phenotype of patients with inherited cone-rod dystrophy in the context of RO development. DRAM2 dystrophy manifests only in the presence of biallelic mutations and sequence analysis outlined here suggests that the affected isoform in CORD21-P1 and -P2 patients is the *DRAM2a* isoform. The contribution of the retinal-specific *DRAM2c* isoform to phenotype remains elusive as only one mutation in our patients, and namely that of CORD21-P2 (c.494 G>A) pertained to the sequence of this isoform. Even though the disease has been shown to only present in a biallelic state, the ability of retinal specific isoforms such as *DRAM2c* to contribute to disease a gain-of-function manner should not be completely ruled out. Further investigation should entail the rigorous analysis of all existing *DRAM2* variants and whether severity of the disease is impacted by *DRAM2c* isoform mutations.

As top-ranking structural DRAM2 analogues emerged the plasma membrane ascorbate-dependent reductase or (CYBRD1/DCytb) and other cytochrome b orthologues (Ganasen *et al.*, 2018). CYBRD1/DCytb is one of three cytochrome b_{561} evolutionary conserved proteins in mammals which exhibit a closely related function in ascorbate-mediated transmembrane transport. GO term annotation further corroborated a potential role for DRAM2 in electron transport and heme-binding. In addition to the Cytochrome b_{561} orthologoues and their related GO terms, an unexpected link was unravelled with cytochrome c oxidase activity pertaining to bacterial proteins associated with ancient forms of aerobic

respiration. GO terms for cellular component thus suggest a putative function in mitochondrial membrane homeostasis and respiration.

The cytochrome b_{561} protein family amongst which are also the CGCytb and the lysosomal LCytb, are a group of intrinsic membrane oxidoreductases comprising 6 transmembrane α-helices and two heme-group homodimers (Su and Asard, 2006). Su *et al.* have proposed a role for DCytb in the recycling of extracellular ascorbate via the reduction of monodehydroascorbate (MDHA) in human erythrocyte membranes (Su *et al.*, 2006). It has been postulated that mature human erythrocytes have lost their ability to reduce iron in favour of ascorbate recycling. DCytb also known as the duodenal cytochrome b is believed to be one of two principal ferric reductases alongside DMT1 (Divalent metal Transporter 1) responsible for dietary absorption of nonheme iron by duodenal enterocytes (Latunde-Dada;Simpson and McKie, 2008). Interestingly, LCtyb knockout in Bukitt lymphoma cells led to a significant depletion of bioavailable cytosolic iron Fe^{2+}, toxic iron accumulation in lysosomes and severe mitochondrial damage due to iron deprivation (Wang *et al.*, 2021). Iron metabolism is essential for lysosomal acidity and mitochondrial health (Yambire *et al.*, 2019; Weber *et al.*, 2020) and its dysregulation could contribute to aberrant redox dynamics and vesicular trafficking impairment in Parkinson's disease (Ma *et al.*, 2021). The reduction of substrate on the extracellular interface of cytochrome b_{561} proteins is enabled by cytoplasmic ascorbate, whereas the heme groups organised by histidine residues facilitate ion electron transfer. Cytochrome b_{561} proteins have been found to differ in the lengths of their C-termini, which could be a major determinant of cellular location as has been shown for LCytb (Zhang *et al*., 2006; Ganasen *et al*., 2018). Consistent with this, DRAM2 structure closely resembles that of monomeric cytochrome b_{561} proteins, suggesting a putative role in ascorbate-mediated transmembrane electron transport as well as ferric ion transport. The putative 3D model of DRAM2 structure reveals a transmembrane conformation consisting of six helical domains and a long cytoplasmic C-terminus (Figure 24). A closer look at the sequence of the C-terminus shows putative tyrosine and dileucine motifs (YDTA/[NE]RTRL[LS]) which would implicate DRAM2 function in plasma membrane/Golgi to endolysosomal trafficking (Bonifacino and Traub, 2003). The dileucine motif has been shown to be particularly important for the binding of clathrin adaptors AP-1 and AP-3 via interaction with their γ1-σ1 and δ-σ3 subunits, respectively (Janvier *et al*., 2003).

Consistent with its principal function as a membrane transporter, DRAM2 localises to lysosomal membranes, where it facilitates the lipidation of endogenous LC3-I to LC3-II and the formation of the autophagosome (Park *et al.*, 2009; Yoon *et al.*, 2012). In addition to being expressed in the ISs of PRs and RPE, which suggests a function in maintaining retinal homeostasis (El-Asrag *et al.*, 2015; Sergouniotis *et al.*, 2015), DRAM2 is also expressed prominently in heart tissue (O'Prey *et al.*, 2009). It has previously been shown that downregulation of DRAM2 by miRNA-125a via sufentanil administration can ameliorate ischemic injury and prevent cardiomyocyte apoptosis (Wu *et al.*, 2021). Furthermore, a causal link between *DRAM2* variants and myocardial ischemia-reperfusion injury has been uncovered by recent GWAS studies (Salo *et al.*, 2015). Despite structural analysis revealing that DRAM2 may have a role in mitochondrial respiration, the premise for a primary role of DRAM2 in mitochondria metabolism remains elusive. Such a role, however, could be relevant to the high levels of DRAM2 expression observed in heart tissue, which is particularly rich in mitochondria.

Following the commercial DRAM2 antibody validation by siRNA knockdown, we have confirmed a significant decrease in DRAM2 protein expression in patients CORD21-P1 and -P2 ROs by WB. Interestingly, no 17kDa band was detected for the DRAM2c isoform despite the ability of the antibody to recognise the C-termini of both isoforms. Since DRAM2 is a small and a relatively low abundant insoluble protein, WB was carried out under enhanced detection (30 µg protein, enhancer + Femto ECL detection) coupled with an additional optimisation under boiled non-reducing conditions. In the future DRAM2c isoform detection by WB could be further addressed by fractionation and the specific enrichment of lysosomes.

The WB findings are consistent with a complete lack of *DRAM2a* protein owing to the c.140delG mutation in CORD21-P1 causing nonsense mediated decay (NMD). NMD is an mRNA degradation mechanism employed for the elimination of transcripts bearing truncating mutations or premature stop codons (PTCs). Previous reports have shown that the efficiency of NMD can vary significantly based on the length of the first reading frame and the intercistronic distance especially in transcripts carrying truncating mutations in their 5' proximal region. This would lead to translation re-initiation at a downstream site (Neu-Yilik *et al.*, 2011; Sato and Singer, 2021). Our WB data seems to suggest, however, that NMD

transcript degradation in CORD21-P1 is particularly efficient. In agreement with the mutation tool prediction analysis, a minimal amount of full length of *DRAM2a* (~10%) protein was detectable by WB in the CORD21-P2. This result varied with biological repeats amongst d220 RO samples, whereby certain CORD21-P2 samples did not exhibit any detectable 26kDa protein. This could be attributed to the translation and subsequent degradation of a dysfunctional *DRAM2a* c.131 G>A variant. Since the c.131 G>A mutation sits at an intron-exon boundary, it is also likely that this allele is going to be mis-spliced to a varying degree leading to the expression of a full-length albeit aberrant *DRAM2a*. As shown by the predictive 3D modelling by L-Tasser, the highly conserved serine residue affected by c.131 G>A localises to an extracellular interface domain. This is a site of potential interaction with the extracellular milieu. Both c.131 G>A and c.140delG mutations are located within this cytoplasmic sheet domain and according to the Clustal alignment for DRAM2, the latter are in close proximity to a conserved cytoplasmic ascorbate binding site, suggesting these mutations may affect the electron transport activities of DRAM2.

As inferred from IF data, no detectable DRAM2 expression was observed in our patient ROs at d220. IF data acquired from WT d220 RO demonstrates that DRAM2 expression resembles that of vesicle-like structures, punctate and spread-out across the IS area of PRs. The $DRAM2^{+}$ immunofluorescence signal is predominantly situated at PRs' cell bodies. Significant overlap is seen with TOMM20 and GM130 markers, suggesting that DRAM2 could indeed be found in mitochondria as well the as the cis-Golgi apparatus. Our qualitative IF analysis confirms that DRAM2 can also be found nested with $LAMP2^{+}$ lysosomes. Consistent with a role in vesicular trafficking, DRAM2 localisation is not permanently and exclusively associated with lysosomes, but is oriented around moving between organelles, as one would expect, if it facilitated cargo delivery by shuffling between membrane structures. A function in membrane-mediated transport role is strongly highlighted by co-staining with clathrin itself as well as clathrin-adaptor proteins AP-1 and AP-3.

4.11.2 DRAM2 disease phenotype of d220 ROs suggests an underlying defect in vesicular trafficking, lipid accumulation and a lysosomal enzyme deficiency.

4.11.2.1 DRAM2 ROs do not show changes in retinal marker expression by IF.

To understand how *DRAM2* mutations contribute to dysfunctional lysosomes and the irreversible loss of PRs in the retina, ROs were differentiated from the CORD21-P1 and -P2 iPSC lines alongside isogenic and WT controls using an optimised Sasai method (Kuwahara *et al.*, 2015; Hallam *et al.*, 2018). Throughout multiple rounds of differentiation CORD21-P1 and -P1c presented with a thick neuroepithelium layer, and the timely expression of all retinal markers investigated, including that of all mature opsins. By contrast, CORD21-P2/P2c exhibited a more cystic morphology and delayed OPN1LW/MW (Opsin 1, long-wavelength/ middle-wavelength sensitive) development. The lack of proper structural lamination of some of the organoids was also reflected in the scattered expression of mature PR markers. As demonstrated by IF analysis, CORD21 DRAM2 patient ROs gave rise to most retinal cell types by d220 including photoreceptor cells (RCVRN), retinal ganglion cells (SNCG), Müller glia (vimentin), bipolar (PKCα), amacrine (AP2α) and horizontal cells (PROX1). The lack of overt changes in the retinal marker expression and more specifically that of opsins is in good agreement with the clinical phenotype of DRAM2 dystrophy developing in the third decade of life. ROs harvested at d220 correspond to the post conception week 29 of development which does not allow sufficient time for a complete phenotypic modelling *in vitro*. ROs are considered to acquire maximum maturity between D210-266 (Capowski *et al.*, 2019; Cowan *et al.*, 2020). Recent publications by the Gamm group (Saha *et al.*, 2022) have demonstrated that that late-stage RO cones (>d180) exhibit the highest levels of light sensitivity and that at this stage they functionally resemble primate foveal cones. The authors postulate that past >d300, RO cones begin to lose their sensitivity which is consistent with an overall structural decay at this stage of RO development. This is mostly due to limitations posed by the lack of proper vascularisation and nutrient exchange which leads to a functional decline and the loss of PRs (Radisic *et al.*, 2006; Zhao *et al.*, 2021). Poor nutrient diffusion and the spatial impediments conferred by the spherical shape of the organoids contribute to the loss of retinal ganglion and inner plexiform cell layers prior to complete PR maturation (Reichman *et al.*, 2014), as well as the inability of RO to undergo central – peripheral retinal specification (Takano *et al.*, 2015). Some well-known challenges to 3D retinal organoid culture are the differential ability of iPSC lines to give rise to mature ROs, the high levels of batch-to-batch variability as well as the incomplete representation of retinal biology due to the lack of microglia (Hallam *et al.*, 2018; Chichagova *et al.*, 2023). Microglia derive from the

haematopoietic lineage and subsequently home to the central neural system. It is heavily hypothesised that they may be crucial for retinal maturation and survival, retinal vascularisation, and synaptic pruning (Li;Jiang and Samuel, 2019).

Further challenges are presented by the sporadic presence of ectopic and improperly aligned RPE. RPE are indispensable for proper retinal lamination and photoreceptor outer disc renewal (Raymond and Jackson, 1995; Fuhrmann;Zou and Levine, 2014). The intrinsic life span of the ROs is affected by the poor synaptic connectivity between bipolar, amacrine cells and ganglion cells i.e., the lack of the so-called ribbon synapses. Due to the early spatiotemporal emergence of retinal ganglion cells, a decline in this cell population is already seen by the time bipolar cells begin to appear (Cepko, 2014; Zhong *et al.*, 2014). Although ROs are responsive to light-stimuli by microelectrode array (MEA) *in vitro* (Hallam *et al.*, 2018), the incomplete maturation of outer segments impedes proper electrophysiology analysis. An additional factor at play is the absence of ON and OFF retinal pathways which endow the retina with a higher order visual processing capacity (Dorgau *et al.*, 2019). It is noteworthy that at d220, DRAM2 patient ROs still showed expression of all major retinal cell types including ganglion cells and bipolar cells. Future work would be aimed at RO generation using an automated platform for maximum reproducibility which may improve the derivation of ROs with more consistent presence of outer segments across all cell lines.

4.11.3 DRAM2 ROs present with autophagy and lipopigment ultrastructural defects.

Autophagy is a major catabolic pathway which converges on the lysosome for intracellular degradation. Autophagy flux experiments based on rapamycin and bafilomycin treatments in d150 RO displayed a fundamental disparity between CORD21-P1 and -P2 in their ability to initiate autophagic processes as indicated by the lack of LC3-II flux upon single bafilomycin treatment in CORD21-P1. By contrast, CORD21-P2 responded to the drug by accumulating LC3-II consistent with lysosomal blockage by bafilomycin. This suggests that a basal level of macroautophagy is active in the CORD21-P2 ROs. The discrepancy between the two patients could be attributed to the presence of some functional DRAM2 protein in CORD21-P2 unlike in the CORD21-P1 ROs which completely lack DRAM2 protein. A study by Yoon *et al*. (2012) demonstrated that transient overexpression of DRAM2 in HEK293 and H1299 cells resulted in the accumulation of endogenous LC3-II as well as degradative autophagic vesicles. Moreover,

the silencing of *DRAM2* attenuated autophagy induction by LC3-II conversion. This reinforces the notion of DRAM2 as a positive regulator of autophagy (Yoon *et al.*, 2012). Altogether, our data provides evidence that DRAM2 is required for the conversion of LC3-I to LC3-II during autophagy initiation.

A key finding upon TEM examination of patient ROs was the accumulation of electron dense lysosome residual bodies with granular cargo. These appear reminiscent of granular osmiophilic deposits (GROD) (Haltia;Rapola and Santavuori, 1973; Lewandowska *et al.*, 2011). Such ultrastructural findings are common in Neuronal Ceroid Lipofuscinoses (NCL) and are broadly characterised as lipopigments. NCL are a group of lysosomal storage disorders (*CLN1-14* genes, *CLN* – ceroid lipofuscinosis, neuronal) associated with the loss of neurons in the brain and retina (Anderson;Goebel and Simonati, 2013). Post-mortem neuropathology analysis uncovered that cortical neuronal loss originates from dendrites and is followed by the pervasive activation of microglia and gliosis (Anderson;Goebel and Simonati, 2013). In the retina, degeneration begins in the outer nuclear layer and proceeds towards the retinal ganglion cells. Retinal degeneration is particularly prominent in *CLN1* (PPT1) and *CLN3* but also characteristic of *CLN5-7*- related deficiency (Santavuori *et al.*, 1993; Santavuori *et al.*, 2000; Sharifi *et al.*, 2010; Badilla-Porras *et al.*, 2022). A significant number of *CLN* genes encode proteins overseeing the delivery of lysosomal enzymes by means of membrane trafficking and ER-Golgi transport (Anderson;Goebel and Simonati, 2013). Histologically, lipopigments resemble age-related lipofuscin but can be seen as distinct structures on ultrastructural analysis (Gilissen and Staneva-Dobrovski, 2013). In recent years, NCL deposits have also been identified by immunohistology and TEM in cells outside of the central nervous system i.e., in rectal ganglion cells, skeletal muscle and lymphocytes (Anderson;Goebel and Simonati, 2013). Their contents likely relate to a mixture of undigested lipid and protein. Further histological analysis suggested that lipopigment deposits include sphingolipid activator proteins (SAPs), mitochondrial ATP synthase (SCMAS) and amyloid precursor/beta-A4 amyloid (Wisniewski *et al.*, 1985; Anderson;Goebel and Simonati, 2013).

The lipopigments described here are also similar to the granular electron dense inclusions present in Mucopolysaccharidosis type III A (deficiency in the heparan N-sulfatase enzyme) (Wisniewski *et al.*, 1985). Further resemblance can be found with curvilinear profiles

reported in hydroxychloroquine intoxication (Costa *et al.*, 2013) and α-galactosidase deficiency in Fabry's disease. The latter condition manifests as the cellular inability to breakdown glycoproteins and glycolipids (Fischer;Moore and Lager, 2006). In summary, the deposits identified on TEM in our patient ROs comprise a mixture of the GROD lipopigments seen in *CLN1* and *CLN10* deficiency, as well as the less electron dense curvilinear profiles (CVPs) associated with other NCL pathologies. To unite our TEM findings under a common umbrella term we have referred to them as 'curvilinear lipopigments' (CLs). Although CLs were significantly upregulated in patient d220 ROs, the DRAM2-deficient CORD21-P1, exhibited a greater degree of granulation, consistent with a more severe disease progression in this patient.

Analysis of d220 retinal samples by TEM also showed increased mitochondrial form factor for CORD21-P1 organoids relative to isogenic control, which is representative of a higher level of mitochondrial branching. Interestingly, no changes were observed for mitochondrial numbers per cell. Dynamic mitochondrial branching in CORD21-P1 PRs was not reflected in any alterations of mitochondrial shape as per mean aspect ratio. Mitochondrial elongation has previously been reported in ROs exposed to high-risk AMD RPE extracellular vesicles and could signify early stages of oxidative stress (Kurzawa-Akanbi *et al.*, 2022). An oxidative burden may be rectified by increased mitochondrial remodelling as a means of avoiding apoptotic death (Jahani-Asl *et al.*, 2007). The current TEM experiment relied on two-dimensional images which provided insufficient visual input through the entirety of PR cell bodies/inner segments. Future experimental work could focus on a combined three-dimensional EM approach coupled with a COX histochemistry to assess subtle changes in mitochondrial shape and fission (Faitg *et al.*, 2020).

4.11.4 DRAM2 may oversee the trafficking of multiple lysosomal enzymes and lipid membrane dynamics.

Differential proteomics analysis revealed 101 commonly changed proteins between both patients (Appendix C). Out the 101, 19 followed the same pattern of expression. Three significantly downregulated proteins of particular interest were CTSD, PPT1 and NPC2. Metascape enrichment analysis (n=19) further revealed vesicle-mediated response, protein processing in endoplasmic reticulum, cellular responses to stress, visual perception, negative

regulation of cellular component organisation, cellular homeostasis and the cone pathway as affected biological processes in the patient samples.

4.11.4.1 CTSD deficiency could be a major roadblock to lysosomal function.

A significant decrease of CTSD in DRAM2 patient ROs was an early key finding by proteomics and WB. The significant deficiency of CTSD was further corroborated by the reduced enzymatic activity in both patients as inferred by a kinetic enzyme activity assay. These data suggest that DRAM2 retinal dystrophy resembles a lysosomal storage disorder with prevalent accumulation of undigested granular osmiophilic material, reminiscent of NCL (Siintola *et al.*, 2006; Steinfeld *et al.*, 2006; Fritchie *et al.*, 2009; Hersheson *et al.*, 2014). NCLs are a heterogenous group of disorders, characterized by deficiencies in *CLN1-14* genes relevant to lysosomal function. *CLN1*, *-2*, *-5*, *-10*, *-11* and *-13* code for luminal lysosomal enzymes, *CLN6* and *-8* for proteins localising to membranes of the ER, *CLN8* for proteins of the ER-Golgi and *CLN3*, *-7*, *-12* for proteins found at lysosomal membranes (Bartsch and Storch, 2022).

Loss-of-function mutations in CTSD protein manifest as postnatal fatal *CLN10* NCL affecting neuromotor development and vision (Williams and Mole, 2012; Schulz *et al.*, 2013). *CLN10* disease is the most severe form of NCL. Clinical presentation includes brain size abnormalities, seizures, and respiratory difficulties (Siintola *et al.*, 2006; Fritchie *et al.*, 2009; Varvagiannis *et al.*, 2018). Only a few cases of *CLN10* deficiency with juvenile manifestation have been reported so far (Steinfeld *et al.*, 2006; Hersheson *et al.*, 2014; Doccini *et al.*, 2016). These patients present with ataxia, steady cognitive decline, retinopathy, and abnormal muscle tissue. Diagnosis may be particularly challenging due to a high clinical overlap with mitochondrial and neurodegenerative disease, accumulation of iron and lipid in various disorders (Hersheson *et al.*, 2014). Two of the patients also suffered from cardiomyopathy (Hersheson *et al.*, 2014; Doccini *et al.*, 2016). Due to the severity of the congenital disease, studies on CTSD deficiency have been mostly limited to murine models (Zhou *et al.*, 2015; Bassal *et al.*, 2021).

Akin to the human disease development, the disease phenotype in animal models depends on the amount of residual CTSD activity (Saftig *et al.*, 1995; Tyynela *et al.*, 2001; Rakoczy *et al.*, 2002; Awano *et al.*, 2006). Mice deficient in CTSD exhibit rapid progression of neurological symptoms marked by the increase in saposin D and mitochondrial ATP synthase

subunit c as well as the presence of GROD deposits (Bassal *et al.*, 2021). These mice recapitulate many features of CTSD disease including retinal degeneration followed by death after 4 weeks of postnatal development. Early loss of cones preceded the decline of rod PRs, gliosis and the extensive demise of secondary and tertiary neurons (Bassal *et al.*, 2021). Importantly, GROD accumulation was one of the earliest features of the disease, initially localising to the inner retina and then spreading out to photoreceptor cells. The loss of PRs early on during the disease progression is also seen with other forms of NCL and likely suggests that these cells are particularly susceptible to cell death in lysosomal storage disorders (Schmitz *et al.*, 2006; Mirza *et al.*, 2013; Jankowiak *et al.*, 2016; Leinonen *et al.*, 2017). CTSD-associated retinal phenotype in murine models has been successfully improved by using compounds with an anti-inflammatory mode of action - fingolimod, teriflumonide, minocycline, curcumin or docosahexaenoic acid (Groh *et al.*, 2013; Mirza *et al.*, 2013; Groh *et al.*, 2016; Groh;Berve and Martini, 2017; Dannhausen;Mohle and Langmann, 2018).

CTSD is one of the main degradative enzymes native to the lysosome. It is an aspartic protease which is indispensable for cellular degradation and is critical for the maintenance of homeostatic processes. The ubiquitously expressed enzyme is involved in the clearance of disease-associated proteins such as α-synuclein (a-syn), amyloid precursor protein (APP) and tau, hence variants in this gene are commonly associated with Alzheimer's and Parkinson's disease (Bunk *et al.*, 2021). Recent success with adeno-associated virus (AAV) therapy has enabled the rectification of CTSD proteolytic function and a significant increase in the life span of $CTSD^{-/-}$ mice (Shevtsova *et al.*, 2010; Pike *et al.*, 2011). These studies have demonstrated that ceroid accumulation and microglia activation are not lethal and can be tolerated provided that enzymatic activity is restored (Shevtsova *et al.*, 2010; Pike *et al.*, 2011). An enzyme replacement therapy using pro-CTSD has also been shown to prolong the longevity of mice, by reducing the accumulation of lysosomal storage material (Marques *et al.*, 2020). A recent study corroborated that gene replacement is superior to the use of recombinant protein as it yields higher levels of enzymatic activity and can attenuate CSTD disease progression (Liu *et al.*, 2022; Bartsch and Storch, 2022).

Based on our results, DRAM2 deficiency recapitulates the retinal phenotype of *CLN10* lipofuscinosis. This is explained by the reduced CTSD activity in both patients, the lack of

autophagic flux in CORD21-P1 and the early presentation of GROD by TEM (Bassal *et al.*, 2021). The early loss of cones in *CLN10* disease in mice (Bassal *et al.*, 2021) is also consistent with the disease progression of most of the clinical cases of DRAM2 dystrophy (El-Asrag *et al.*, 2015; Sergouniotis *et al.*, 2015; Abad-Morales *et al.*, 2019; Bassal *et al.*, 2021). The visual impairment is in line with reduced CTSD activity being sufficient to sustain cellular activities but leading to retinal decline over time. Future work may benefit from CTSD and/or DRAM2 AAV treatment to alleviate the observed CTSD deficiency in patient ROs.

4.11.4.2 NPC2 lysosomal deficiency might be attributed to a trafficking defect resulting in extracellular secretion.

Analysis by proteomics and WB revealed a significant downregulation of NPC2 in d220 organoids. Further analysis by WB demonstrated that NPC2 lysosomal deficiency may be due to protein secretion to the extracellular media. Unlike CTSD, which is indispensable for cellular homeostasis, and has evolved multiple ways of delivery (via CI-M6PR as well as sortilin receptors etc.) (Saftig and Klumperman, 2009), NPC2 may be more limited by the way of lysosomal entry (Wei *et al.*, 2017).

NPC2 is a lysosomal lumen protein which functions alongside NPC1 in the removal of cholesterol from lysosomes (Infante *et al.*, 2008). It sequesters free cholesterol and delivers it to NPC1 to be integrated into the lysosomal glycocalyx (Infante *et al.*, 2008; Kwon *et al.*, 2009; Wang *et al.*, 2021). Structural elucidation of NPC1 indicated that a low lysosomal pH is critical for NPC1 and -2 to carry out their concerted action (Qian *et al.*, 2020).

Niemann-Pick disease type C (NPC) is as a cholesterol and sphingolipid storage disorder with severe implications for cognitive, liver and spleen function (Ribeiro *et al.*, 2001; Park *et al.*, 2003; Vanier and Millat, 2003; Pentchev, 2004; Chang *et al.*, 2005; Evans and Hendriksz, 2017). NPC1 and -2 fibroblast mutant cells accrue significant amounts of unesterified cholesterol in their lysosomal compartments (Steinberg;Mondal and Fensom, 1996; Vanier *et al.*, 1996). Reduced sterol trafficking to the ER leads to the induction of cholesterol uptake and biosynthesis by sterol regulatory element-binding proteins (SREBPs) (Brown and Goldstein, 1999). Disease phenotype is thus attributed to the inability of NPC mutants to downregulate cholesterol biosynthesis through the generation of oxysterols (Frolov *et al.*, 2003). The latter are potent activators of an LXR- cholesterol negative feedback

loops and master regulators of sterol homeostasis (Willy *et al.*, 1995; Fu *et al.*, 2001). Since cholesterol is an indispensable component of the membrane phospholipid bilayers, its aberrant distribution across the cell is likely to perturb the dynamics of membrane trafficking (Puri *et al.*, 1999; Radhakrishnan *et al.*, 2008). Hence, the failed egress of cholesterol from the lysosomes could lead to membrane trafficking defects (Brogden *et al.*, 2020), further exacerbated by the upregulation of cholesterol synthesis (Frolov *et al.*, 2003).

In addition to the primary deposition of cholesterol, NPC patients also exhibit a secondary accumulation of sphingomyelin in their lysosomes (Vanier, 1983; Sandhoff and Sandhoff, 2018; Breiden and Sandhoff, 2019b). The concerted sequestration of lipid by NPC1 and -2 from intraluminal vesicles (ILVs) enables the degradation of sphingolipids, phospholipids and ganglioside glycosphingolipids (Piret *et al.*, 2005; Abdul-Hammed *et al.*, 2010; Wang *et al.*, 2010; Oninla *et al.*, 2014; Anheuser *et al.*, 2015; Breiden and Sandhoff, 2019a). Considering the NPC2 requirement for sphingolipid metabolism, it is not surprising that ganglioside (GM3 and GM2), glucosylceramide and lactosylceramide are seen to accumulate in NPC-deficient brains (Vanier, 1999). These literature reports align nicely with the accumulation of GM3 ganglioside glycosphingolipid and ceramide sphingolipid species in patient CORD21 ROs. The ganglioside and ceramide findings have also been associated with beta-amyloid brain plaques (Kaya *et al.*, 2017) as well as the formation of neurofibrillary tangles, which are the pathological hallmarks of Alzheimer's disease. There further exists a strong correlation between altered ceramide metabolism and heterozygous NPC mutations and Parkinson's (Saito *et al.*, 2004; Lloyd-Evans *et al.*, 2008; Newton *et al.*, 2017; Newton;Milstien and Spiegel, 2018). These data suggest that the putative sphingolipid degradation defect associated with NPC2 deficiency in our patients may share common pathology with other prevalent neurodegenerative conditions.

As the NPC2 lysosomal deficiency in CORD21 ROs likely arises due to misrouting to the extracellular media, current efforts were directed at dissecting the putative mechanisms of NPC2 transport. A recent publication from 2017 (Wei *et al.*, 2017) afforded key insight into the mechanisms of lysosomal NPC2 delivery. The study implicated the Golgi-associated retrograde protein (GARP) complex in the lysosomal sorting of NPC2. The function of GARP has been linked to the sorting of lysosomal enzymes (Figure 39) as well as the anterograde

transport and the secretion of glycosylphosphatidylinositol (GPI)-anchored and transmembrane proteins (Perez-Victoria;Mardones and Bonifacino, 2008; Hirata *et al.*, 2015). Deficiency in GARP has been shown to closely mimic NPC cholesterol phenotype *in vitro* (Perez-Victoria and Bonifacino, 2009; Wei *et al.*, 2017). *Wobbler* mice, which carry a point mutation in *VPS54* of GARP, exhibit a profound defect in protein missorting, characterised by the retention of lysosomal hydrolases at the Golgi in embryonic fibroblasts and spinal cords (Moser;Bigini and Schmitt-John, 2013; Petit *et al.*, 2020).

NPC2 is known to be delivered to the lysosome by CI-M6PR and CD-M6PR receptors (Willenborg *et al.*, 2005). Depletion of the GARP complex would attenuate the retrieval of M6PR receptors to the trans-Golgi network (TGN) and affect the lysosomal distribution of NPC2. Although CI-M6PR and CD-M6PR both facilitate the lysosomal transport of NPC2 (Willenborg *et al.*, 2005), the knockdown of CI-M6PR suffices to redirect NPC2 to the extracellular media (Wei *et al.*, 2017). Furthermore, knockdown of VPS53 but not other GARP proteins, led to the extracellular release of NPC2 and CTSD (Wei *et al.*, 2017). Wei *et*

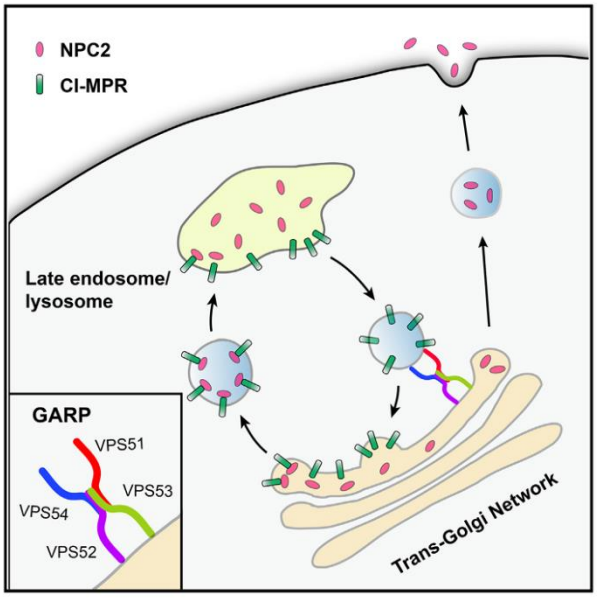

Figure 39. Golgi-associated retrograde protein (GARP) complex regulates NPC2-mediated cholesterol egress from lysosomes. GARP retrieves CI-M6PR receptors from the late endosomes (LE) and lysosomes. Absence of GARP leads to the retention of NPC2 at the TGN, the failed recycling of CI-M6PRs and cholesterol accumulation in the lysosome. Retention of NPC2 at the TGN could subsequently lead to its extracellular secretion. Image taken from Wei *et al.* (2017).

al., (2017) revealed further deficiency in the PSAP and β-hexosaminidase enzymes providing more evidence in favour of a sphingolipid degradation defect in the absence of NPC2 (Piret *et al.*, 2005; Abdul-Hammed *et al.*, 2010; Wang *et al.*, 2010; Oninla *et al.*, 2014; Anheuser *et al.*, 2015). These literature reports are in line with the VPS53 deficiency in CORD21-P2 and provide a potential mechanistic link between a putative GARP dysfunction and the NPC2 media secretion in patient samples. A potential sorting defect caused by *DRAM2* mutations could therefore impede GARP-mediated lysosomal delivery. Future work may explore any conformational or mass changes in GARP by native SDS-PAGE. This would allow us to gain a more comprehensive insight into a potential inactivation of the complex which may be common to both patients.

ARF6 is another protein that has been implicated in the lysosomal targeting of NPC2. ARF6 links the function of GARP and the endosome-associated recycling protein (EARP) complexes (Ibuchi *et al.*, 2020). EARP shares VPS51, VPS52 and VPS53 subunits with GARP (Liewen *et al.*, 2005), therefore VPS53 downregulation in CORD21-P2 may entail a combined GARP-EARP dysfunction.

Further links to the regulation of M6PR trafficking have been demonstrated in light of the recent LYSET (Lysosomal Enzyme Trafficking Factor) discovery during a CRISPR screen. LYSET was shown to be a key component of the M6P-tagging pathway (Figure 40). The novel protein enables the addition of a mannose-6-phosphate on lysosomal enzymes by retaining the GlcNAc-1-phosphotransferase at the Golgi. Indeed, abrogation of the LYSET protein, leads to a lysosomal storage-like phenotype associated with the deficiency of numerous lysosomal enzymes including TPP1, PPT1, CTSD, NPC2, MAN2B1. Another recent paper, further demonstrated that PPT1, NPC2 and MAN2B1 are amongst the secreted lysosomal luminal proteins in human LYSET knockout MEF cells (Richards *et al.*, 2022). This stands in a strong agreement with our findings and could indicate a potential role for DRAM2 in regulating M6P trafficking via LYSET (Pechincha *et al.*, 2022; Richards *et al.*, 2022; Zhang *et al.*, 2022). Future work may assess the expression of LYSET in patient CORD21 ROs by both IF and WB.

Moreover, enhanced secretion of NPC2 and CTSD has been reported in BORC, ARL8 or HOPS knockout cells (Anderson;Walker and Pu, 2022). Depletion of the BORC-ARL8-HOPS complex led to cholesterol accumulation and the increased degradation of CI-M6PR receptors

(Anderson;Walker and Pu, 2022). The aforementioned complex is involved in endolysosomal maturation and fusion. When defective, this could impede CI-M6PR endosome recycling and the delivery of luminal lysosomal enzymes (Anderson;Walker and Pu, 2022).

Last but not least, NPC2 transport has also been shown to rely on the clathrin AP-1 and AP-3 adaptor proteins which regulate M6PR transport along endocytic and secretory pathways (Berger *et al.*, 2007). This is very much in line with our WB data showing AP-1 downregulation in CORD21-P1 ROs, and would support a hypothetical scenario whereby CI-M6PR delivery to the late endosome by AP-1 is reduced. Furthermore, clathrin adaptor AP-3 has been shown to interact with HOPS-specific factor VPS41 for cargo tethering at the lysosome (Schoppe *et al.*, 2020). Defective lysosomal targeting by AP-3 could also impact NPC2 delivery by creating a lysosomal delivery bottleneck. Future studies may benefit from establishing the precise location of DRAM2 within the endolysosomal system based on the co-expression with the novel ARL8 marker, which is lysosome-specific and can be used to distinguish between late endosomes and lysosomes (Schleinitz *et al.*, 2023).

Considering all of the above, NPC2 deficiency is strongly suggestive of a lysosomal targeting defect, which negatively impacts lipid degradation. As demonstrated by links to exisiting literature, the pathology of NPC2 deficiency bears strong resemblance to other common neurodegenerative conditions with regards to alterations in sphingolipid and glycosphingolipid metabolism. An underlying DRAM2/NPC2 deficiency could entail the inability to successfully recycle CI-M6PRs as suggested by the multiple lines of evidence. The delivery of NPC2 could be affected by the reduced M6PR- trafficking by GARP, LYSET, BORC/ARL8/HOPS, AP-1 or AP-3 (Figure 41). GARP dysfunction could impede the lysosomal targeting of NPC2 by failing to recycle CI-M6PRs to the TGN. Compromised M6PR trafficking of NPC2 could also arise due to a LYSET or a HOPS-related dysfunction at the TGN and/or the lysosome, respectively. Furthermore, NPC2 transport has also been shown to rely on the clathrin AP-1 and AP-3 adaptor proteins which enable M6PR transport to the endosome and the lysosome (Berger *et al.*, 2007). It would be of interest to determine the overall levels of different vesicular complexes and whether they associate with their respective cellular components in patient ROs. Further work on the expression of DRAM2 within vesicular pathways will shed more light onto the role of DRAM2 in NPC2 transport.

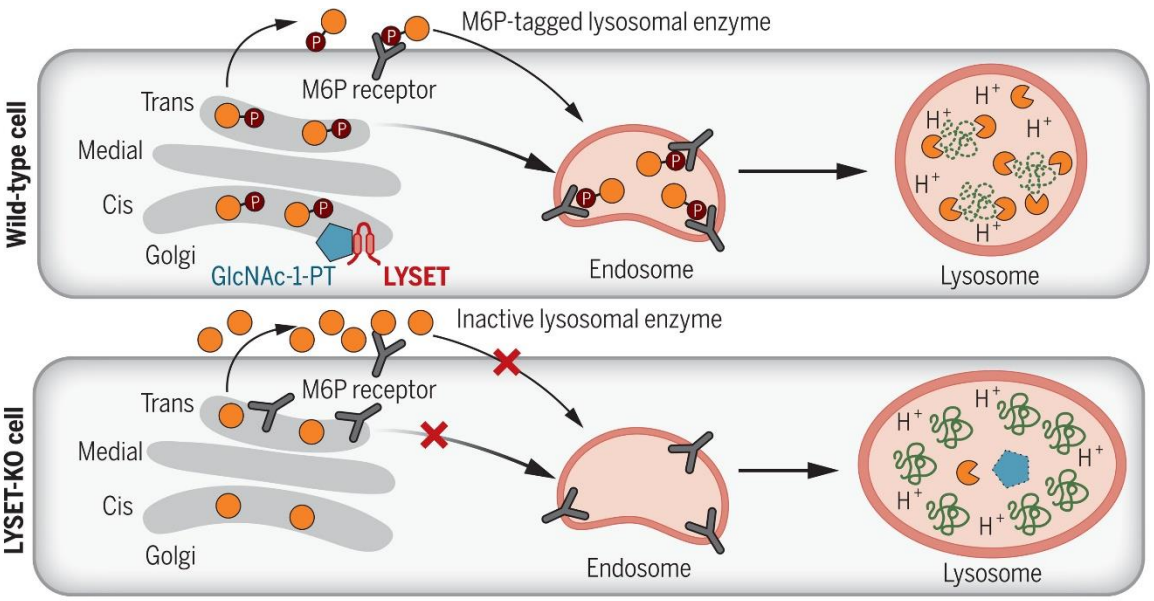

Figure 40 LYSET plays an important role in the M6P-tagging of lysosomal enzymes. Schematic taken from Richards *et al*. (2022) shows that in LYSET-KO cells, GlcNAc-1-phosphotransferase (GlcNAc-1-PT) is not retained at the Golgi, resulting in improper M6P-tagging of hydrolases targeted for lysosomal delivery. Instead hydrolases are secreted to the extracellular media leading to the accumulation of undegraded waste in the lysosomes.

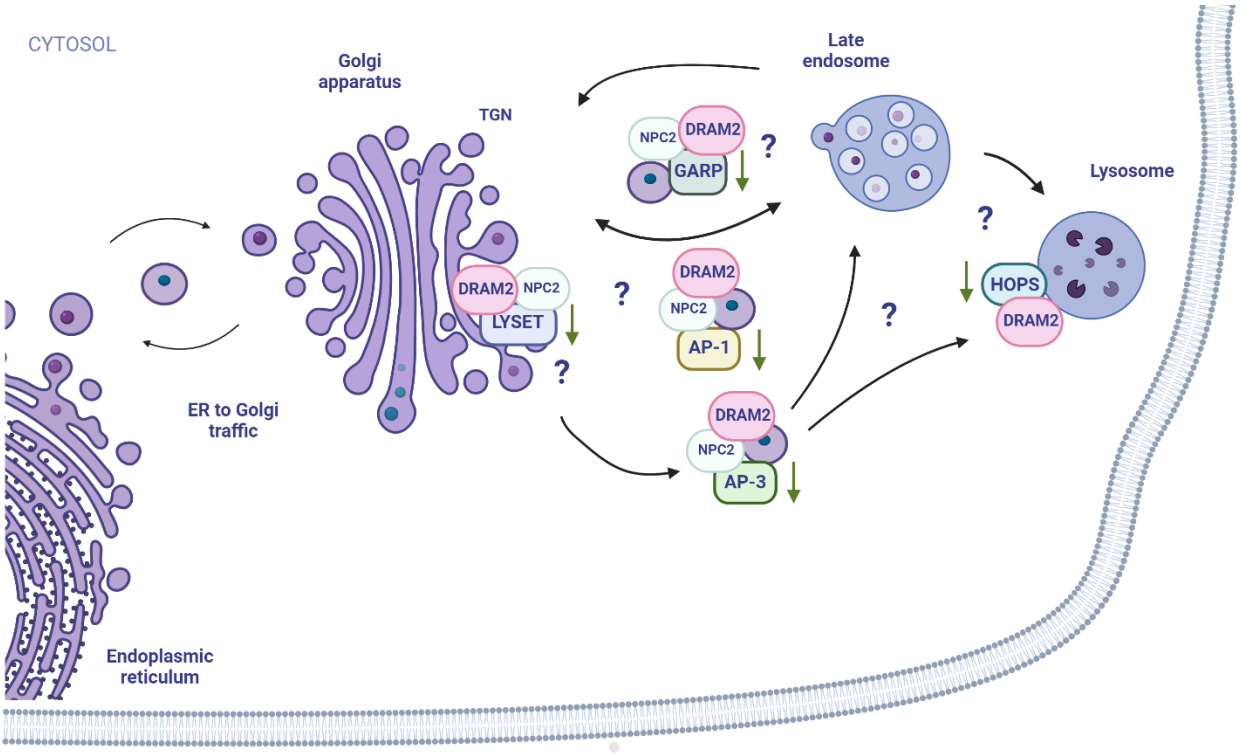

Figure 41. Schematic depicts putative intracellular transport mechanisms which could affect the lysosomal targeting of NPC2 in patient d220 ROs. Illustration shows that DRAM2 may enable the lysosomal delivery of NPC2 by interacting with any of the shown proteins. NPC2 deficiency could arise due to the unsuccessful retrieval of CI-M6PRs from LE at the TGN by the GARP complex. NPC2 transport could additionally be compromised by the defective M6P-tagging of lysosomal enzymes mediated by LYSET at the TGN. Stalling of AP-1 mediated trafficking to the LE or AP-3 to the LE/Lysosome may also impact NPC2 delivery. The lack of HOPS at the lysosome could affect both cargo delivery from incoming AP-3 vesicles as well as LE-lysosomal fusion. The downregulation of proteins likely to affect NPC2 transport is denoted by green arrows. Image was generated using Biorender.

4.11.4.3 PPT1 lysosomal deficiency and extracellular secretion might be due to vesicular mistrafficking.

Similar to NPC2, PPT1 lysosomal deficiency could be attributed to extracellular secretion in patient ROs. Although PPT1 displays ubiqutous expression, it exhibits significant enzymatic activity in the brain and, more specifically, in the retina (Chattopadhyay and Pearce, 2000; Dearborn *et al.*, 2016).

Palmitoyl-protein thioesterase 1 (PPT1) is a soluble protein, which enables the lysosomal breakdown of lipidated proteins by eliminating thioester-linked fatty acyl moieties from cysteines. Previous reports have associated the function of the protein with the regulation of synaptic vesicle transport, vesicular trafficking and sphingolipid metabolism (Kollmann *et al.*, 2013; Carcel-Trullols;Kovacs and Pearce, 2015; Johnson *et al.*, 2019). PPT1 is encoded by *CLN1*, and mutations in this gene are associated with infantile Neuronal Ceroid Lipofuscinosis (INCL) otherwise knowns as Batten disease. Batten disease is a particularly severe neurological condition characterised by an average life expectancy of about 10 years, early-onset brain atrophy, visual impairment and the loss of motor function (Santavuori *et al.*, 1973; Weleber, 1998; Weleber *et al.*, 2004; Jalanko and Braulke, 2009). A more benign clinical presentation has also been described in adult onset *CLN1* deficiency, whereby afflicted individuals exhibit normal life expectancy (Mazzei *et al.*, 2002; Kalviainen *et al.*, 2007; Ramadan *et al.*, 2007). Visual decline in the classical form of Batten disease usually manifests within the first two years of life and presents as one of the earliest signs of *CLN1* disease (Santavuori, 1988). Visual impairment is marked by the accumulation of autofluorescent ceroid storage material in the retina, the loss of PR cells and shortening of their outer segments, dysfunctional second order neurons and retinal ganglion cells (Weleber *et al.*, 2004). A PPT1 mouse knockout model presented with strong immunoreactivity of saposin D in the inner nuclear layer of the retina, GROD accumulation in microglia cells and upregulation of gliosis marker GFAP in Müller glia. Immunohistochemistry showed a more significant reduction in cones and cone-related PR cell types as compared to rods, the death of interneurons as well as retinal ganglion cells, which closely recapitulates the PPT1 disease progression in humans (Atiskova *et al.*, 2019).

A recent study has demonstrated that decreased S-palmitoylation of NFATC4 in *CLN1*$^{-/-}$ mice impaired lysosomal Ca^{++} dynamics, which could secondarily affect the activity of Ca^{++}-dependent lysosomal hydrolases (Mondal *et al.*, 2022). More recently, it has been shown that *CLN-1* deficiency in fibroblasts is associated with an anterograde ER-to-Golgi transport malfunction. This led to the aggregation of COPII vesicle proteins at the ER and the induction of an unfolded protein response (UPR). An accompanying secretion of S-palmoylated COPII proteins through the plasma membrane (PM) informed on an underlying ER-to-Golgi vesicular trafficking defect (Plavelil, 2023). The same group also recently outlined a role for PPT1 in the

delivery of V0a1 ATPase to lysosomes. The authors of the study propose that co-localisation of V0a1 and PPT1 at vesicular membranes facilitates the depalmitoylation of V0a1 and its subsequent targeting to the lysosome via AP-3 (Bagh *et al.*, 2017) (Figure 42). The disrupted V0a1 lysosomal localisation correlated with elevated lysosomal pH and the higher abundance of V0a1 at the PM in *CLN1*$^{-/-}$ mice due to increased interaction with AP-2 (Bagh *et al.*, 2017). Altered lysosomal pH underlies many lysosomal storage disorders (Hu *et al.*, 2015) and would secondarily affect the maturation of crucial lysosomal enzymes such as CTSD in infantile and congential forms of NCL (Chandra *et al.*, 2015). Hence, the significant downregulation of PPT1 in DRAM2 ROs could be associated with the extracellular release of both V0a1 and PPT-1 due to vesicular mistrafficking (Figure 42). As a result, improprerly acidified lysosomes would fail to provide a suitable environment for the maturation of degradative hydrolases in patient CORD21 ROs. Rectifying lysosomal acidification by using the thioesterase mimetic NtBuHA (Bagh *et al.*, 2017) or acidic nanoparticles (Bourdenx *et al.*, 2016) may hold promise in restoring lysosomal function in PPT1 deficiency. AAV2 treatment has also been shown to ameliorate the visual decline but not to prevent the progression of the disease in the brains of in PPT1-deficient mice suggesting that further targeted therapies may be needed (Griffey *et al.*, 2005).

In summary, the combined DRAM2/PPT1 deficiency aligns with the visual impairment and ceroid accumulation in childhood and adult forms of *CLN1* (PPT1) disease. The accumulation of CLs in our patient ROs bears strong resemblance to the curvilinear profiles reported in *CLN1* deficiency and the GROD deposits seen in *CLN1*$^{-/-}$ mice. A predominant cone phenotype is in agreement with the *CLN1*$^{-/-}$ disease progression in mice and humans as macular decline is the primary insult of DRAM2 retinal dystrophy. DRAM2/PPT1 phenotype could be associated with a PM trafficking issue common to both V0a1 and PPT1 resulting in an elevated lysosomal pH (Figure 42). The failed transport activities of PPT1 would secondarily affect lysosomal acidification and Ca^{++} homeostasis, compromising the function of hydrolases relying on acidic pH and calcium abundance. As shown by links to existing literature, the PPT1-associated trafficking defect could be related to an ER-Golgi bottleneck and more specifically to a role for PPT1 in regulating COPII-vesicle budding (Plavelil, 2023). PPT1-mediated traffic could also be relevant to the lysosomal targeting of ER-calcium transporter IP3R1 (Mondal *et al.*, 2022). An ER-to-Golgi transport function is consistent with the multiple extralysosomal

locations reported for PPT1 i.e. the ER, Golgi, membrane rafts, synaptic vesicles as well as the extracellular millieu (Kollmann *et al.*, 2013; Segal-Salto;Sapir and Reiner, 2016; Segal-Salto *et al.*, 2017; Sapir *et al.*, 2019) but also the co-localisation of DRAM2 with cis-Golgi marker GM130 observed in our study. An underlying DRAM2/PPT1 deficiency could thus share functional overlap with the aforementioned vesicular pathways. Future work may interrogate the status of lysosomal pH in CORD21 ROs and outline the precise role of DRAM2 in facilitating PPT1-mediated transport activities.

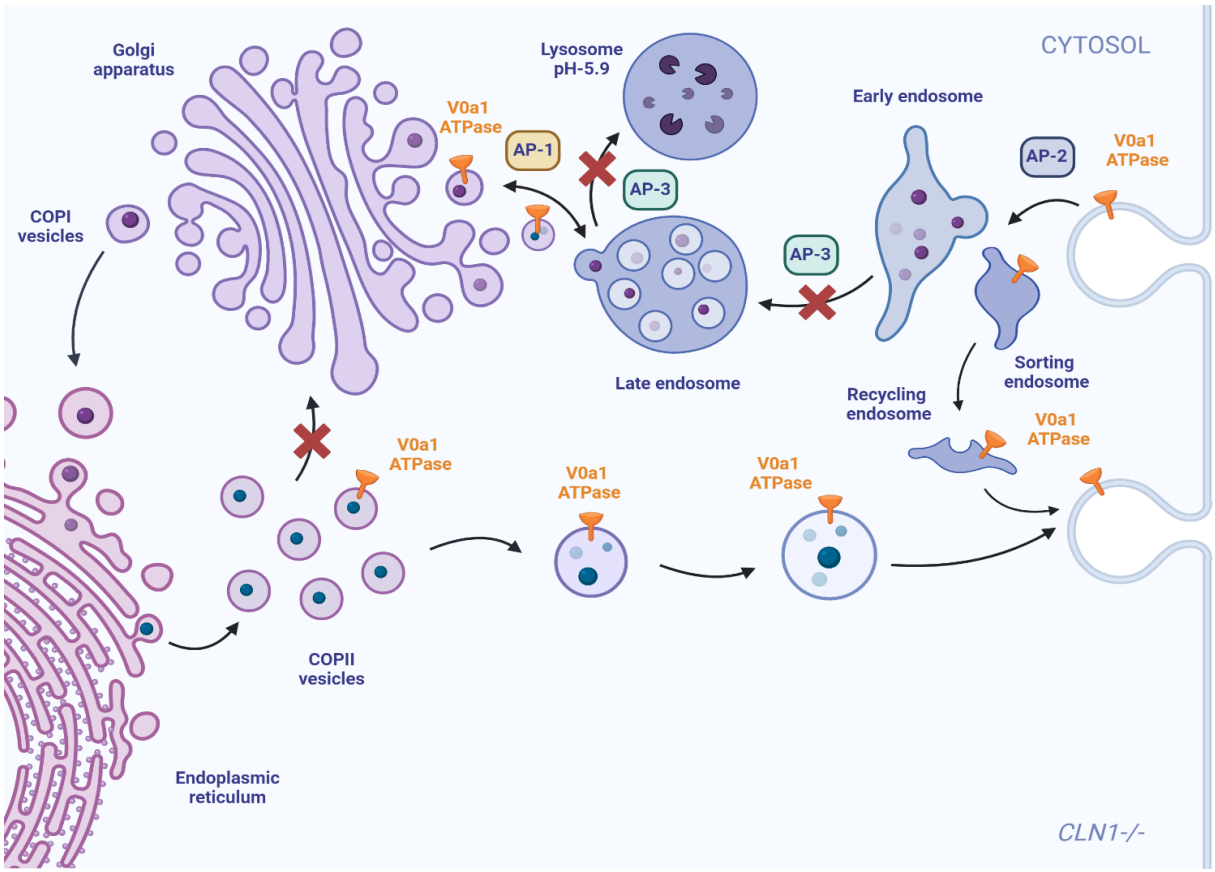

Figure 42. Schematic shows intracellular transport defects associated with PPT1 deficiency. In the absence of PPT1 (*CLN1*$^{-/-}$), ER stress accumulates in the form of COPII vesicles, which instead of arriving at the Golgi, are being rerouted for extracellular release throμgh the PM (Plavelil, 2023). In the absence of PPT1, V0a1 ATPase is not depalmitoylated at vesicular membranes, therefore an interaction of V0a1 ATPase with AP-2 favoured, leading to V0a1 ATPase secretion. A higher affinity of V0a1 ATPase for AP-2 results in the failure of V0a1 ATPase to be delivered to the late endosome (LE)/lysosome via AP-3. At the lysosome V0a1 ATPase plays a crucial role in lysosomal acidification. The lack of PPT1 expression hence leads to elevated lysosomal pH and to the improper maturation of lysosomal hydrolases. Image was generated using Biorender.

4.11.4.4 Defective membrane trafficking in DRAM2 ROs associates with changes in LAMP2, LIMP2, GBA, CD63, VPS53 and AP-1γ RO expression.

In agreement with the pronounced CTSD, NPC2 and PPT1 lysosomal depletion, extensive WB screening was conducted for endolysosomal and transport markers. In general, the different patterns of protein expression detected by WB reflected the different genetic backgrounds of CORD21-P1 and -P2. Whereas CORD21-P1 did not show expression of any DRAM2 protein, some albeit dysfunctional full-length DRAM2 may be present in CORD21-P2.

The results revealed significant glycosylation changes in the late lysosomal marker LAMP2 but not the early one, LAMP1. As previously mentioned, abrogation of the GARP complex can lead to global glycosylation alterations, mistrafficking of Golgi glycosylation enzymes to the lysosome where they can get degraded (Khakurel *et al.*, 2021). Consequently, some DRAM2 is required for the glycosylation of LAMP2 as evident by the hypoglycosylation in CORD21-P1. Conversely, the hyperglycosylation observed in CORD21-P2 may indicate a different mechanism at play. Polylactosamine glycosylation of LAMP2 and other lysosomal membrane proteins facilitates a protective glycocalyx barrier preventing the lysosomal membrane from permeabilizing. Indeed, hyperglycosylation mediates prolonged Golgi LAMP2 transit and reduced lysosome turnover (Nabi and Rodriguez-Boulan, 1993). In the case of CORD21-P2, a small amount of dysfunctional DRAM2 may enable retention of LAMP2 at the Golgi, where a residual level of glycosylation is still taking place.

DRAM2 is a putative transmembrane protein which eventually becomes embedded in the lysosomal membrane. A recent study demonstrated that DRAM2 can physically interact with LAMP2 (Kim *et al.*, 2017). It remains to be established whether the c.131G>A mutation in CORD21-P2 alters the conformation of DRAM2 thereby preventing a viable interaction with LAMP2 at the lysosomal interface. Of note, LAMP2 deficiency has been shown to confer increased susceptibility to cell death in cortical neurons (Law *et al.*, 2016), whereas restoration of protein expression prevents cell death associated with lysosomal membrane permeabilization (LMP) (Cui *et al.*, 2020). It would be of particular interest to examine, whether the hypoglycosylation of LAMP2 in CORD21-P1 can lead to compromised lysosomal integrity. Another study has shown that knocking out LAMP2 in mice significantly accelerated

the formation of basal laminar deposits, further reiterating its role in autophagic clearance in the retina (Notomi *et al.*, 2019).

The downregulation of LIMP2 in patients was corroborated by a reduction in its substrate GBA in CORD21-P2. Despite the lack of GBA change between CORD21-P1 and its isogenic control, a significant decrease in GBA enzymatic acitvity was confirmed for both patients. Furthermore, the complete lack of DRAM2 protein in CORD21-P1 correlated with a stronger depletion of LIMP2. Interestingly, the levels of LIMP2 glycosylation also appeared to depend on the relative DRAM2 abundance in patients. β-Glucocerebrosidase (GBA) is a glucosylceramide and -sphingosine hydrolase shuttled to the lysosome in an M6PR-independent manner. This delivery mechanism involves the LIMP2 receptor. Reduced GBA activity pertains to patients bearing GBA mutations (Alcalay *et al.*, 2015; Rocha *et al.*, 2015; Garcia-Sanz *et al.*, 2017) but has also been observed in the absence of such in sporadic forms of Parkinson's disease (Murphy *et al.*, 2014). Indeed the reduction in GBA activity in idiopathic cases has been attributed to the impaired trafficking of LIMP2 and the subsequent retention of GBA at the ER (Thomas *et al.*, 2021). The ER to Golgi delivery of GBA via LIMP2 is in turn mediated by AP-1 and AP-3 (Honing;Sandoval and von Figura, 1998; Fujita *et al.*, 1999; Reczek *et al.*, 2007; Blanz *et al.*, 2015; Zunke *et al.*, 2016). Interestingly, in LIMP2-deficient mice, GBA is secreted extracellularly (Reczek *et al.*, 2007). Future work may further acknowledge whether similarly to PPT1 and NPC2, GBA deficiency is also attributed to secretion. The downregulation of LIMP2 and GBA activity in both patient ROs hence represents an aspect of sphingolipid deficiency which could be affected by the M6PR trafficking mediated by AP-1 and AP-3.

The tetraspanin and late endosomal marker CD63 was shown to be completely depleted in the CORD21-P1 but not the CORD21-P2 patient. This suggests that DRAM2 expression is indispensible for CD63 expression and function at the late endosome. Interestingly, however, CD63 knockout mice do not show any gross endolysosomal abnormalities (Schroder *et al.*, 2009). More recently it has been shown that as an integral membrane component of extracellular vesicles (EVs), CD63 is not essential for cargo delivery and uptake of EVs (Tognoli *et al.*, 2023). Conversely, however, CD63 has been shown to be required for intraluminal vesicle formation (ILVs) and PMEL sorting via ESCRT-independent

mechanisms. In the absence of CD63, PMEL is instead subjected to ESCRT-dependent sorting and is degraded (van Niel *et al.*, 2011), suggesting impaired PMEL sorting and deleterious implications for melanosome maturation in CORD21 RPE. The significant downregulation of CD63 in DRAM2 RO suggests a putative sorting function of DRAM2 at the late endosome which may affect the balance of ESCRT-dependent and independent endosomal sorting pathways.

As discussed, the inactivation of GARP could affect the trafficking of M6PR proteins and affect lysosomal delivery. Multiple lines of evidence indicate the direct or indirect involvement of GARP in DRAM2 deficiency. This is apparent not just from the downregulation of VPS53 in CORD21-P2 but also the glycosylation changes observed by WB in heavily glycosylated lysosomal receptors (LIMP2 and LAMP2), the deficiency of GARP target NPC2, as well as the global phospholipid changes seen in both of our patients. The absence of consistent VPS53 changes between RO samples, however, should only be taken into consideration following further validation of GARP inactivation by native SDS-PAGE in both patients.

Further to the lack of CTSD changes in extracellular media, a significant depletion of CTSD heavy chain was observed in both patients. The lack of mature heavy chain CTSD is very much in line with PPT1 findings suggesting that the lysosomal environment in CORD21 ROs is not permissive of efficient CTSD maturation (Bagh *et al.*, 2017). Due to the absolute necessity for CTSD to lysosomal homeostasis, the enzyme has likely evolved multiple ways of entering the organelle. Lysosomal targeting via the sortilin receptor represents one such mechanism of targeting diversification (Canuel *et al.*, 2008). Interestingly, sortilin expression is not significantly affected and this could account for the minimum amount of heavy chain CTSD in our patients. Furthermore, the tendency for pro-CTSD reduction in patients and the downregulation in active intermediate in CORD21-P1, suggest that the scarce amount of CTSD present is either immediately being converted to mature CTSD to avert lethality, or is that immature CTSD is being delivered to the lysosome at insufficient levels. It is likely that the data presented here is a combination of both. Furthermore, data here shows no direct impact of *DRAM2* mutations on the expression of early and late endosomal markers rab5 and 7, CTSB, retromer component VPS35, as well as clathrin adaptors AP-2 and -3 in DRAM2 ROs.

Interestingly, despite the prevalent involvement of M6PR receptors in lysosomal targeting, the expression levels of CI-M6PR and CD-M6PR were not affected. This is suggestive of an indirect mechanism which impedes M6PR trafficking. As mentioned previously, aberrant M6PR trafficking in CORD21 ROs could encompass GARP, LYSET, BORC/ARL8/HOPS or the overarching regulators of clathrin transport AP-1 or AP-3. These could exist as distinct but overlapping mechanisms of M6PR regulation.

With regards to this, clathrin adaptors carry out a significant load of the M6PR traffic. Downregulation of AP-1 adaptor protein in the patient lacking any DRAM2 (CORD21-P1) would suggest a requirement for DRAM2 in the assembly of clathrin-coated vesicles at the TGN via AP-1 (Liu *et al.*, 2008). At the TGN AP-1 binds cargo carrying tyrosine YXXØ and dileucine [DE[XXXL]LI] lysosomal motifs (Guo;Sirkis and Schekman, 2014), but AP-1 can also be found at the endosomes where it regulates the retrieval of CI-M6PR back to the TGN. Indeed AP-1 knocksideways approaches, which trap AP-1 protein onto mitochondria, demonstrate the widespread depletion of lysosomal hydrolases, transmembrane receptors and coat accessory proteins upon AP-1 sequestration (Honing *et al.*, 1996; Meyer *et al.*, 2000; Hirst *et al.*, 2004; Hirst *et al.*, 2012). The involvement of both anterograde and retrograde pathways for AP-1 would suggest that DRAM2 is a crucial regulator of bidirectional lysosomal trafficking. Considering its prominent role in PM cargo delivery, a significant AP-1 decrease in CORD21-P1 could enable a negative feedback loop to minimise the secretion of lysosomal hydrolases (Duncan, 2022). In summary, the reduced expression of the key clathrin adaptor AP-1 in CORD21-P1 ROs is consistent with both a TGN cargo trafficking issue and the attempt to downregulate hydrolase secretion from the early endosome.

Notwithstanding the lack of change in AP-3 expression in ROs by WB, the pathways affecting lysosomal targeting appear to be by and large affected in this study. Our IF data shows co-localisation of DRAM2 with AP-1^{+} and even more so with AP-3^{+} vesicles. AP-3 is the main clathrin adaptor regulating delivery to the lysosome (Peden *et al.*, 2004). AP-3 deficiency is associated with Hermansky-Pudlak syndrome, a disorder characterised by ocular albinism and a significant loss of visual acuity (Introne *et al.*, 1993). As previously mentioned, NPC2 and GBA lysosomal delivery depends on both AP-1 and AP-3 (Honing;Sandoval and von Figura, 1998; Fujita *et al.*, 1999; Berger *et al.*, 2007; Reczek *et al.*, 2007; Blanz *et al.*, 2015; Zunke *et*

al., 2016). AP-3, particularly, plays an important role in the fusion of late endosomes and lysosomes by enabling HOPS-mediated tethering at the lysosome (Schoppe *et al.*, 2020). Furthermore, the binding of Golgi-incoming AP-3 vesicles also depends on HOPS (Cabrera *et al.*, 2010). A recent paper on plant vesicular transport postulated that defective AP-3 transport leads to cargo retention at the Golgi (Feng *et al.*, 2017; Gao *et al.*, 2022) and PM secretion (Feng *et al.*, 2017). In addition to HOPS, the authors also outline a requirement for COPII tethers in lysosomal trafficking which may provide further links to ER-to-Golgi transport for DRAM2-mediated transport (Feng *et al.*, 2017). Despite the lack of changes in AP-3 expression by WB in patient ROs, DRAM2 co-localisation with AP-3 in WT ROs provides strong evidence in favour of a DRAM2 role in AP-3 lysosomal targeting. Future work may outline putative mechanisms which may provide a mechanistic understanding of these processes.

4.11.4.5. Disturbed lipid metabolism in DRAM2 patient ROs may lead to photoreceptor toxicity.

Lipids and proteins within cellular membranes undergo constant remodelling to meet the demands of the cellular homeostasis. Data obtained from our lipidomics experiment revealed a significant phospholipid depletion accompanied by the accumulation of ceramide, ganglioside and dolichol lipid species in patient samples. Ceramide accumulation in patients was additionally confirmed by IF in d220 DRAM2 ROs. Interestingly, our patient samples were not consistent with cholesterol accumulation at d220 or ergosterol esters as evident in Frohlich *et al*. paper (2015). This could reflect insufficient time for NPC2 phenotype to develop as DRAM2 disease usually manifests in the third decade of life (El-Asrag *et al.*, 2015; Sergouniotis *et al.*, 2015; Abad-Morales *et al.*, 2019).

As discussed previously, the GARP complex is involved in the retrograde transport of sphingolipids as demonstrated by the gross accumulation of hexosylceramide, ceramide, sphingosine and sphinganine species following VPS53 knockdown in HeLa cells (Frohlich et al., 2015). This study implied that the accumulation of toxic ceramide intermediates occurred at the expense of more complex sphingolipid species in these cells leading to an exacerbated sphingolipid synthesis. Our lipidomics data concur with the accumulation of ceramide and hexosylceramide but also show sphingomyelin accumulation in patient samples. This suggests that lysosomal degradation of complex sphingolipids is likely not associated with early DRAM2

pathology in CORD21 ROs. As mentioned previously, GARP data should be further validated by additional methods.

Consistent with these data, however, GM3 gangliosides and sphingomyelin which are associated with NPC2 deficiency (Locatelli-Hoops *et al.*, 2006; Remmel *et al.*, 2007; Anheuser *et al.*, 2015) are also upregulated in our patient ROs. Indeed, hexosylceramides are precursors for lactosylceramides which enable the synthesis of gangliosides (Simon *et al.*, 2021). The increase in hexosylceramides in patient ROs could be an early indicator of enhanced GM3 accumulation corroborating the glycosphingolipid defect associated with NPC2 disease. Long-chain base sphingolipids such as hexosylceramides also play a role in the lateral organisation of lipid rafts where receptors are abundant (Prinetti *et al.*, 2009). This suggests that aberrant lipid raft signalling could accompany the vesicular trafficking defect seen in CORD21 ROs.

In general, the accumulation of sphingolipids in the lysosome may lead to membrane permeability but can also incur toxicity by inhibiting glycerolipid synthesis (Wu *et al.*, 1993; Contreras *et al.*, 2006), and by causing calcium depletion as well as profound defects in lysosomal trafficking (Lloyd-Evans *et al.*, 2008). Increased levels of ceramide have been shown to be toxic to retinal ganglion cells (Fan *et al.*, 2021), photoreceptor (German *et al.*, 2006; Chen *et al.*, 2013) as well as RPE cells (Levitsky *et al.*, 2020), providing a direct explanation for the retinal toxicity associated with DRAM2 retinal dystrophy.

A recent study in yeast unravelled that some of the earliest events of GARP depletion are exemplified by the loss of proteins involved in phospholipid recycling (Eising;Thiele and Frohlich, 2019). The latter phospholipid flippases are essential to the maintenance of PM phospholipid composition (Nakano *et al.*, 2008; Hachiro *et al.*, 2013), sphingolipid metabolism (Roelants *et al.*, 2010; Hachiro *et al.*, 2013) and GARP function (Takagi *et al.*, 2012). The shift from PM recycling to vacuolar degradation of these flippases suggests compromised PM integrity (Eising;Thiele and Frohlich, 2019). These reports are very much in line with the alterations in phospholipid abundance observed in our lipidomics experiment, showing a severe depletion of a whole range of phospholipids (PE, PS, PC, PI, PG) in patients relative to isogenic controls. This phospholipid deficiency could be related to a similar mechanism of flippase misrouting and degradation in the lysosomes of CORD21 ROs.

An interesting lipidomics finding was the increase of dolichols in CORD21 ROs. Dolichols have been shown to play a key role in rhodopsin glycosylation as the generation of dolichol enables a general template for glycosylation (Kean, 1980). Defects in the dolichol biosynthesis pathway have previously been reported in congenital disorders of glycosylation (Buczkowska;Swiezewska and Lefeber, 2015). Consistent with this, mutations in the dolichol biosynthesis gene *DHDDS* are associated with decreased rhodopsin expression and an aberrant aggregation of ER membranes in *Drosophila melanogaster* (Brandwine *et al.*, 2021). *DHDDS* is required for cells to specifically carry out N-glycosylation which is deemed essential to the proper functioning of the retina (White *et al.*, 2007; Murray;Fliesler and Al-Ubaidi, 2009; Park *et al.*, 2014). Although dolichol-mediated glycosylation is not essential for rhodopsin disc assembly, overall reduction in opsin glycosylation can undermine the ability of PRs to participate in the visual cycle (Kean, 1999). Furthermore, inhibition of dolichol synthesis can impede phagocytosis (Hall *et al.*, 1990) and cause a geographic atrophy-like appearance in RPE cells (DeRamus *et al.*, 2020).

Recently, an increase and shortening in dolichols was also described in the ageing retina (Guan *et al*., 2015). A reduction in dolichol species (dolichol-19 to dolichol 18) has been further detailed in retinitis pigmentosa patients (Wen;Lam and Guan, 2013; Wen *et al.*, 2014) and in studies on the NPC2 interactor NgBR (Park *et al.*, 2014). Although a significant reduction of dolichol species is not seen in this study (Dolichols 19 and 20), the increase of this lipid species in CORD21 ROs could relate to glycosylation changes that could undermine rhodopsin function. Furthermore, dolichol is particularly abundant in ceroid deposits associated with NPC2 deficiency (Seehafer and Pearce, 2006), providing further links for DRAM2 with NPC2 disease. In summary, the abundance of dolichols implies inefficient glycosylation of enzymes key to the visual cycle such as rhodopsin but also the putative depletion of glycosylation enzymes which could be relevant to the overall functioning of the Golgi in our patient ROs.

In summary, lipidomics data provided evidence in favour of a sphingolipid defect in CORD21 ROs as evident by the accumulation of ceramide and GM3 gangliosides. The depletion of phospholipid species suggested compromised PM integrity and a putative mistargeting of phospholipid species. Furthermore, an increase in the level of dolichols

suggested that CORD21 ROs likely also exhibit reduced protein glycosylation with potential repercussions for the function of the photoreceptor marker rhodopsin.

4.12. Concluding remarks

In summary, the work outlined in this chapter provides significant evidence for a lysosomal storage defect in DRAM2 patient ROs. The lysosomal deficiency was marked by the downregulation of key lysosomal enzymes CTSD, NPC2 and PPT1 and the accumulation of lysosomal waste in the form of CLs, which were reminiscent of the GROD deposits reported in PPT1 and CTSD forms of NCLs (*CLN1 and CLN10*). The absence of NPC2 and PPT1 in lysosomes could be explained by enzyme misrouting to the extracellular media. These data were suggestive of aberrant trafficking which could prevent degradative hydrolases from reaching their designated location, the lysosome. Based on scientific literature, depletion of the aforementioned enzymes leads to gross lysosomal abnormalities preventing waste degradation, the unsuccessful cholesterol egress from lysosomes as well as the improper acidification of lysosomes, which renders many lysosomal hydrolases such as CTSD inactive. A combination of protein assays revealed a downregulation in the lysosomal receptor LIMP2 (both patients), the clathrin-adaptor AP-1 (CORD21-P1) and the GARP complex subunit VPS53 (CORD21-P2). These results indicate that DRAM2 deficiency affects various modes of intracellular transport such as anterograde M6PR-lysosomal trafficking, bidirectional AP-1-mediated clathrin transport as well as retrograde trafficking enabled by the GARP complex. Secretion of CTSD, NPC2 and PPT1 provided valuable clues into other intracellular trafficking mechanisms that could be affected. NPC2 deficiency and secretion has previously been reported in LYSET and HOPS mutants which suggests further bottlenecks at the Golgi due to M6PR-lysosomal targeting and one at the lysosome due to the inefficient TGN cargo delivery via AP-3, respectively. Furthermore, PPT1 deficiency informs on a putative ER stress response and rerouting of COPII vesicles to the PM due to an ER-Golgi traffic malfunction. Further work on DRAM2 in patient ROs will outline specific transport mechanisms that are common to both patients.

Chapter 5: Assessment of lysosomal activity in CORD21 Retinal Pigment Epithelial cells

5. Introduction

The pilot study of *DRAM2* mutations in cone-rod dystrophy patients revealed that in addition to being expressed in the IS of photoreceptors (PR), DRAM2 is also present in the apical side of RPE cells in murine retina (El-Asrag *et al.*, 2015). Clinical assessment of DRAM2 patients' retina by fundus retinography and autofluorescence showed disturbances in RPE located in the macula and in the periphery (El-Asrag *et al.*, 2015; Sergouniotis *et al.*, 2015; Abad-Morales *et al.*, 2019; Krasovec *et al.*, 2022). Although in some presymptomatic patients, the optical coherence tomography analysis (OCT) indicated that PR death may occur prior to RPE degeneration, the alternate scenario of a primary RPE defect and secondary PR decline cannot be ruled out (El-Asrag *et al.*, 2015; Sergouniotis *et al.*, 2015). Therefore, this study extended the investigation of *DRAM2* mutations in RPE cells, and the potential mechanisms that could lead to their degeneration.

RO data presented in chapter 4 provided evidence for an inherent lysosomal deficiency caused by a vesicular trafficking defect in patients. IF characterisation of ROs at d220 corroborated the presence of main retinal cell types, but did not show a reduction in either rods or cones. Close to complete loss of DRAM2 expression in CORD21-P1 correlated with the lack of autophagy flux. Furthermore, patients displayed a significant accumulation of CLs reminiscent of *CLN1* and *CLN10* NCL disease. Proteomics and western blot analysis subsequently revealed that the reduced expression of key lysosomal enzymes such as CTSD, PPT1 and NPC2 was a common finding in both CORD21-P1 and -P2 ROs. A cytosolic deficiency was explained by misrouting of the enzymes to the cell culture media, suggesting impairment in the trafficking of these proteins. Lipidomics analysis further showed that the accumulation of ceramide, ganglioside and dolichol, as well as the significant loss of phospholipids, which may exacerbate PR toxicity in ROs. DRAM2 was also shown to be co-expressed with IS mitochondrial marker TOMM2, cis-Golgi protein GM130 as well as the key clathrin adaptors AP-1 and AP-3.

In order to assess the contribution of *DRAM2* mutations to RPE degeneration, RPE cells were differentiated from patient iPSC lines alongside wild-type and isogenic controls. This chapter details the characterisation of DRAM2 RPE by IF, Transepithelial electrical measurement analysis (TEER), analysis of Pigment epithelium-derived factor (PEDF) and

Vascular endothelial growth factor (VEGF) secretion by ELISA, as well as the results of in-depth proteomics and WB analyses. Experimental work carried out in this chapter aimed at establishing whether the pathomechanism of DRAM2 deficiency in RPE cells, analogously to ROs, is due to a lysosomal defect arising from the vesicular mistrafficking of lysosomal enzymes.

5.1 Results

5.1.1 Patient DRAM2 RPE shows aberrant TEER barrier resistance despite expression of ZO-1.

A schematic shown in Figure 43, A outlines the directed differentiation method used to generate RPE cells from iPSC lines. Qualitative characterisation of iPSC-derived RPE by IF showed preservation of apical-basal polarity in all RPE cell lines (Figure 43, B). This was inferred by the expression of apical marker EZRIN and the basal protein Collagen IV (COLLIV). Similarly to the wild-type (WT) control all cell lines expressed the tight junction marker ZO-1 (Figure 43, C). Despite the presence of tight junctions, transepithelial electrical measurements (TEER) indicated a compromised barrier function in CORD21-P1 RPE relative to isogenic control (Figure 43, D). Conversely, a higher barrier function was observed in the CORD21-P2 patient compared to CORD21-P2c. Additional assays of the phagocytotic ability of RPE showed no significant differences in the ability of patient RPE to phagocytose photoreceptor outer segments (POS). Furthermore, no changes were observed between patient and control in the apical and basal media secretion of PEDF and VEGF, respectively (Figure 43, D).

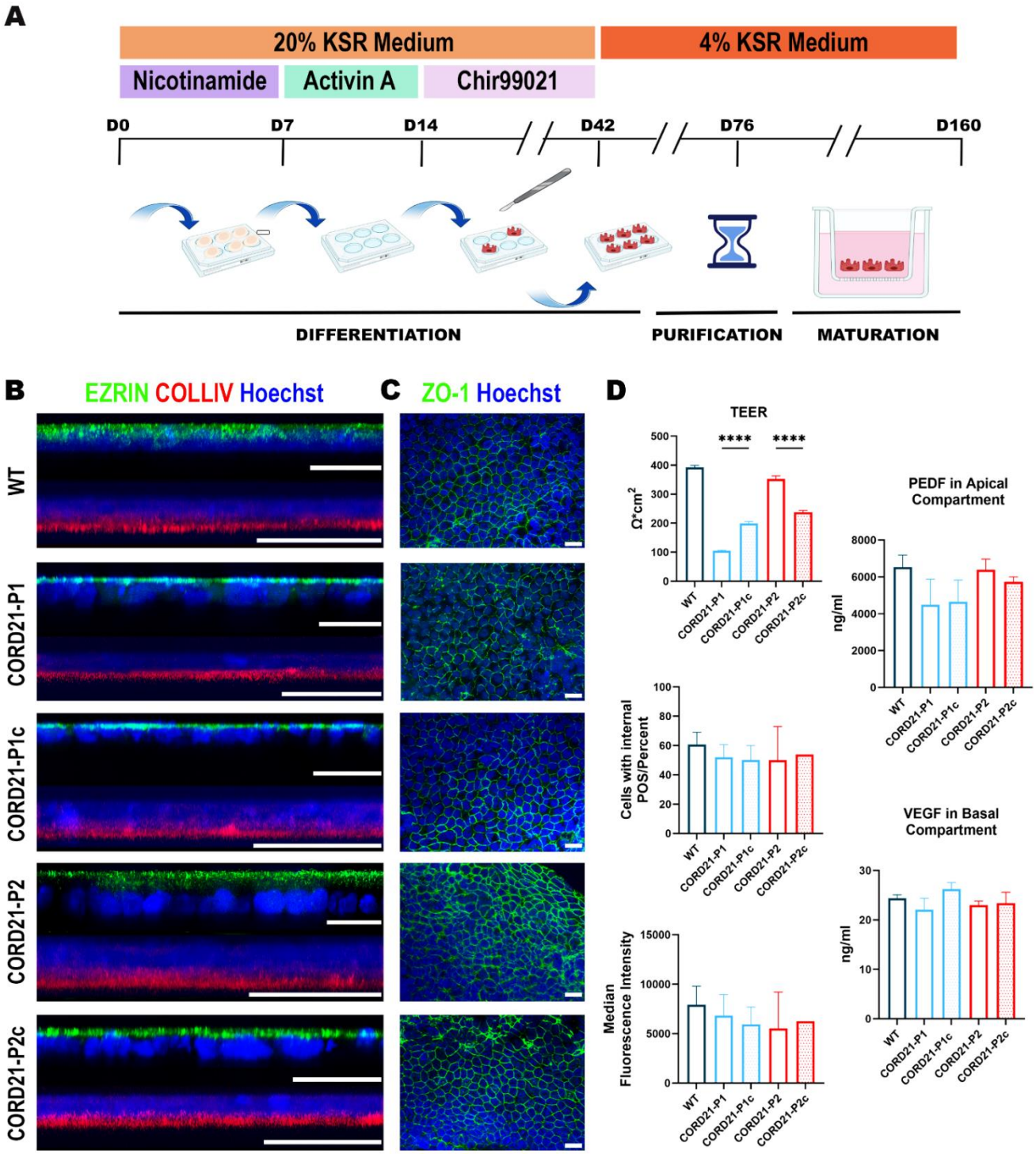
A
20% KSR Medium
4% KSR Medium
Nicotinamide
Activin A
Chir99021
D0
D7
D14
D42
D76
D160
DIFFERENTIATION
PURIFICATION
MATURATION
B
EZRIN COLLIV Hoechst
C
ZO-1 Hoechst
WT
CORD21-P1
CORD21-P1c
CORD21-P2
CORD21-P2c
D
TEER
Ω*cm2
****
****
PEDF in Apical Compartment
ng/ml
Cells with internal POS/Percent
VEGF in Basal Compartment
Median Fluorescence Intensity

Figure 43. RPE generation and characterisation by IF, TEER and ELISA assays. (A) RPE directed differentiation procedure by Regent *et al*. 2019. Briefly, iPSCs are differentiated in the presence of 20% KSR for the first 42 days. In the first 7 days of the differentiation, the cells are subjected to nicotinamide, which is replaced by Activin A until day 42. The presence of Chir99021 facilitates the emergence of RPE patches day 14 onwards. The patches are excised and nascent RPE (P0) are reseeded and expanded for two passages under reduced serum conditions (4% KSR). RPE maturation is observed over the course of the following 160 days. (B) RPE IF showed positive expression for apical and basal markers EZRIN and COLLIV, respectively in all RPE cell lines. Scale bar corresponds to 20µm (n=3). (C) RPE cells lines express the tight junction marker ZO-1. Scale bar shows 20µm (n=3). (D) TEER measurements ($\Omega*cm^2$) showed reduced or increased barrier function in CORD21-P1 and -P2 relative to their isogenic controls (ANOVA) respectively. Furthermore, no difference was observed in the phagocytic ability of RPE cells (% phagocytic cells and mean fluorescence intensity, MFI, n=1-3). No significant differences were also observed for apically secreted PEDF (ANOVA) as well as basally secreted VEGF of RPE cells (ANOVA). Data presented as means + SEM (n=3).

*Statistical comparisons for CORD21-P1vs -P1c and CORD21-P2vs-P2c are denoted by * P<.05, **P<.01, ***P<.001, ****P<0.0001. The WT sample was excluded from the statistical analysis.*

5.2. Treatment of DRAM2 patient RPE with POS leads to ultrastructural abnormalities.

To assess the ability of DRAM2 RPE to respond to POS-induced metabolic stress, cells were subjected to POS every day over the course of two weeks. This was carried out to recapitulate *in vivo* mechanisms that underlie the DRAM2 molecular defect in RPE. The treatment revealed a variety of aberrant ultrastructural findings in CORD21-P1 POS (+) relative to CORD21-P1 POS (-) and -P1c POS (+) (Figure 44). These included the accumulation of lipid-containing organelles (LCO), lamellar bodies (LB) and stage II mitochondria in the CORD21-P1 POS (+) sample (Figure 44, B and C). LCO is a term we use to describe vesicles resembling lipid droplets (LD) which exhibit more irregular demarcations compared to LD (Figure 44, B). LBs are residual autolysosomal derivatives which indicate an active and/or incomplete degradatation process. We also identified melanolipofuscin (MLF) lipid-containing structures which did not differ significantly with the numbers of MLF between the pre-selected pairs (patient vs isogenic control, POS (-) vs POS (+) (Figure 44, B). Across samples, two different types of aberrant mitochondrial morphology were observed – stage I mitochondria, exhibiting a parallel straigthening of the cristae, and stage II mitochondria, which showed concentric accumulation of the cristae (Figure 44, B). Three different types of melanin-containing organelles were identified – stage III and stage IV melanosomes as well as melanolysosomes

(Figure 44, B). POS treatment resulted in the reduction of stage III melanosomes in both CORD21-P1 and -P1c. We also observed a marginal increase of stage IV melanosomes in CORD21-P1c but not in -P1 POS (+) treated samples. Data from CORD21-P2/P2c comparisons did not show any significant changes (data not shown).

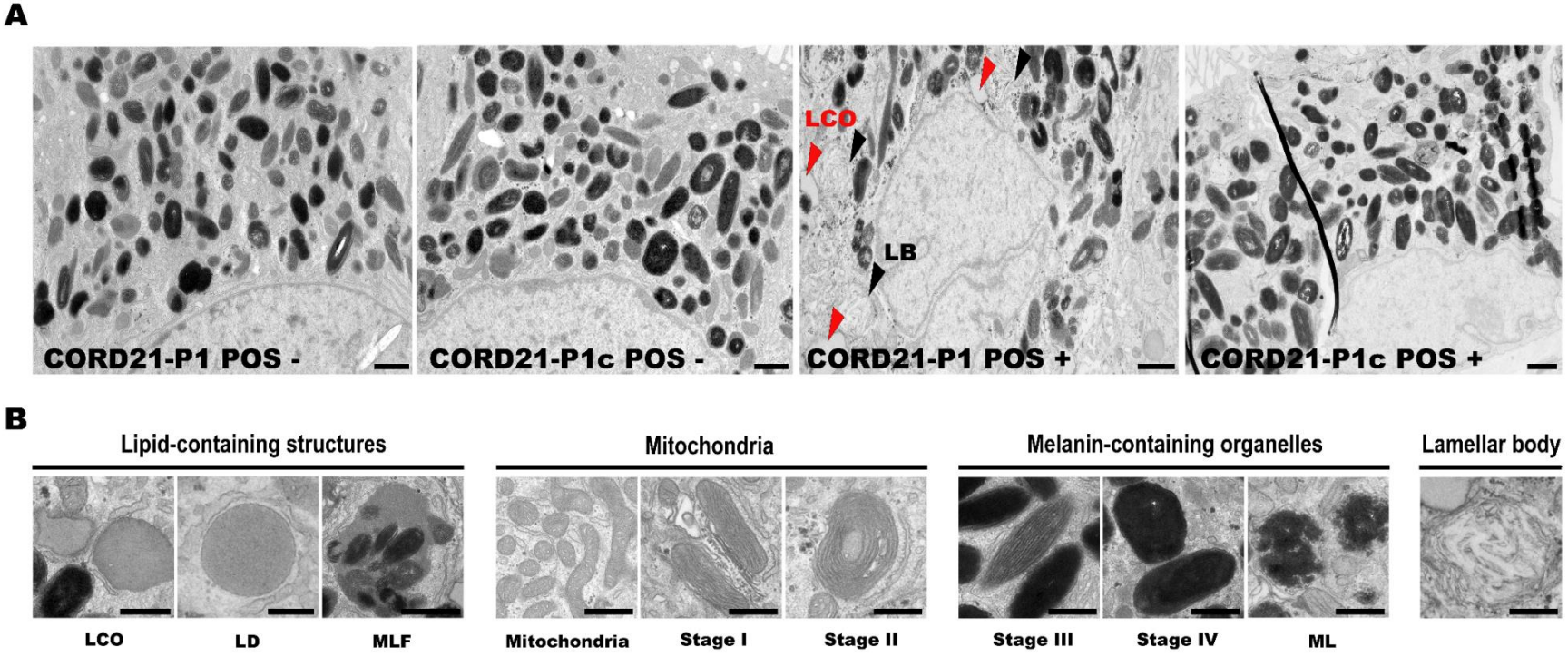
A
LCO
LB
CORD21-P1 POS -
CORD21-P1c POS -
CORD21-P1 POS +
CORD21-P1c POS +
B
Lipid-containing structures
Mitochondria
Melanin-containing organelles
Lamellar body
LCO
LD
MLF
Mitochondria
Stage I
Stage II
Stage III
Stage IV
ML
C
LCO
Stage II mitochondria
Stage III melanosomes
Stage IV melanosomes
LB
organelle per cell
CORD21-P1 POS (-)
CORD21-P1c POS (-)
CORD21-P1 POS (+)
CORD21-P1c POS (+)

Figure 44. TEM shows accumulation of lipid-containing organelles (LCO), stage II abnormal mitochondria, lamellar bodies and depletion of stage III melanosomes in POS treated CORD21-P1 RPE. (A) POS treatment shows accumulation of LCO (red arrow heads) and LBs (black arrow heads) in CORD21-P1 POS (+) RPE as compared to untreated CORD21-P1 POS (-) or the CORD21-P1c POS (+) samples (scale bar corresponds to 1µm). (B) Legend for quantified cellular RPE findings on TEM. Lipid-containing structures pertain to Lipid-Containing Organelles (LCO) (scale bar=0.5µm), Lipid droplets (LD) (scale bar=0.25µm), Melanolipofuscin (MLF) (scale=1µm). Normal mitochondria was distinguished from stage I and stage II aberrant mitochondria (scale=0.5µm). Melanin-containing organelles were categorized as stage III and stage IV melanosomes as well as melanolysosomes (scale bar shows 0.5µm). LB stands for lamellar body (scale=0.5µm). (C) POS treatment results in the accumulation of LCO (Kruskal-Wallis), Stage II mitochondria (Kruskal-Wallis) and LBs in CORD21-P1 POS (+) RPE (Kruskal-Wallis) relative to CORD21-P1 POS (-) and CORD21-P1c POS (+) RPE. Furthermore, stage III melanosomes were significantly reduced in POS treated samples for both CORD21-P1 and -P1c (ANOVA). A marginal, non-significant increase is seen with stage IV melanosomes between CORD21-P1 POS (+) and CORD21-P1c POS (+) (Kruskal-Wallis). All data were presented as means + SEM (n=8).

*Statistical comparisons for CORD21-P1 POS (-) vs CORD21-P1 POS (+), CORD21-P1c POS (-) vs CORD21-P1c POS (+) and CORD21-P1 POS (-) vs CORD21-P1c POS (+) are denoted by * P<.05, **P<.01, ***P<.001, ****P<0.0001. The WT sample was excluded from the statistical analysis.*

5.3 Proteomics RPE data shows an inherent mitochondrial deficiency and a vesicle-mediated trafficking defect in DRAM2 patient RPE cells.

Approximately 15 µg of total protein lysate was analysed by LC-MS/MS per sample, processed for protein identification and further analysed using Perseus software. Analogously to RO proteomics, the wild-type control was omitted from the dataset to improve the statistical power of the CORD21-P1/CORD21P1c and CORD21-P2/CORD21-P2c comparisons. RPE proteomics analysis led to the identification of 4559 proteins in our RPE samples (n=7) per sample. Principal component analysis showed distinct segregation between patient samples and isogenic controls (Figure 45, A), whereby most of the variation could be explained by Component 1 (45.9%) and Component 2 (8.3%). Statistical analysis entailed a modified ANOVA (FDR<0.05) followed by a subsequent Tuckey's post hoc t-test (FDR<0.05). This resulted in the identification of a total of 1759 protein changes shared between both groups (Figure 45, B). Plot shown in Figure 45, C, outlines 671 tandemly changed proteins, out of which 296 are showing increased expression and 375 are downregulated. GO enrichment for all the shared changed proteins (n=671) revealed mitochondrial respiration (respiratory chain complex I) as a highly affected biological process (Figure 45, D). Further analysis revealed

carbohydrate metabolic process, carbon metabolism, generation of precursor metabolites and energy, vesicle mediated transport and transport of small molecules to also be enriched in GO terms. Volcano plots in Figure 45, E show key novel targets involved in vesicular transport in both groups (logged FC>2, logged p value<0.05) (P1/P1c, n=32) (P2/P2c, n=20). Key proteins for P1/P1c were SYP, GFAP, RAB3A, RPE65, BIN1, KIF1A, AP3B2, EIPR1, CLTRN, RABEP1, TRAPPC6B. For the P2/P2c comparison these include but are not limited to FBN1, FN1, LIPG, NES, FBLN5, COG7, MT-ND5, COL12A1, GFRA2, VCAN, DCN.

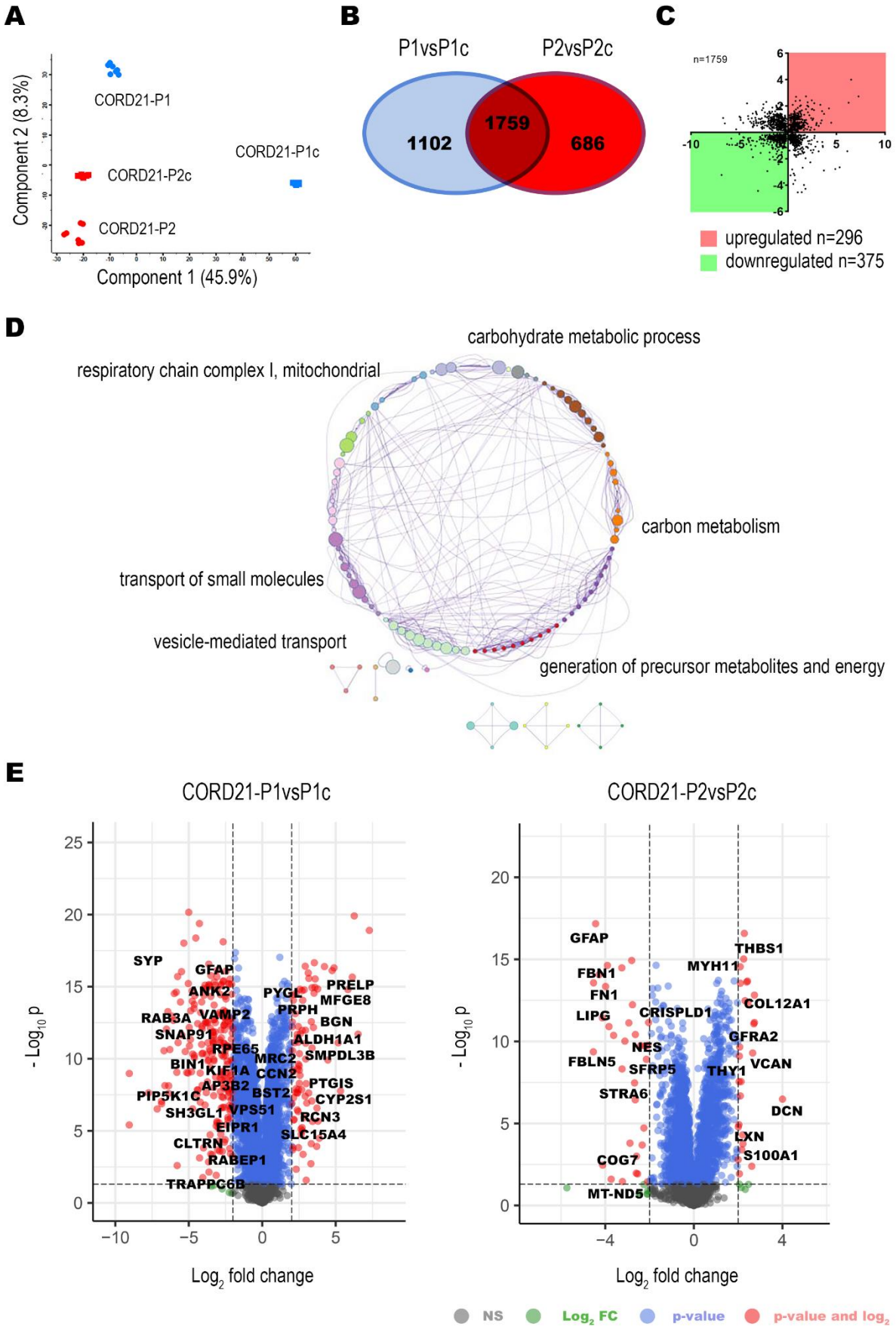
A
CORD21-P1
CORD21-P1c
CORD21-P2c
CORD21-P2
Component 2 (8.3%)
Component 1 (45.9%)
B
P1vsP1c
P2vsP2c
1102
1759
686
C
n=1759
upregulated n=296
downregulated n=375
D
carbohydrate metabolic process
respiratory chain complex I, mitochondrial
carbon metabolism
transport of small molecules
vesicle-mediated transport
generation of precursor metabolites and energy
E
CORD21-P1vsP1c
CORD21-P2vsP2c
- Log10 p
Log2 fold change
SYP
GFAP
ANK2
RAB3A
VAMP2
SNAP91
RPE65
BIN1
KIF1A
AP3B2
PIP5K1C
SH3GL1
VPS51
EIPR1
CLTRN
RABEP1
TRAPPC6B
PYGL
PRPH
PRELP
MFGE8
BGN
ALDH1A1
SMPDL3B
MRC2
CCN2
PTGIS
BST2
CYP2S1
RCN3
SLC15A4
GFAP
FBN1
FN1
LIPG
FBLN5
STRA6
COG7
MT-ND5
MYH11
CRISPLD1
NES
SFRP5
THBS1
COL12A1
GFRA2
THY1
VCAN
DCN
LXN
S100A1
NS
Log2 FC
p-value
p-value and log2

Figure 45. RPE proteome analysis of DRAM2-deficienct RPE identifies changes in key novel proteins linked to vesicular-mediated transport. (A) Principal Component Analysis (PCA) showed distinct separation between CORD21-P1/P1c (blue) and CORD21-P2/P2c samples (red). The WT sample was excluded from the proteome analysis. Variation in the samples can be accounted for by variation in Component 1 (45.9%) and Component 2 (8.3%). (B) Venn diagram illustrates that 1759 proteins are commonly changed between P1/P1c and P2/P2c (Tukey's post-hoc, FDR<0.05, n=7). (C) Dot plot revealed a total of 296 (red) and 375 (green) proteins that are up- and downregulated, respectively. (D) GO enrichment analysis of RPE proteomics conducted using Metascape identifed respiratory chain complex I, carbohydrate metabolic process, carbon metabolism, generation of precursor metabolites and energy, transport of small molecules and vesicle-mediated transport as affected biological processes. (E) Volcano plots showed key novel targets involved in cellular transport in both comparison groups with logged FC>2 that represents statistically significant changes ($p<0.05$) (P1/P1c, n=32) (P2/P2c, n=20).

5.4. Western blot analyses partially corroborate CTSD reduction and suggest involvement of DRAM2 in AP-3γ clathrin transport.

To validate the proteomics LC-MS analysis, RPE lysates and media were examined by WB. As expected DRAM2 was found to be significantly downregulated in both patients (Figure 46, A and B). CTSD was only partially corroborated by WB in RPE, despite proteomics and kinetic assays demonstrating a consistent reduction in patient samples. Indeed, WB showed a significant decrease of CTSD heavy chain in CORD21-P1 but not CORD21-P2 (Figure 46, A and B). Moreover, no changes were observed for lysate pro-CTSD/active intermediate or heavy chain in the media of RPE. Contrary to what is observed in ROs, expression of lysosome marker LAMP2 and GARP complex protein VPS53 also remained unchanged.

To ascertain a vesicular trafficking defect, RPE lysates were probed for the expression of major subunits of clathrin adaptors, AP-1γ, AP-2α and AP-3β. Despite the lack of changes in AP-1γ and AP-2α, AP-3β expression was significantly diminished in CORD21-P2 relative to isogenic control. Analogously to RO data, CTSD and PPT1 were shown to be downregulated by LC-MS/MS in both DRAM2 patients. WB further corroborated a significant PPT1 downregulation in patient lysates at the expense of protein abundance in RPE media (Figure 46, A and B). Interestingly, NPC2 was reduced only in the lysate of CORD21-P1, however an upregulation was observed in the media of both CORD21-P1 and -P2. Last but not least, enzymatic activity assays revealed the reduced activities of CTSD, GBA and α-Mannosidase in both patient RPE lysates (Figure 46, C).

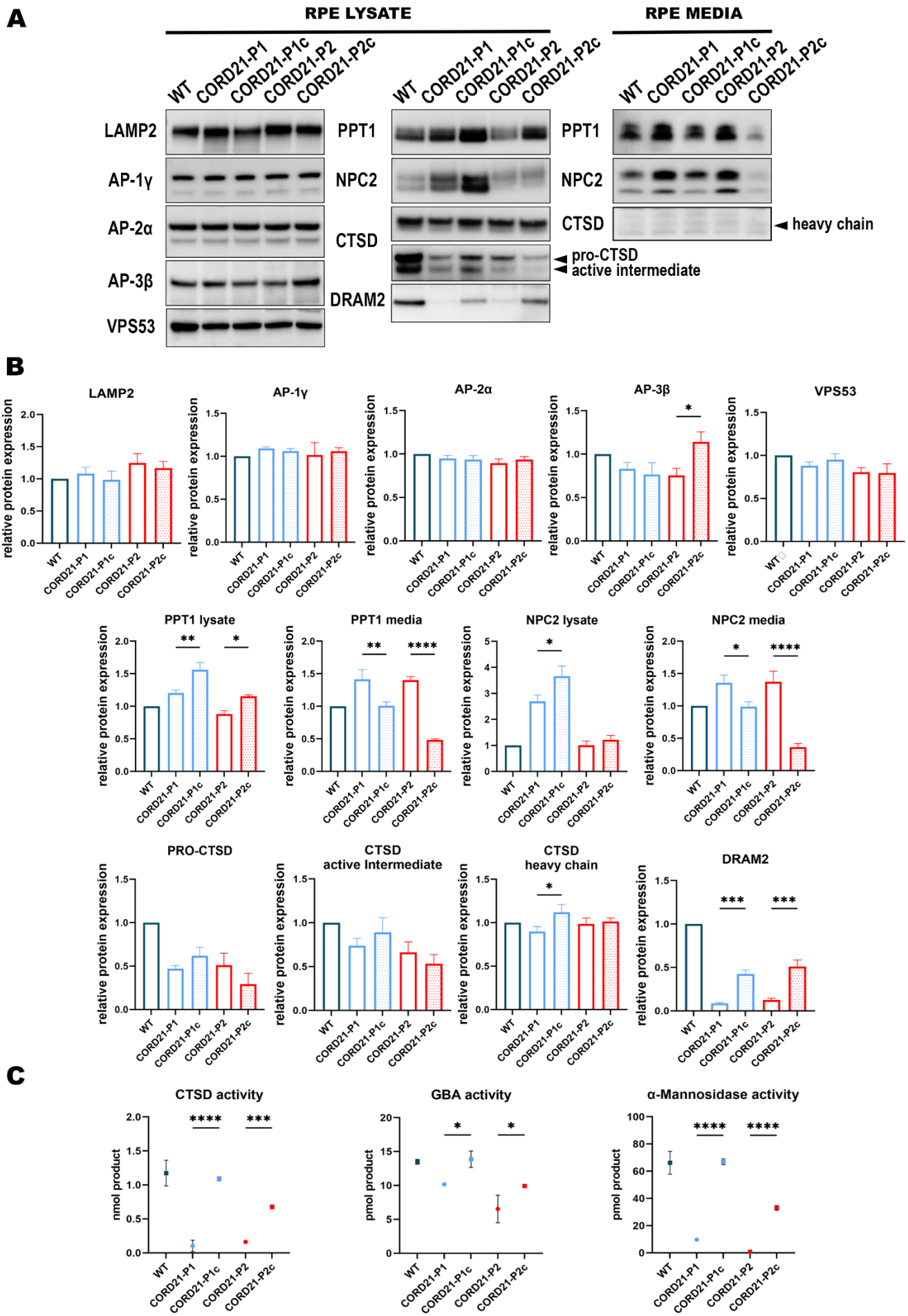
A
RPE LYSATE
RPE MEDIA
WT
CORD21-P1
CORD21-P1c
CORD21-P2
CORD21-P2c
LAMP2
AP-1γ
AP-2α
AP-3β
VPS53
PPT1
NPC2
CTSD
DRAM2
heavy chain
pro-CTSD
active intermediate
B
LAMP2
AP-1γ
AP-2α
AP-3β
VPS53
relative protein expression
PPT1 lysate
PPT1 media
NPC2 lysate
NPC2 media
PRO-CTSD
CTSD active Intermediate
CTSD heavy chain
DRAM2
C
CTSD activity
GBA activity
α-Mannosidase activity
nmol product
pmol product

Figure 46. WB corroborates DRAM2 deficiency in patient RPE, and shows downregulation of CTSD heavy chain and AP-3β in CORD21-P1 and -P2, respectively. (A-B) WB RPE analysis indicated a significant reduction in the expression of CTSD heavy chain in CORD21-P1 as well as of the clathrin transporter AP-3β in CORD21-P2 relative to isogenic controls (n=3). Furthermore, DRAM2 was found to be significantly downregulated in both patient samples. WB data showed PPT1 and NPC2 RPE intracellular deficiency is due to secretion to the extracellular media. Plots indicated a significant reduction of PPT1 and NPC2 in the lysates of patient RPE. This was accompanied by an increase of these lysosomal proteins in the media of age-matched samples. No consistent changes were observed for lysosomal marker LAMP2, AP-1γ, AP-2α, VPS53, media-released CTSD as well as lysate pro-CTSD and active intermediate. Equal protein loading was visualised by the total protein stain and data was normalised to the WT sample. Plots show pre-selected ANOVA comparisons Data is shown as means + SEM (n=3). (C) Reduced CTSD enzymatic activity in patient RPE lysates relative to isogenic controls. Endpoint activity assays for GBA and α-Mannosidase demonstrated a similar enzymatic reduction in patient RPE lysates. All plots show ANOVA comparisons. Data is shown as means + SEM (n=3).

*Statistical comparisons for CORD21-P1vs -P1c and CORD21-P2vs-P2c are denoted by * P<.05, **P<.01, ***P<.001, ****P<0.0001. The WT sample was excluded from the statistical analysis.*

5.5 Discussion

5.5.1 DRAM2 RPE cells do not show overt pathological features at baseline, however, exhibit ultrastructural abnormalities on transmission electron microscopy upon POS challenge.

5.5.1.1 IF, TEER, and ELISA

RPE obtained in this study have been derived using a directed differentiation protocol outlined by Regent *et al*. (2019). As analysis of DRAM2 RPE cells represented a secondary aspect of the project, help was kindly provided by MRes student Eldo Galo under supervision (RPE maintenance, TEER and TEM analysis), PhD student Rodrigo Cerna-Chavez (IF) and PhD student Rob Atkinson (ELISA assays).

All RPE cell lines exhibited cobblestone, hexagonal shape, and melanin pigmentation (data not shown). DRAM2 patient RPE showed preservation of apical-basal polarity as inferred by the apical expression of EZRIN and the basal localisation of COLIV. Lower TEER measurements of CORD21-P1 relative to isogenic control indicated a reduced barrier function in this patient. These results were intriguing despite the expression of the tight junction marker ZO-1 in all cell lines. Expression was inferred qualitatively and not quantified.

Surprisingly, CORD21-P2 exhibited higher TEER values compared to CORD21-P2c (Figure 43, B and D).

RPE integrity is enabled by tight and adherent junctions between neighbouring cells (Citi, 2019; Wang;Li and Wang, 2022). Tight junctions, are of particular importance to the establishment of the RPE barrier function and apical basal polarity. They are positioned apically and prevent the free diffusion of molecules between apical/basal compartments in addition to also enabling active ion transport (Dvoriashyna *et al.*, 2020; Napoli and Strettoi, 2023). Tight junctions are facilitated by the interaction of occludins and claudins and are stabilised by the expression of zona occludens (ZO-1) (Tsukita;Furuse and Itoh, 2001). This insulatory function of the RPE renders protection to the retina from inflammatory molecules circulating in the choriocapillaris (Benedicto *et al.*, 2017; Fields *et al.*, 2020). TEER provides a quantifiable measurement of the tight junction integrity and barrier function. Compromised RPE integrity has previously been reported in human iPSC-derived RPE from diabetic patients (Kiamehr *et al.*, 2019). Decreased TEER has also been observed in hESC- and hiPSC-derived RPE following treatment with retinoblastoma drugs within the clinical range (Cerna-Chavez *et al.*, 2023). Impairment of the tight junction network undermines the outer blood-retinal barrier leading to a plethora of retinal conditions such as infectious and autoimmune uveitis, AMD, diabetic retinopathy, glaucoma, proliferative vitreoretinopathy and retinitis pigmentosa (Simo *et al.*, 2010; Naylor *et al.*, 2019; Yang *et al.*, 2020).

Factors that can affect TEER include the composition and porosity of transwell inserts, RPE cell passage, media formulation and temperature conditions (Thwaites;Hirst and Simmons, 1993; Lu *et al.*, 1996; Matter and Balda, 2003; Ferruzza *et al.*, 2013). Errors could also occur in establishing TEER due to improper electrode placement and available growth surface area (Srinivasan *et al.*, 2015; Henry *et al.*, 2017; Karakocak *et al.*, 2023). Even though a minimum of 200 Ωcm^2 is considered a prerequisite for RPE maturity, prolonged *in vitro* cell culture in the case of fetal human RPE can lead to increased TEER values of ~ 1000 Ωcm^2 (Ablonczy *et al.*, 2011). Other studies have reported a peak of 400 Ωcm^2 for iPSC-RPE and a subsequent decline in the TEER values with continuous culture on transwell inserts (Chen *et al.*, 2022). In the current study it is likely that TEER reduction in CORD21-P1 is associated with a more severe DRAM2 phenotype, whereas increased TEER values in CORD21-P2 relative to

CORD21-P2c, could represent a deviation in values due to prolonged cell culture. Conversely, this could be owing to an unintentional difference in seeding density, insert surface area or porosity discrepancy between cell inserts. Problems linked to the inconclusive TEER data could be mitigated by repeating the experiment on newly differentiated RPE cell with both technical and biological replicates as well as by conducting transepithelial potential difference measurements (TEPD), which may represent an alternative readout of RPE barrier function. Future work on DRAM2 RPE may help to resolve the validity of these data.

Despite the differences observed in TEER, apical-basal polarity appeared to be preserved in DRAM2 RPE, as suggested by the apical expression of EZRIN and the basal localisation of Collagen IV (COLLIV) in all cell lines. The maintenance of polarisation was also reflected in the comparable levels of apical and basal secretion of PEDF and VEGF between samples (within groups), respectively. Aberrant expression of PEDF is deemed to play an important role in the pathological neovascularisation of the retina (Shweiki *et al.*, 1992; Adamis *et al.*, 1994; Dawson *et al.*, 1999). In addition to being able to induce cellular differentiation (Tombran-Tink;Chader and Johnson, 1991), PEDF is a potent angiogenesis inhibitor capable of impeding endothelial migration under normoxic conditions (Dawson *et al.*, 1999). Apical secretion of PEDF by RPE prevents the invasion of blood vessels into the photoreceptor (PR) layer. Conversely, the basolateral release of VEGF is essential for the maintenance of the choriocapillaris, as loss of VEGF expression can lead to geographic atrophy i.e., secondary death of the PRs due to RPE degeneration (Saint-Geniez *et al.*, 2009). The preservation of RPE apicobasal polarity and tight junction expression is, hence, of utmost importance to the homeostasis of PRs and the choriocapillaris. The lack of changes in PEDF/VEGF secretion in DRAM2 RPE may relate to the relative resilience of RPE as a postmitotic retinal cell type which may require continuous exposure to POS *in vitro* to mimic the RPE disturbances observed in some of the DRAM2 patients. Clinical signs of RPE degeneration often coincide with peripheral degeneration during advanced stages of the disease. Frameshift and splicing mutations usually present as severe RPE disturbances recognisable as dark specks spanning the whole periphery of the retina on fundus autofluorescence (Abad-Morales *et al.*, 2019). Future work may benefit from establishing the expression of polarity complexes Par, Crb and Scribble to gain additional insight into the early state of tight and adherent junctions (van de Pavert *et al.*, 2004; Luo *et al.*, 2006; Park *et al.*,

2011; Paniagua *et al.*, 2015; Abad-Morales *et al.*, 2019; Paniagua *et al.*, 2021; Segurado *et al.*, 2022). In summary, a combined TEER, IF and ELISA approach did not conclusively establish reduced barrier function in DRAM2 RPE.

5.5.1.2 Ultrastructural findings

Flow cytometry analysis revealed no differences in the ability of DRAM2 RPE to carry out phagocytosis following treatment with FITC-labelled POS (20 POS/cell). This pertained to the lack of changes in the percentage of phagocytic cells as well as the mean fluorescence intensity of POS per cell (MFI) (Figure 43, D). However, treatment of RPE with POS over the course of two weeks resulted in a marked accumulation of LCO, lamellar bodies and stage II aberrant mitochondria in CORD21-P1 POS (+) samples relative to CORD21-P1 POS (-) and -P1c POS (+). LCOs resembled LDs, however they differed from LDs in the way that they didn't present a perfectly spherical structure. Indeed they were commonly found in close proximity to stage II mitochondria (Figure 44, B). The mitochondria observed here, were categorised as stage I and stage II aberrant mitochondria similar to findings reported in cases of chronic polymyositis (Chou, 1968). A shown by Chou *et al*. (1968) a sequential deterioration of mitochondria in muscle may initially present with the parallell straightening of cristae (stage I), followed by the formation of membranous mitochondrial whorls (stage II) (Chou, 1968). Polymyositis represents a group of autoimmune systemic disorders characterised by muscle inflammation and fatigue. Studies have demonstrated a correlation between polymyositis and altered lipid profiles during early stages of the disease (Wang *et al.*, 2014; Raouf *et al.*, 2018). Analogously, ultrastructural findings in CORD21-P1 POS (+) RPE could present a secondary mitochondrial dysfunction accompanied by an underlying lipid metabolic defect.

Lipid droplets are dynamic intracellular storage deposits composed of esterified cholesterol and triacylglycerol (Greenberg *et al.*, 2011). Dysregulation of lipid homeostasis and lipid droplet accumulation is at the root of major neurodegenerative conditions such as Alzheimer's, Parkinson's and Amyotrophic Lateral Sclerosis (ALS) (Fernandes *et al.*, 2023). A specific type of peridroplet mitochondria (PDM) has been reported in literature (Benador *et al*., 2018; Talari *et al*., 2023; Yang *et al*., 2022). PDM differ from cytoplasmic mitochondria in the way that they exhibit lower fatty acid degradation capacity. The interaction of mitochondria and lipid droplets has been associated with the expansion of lipid droplets. This

relates to a mitochondrial role in adipose tissue which favours triglyceride synthesis (Benador *et al.*, 2018). Contrary to these data, another study has reported a liver-specific function of PDM in the preferential oxidation of fatty acids (Talari *et al.*, 2023). The disparate outcome of these findings could relate to the opposing roles of lipid droplet-mitochondrial contacts in functionally distinct cell types. Alternatively, this may also suggest a differential response of mitochondria to nutrient abundance. Under conditions of nutrient excess these interactions could trigger lipid droplet formation. Conversely, nutrient deprivation may prompt an energetic exchange with lipid droplets to increase fatty acid oxidation (Yang *et al.*, 2022).

The observed increase in stage II aberrant mitochondria and their close association with LCOs could be explained by a pathological lipid transfer to mitochondria in CORD21-P1 POS (+) RPE. This may represent an attempt to alleviate the disproportionate lipid accumulation in the form of LCOs (Figure 44, B and C) or could have arisen in response to a mitochondrial deficiency. Studies have demonstrated that stress-induced mitochondrial dysfunction can indeed stimulate the formation of lipid droplets (Lee *et al.*, 2013). The enhanced generation of LCOs may represent a cellular defense strategy against further ROS generation in an already compromised mitochondrial setting (Sekiya *et al.*, 2008). Fundamentally, the sequestration of free fatty acids in lipid droplets could avert lipotoxicity and therefore enable a cytoprotective role. In summary, these data suggest a mitochondrial defect compounded by lipid accumulation in the form of LCOs in the more severely affected CORD21-P1 POS (+) RPE.

In line with a prominent lysosomal defect, POS treatment in CORD21-P1 led to the accumulation of LBs on TEM (Figure 44, B). LBs have classically been described as lysosome-related organelles (LROs) which enable the release of pulmonary surfactant in the extracellular space of alveoli upon exocytosis (Sever *et al.*, 2021). LBs have also been shown to arise as a result of the selective inhibition of autophagic degradation (Hariri *et al.*, 2000). This has been demonstrated via the inhibition of leupeptin in alveolar cells transfected with β-1– 6-N-acetyl glucosaminyl transferase V (GlcNAc-TV). GlcNAc-TV enhances the polylactosamine glycosylation of LAMP2 and its transfection in alveolar cells leads to the formation of swollen $LAMP2^{+}$ lysosomes. Leupeptin treatment of GlcNAc-TV-transfected cells results in the replacement of multilamellar bodies with AVds (late autophagic vesicles).

Analogously, withdrawal of leupeptin leads to the re-emergence of multilamellar bodies. In the case of the autophagy blocker 3-MA, application of the drug can transform LBs into early autophagic vesicles (AVis). These experiments provide direct evidence that the formation of LBs is dependent on autolysosome biogenesis and degradation (Hariri *et al.*, 2000). Earlier studies have shown that galactosidase and/or sialidase deficiency can also lead to the accumulation of LBs (Amano *et al.*, 1983; Allegranza *et al.*, 1989; Ohshima *et al.*, 1997). The distinct LB findings in CORD21-P1 POS (+) therefore indicate an attempt at autophagic POS degradation but may also suggest inefficient or partial waste clearance due to lysosomal deficiency.

Melanosomes are specialised lysosomes which have recently been shown to play a crucial role in the degradation of autofluorescent lipofuscin (Lyu *et al.*, 2023). The chemiexcitation of melanin, the hallmark protein of melanosomes, has emerged as an important prerequisite for the routine digestion of POS by RPE. This was inferred by the deposition of PR disc lamellar membranes in the RPE cells of albino *Abca4*$^{-/-}$ mice. Nitric oxide treatment resulted in the significant clearance of lipofuscin-related lamellar membranes in pigmented but not albino mice. Data obtained here shows a clear downregulation of stage III melanosomes in CORD21-P1 and P1c POS (+) treated samples (Figure 44). The specific effect on melanosome maturation was also reflected by the marginal increase in stage IV melanosomes in CORD21-P1c POS (+) compared to patient. The CORD21-P1 POS (+) sample could therefore present with compromised melanin-dependent degradation due to the incomplete maturation of stage IV melanosomes. One of the distinguishing features of maturing melanosomes (stage III to stage IV) is the expression of proteins enabling melanin biosynthesis such as tyrosinase, tyrosinase-related protein-1 (TYRP1) and DOPAchrome tautomerase (DCT). By contrast, stage II and I are more abundant in the PMEL enzyme, which is important for fibril deposition during early melanosome formation (Raposo and Marks, 2007).

Similar deficiencies are observed in the Hermansky-Pudlack Syndrome (HPS). HPS is a genetic condition presenting with ocular albinism and bleeding. The disease arises due to an impairment of LRO biogenesis characterised by the incomplete maturation of pigmented melanocytes (Wei, 2006; Velazquez-Diaz *et al.*, 2021). The defect in HPS appears to be caused

by mutations in AP-3, HOPS, BLOC-1, -2 or -3, which facilitate the trafficking of melanogenic enzymes. AP-1 and -3 are believed to carry out redundant roles in the melanosome delivery of tyrosinase, whereas AP-1 is believed to have a more specialised function in the trafficking of TYRP1. Furthermore, BLOC-1 and BLOC-2 complexes may facilitate melanosome transport in the same pathway as AP-1. AP-3 δ-subunit deficiency, in particular, is known to result in the stalling of tyrosinase at the early endosome (Wei, 2006). Thus, by controlling endolysosomal transport of enzymes such as tyrosinase, AP-3 would be able to affect the maturation of stage III to stage IV melanosomes (Raposo and Marks, 2007). Collectively, the improper maturation of melanosomes in CORD21-P1 POS (+) RPE implies a defect in the trafficking of melanin biosynthetic enzymes and suggests an important role for DRAM2 in the latter process.

5.5.2 Differential proteomics analysis reveals severe mitochondrial deficiency and novel targets involved in the vesicular transport of patient RPE.

Proteomics analysis was performed by Dr. Pawel Palmowski and MRes student Eldo Galo. It led to the identification of a total of 4559 proteins, out of which 1759 were differentially expressed in both groups (Figure 45, C and D). The analysis confirmed the downregulation of CTSD and PPT1, but not NPC2. This stands in contrast to RO data, whereby all three proteins were significantly downregulated in both patients. WB corroborated that intracellular NPC2 was not significantly downregulated in CORD21-P2, however, media secretion of NPC2 was still found to be upregulated in CORD21-P1 and -P2 (Figure 46, A and B). Similarly, the lysosomal CTSD heavy chain decrease was only partially corroborated by WB, despite a common downregulation for both affected cell lines according to proteomics and kinetic assay data. These inconsistencies most likely pertain to slight variability amongst biological replicates and the insufficient power of our WB experiment to detect these differences (n=3). Despite these differences, the activities of all CTSD, GBA and MAN2B1 were reduced in both patients, suggesting that lysosomal deficiency in RPE may occur in an identical fashion to ROs. This was also corroborated by the increased secretion of NPC2 and PPT1, which appears to be an underlying feature of DRAM2 disease (Figure 46, A and B). Furthermore, Metascape enrichment showed (n=671) that a majority of the tandemly expressed proteins are linked to a mitochondrial respiration deficiency, manifesting as a failing of the mitochondrial

respiratory chain complex I (Figure 45, D). Additional enriched GO terms included carbohydrate metabolic process, carbon metabolism, generation of precursor metabolites and energy, vesicle mediated transport and transport of small molecules.

5.5.2.1 Implications for CTSD depletion in DRAM2 patient RPE cells.

As mentioned in chapter 4, the complete absence of CTSD expression leads to a lethal form of *CLN10* NCL characterised by a severe lysosomal failure (Williams and Mole, 2012; Schulz *et al.*, 2013). Several studies have examined the effects of CTSD deficiency on RPE in mice (Valapala *et al*., 2014; Rakoczy *et al*., 1997; Bassal *et al*., 2021; Liu *et al*., 2022). For instance, knockout of *CRYBA1* (Crystallin Beta A1), a major protein of the lens, in mice leads to a significant reduction in CTSD activity. These effects appear to be mitigated by the inhibition of v-ATPase activity, leading to elevated lysosomal pH and autophagy downregulation. These were also accompanied by the loss of cones, the accumulation of autophagic vacuoles and LDs in the RPE (Valapala *et al.*, 2014). The study showed that upon overexpression of CRYBA1, CTSD activity can be restored. Therefore, *CRYBA1* KO may impede autophagic and phagocytosis processes normally carried out by RPE. Since CTSD is the principal enzyme responsible for rhodopsin degradation, reduced CTSD expression in RPE is going to significantly impact their ability to phagocytose POS (Rakoczy *et al.*, 1997). Even though our results did not show any changes in the ability of patient CORD21 RPE to carry out phagocytosis, it follows that continuous exposure of DRAM2 RPE to POS with reduced CTSD activity is going to affect their long-term ability to phagocytose POS. This may need to be validated experimentally following continuous POS challenge in CORD21-P1 and -P2 RPE. Another study using CTSD-deficient mice did not reveal any significant morphological RPE changes until the very advanced stages of disease. One of the key early observations, however, was the elevated expression of LAMP2 and saposin D (Bassal *et al.*, 2021). Further research on *Abca4*$^{-/-}$ mice focussing on Stargardt disease showed a substantial decrease of mature CTSD at the expense of immature protein. A recent AAV therapy approach restored CTSD expression in the RPE of knockout mice, thereby improving PR survival and POS renewal (Liu *et al.*, 2022). In summary, CTSD deficiency suggests that the degradation capacity of lysosomes is significantly impaired in the RPE of CORD21-P1 and -P2 patients. Although this may not have an acute effect on cell functionality, over time it would negatively impact PR

and RPE survival due to aberrant phagocytosis and autophagy converging at the level of the lysosome.

5.5.2.2 Implications for the significant downregulation of PPT1 in DRAM2 patient RPE cells.

Owing to the progressive nature of neuronal cell death in *CLN1* (PPT1) deficiency, RPE degeneration has not been thoroughly investigated in the absence of PPT1 expression. Studies on progressive childhood forms of *CLN1* NCL suggest that the onset of cognitive and motor decline is at the 2 years of age (Santavuori *et al.*, 1973; Weleber, 1998; Weleber *et al.*, 2004; Jalanko and Braulke, 2009). Recent studies indicate that the disease is driven by strong immunoreactivity in the form of gliosis leading to the significant loss in PRs and ganglion cells in mice (Atiskova *et al.*, 2019). As the death of retinal neurons precedes the decline of RPE in this condition, not much is known about the progression of the disease in RPE. Based on the current knowledge, it could be hypothesised that the reduced PPT1 expression could lead to the accumulation of undigested cellular material and a secondary reduction in mature CTSD due to elevated lysosomal pH, however this requires further experimental validation (Bagh *et al.*, 2017) (see chapter 4.12.4.3).

5.5.2.3 Explaining NPC2 deficiency in patient CORD21-P1 RPE cells.

Similarly to PPT1 disease, the complete absence of NPC2 expression correlates with the severity of NPC disease, precluding the detailed study of protein depletion in RPE due to premature death (Ribeiro *et al.*, 2001; Park *et al.*, 2003; Vanier and Millat, 2003; Pentchev, 2004; Chang *et al.*, 2005; Evans and Hendriksz, 2017). In addition to the aberrant accumulation of cholesterol, other lipid species have been shown to be deposited in NPC-afflicted lysosomes such as sphingomyelin, sphingosine, ceramides and gangliosides (Pentchev *et al.*, 1984; Lloyd-Evans *et al.*, 2008; Patterson *et al.*, 2012). Interestingly, despite being primarily responsible for sterol redistribution to the ER and/or PM, NPC2 has also been found to play a role in the delivery of endosomal cholesterol to the mitochondrial inner membrane. The tranfer of oxysterol and steroids in this manner has been shown to contribute to the homeostatic maintenance of mitochondrial membrane integrity (Kennedy;Charman and Karten, 2012). This perspective means of transport enabled by NPC2 can account for the upregulation of mitochondrial cholesterol in the absence of NPC1 expression (Blom *et al.*,

2003; Balboa *et al.*, 2017). Notwithstanding, the increased mitochondrial cholesterol correlates with decreased glutathione content and respiration capacity suggesting a potential mechanism of mitochondrial impairment but also a requirement for NPC2 in the maintenance of mitochondrial homeostasis (Balboa *et al.*, 2017). More recently, NPC2 knockdown has been associated with reduced levels of mitophagy. Inefficient clearance of damaged mitochondria causes further mitochondrial dysfunction as shown by the aberrant mitochondrial activity of NPC2-depleted adipocytes (Guo *et al.*, 2016). These literature findings outline a scenario, whereby attempting to relieve lysosomes of their sterol overload, the residual NPC2 mitigates increased cholesterol transfer to mitochondria. An offset in sterol balance can then cause irrepairable mitochondrial damage further exacerbated by the reduced mitophagic clearance. Hence, the significant depletion of NPC2 in CORD21-P1 may, at least, partially explain the mitochondrial phenotype observed in CORD21-P1 POS (+) RPE by TEM, which as outlined above may be also linked to LCO formation in these cells. A pronounced mitochondrial dysfunction in DRAM2 RPE is also supported by the high number of protein targets in RPE proteomics associated with aberrant mitochondrial respiration.

5.5.2.4 Depletion of TRAPIII and TRAPII vesicular complex subunits in patient RPE cells may lead to defective ER-Golgi and Golgi-PM trafficking as well as autophagy.

Tremendous insight into the molecular mechnisms of DRAM2 disease has been rendered by the novel findings from RPE proteomics. These exciting data suggest that DRAM2 function may be affected at multiple stages of membrane trafficking with major bottlenecks impeding vesicle-mediated transport at the ER-Golgi and retrograde Golgi transport as well as during the late stages of endosome-lysosomal fusion. Involvement of early Golgi traffic is unanimously indicated by the significant downregulation of multiple TRAPP complex subunits in CORD21-P1 vs -P1c (TRAPPC1, TRAPPC8, TRAPPC2L, TRAPPC10, TRAPPC5, TRAPPC6B, TRAPPC4, TRAPPC3), in CORD21-P2 vs -P2c (TRAPPC8, TRAPPC1) as well as in both patients (TRAPPC1, TRAPPC8). TRAPP is a multi-subunit tethering NON-CATCHR complex which mediates ER-Golgi, Golgi-PM transport as well as endosome recycling (Figure 47). Two major types of TRAPP have been distinguished in mammals -TRAPPII and TRAPPIII. The TRAPP complex has been shown to exhibit GEF (Guanine nucleotide exchange factor) activity and is composed of a protein core which can be modified by the addition of C8, C11, C12 and C13

subunits in the case of TRAPIII, and C9, C10 for TRAPII. The latter subunits confer Rab specificity, whereby TRAPIII and TRAPII activate Rab1 and Rab11, respectively (Yu and Hughson, 2010; Galindo and Munro, 2023).

Rab1 exerts an important role in the regulation of the ER-to-Golgi trafficking by binding to cis-Golgi tethers GM130, golgin84 and p115 (Allan;Moyer and Balch, 2000; Moyer;Allan and Balch, 2001; Weide *et al.*, 2001; Diao *et al.*, 2003) (Figure 47). Further to enabling transport along the biosynthetic pathways, Rab1 has been shown to play a crucial role in the initiation of autophagy by orchestrating the assembly of the $Atg11^{+}$ preautophagosome structure (Lipatova *et al.*, 2012; Wang *et al.*, 2013; Wang *et al.*, 2015; Homma;Hiragi and Fukuda, 2021; Tremel *et al.*, 2021). On the other hand, Rab11, which is activated by TRAPPII, functions along the secretory and recycling endosome pathways (Welz;Wellbourne-Wood and Kerkhoff, 2014). Interestingly, mainly TRAPPIII and TRAPP core subunits appear to be downregulated in RPE patients, with a significant depletion of TRAPPIII being apparent in CORD21-P1.

Collectively, this indicates a potential inactivation of the TRAPPIII complex leading to a defective ER-Golgi traffic and aberrant Golgi morphology concomittant with an autophagic impairment (Figure 47). Future work may benefit from closer examination of TEM data for disruption of the Golgi (Golgi fragmentation) in both cell models. A caveat here, however, is that Golgi fragmentation is also a sign of apoptosis. So an assay ruling out apoptosis or an apoptosis inhibitor must be used before further investigation into this particular type of deficiency can start. Furthermore, TRAPPII function may also be compromised. This was made evident by the downregulation of core units but also the reduction of the TRAPPC10 subunit in CORD21-P1. The relevance of the TRAPPII complex clearly pertains to a possible misrouting of lysosomal enzymes to the PM within the endocytic system, endosome to Golgi traffficking but also the involvement of TRAPPII in the activation of Rab18 (Li *et al.*, 2017; Zappa;Venditti and De Matteis, 2017). The Rab18 GTPase contributes to the growth and maturation of LDs and its depletion has previously been linked to the occurrence of abnormally large LDs (Xu *et al.*, 2018). Further research into the expression of TRAPPII in DRAM2 RPE may be able to account for the LD phenotype observed in CORD21-P1 POS (+) RPE, but also the misrouting of PPT1 and NPC2 lysosomal enzymes to the extracellular media.

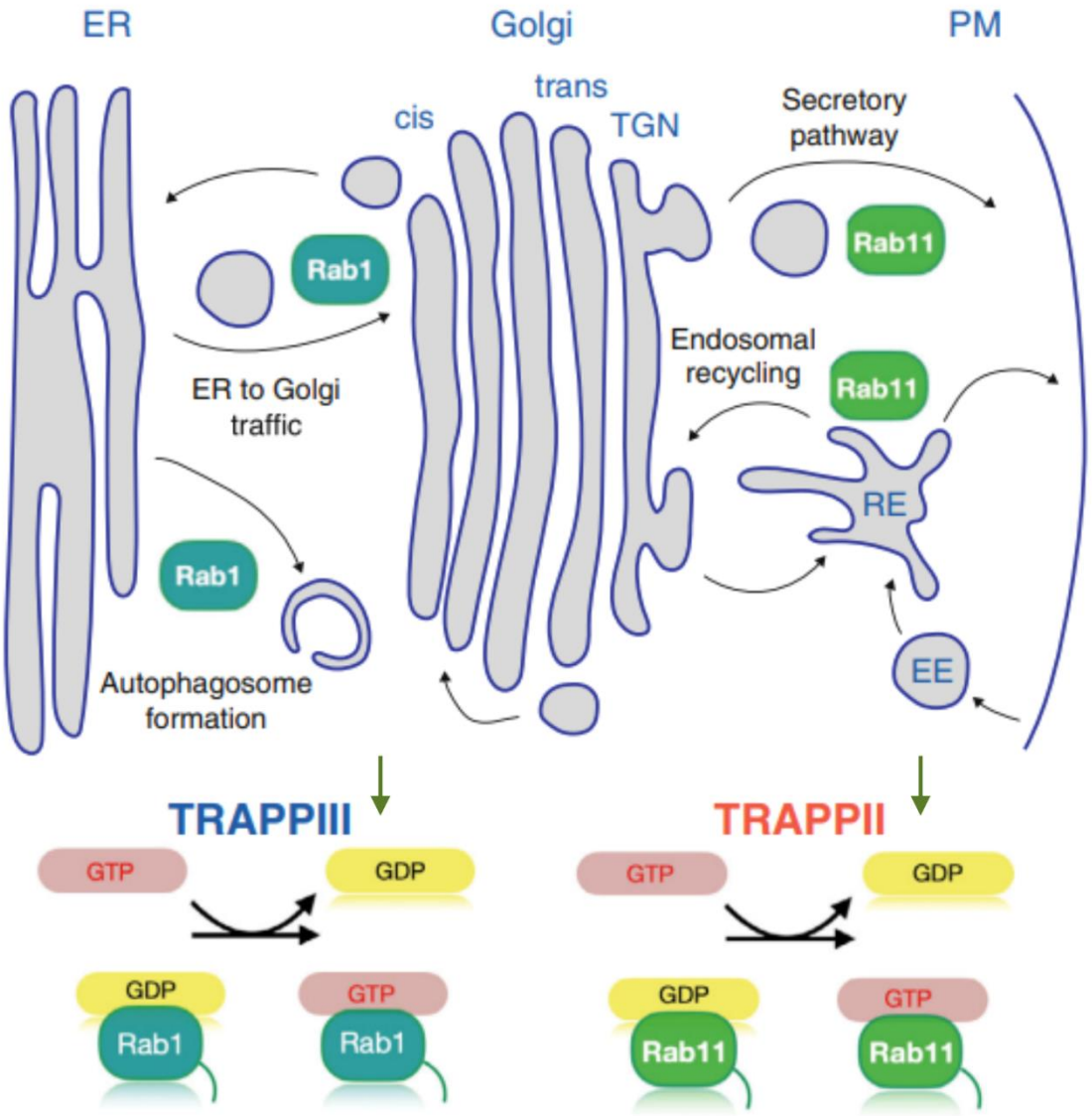

Figure 47. Roles of TRAPPII and TRAPPIII vesicular complexes in intracellular transport. Activation of the Rab1 and Rab11 GTPases is governed by nucleotide exchange factors (GEFs) TRAPPIII and TRAPPII, respectively. Whereas TRAPPIII activates Rab1 to activate conventional autophagy and facilitate ER-Golgi traffic, TRAPPII enables the activity of Rab11 which plays important roles in the TGN-PM secretory pathway as well as bidirectional endosomal recycling to and from the TGN and the PM. Green arrows indicate the potential downregulation of TRAPPIII and TRAPPII complexes in DRAM2 RPE. Image taken from Galindo and Munro, 2023.

5.5.2.5 Depletion of COG6 complex subunit in patient DRAM2 RPE cells suggests a defect in intra-Golgi and Golgi-ER trafficking.

Another notable observation was the consistent downregulation of COG6 in RPE patients. Moreover, CORD21-P2 exhibited downregulation of nearly all COG subunits apart from COG8. The COG complex (Conserved oligomeric Golgi complex) is the predominant vesicle tethering machinery overseeing intra-Golgi and Golgi-to-ER retrograde transport (Figure 48) (Blackburn;D'Souza and Lupashin, 2019). It belongs to the CATCHR family of multisubunit tethering complexes including Dsl1p, GARP, EARP and Exocyst. Similarly to other tethering complexes its main function is to prime incoming vesicles for fusion with membranous trafficking structures. The COG complex exists in two individual tetrameric conformations (COG1-4 and COG5-8), as well as an all-encompassing octamer (Willett *et al.*, 2016). Mutations in proteins of the COG complex are associated with congenital disorders of N- and O- glycosylation (Wu *et al.*, 2004; Foulquier, 2009). In yeast, depletion of the COG1-4 complex leads to the accumulation of untethered COPI-coated COG-dependent vesicles. This blockage in retrograde Golgi trafficking is said to precede Golgi fragmentation (Zolov and Lupashin, 2005). *S. cerevisiae* COG mutants exhibit extensive defects in glycosylation, protein transport and extracellular release of vacuolar proteases, whereby the depletion of one subunit often leads to the depletion of the whole tetramer (Spelbrink and Nothwehr, 1999; Ram;Li and Kaiser, 2002; Suvorova;Duden and Lupashin, 2002). Hypoglycosylation is deemed to occur secondarily to the mistrafficking of Golgi glycosylation enzymes. In a key study conducted on HeLa cells, knockdown of COG subunits led to the mislocalisation of key *medial*- and *trans*-enzymes (ST6GAL1, MGAT1, MAN2A1 and B4GALT1) (Pokrovskaya *et al.*, 2011). The same study showed that COG6 and COG8 are expressed in vesicular structures carrying glycosyltransferases. CRISPR knockout of individual COG subunits in HEK293T cells revealed severe Golgi cisternae fragmentation in all mutants, particularly in the COG 1-4 and COG 6 subunits. All knockouts displayed aberrant sialylation, fucosylation and oligomannose modification. By contrast, the trafficking defect was shown to affect all areas of the Golgi, including the *cis*-Golgi. Secretion of pro-CTSD and in some cases mature CTSD was a consistent finding with COG KOs with the exception of COG6 KO, which did not show any media CTSD expression. Further to this, LAMP2 hypoglycosylation was also very pronounced in all mutants apart from the COG6 one (Blackburn and Lupashin, 2016).

Additionally, the Blackburn and Lupashin paper from 2016 also showed the accumulation of enlarged lysosomal-like structures in COG Kos (Blackburn and Lupashin, 2016). A later study by the same group revealed the accumulation of missorted glycosylation enzymes in acidic endocytic-like organelles in COG-deficient cells (D'Souza *et al.*, 2019). These hybrid organelles were shown to originate from the Golgi due to the enrichment of cholesterol and Phosphatidylinositol 4-phosphate (PI4P). A hypothesis was brought forward whereby in the absence of functional retrograde Golgi traffic, GARP donates endocytic cargo to these intermediary Golgi-like compartments containing missorted glycosylation enzymes, resulting in the degradation of the latter. The generation of these intermediary structures was shown to be dependent on COG4 and VPS54 of GARP. Interestingly, though, these hybrid organelles lacked the expression of some lysosomal proteases such as cathepsin B (D'Souza *et al.*, 2019). It would be of particular interest to find out whether COG-deficiency in DRAM2 RPE also underlies the existence of similar hybrid structures. WB shown in Figure 46, A and B, does not show downregulation of VPS53 of GARP. The latter, however is significantly downregulated in CORD21-P1 RPE, alongside VPS51, as demonstrated by proteomics data. VPS53 and VPS51 are shared subunits between GARP and EARP, so both complexes may be affected. Still more conclusive evidence is required to establish the existence of such structures in DRAM2 RPE.

Given the changes in COG expression in CORD21-P1 and -P2, COG6 deficiency is in line with the neglible secretion of CTSD to the extracellular media, as well as there being no changes in the glycosylation status of LAMP2 in patient RPE cells (Figure 46, A and B). Based on literature findings, COG6 depletion observed here may likely be associated with pronounced structural and Golgi trafficking abnormalities. Interestingly, total COG6 deficiency has also been linked to the early postnatal lethality (Lubbehusen *et al.*, 2010). Future work could focus on combined IF and WB approaches looking into the lysosomal cargo localisation along with EGIC53 (ER-Golgi intermediate), GM130 (cis-Golgi) or TGN46 (trans-Golgi) trafficking compartments. Since Golgi fragmentation is a sign of apoptotic cells, experiments addressing the state of Golgi, should also entail the use of an apoptosis inhibitor. Consequently, Golgi examination could be carried out by TEM, WB (for the aforementioned markers), or a Cell Painting-High Content Image assay which would allow for assessment of spatial organisation and size of the Golgi compartment.

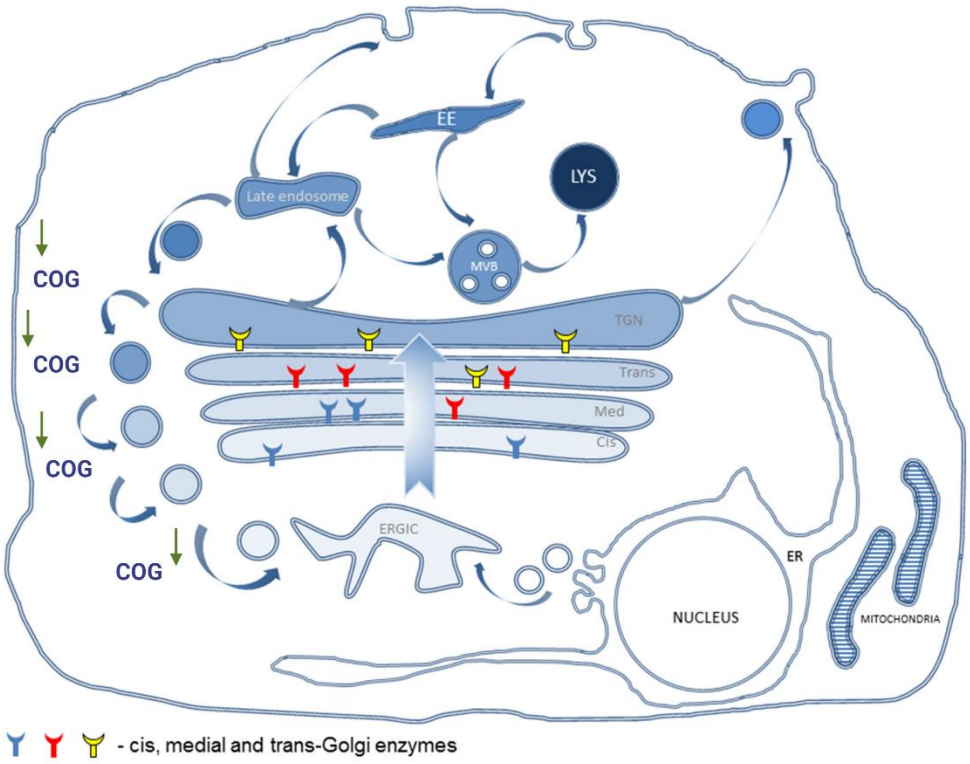

Figure 48 Schematic depicts the roles of COG in intra-Golgi retrograde and Golgi-ER-Golgi intermediate compartment (ERGIC) vesicular trafficking. The complex binds vesicular tethers at the TGN, Trans, Medial and Cis-Golgi and oversees retrograde vesicle delivery to the ER-Golgi intermediate (ERGIC). The multiprotein complex plays crucial roles in protein localisation along the secretory pathway, the maintenance of Golgi structural integrity and the trafficking of glycosylation enzymes. Green arrows indicate the potential downregulation of the COG complex in DRAM2 RPE. Image adapted from Blackburn, D'Souza and Lupashin, 2019.

5.5.2.6 Proteomics shows significant depletion of exocyst complex components in patient RPE cells.

Interestingly, RPE proteomics data also showed a significant downregulation of exocyst subunit components in CORD21-P1 (EXOC1-8, apart of from EXOC6). As mentioned

previously, exocyst belongs to the CATCHR family of tethering complexes. It enables TGN to PM transport along actin myotubules and plays an indispensable role in the recycling of primary cillia (Rivera-Molina *et al.*, 2021). A specific function has been outlined in POS maintenance in carrying out cilliary protein transport in zebrafish and the mouse (Lobo *et al.*, 2017). The same group later also uncovered that exocyst is essential for the maintenance of RPE, as conditional ablation of the major exocyst component, EXOC5, reduces melanosome number and impairs opsin expression in PRs of the same model organisms (Rohrer *et al.*, 2021). Exocyst depletion in CORD21-P1 could therefore explain a putative negative feedback loop aimed at minimising the PM secretion as evident from the significant extracellular release of PPT1 and NPC2 in DRAM2 RPE. Ultimately, this presents a mechanism of extracellular secretion directly from the TGN. Future experiments may thus investigate a potential involvement of DRAM2 in the regulation of exocyst tethers.

5.5.2.7 Depletion of AP-3, Arl8 and HOPS subunits indicates a major bottleneck at the level of the lysosome.

The key DRAM2 defect pertaining to lysosomal deficiency, however, poses the possibility of an endolysosomal bottleneck preventing endocytic cargo from being delivered to the lysosome. Regarding this, a fascinating new finding by the RPE proteomics was the downregulation of nearly all HOPS subunits in the more severely affected CORD21-P1 patient (VPS39, -18, -11, -16, -33B, -33B). CORVET and HOPS belong to the non-CATCHR family of multiprotein tethers functioning within the endolysosomal system. A protein core comprising VPS18, -11, -16 and -33 is shared between the two complexes. Yeast mutants of these proteins present with the most severe endolysosomal deficiencies (Balderhaar and Ungermann, 2013). CORVET is involved in endosome sorting and the fusion of early endosomal compartments by binding to the Rab5 GTPase. HOPS, on the other hand, has a specialised role in enabling the fusion of $Rab7^{+}$ late endosomes (LE) with lysosomes (Spang, 2016). A compounded CORVET/HOPS deficiency in CORD21-P1 may thus be associated with severe endosome maturation defects. The CORVET to HOPS tether switch underlies one of the key molecular transitions of a LE to a lysosome. The sequential order of events in endolysosomal fusion was detailed by Schleinitz *et al*., (2023) (Figure 49). Initially, recruitment of Rab7 by LE promotes the movement of LE towards lysosomes along dynein-bound microtubules. The transient

interaction of Rab2 GTPase with the LE in turn summons the HOPS tethering complex which establishes a bridge with Arl8/BORC^{+} lysosomes. Here, Arl8 is outlined as a novel lysosome-specific marker, which can be used to distinguish between the two structures (Schleinitz *et al.*, 2023). Once the organelles are bridged, HOPS enables the binding of SNARE proteins Syntaxin 8, Syntaxin 7, Vti1b with Vamp8,-7 or Ykt6 to facilitate fusion (Pryor *et al.*, 2004; Davis *et al.*, 2021). The process of cargo delivery was found to depend on the expression of Rab2, Rab7, Arl8, HOPS and BORC. Although Rab2a knockdown significantly reduced the merging of the two structures, neither Arl8 nor Rab2a were indispensible for the anchoring of HOPS, suggesting that additional proteins may facilitate this process. Rab2a's localisation pertains to the Golgi, whereby it is hypothesised that it enters the endocytic pathway as a membrane-bound protein (Chavrier *et al.*, 1990). The authors of the paper outline HOPS interactors as crucial coordinators of LE-lysosome fusion, with the role of Arl8 needing further clarification, as to whether it solely enables fusion or represents a transport regulator.

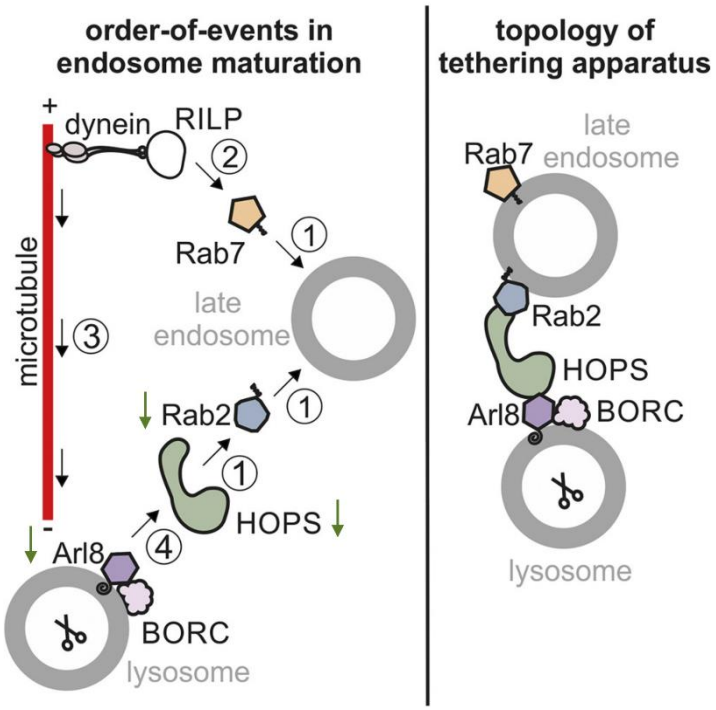

Figure 49. Late endosomes (LEs) mobilise Rab7, Rab2 GTPases and HOPS prior to fusion with Arl8-expressing lysosomes. Rab7 is not present at sites of HOPS-mediated LE-lysosome fusion, however, indirectly promotes the fusion process by positioning LE close to lysosomes via microtubule-attached dynein. HOPS then facilitates LE-LYS fusion by enabling an

interaction between late endosomal Rab2a with lysosomal BORC-bound Arl8. Green arrows show proteins downregulated in DRAM2 ROs and RPE. (Image taken from Schleinitz et al. (2023).

Interestingly, Arl8a was downregulated in CORD21-P1 ROs as well as CORD21-P2 RPE according to the proteomics data. RPE proteomics inequivocally suggests the downregulation of Rab2a GTPase in both patients. Collectively, this indicates that a compromised LE-Lysosomal fusion may highlight an important aspect of the DRAM2 disease. The inconsistency of some of these differences between patients may be explained by the dynamic and transient nature of vesicular interactions. Alternatively, acquisition of *in vitro* phenotype requires more time to develop, considering the adult onset of the condition. These data provide important first steps in the unravelling of DRAM2 molecular phenotype.

The relevance of AP-3 to HOPS-mediated LE-lysosome fusion has been outlined previously (chapter 4). AP-3 is a known lysosomal transporter and an interactor of HOPS, suggesting that HOPS enables the tethering of incoming AP-3 $^{+}$ clathrin coated vesicles (Schoppe *et al.*, 2020). Binding of AP-3 vesicles arriving from the Golgi only becomes feasible after the phoshorylation of HOPS following a VPS41-curvature sensing mechanism activated at the lysosomal interface (Cabrera *et al.*, 2010). Aberrant AP-3 targeting has been linked to protein retention at the Golgi and PM protein rerouting (Feng *et al.*, 2017) and inactivation of HOPS, has further been shown to lead to the mislocalisation of AP-3 transport of EGOC (EGO complex) targets to the Golgi (Gao *et al.*, 2022).

According to our WB data, AP-3 is significantly downregulated in the RPE of CORD21-P2. Proteomics data in RPE also corroborrated the downregulation of AP-3 in CORD21-P1 (AP3B2, AP3D1, AP3M2, AP3M1, AP3S1 subunits). AP-3 deficiency in RPE could furthermore explain the defective NPC2 lysosomal delivery, as the latter depends partially on AP-3 mediated transport (Berger *et al.*, 2007). Moreover, AP-3 depletion in our dataset may underlie the inefficient maturation of stage III to stage IV melanosomes due to the compromised transport of melanogenic enzymes (Figure 46) (Raposo and Marks, 2007). In light of this, DRAM2 co-localisation with AP-3 suggests the involvement of DRAM2 in AP-3-mediated lysosomal transport (chapter 4). Further work on DRAM2 ROs and RPE could establish the exact role of DRAM2 in regulating AP-3 trafficking and and how this may affect HOPS-mediated lysosomal fusion.

5.6. Concluding remarks

Additional insight into the vesicular trafficking is rendered by the volcano plots shown in Figure 45, E. Individual comparison between CORD21-P1 vs -P1c reveals the CORD21-P1 downregulation of novel targets related to membrane trafficking and the maintenance of membrane dynamics such as Synaptophysin (SYP), Ras-related protein Rab-3A (RAB3A), Vesicle-associated membrane protein 2 (VAMP2), Clathrin coat assembly protein AP180 (SNAP91), Bridging integrator 1 (BIN1), Kinesin-like protein KIF1A (KIF1A), Phosphatidylinositol 4-phosphate 5-kinase type-1 gamma (PIP5K1C), EARP and GARP complex-interacting protein 1 (EIPR1), Collectrin (CLTRN) and AP-1 complex subunit gamma-1 (RABEP1).

SYP is a presynaptic vesicles membrane protein but also a marker for synaptic connectivity in RO cultures (Wiedenmann *et al.*, 1986; Ludwig *et al.*, 2023). Reduced expression of SYP leads to the poor expression of synaptic processes but also reduced endocytic recycling in neuronal tissue (Kwon and Chapman, 2011; Ludwig *et al.*, 2023). Rab3a is involved in the positioning of lysosomes close to the PM in the facilitation of PM repair by lysosomal exocytosis (Encarnacao *et al.*, 2016). VAMP2 governs the merging of membranes in the presynaptic secretory domain and exocytosis (Yan *et al.*, 2022), whereas BIN1 is a key protein involved in membrane curvature remodelling, and its overexpression has been associated with aberrant endocytic size reported in Alzheimer's disease (Lambert *et al.*, 2022). Furthermore, PIP5K1C regulates the attachment of exocyst to the PM (Maib and Murray, 2022). CLTRN has been shown to be able to regulate exocytosis of insulin by interacting with SNAPIN, thereby affecting the assembly of the SNARE complex (Fukui *et al.*, 2005). Collectively, these data may indicate an attempt to limit exocytic mechanisms leading to the loss of lysosomal enzymes in CORD21 RPE.

Further evidence for the involvement of DRAM2 in the cellular transport dynamics is shown by the reduced expression of KIF1A, EIPR1 and RABEP1, amongst others. KIF1A governs vesicular trafficking in neuronal cells by controlling microtubule dynamics (Oriola *et al.*, 2015). EIPR1 oversees the sorting of dense-core vesicles at the TGN together with Rab2 and the EARP complex (Topalidou *et al.*, 2016), and regulates endocytic recycling and the localisation of the EARP complex (Topalidou *et al.*, 2020). RABEP1 is a protein that mediates

a crosstalk between endosomes and autophagy. Indeed, membrane endosomal damage can trigger the initiation of selective autophagy via RABEP1 (Millarte and Spiess, 2022).

By contrast, the most significantly changed targets by logged FC and p value in Figure 45, E for CORD21-P2 vs -P2c (FBN1, FN1, LIPG, CRISPLD1, NES, FBLN5, SFRP5, STRA6, COG7, MT-ND5, THBS1, MYH11, COL12A1, GFRA2, VCAN, THY1, DCN, LXN, S100A1), show an emphasis on protein response to metabolic stimuli, mitochondrial stress and fiber assembly, which can be a substrate for RPE growth and structural support (Srivastava *et al.*, 2011; Navneet and Rohrer, 2022). Further WB experiments on AP-1, AP-2 did not show downregulation of these proteins, despite proteomics data corroborating the downregulation of both clathrin adaptors in CORD21-P1 and -P2 (AP1M1, AP1B1, AP1G1, AP2M2, AP2A2, AP2A1).

In summary, data outlined in this chapter provides evidence for a vesicular trafficking defect leading to a pronounced lysosomal deficiency in the RPE of DRAM2 patients. In support of this are the CTSD, PPT1 and NPC2 lysate deficits established by proteomics and WB. An inherent lack of lysosomal hydrolases was further corroborated for CTSD, GBA and MAN2B1 as determined by enzyme activity assays. These data were in line with the concomitant secretion of PPT1 and NPC2 explaining the loss of these enzymes due to potential misrouting to extracellular media. The lack of lysosomal enzymes was consistent with ultrastructural findings suggesting LCO accumulation and the presence of abnormal mitochondria in CORD21-P1 challenged RPE cells. Comprehensive proteomics analysis further suggested the involvement of DRAM2 in the regulation of TRAPP, COG and exocyst multiprotein complexes which collectively govern ER-Golgi, Golgi-ER, Golgi-PM transport as well as autophagy. Furthermore, volcano plots revealed numerous proteins that are heavily involved in the regulation of exocytosis. The mistrafficking of NPC2 could be explained by AP-3 deficiency in CORD21-P2 by WB and in CORD21-P1 RPE cells by proteomics. A deficit in clathrin-mediated transport also referred to in the previous chapter (AP-1 downregulation in CORD21-P1) stands in agreement with the broad downregulation of AP-1 and AP-2 subunits in both CORD21-P1 and -P2 RPE patients by proteomics. Deficiencies observed in AP-3, HOPs as well as Arl8 by proteomics unequivocally suggest the existence of an endolysosomal bottleneck. Such a bottleneck could prevent the delivery of lysosomal hydrolases and melanogenic enzymes, the

latter of which are crucial for the maturation of melanosomes and the phagocytic potential of RPE cells. Future work may entail the careful investigation of all putative mechanisms in which DRAM2 may be able to exert vesicular control over the delivery of lysosomal cargo.

6. General discussion

DRAM2 retinopathy is a recessive form of cone-rod dystrophy presenting with a clinical phenotype between the third and the sixth decades of life. The onset and severity of the disease have been shown to differ significantly based on the type of genetic defect observed. A pilot study conducted by El-Asrag *et al*. (2015), was the first one to show that biallelic missense, frameshift, and in-frame deletion variants in *DRAM2* lead to macular degeneration consistent with early cone PR loss. This was often followed by peripheral retinal damage as the disease progressed.

A subsequent paper by the same group and collaborators (Sergouniotis *et al.*, 2015), established that loss-of-function mutations exhibit a more severe phenotype than missense variants or in-frame deletions, presenting with an earlier disease onset. This is in keeping with the initial proposition made by El-Asrag *et al*. (2015) that more severe retinal dysfunction may be delayed in patients with in-frame deletions. Fundus autofluorescence imaging (FAF) conducted by Sergouniotis *et al*., suggested that rings of hyperautofluorescence correspond to regions where loss of POS in the PRs still presents with normal RPE function. This could be explained by the increased detection of RPE cells in the absence of PRs or simply the higher accumulation of lipofuscin in degenerating retinal cells (Krasovec *et al.*, 2022). These hyperautofluorescent rings surround macular lesions of hypoautofluorescence where RPE is completely lost. Over time, these rings would enlarge and spread over to the rest of the retina. OCT findings in pre-symptomatic patients agree with these data and indicate that loss of PRs may be a key initial feature of the disease. Abad-Morales *et al*., (2019) and others, have further expanded on the phenotype of *DRAM2* retinopathy, showing that the disease can also manifest in the sixth decade of life (frameshift variant). The latter conclusion has also been corroborated in the case of a more benign missense mutation leading to misdiagnosis of the condition for AMD in the sixth decade of life (patient II, c.3G > A/, c.737T > C) (Krasovec *et al.*, 2022).

Abad-Morales *et al*., (2019) assessed the contribution of homozygous frameshift and alternative splicing variants to peripheral retinal degeneration. They outline that frameshift mutations exhibit a less severe phenotype (also depending on the level of transcript degradation, i.e., PTC location) compared to mutations associated with alternative splicing (c.693 +2T>A patient). Frameshift mutations contained the processes of retinal degeneration to the mid-periphery, whereas an alternative splicing variant led to a severe retinal decline and RPE disturbances. According to Abad-Morales *et al*. alternative splicing did not lead to a reduction in transcript expression, as was the case for frameshift mutations, which lead to the removal of aberrant transcripts by NMD. Interestingly, frameshift variants, presented with initial foveal sparing on FAF in this study. The nature of the foveal sparing remains unclear; however, the latter has previously been reported in ABCA4 and PRPH2 dystrophies (Krasovec *et al.*, 2022). These data hold implications for extensive RPE damage pertaining to mutations spanning the sequence of the *DRAM2c* isoform. *DRAM2c* (exons 6-9) is shorter than the *DRAM2a* isoform (exons 3-9), and all sequence of *DRAM2c* is also present in the *DRAM2a* isoform. In this study the extent of RPE damage is particularly extensive for the patient carrying a splicing mutation which could affect both isoforms (c.693+2T>A). Alternative splicing then appears to correlate with higher phenotypic severity in RPE which could be related to the malfunctioning or gain-of-function of *DRAM2a* and *DRAM2c* isoforms. Naturally this would be compounded by a defect in both isoforms, as both isoforms are relevant to retinal function, leading to a more pronounced defect and an earlier disease onset.

Collectively, *DRAM2* mutations can be grouped into two major categories based on the type of genetic impact – null and non-null mutations. Missense and in-frame variants which are more benign and result in delayed phenotypic development compared to the more severe loss-of-function mutations, which manifest by the third decade of life (El-Asrag *et al.*, 2015; Sergouniotis *et al.*, 2015). An even more severe phenotype, however, is seen with mutations which could lead to alternative splicing due to the potential toxic gain-of-function or the expression of a dysfunctional DRAM2 protein (Abad-Morales *et al.*, 2019). Considering all the clinical reports to date as well as the RO and RPE phenotypes observed here, the severity of DRAM2 deficiency should be assessed based on whether it affects both isoforms of the protein. An interesting observation has been that a lot of the clinical cases, pertaining to a more benign disease progression in the case of missense mutations, (with all missense

variants except for one), appear to affect the ubiquitously expressed DRAM2a but not the DRAM2c isoform (c.737T > C). The aforementioned variant has previously been designated as a variant of uncertain significance (p. Leu246Pro), and as mentioned above, in a heterozygous state leads to a significantly delayed disease onset. Notwithstanding, more severe phenotypes correlate with frameshift and alternative splicing mutations, particularly such that affect both isoforms (Krasovec *et al.*, 2022) .

Even though, CORD21-P2 also contains a mutation that likely affects alternative splicing (c.131G>A), this mutation is not present in the retinal-specific *DRAM2c* isoform. This would suggest that the CORD21-P2 phenotype is milder and not comparable to the one observed in patient III (c.693 +2T>A) (Abad-Morales *et al*., 2019). This is consistent with what is seen in the original El-Asrag paper, showing that CORD21-P2 exhibits significantly slower disease progression to CORD21-P1 which lacks the DRAM2a isoform, but should be expected to express isoform DRAM2c, even though our protein experimental approaches did not succeed in detecting it by WB (~17kDa). Our study presents an interesting case, whereby phenotype appears to arise due to dysfunctional DRAM2a isoform, since both c.140G>A (CORD21-P1, homozygote) and c.131G>A (CORD21-P2, compound heterozygote) refer to genetic sequence, not present in the retinal-specific *DRAM2c* isoform. Only the c.494G>A mutation borne by the CORD21-P2 patient would be expected to affect the *DRAM2c* isoform. Hence, DRAM2c- related phenotype would not be outcome for CORD21-P1 and -P2. Future work ought to focus on the qPCR expression of the retinal-specific *DRAM2c* isoform in RO and RPE and its relative contribution to disease.

To date, all information regarding this form of dystrophy comes from 19 unique variants describing DRAM2 disease as a recessive condition. Our data unanimously suggests that DRAM2 retinopathy can arise as a recessive condition affecting both PRs and RPE due to a deficiency in the ubiquitously expressed DRAM2a isoform. The importance of this main isoform is also further corroborated by the severe disease progression seen in the homozygous c.3G > A/ patient (Krasovec *et al.*, 2022). Deficiency in DRAM2a could have a tissue-specific effect due to the essential function of DRAM2 in maintaining lysosomal and autophagy function of PRs and RPE, as shown by the particular susceptibility of these cell types in this PhD study. Ultimately, mutations affecting both isoforms may result in an even

more severe phenotypic progression that could be particularly relevant for DRAM2c expression in the RPE (Abad-Morales *et al.*, 2019). Due to its apical expression in the RPE, DRAM2 could be affecting apicobasal polarity and future work may focus on establishing expression patterns with regards to Par, Scribble and Crb. As becomes obvious from this study, CORD21-P1 and CORD21-P2 RPE display similar vesicular trafficking defects (NPC2 and PPT1) and lysosomal deficiency to patient-derived ROs. Based on DRAM2 literature data, however, more severe RPE phenotype may be expected for patients that carry mutations in the genetic sequence of both isoforms. The role of both isoforms in retinal tissue remains to be further elucidated with regards to PRs and RPE. Detailed expression analyses of both isoforms in retinal tissues and the examination of a further cohort of DRAM2 patients would enable us to bridge the gap with clinical data in the future.

As major responders to cell stress and environmental cues, lysosomes are particularly relevant to the maintenance of postmitotic neuronal tissue. Lysosomal vulnerability is additionally compounded during the course of ageing as one of the main roles of endolysosomes besides degradation pertains to the maintenance of synaptic function via the dynein-facilitated neuronal transport of maturing endolysosomes. This can turn out to be challenging in axons with particularly long neurites. It is hence not surprising that many neurodegenerative conditions present with disturbances in lysosomal trafficking (Lie and Nixon, 2019). Data acquired throughout this project suggests that DRAM2 deficiency leads to the depletion of CTSD, NPC2, PPT1, MAN2B1 and GBA in the lysosomes of ROs and RPE due to vesicular mistrafficking. As shown, the lysosomal downregulation of PPT1 and NPC2 might be due to the secretion of these lysosomal enzymes to extracellular media in both patient cell models. The lack of PPT1 is expected to lead to elevated lysosomal pH which in turn would render CTSD unable to mature fully to be able to carry out its crucial function in bulk lysosomal degradation (Bagh *et al.*, 2017). The severely compromised CTSD function would inevitably lead to the accumulation of lysosomal waste and the formation of GROD deposits, here reported as curvilinear lipopigments (CLs). The CLs observed here, represent a mix of the types of GROD features reported in *CLN1* (PPT1) and *CLN10* (CTSD) NCL deficiencies, which is in line with our findings. The presence of a minimal amount of these enzymes in the lysosomes of our patient ROs and RPE is consistent with the observed retinal phenotype. Notably, complete loss of either of these proteins is strongly associated with cognitive decline but also

poor survival prognosis (Williams and Mole, 2012; Schulz *et al*., 2013; Ribeiro *et al*., 2001; Park *et al*., 2003; Vanier and Millat, 2003; Pentchev, 2004; Chang *et al*., 2005; Evans and Hendiksz, 2017, Santavuori *et al*., 1973, Weleber 1998; Weleber *et al*., 2004; Jalanko and Braulke, 2009). As previously mentioned, some functional redundancy exists in the case of CTSD which can be shuffled to the lysosome by both M6PRs and sortilin, and this appears to also be the case for NPC2 and PPT1. The lack of CTSD in RO and RPE media is in line with the COG6 deficiency identified in patient RPE samples (Blackburn and Lupashin, 2016). Interestingly, COG-deficiency has been associated with the occurence of hybrid Golgi-endocytic compartments, which in the absence of functional retrograde Golgi transport would accumulate and degrade missorted glycosylation enzymes (D'Souza *et al.*, 2019). Notably, hypoglycosylation changes have also been observed on multiple accounts for protein targets subjected to WB in this study (LIMP2, LAMP1 and LAMP2).

Collectively, the lysosome deficiencies appear to be affected by the overarching clathrin-mediated mechanisms pertaining to the function of AP-1, AP-3 and AP-2 (requires further validation of proteomics data) (Figure 50). The co-localisation of DRAM2 expression with both AP-1 and AP-3 at the IS of WT ROs on IF corroborated WB and proteomics findings in patient ROs and RPE. AP-1 and AP-3 clathrin adaptors regulate the bidirectional transport of cargo and receptors (M6PRs, LIMP2 etc) from the TGN to endosomes (AP-1), endolysosomal cargo delivery (AP-3) and secretion through the PM (AP-2). Furthermore, the transport of the NPC2 and GBA via LIMP2 is known to be controlled by both AP-1 and AP-3 (Honing;Sandoval and von Figura, 1998; Fujita *et al.*, 1999; Berger *et al.*, 2007; Reczek *et al.*, 2007; Blanz *et al.*, 2015; Zunke *et al.*, 2016).

The deficiencies of NPC2 and GBA are in agreement with the accumulation of sphingolipid species observed by lipidomics analysis -the upregulation of ceramide and GM3 ganglioside species. The depletion of phospholipids and the glycosylation changes seen in patient samples are furthermore in line with a dysfunction in the GARP complex, however further experimental work is required to confirm the potential deficiency of this complex. Collectively, these would be consistent with the features of NPC disease and the transport mechanisms which could affect the delivery of NPC2 such as M6PR, GARP and clathrin-adaptor proteins. Another mechanism governed by LYSET, has recently been described,

which enables GlcNAc-1-phosphotransferase retention at the Golgi (Pechincha *et al.*, 2022; Richards *et al.*, 2022; Zhang *et al.*, 2022). In LYSET KO cells, a broad depletion of TPP1, PPT1, CTSD, NPC2, MAN2B1 enzymes and their extracellular secretion could provide a viable explanation for the phenotypes observed here. Additionally the ER-Golgi defect and protein PM secretion, pertaining to PPT1 deficiency provides an additional mechanism that may link the absence of DRAM2 with the secretion of protein cargo through the PM (Figure 50).

Notably, the downregulation of AP-3, HOPS and Arl8 points towards a problem with endo-lysosomal fusion or tethering of incoming AP-3 vesicles at the lysosome, which would directly impact the delivery of lysosomal cargo and the maturation of melanosomes in the RPE (Figure 50). Schematic outlined below shows the putative transport mechanisms which could liase with DRAM2 to enable the delivery of lysosomal enzymes (Figure 50). NPC2 secretion has been described in the absence of LYSET and HOPS reiterating the potential existence of cargo stalling at the TGN and at the lysosome. As revealed by proteomics analysis the downregulation of multi-subunit complexes TRAPPIII, TRAPPII, COG and exocyst in patient RPE likely affects intracellular dynamics at multiple stages of the protein secretory pathway (Figure 50). Particularly interesting would be to examine the involvement of ER-Golgi traffic (TRAPPIII) and intra-Golgi traffic (COG complex). This is because we have been able to confirm co-localisation of DRAM2 with the cis-Golgi marker GM130 (chapter 4), but also due to the multiple extra-lysosomal locations having been reported for PPT1, including the ER, Golgi, and membrane rafts (Kollmann *et al.*, 2013; Segal-Salto;Sapir and Reiner, 2016; Segal-Salto *et al.*, 2017; Sapir *et al.*, 2019). Co-localisation of DRAM2 and PPT1 would also be logical provided that PPT1 is transported in $DRAM2^{+}$ vesicles. An involvement of DRAM2 in the regulation of TRAPPIII and COG traffic would hence explain a malfunction in anterograde and retrograde ER-Golgi traffic. In addition, TRAPPIII has also been shown to be important for the activation of conventional autophagy which may provide further clues to the accumulation of CLs, LBs, LCOs and aberrant mitochondria in patient RO and RPE samples.

Here, for the first time we describe RO and RPE phenotypes associated with DRAM2 retinal dystrophy. We have confirmed the expression of DRAM2 in the IS of WT and isogenic controls, as well as the expression of DRAM2 in the cis-Golgi, mitochondria and AP-1 and -3

coated vesicles. Further work on this project will be aimed at clarifying the exact mechanisms by which DRAM2 is able to facilitate the transport of lysosomal cargo.

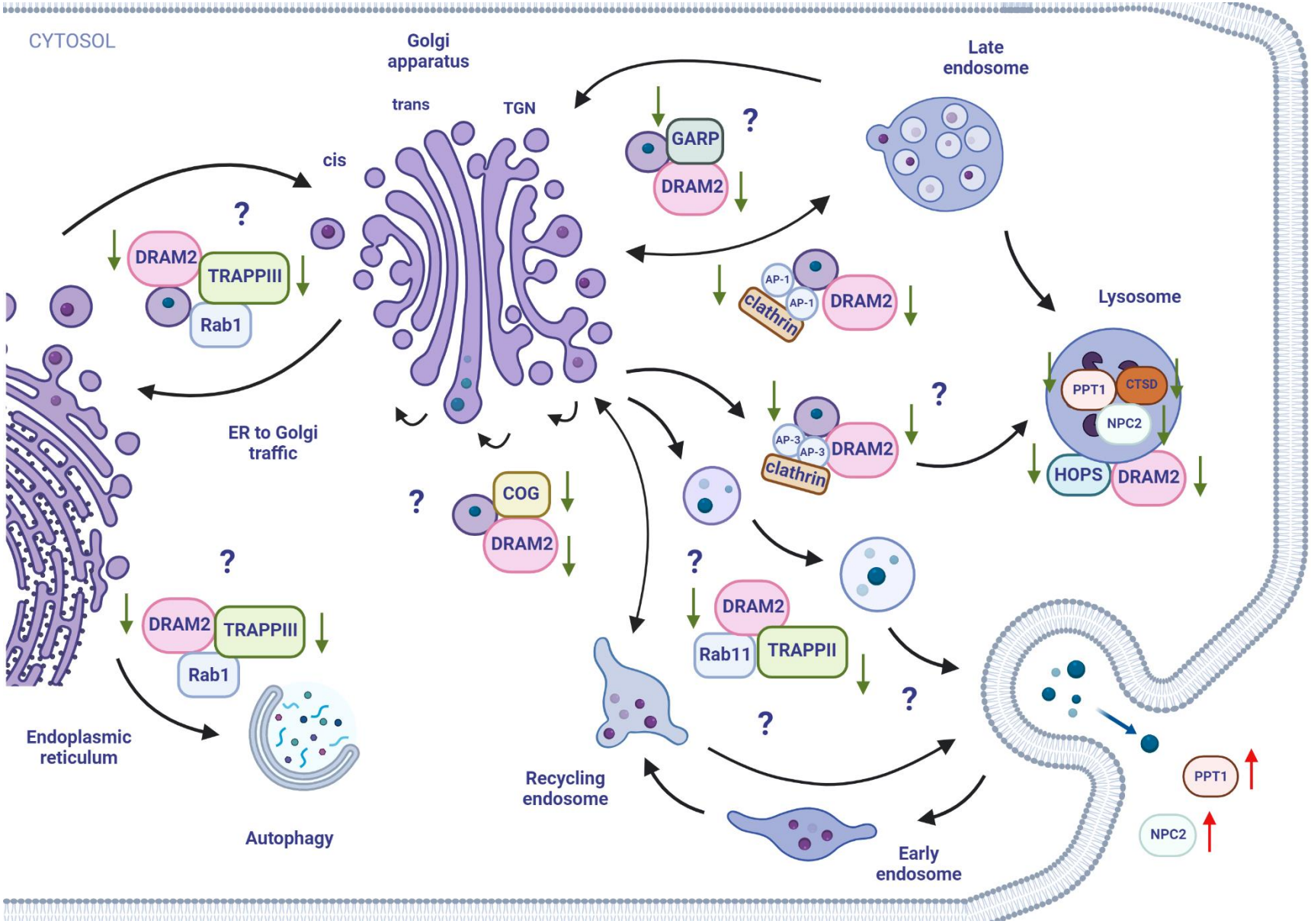
CYTOSOL
Golgi apparatus
trans
TGN
cis
Late endosome
Lysosome
GARP
DRAM2
TRAPPIII
Rab1
AP-1
clathrin
AP-3
COG
HOPS
PPT1
CTSD
NPC2
Rab11
TRAPPII
ER to Golgi traffic
Endoplasmic reticulum
Autophagy
Recycling endosome
Early endosome

Figure 50. Hypothetical roles of DRAM2 in vesicular-mediated transport. Illustration depicts putative scenarios in which DRAM2 protein could affect cellular trafficking. Depletion of TRAPPIII subunits as a result of DRAM2 deficiency could directly or indirectly compromise bidirectional membrane transport from ER-to-Golgi via downregulation of Rab1 activity. Reduced activity of Rab1 could also abrogate the activation of the conventional autophagy pathway, resulting in inefficient autophagic clearance. Analogously, downregulation of TRAPPII could affect Rab11-dependent Golgi-to-PM transport via the recycling endosome. Depletion of COG6 components could account for a dysfunction in intra-Golgi and Golgi-to-ER retrograde traffic, leading to Golgi structural defects and the mistrafficking of glycosylation enzymes. In the absence of a functional COG complex, these could get degraded in hybrid Golgi-endolysosomal structures. DRAM2 could also orchestrate retrograde transport from the late endosome to the TGN by recruiting the GARP complex. Analogously, DRAM2 could be important for the bidirectional delivery of cargo between the endosome and the TGN mediated by AP-1. Depletion of HOPS could crucially underlie a major lysosomal bottleneck i.e., endosome-to-lysosome maturation as well as the tethering of AP-3 vesicles to $HOPS^{+}$ lysosomes, thereby downregulating lysosomal targeting with a major impact on the lysosomal enzyme abundance. Protein downregulation and upregulation is marked by green and red arrows, respectively. Ultimately, DRAM2 deficiency leads to the lysosomal deficiency of CTSD, PPT1 and NPC2 and the extracellular secretion of the latter enzymes.

Appendices

Appendix A

Table 24. Cas9 gRNA synthesis primers

ID	Gene	Mutation target	Target F1 primer sequence	Target R1 primer sequence
1	*DRAM 2*	c.140delG	TAATACGACTCACTATAGTGGGGCAATGC TAAAT	TTCTAGCTCTAAAACCAATATTTAGCAT TGCCCC
2	*DRAM 2*	c.131G>A	TAATACGACTCACTATAGACTTGATATAA GGTAA	TTCTAGCTCTAAAACGGCTTTACCTTAT ATCAAG

Table 25. Cas9 target gRNA details

Cut Position	Strand	Mutation target	gRNA sequence	PAM	Efficiency (on-target) score	Specificity (off-target) score
111126242	-	c.140delG	TGGGGCAATGCTAAATATTG	CGG	57.4	49.0
111131439	+	c.131G>A	ACTTGATATAAGGTAAAGCC	GGG	61.7	74.7

Table 26. ssODN sequence

Strand	Mutation target	ssODN sequence
+	c.140delG	AGAAGAAATATATGTGTTTATCTAGTATGAGAAATCCACATACCTTCCT TTTTTTCTTTCAGTGACCTGGTACAGTAGCTCCAGAAAAATGCTTATTTG GGGCAATGCTAAATATTGCAGCCGTTTTATGTAAGTAATGA
-	c.131G>A	TGGACATCTGCTGCTTTCATATTTTCATACATTACTGCAGTAACACTCCA CCATATAGATCCAGCTTTACCTTATATCAGGTAAGTGAAATGTATTCTTT G

Appendix B

Fig.1S -Supplementary off-target sequencing blastn data

C.140delG off-targets:

1)

Homo sapiens DNA damage regulated autophagy modulator 2 (DRAM2), transcript variant 1, mRNA.

Sequence ID: NM_001349881.2 **Length:** 2143 **Number of Matches:** 1

Range 1: 473 to 545 GenBank Graphics ▼ Next Match ▲ Previous Match

Score	Expect	Identities	Gaps	Strand
132 bits(146)	5e-29	73/73(100%)	0/73(0%)	Plus/Plus

```
Query  31   TCAGTGACACTGGTACAGTAGCTCCAGAAAAATGCTTATTTGGGGCAATGCTAAATATTG  90
            ||||||||||||||||||||||||||||||||||||||||||||||||||||||||||
Sbjct  473  TCAGTGACACTGGTACAGTAGCTCCAGAAAAATGCTTATTTGGGGCAATGCTAAATATTG  532

Query  91   CGGCAGTTTTATG  103
            |||||||||||||
Sbjct  533  CGGCAGTTTTATG  545
```

2)

Homo sapiens chromosome 4, GRCh38.p14 Primary Assembly

Sequence ID: NC_000004.12 **Length:** 190214555 **Number of Matches:** 1

Range 1: 98112899 to 98112949 GenBank Graphics ▼ Next Match ▲ P

Score	Expect	Identities	Gaps	Strand
93.3 bits(102)	8e-18	51/51(100%)	0/51(0%)	Plus/Plus

Features: sperm-tail pg-rich repeat-containing protein 2 isoform x3
sperm-tail pg-rich repeat-containing protein 2 isoform x2

```
Query  1         AAAAGAGTGGCAATGCTAAATACTGGGGATTTTCTGTCAACTGGGTTTGCG  51
                 |||||||||||||||||||||||||||||||||||||||||||||||||||
Sbjct  98112899  AAAAGAGTGGCAATGCTAAATACTGGGGATTTTCTGTCAACTGGGTTTGCG  98112949
```

3)

Homo sapiens chromosome 21, GRCh38.p14 Primary Assembly

Sequence ID: NC_000021.9 **Length:** 46709983 **Number of Matches:** 1

Range 1: 14242048 to 14242161 GenBank Graphics ▼ Next Match ▲ Previous Ma

Score	Expect	Identities	Gaps	Strand
196 bits(216)	3e-48	110/114(96%)	0/114(0%)	Plus/Plus

Features: 14755 bp at 5' side: splicing regulator rbm11 isoform x3
131456 bp at 3' side: heat shock 70 kda protein 13 precursor

```
Query  2         ATAGACTTGGCAATGCWAAATACTGGGTTCTGTAATAACAGCCCTCACAACWAGGAGTTG  61
                 |||||||||||||||| ||||||||||||||||||||||||||||||| ||||||||
Sbjct  14242048  ATAGACTTGGCAATGCTAAATACTGGGTTCTGTAATAACAGCCCTCACAACTAGGAGTTG  14242107

Query  62        GCTTTTGACWAAATTGGCTGGTCAGTGCTATRAGATTCATGAGCGTCCTATTAG  115
                 ||||||||| |||||||||||||||||||| |||||||||||||||||||||
Sbjct  14242108  GCTTTTGACTAAATTGGCTGGTCAGTGCTATGAGATTCATGAGCGTCCTATTAG  14242161
```

4)

Homo sapiens chromosome 17, GRCh38.p14 Primary Assembly

Sequence ID: NC_000017.11 **Length:** 83257441 **Number of Matches:** 1

Range 1: 10978959 to 10979083 GenBank Graphics ▼ Next Match ▲ Previous Match

Score	Expect	Identities	Gaps	Strand
221 bits(244)	9e-56	123/125(98%)	0/125(0%)	Plus/Plus

Features: 153314 bp at 5' side: phosphoinositide-interacting protein
262340 bp at 3' side: protein shisa-6 isoform 1 precursor

```
Query  1         AAATAATGTAGGGAAATGCWAGATATTGGGGTTCAGAAGTCTGCCTAATCTGAATCAAAT  60
                 |||||||||||||||||| ||||||||||||||||||||||||||||||||||||||||
Sbjct  10978959  AAATAATGTAGGGAAATGCTAGATATTGGGGTTCAGAAGTCTGCCTAATCTGAATCAAAT  10979018

Query  61        CCTTAGGCACCACAATTGTTTGAAGGACTCCATAGTGCTGCGCAGCMAGAGAGCAGCAAT  120
                 |||||||||||||||||||||||||||||||||||||||||||| ||||||||||||
Sbjct  10979019  CCTTAGGCACCACAATTGTTTGAAGGACTCCATAGTGCTGCGCAGCCAGAGAGCAGCAAT  10979078

Query  121       ACAAA  125
                  |||||
Sbjct  10979079  ACAAA  10979083
```

5)

Homo sapiens chromosome 9, GRCh38.p14 Primary Assembly

Sequence ID: NC_000009.12 **Length:** 138394717 **Number of Matches:** 1

Range 1: 109805515 to 109805651 GenBank Graphics ▼ Next Match ▲ Previous Match

Score	Expect	Identities	Gaps	Strand
248 bits(274)	7e-64	137/137(100%)	0/137(0%)	Plus/Minus

Features: paralemmin-2 isoform 2 (palm2)
palm2-akap2 protein isoform x8

```
Query  1          ACTGGGGCAGCTCTAAATATTGAGGAATTTTTTCCTTATCTTGCATTGACAGCTGCCTCC  60
                  ||||||||||||||||||||||||||||||||||||||||||||||||||||||||||||
Sbjct  109805651  ACTGGGGCAGCTCTAAATATTGAGGAATTTTTTCCTTATCTTGCATTGACAGCTGCCTCC  109805592

Query  61         CCGAAACTGATAGCCACAGGTTTTGGACTTGATCCTACTTTTATAACTAGTTGTACATTT  120
                  ||||||||||||||||||||||||||||||||||||||||||||||||||||||||||||
Sbjct  109805591  CCGAAACTGATAGCCACAGGTTTTGGACTTGATCCTACTTTTATAACTAGTTGTACATTT  109805532

Query  121        GTGTTTCCAGTGCCAAA  137
                  |||||||||||||||||
Sbjct  109805531  GTGTTTCCAGTGCCAAA  109805515
```

6)

Homo sapiens forty-two-three domain containing 1 (FYTTD1), transcript variant 2, mRNA.

Sequence ID: NM_001011537.3 **Length:** 6824 **Number of Matches:** 1

Range 1: 4003 to 4160 GenBank Graphics ▼ Next Match ▲ Previous Match

Score	Expect	Identities	Gaps	Strand
272 bits(301)	8e-71	153/158(97%)	0/158(0%)	Plus/Plus

```
Query  1     AGTGACACTCTGTCTTaaaaaaacaaaaaaaaaGAATCMAGTATACTTTGCAATGCARAA  60
             ||||||||||||||||||||||||||||||||||| |||||||||||||||||||| ||
Sbjct  4003  AGTGACACTCTGTCTTAAAAAAACAAAAAAAAAGAATCCAGTATACTTTGCAATGCAGAA  4062

Query  61    TATTGGGTTAGATGAGCCTTTAGAGACWAATCMAGTTTAACCCCTCCTTTTTACACCTTA  120
             ||||||||||||||||||||||||||| |||| ||||||||||||||||||||||||||
Sbjct  4063  TATTGGGTTAGATGAGCCTTTAGAGACTAATCCAGTTTAACCCCTCCTTTTTACACCTTA  4122

Query  121   GTAAAGTGAGTCCWAGTGTTTTCAAGACTTGCATGTGG  158
             |||||||||||| |||||||||||||||||||||||||
Sbjct  4123  GTAAAGTGAGTCCTAGTGTTTTCAAGACTTGCATGTGG  4160
```

7)

Homo sapiens chromosome 6, GRCh38.p14 Primary Assembly

Sequence ID: NC_000006.12 **Length:** 170805979 **Number of Matches:** 1

Range 1: 20328749 to 20328943 GenBank Graphics ▼ Next Match ▲ Previous Match

Score	Expect	Identities	Gaps	Strand
338 bits(374)	8e-91	192/196(98%)	1/196(0%)	Plus/Minus

Features: 116515 bp at 5' side: lysophospholipid acyltransferase 1 isoform x2
72612 bp at 3' side: uncharacterized protein loc124901482

```
Query  1         ACTCCTCCTTCAGAGTTGAGGAGGGTGTAGAAACACCMAGGTAGTTTTGTGGCAATGCAG  60
                 |||||||||||||||||||||||||||||||||||| |||| ||||||||||||||||||||
Sbjct  20328943  ACTCCTCCTTCAGAGTTGAGGAGGGTGTAGAA-CACCCAGGTAGTTTTGTGGCAATGCAG  20328885

Query  61        AATATTGGGGTAGATTCCTGCTTCTTTGGACATTATTTGGGGGTAATTCATCACATCACC  120
                 ||||||||||||||||||||||||||||||||||||||||||||||||||||||||||||
Sbjct  20328884  AATATTGGGGTAGATTCCTGCTTCTTTGGACATTATTTGGGGGTAATTCATCACATCACC  20328825

Query  121       ACATCMAATATGACACAAGAACAGTAGAATAGCATTGGCAGAGGACAAATCWAAATATAG  180
                 ||||| |||||||||||||||||||||||||||||||||||||||||||| ||||||||
Sbjct  20328824  ACATCCAATATGACACAAGAACAGTAGAATAGCATTGGCAGAGGACAAATCTAAATATAG  20328765

Query  181       GGGTGTGAGACAGTGC  196
                 ||||||||||||||||
Sbjct  20328764  GGGTGTGAGACAGTGC  20328749
```

8)

Homo sapiens forty-two-three domain containing 1 (FYTTD1), transcript variant 2, mRNA.

Sequence ID: NM_001011537.3 **Length:** 6824 **Number of Matches:** 1

Range 1: 3993 to 4158 GenBank Graphics ▼ Next Match ▲ Previous Match

Score	Expect	Identities	Gaps	Strand
287 bits(317)	4e-75	161/166(97%)	0/166(0%)	Plus/Plus

```
Query  1     TGGGTGACAGAGTGACACTCTGTCTTaaaaaaacaaaaaaaaaGAATCMAGTATACTTTG  60
             ||||||||||||||||||||||||||||||||||||||||||||||||||| ||||||||||
Sbjct  3993  TGGGTGACAGAGTGACACTCTGTCTTAAAAAAACAAAAAAAAAGAATCCAGTATACTTTG  4052

Query  61    CAATGCARAATATTGGGTTAGATGAGCCTTTAGAGACWAATCMAGTTTAACCCCTCCTTT  120
             ||||||| ||||||||||||||||||||||||||||| |||| ||||||||||||||||||
Sbjct  4053  CAATGCAGAATATTGGGTTAGATGAGCCTTTAGAGACTAATCCAGTTTAACCCCTCCTTT  4112

Query  121   TTACACCTTAGTAAAGTGAGTCCWAGTGTTTTCAAGACTTGCATGT  166
             ||||||||||||||||||||||| ||||||||||||||||||||||
Sbjct  4113  TTACACCTTAGTAAAGTGAGTCCTAGTGTTTTCAAGACTTGCATGT  4158
```

9)

Homo sapiens chromosome 11, GRCh38.p14 Primary Assembly

Sequence ID: NC_000011.10 **Length:** 135086622 **Number of Matches:** 1

Range 1: 134742377 to 134742542 GenBank Graphics ▼ Next Match ▲ Previous Match

Score	Expect	Identities	Gaps	Strand
281 bits(311)	2e-73	159/166(96%)	0/166(0%)	Plus/Plus

Features: 354718 bp at 5' side: galactosylgalactosylxylosylprotein 3-beta-glucuronosyltra...

```
Query  2          ACTCTCTGAGCTCATCACCACCATCGTCATCCTCTCCGGCAATGCWAAATATGGAGGCTC  61
                  ||||||||||||||||||||||||||||||||||||||||||||| ||||||||||||||
Sbjct  134742377  ACTCTCTGAGCTCATCACCACCATCGTCATCCTCTCCGGCAATGCTAAATATGGAGGCTC  134742436

Query  62         CWAGTGCMAGGAGTGAAGCWTGCTGAGATCTGGTGTCAGAAAGAAACCACWAACATCCWT  121
                  | ||||| |||||||||||| |||||||||||||||||||||||||||| |||||||| |
Sbjct  134742437  CTAGTGCCAGGAGTGAAGCTTGCTGAGATCTGGTGTCAGAAAGAAACCACTAACATCCTT  134742496

Query  122        GAAGCTCTAAACGCGTGCCTCCWAGGCTCACAGCCTTACCACATGC  167
                  ||||||||||||||||||||||| |||||||||||||||||||||
Sbjct  134742497  GAAGCTCTAAACGCGTGCCTCCTAGGCTCACAGCCTTACCACATGC  134742542
```

10)

Homo sapiens chromosome 3, GRCh38.p14 Primary Assembly

Sequence ID: NC_000003.12 **Length:** 198295559 **Number of Matches:** 1

Range 1: 47891727 to 47891787 GenBank Graphics ▼ Next Match ▲ Previous Match

Score	Expect	Identities	Gaps	Strand
111 bits(122)	4e-23	61/61(100%)	0/61(0%)	Plus/Plus

Features: microtubule-associated protein 4 isoform 56
microtubule-associated protein 4 isoform 4

```
Query  2         AGTGATTGGCGGAATGGTGGTGGGTGAATGCTCAATAATGGGGGCTGGGTGGGCTAGAGA  61
                 ||||||||||||||||||||||||||||||||||||||||||||||||||||||||||||
Sbjct  47891727  AGTGATTGGCGGAATGGTGGTGGGTGAATGCTCAATAATGGGGGCTGGGTGGGCTAGAGA  47891786

Query  62        C  62
                 |
Sbjct  47891787  C  47891787
```

C.131G>A off-targets:

1)

225

Homo sapiens DNA damage regulated autophagy modulator 2 (DRAM2), transcript variant 1, mRNA.

Sequence ID: NM_001349881.2 **Length:** 2143 **Number of Matches:** 1

Range 1: 405 to 476 GenBank Graphics ▼ Next Match ▲ Previous Match

Score	Expect	Identities	Gaps	Strand
122 bits(66)	3e-26	69/72(96%)	0/72(0%)	Plus/Minus

```
Query  48   CTGATATAAGGTAAAGCNGGNTCTATATGGTGGAGNGTTACTGCAGTAATGTATGAAAAT  107
            |||||||||||||||||| || ||||||||||||||| ||||||||||||||||||||||
Sbjct  476  CTGATATAAGGTAAAGCCGGGTCTATATGGTGGAGTGTTACTGCAGTAATGTATGAAAAT  417

Query  108  ATGAAAGCAGCA  119
            ||||||||||||
Sbjct  416  ATGAAAGCAGCA  405
```

2)

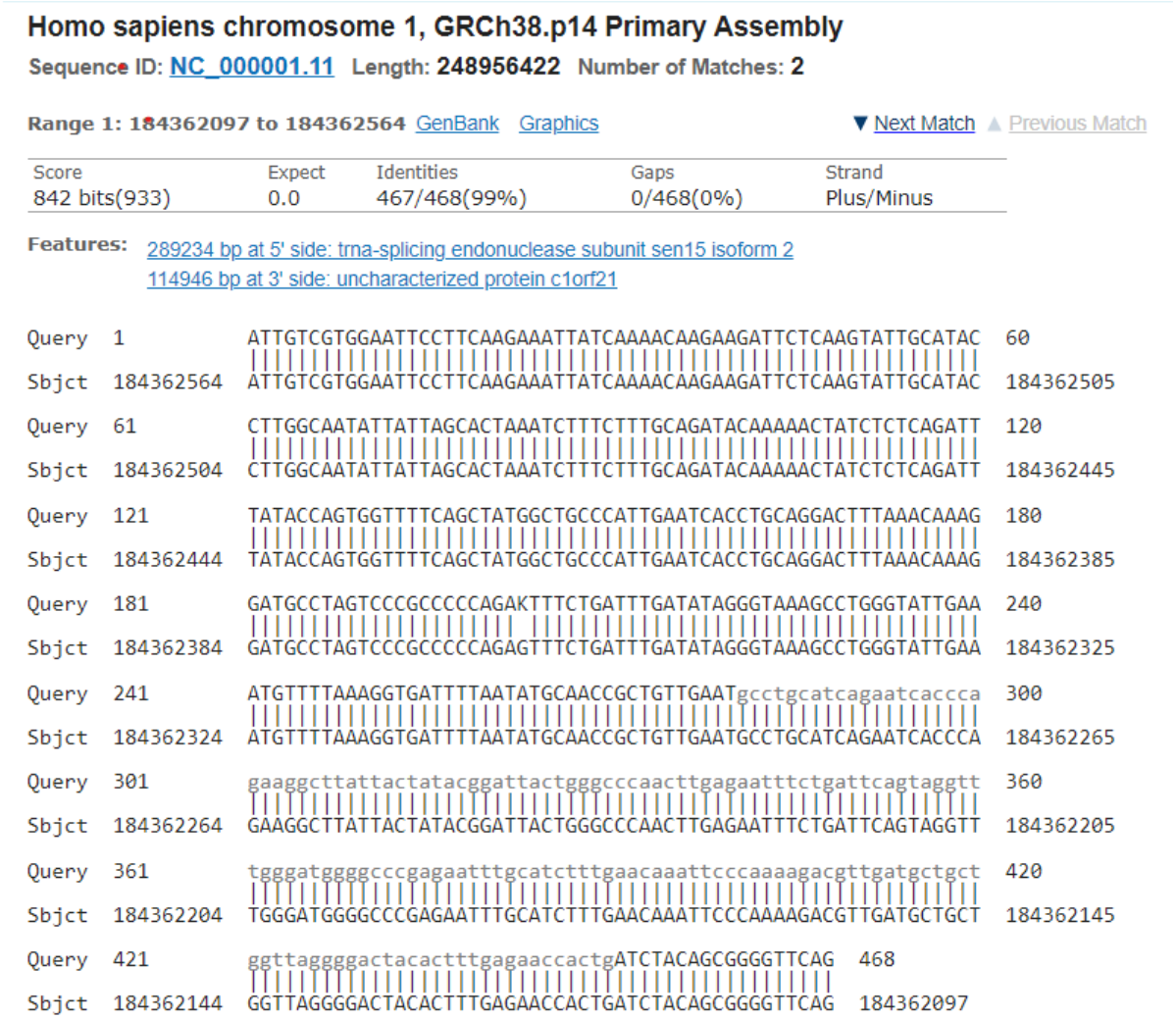

Homo sapiens chromosome 1, GRCh38.p14 Primary Assembly

Sequence ID: NC_000001.11 **Length:** 248956422 **Number of Matches:** 2

Range 1: 184362097 to 184362564 GenBank Graphics ▼ Next Match ▲ Previous Match

Score	Expect	Identities	Gaps	Strand
842 bits(933)	0.0	467/468(99%)	0/468(0%)	Plus/Minus

Features: 289234 bp at 5' side: trna-splicing endonuclease subunit sen15 isoform 2
114946 bp at 3' side: uncharacterized protein c1orf21

```
Query  1          ATTGTCGTGGAATTCCTTCAAGAAATTATCAAAACAAGAAGATTCTCAAGTATTGCATAC  60
                  ||||||||||||||||||||||||||||||||||||||||||||||||||||||||||||
Sbjct  184362564  ATTGTCGTGGAATTCCTTCAAGAAATTATCAAAACAAGAAGATTCTCAAGTATTGCATAC  184362505

Query  61         CTTGGCAATATTATTAGCACTAAATCTTTCTTTGCAGATACAAAAACTATCTCTCAGATT  120
                  ||||||||||||||||||||||||||||||||||||||||||||||||||||||||||||
Sbjct  184362504  CTTGGCAATATTATTAGCACTAAATCTTTCTTTGCAGATACAAAAACTATCTCTCAGATT  184362445

Query  121        TATACCAGTGGTTTTCAGCTATGGCTGCCCATTGAATCACCTGCAGGACTTTAAACAAAG  180
                  ||||||||||||||||||||||||||||||||||||||||||||||||||||||||||||
Sbjct  184362444  TATACCAGTGGTTTTCAGCTATGGCTGCCCATTGAATCACCTGCAGGACTTTAAACAAAG  184362385

Query  181        GATGCCTAGTCCCGCCCCCAGAKTTTCTGATTTGATATAGGGTAAAGCCTGGGTATTGAA  240
                  |||||||||||||||||||| ||||||||||||||||||||||||||||||||||||||
Sbjct  184362384  GATGCCTAGTCCCGCCCCCAGAGTTTCTGATTTGATATAGGGTAAAGCCTGGGTATTGAA  184362325

Query  241        ATGTTTTAAAGGTGATTTTAATATGCAACCGCTGTTGAATgcctgcatcagaatcaccca  300
                  ||||||||||||||||||||||||||||||||||||||||||||||||||||||||||||
Sbjct  184362324  ATGTTTTAAAGGTGATTTTAATATGCAACCGCTGTTGAATGCCTGCATCAGAATCACCCA  184362265

Query  301        gaaggcttattactatacggattactgggcccaacttgagaatttctgattcagtaggtt  360
                  ||||||||||||||||||||||||||||||||||||||||||||||||||||||||||||
Sbjct  184362264  GAAGGCTTATTACTATACGGATTACTGGGCCCAACTTGAGAATTTCTGATTCAGTAGGTT  184362205

Query  361        tgggatggggcccgagaatttgcatctttgaacaaattcccaaaagacgttgatgctgct  420
                  ||||||||||||||||||||||||||||||||||||||||||||||||||||||||||||
Sbjct  184362204  TGGGATGGGGCCCGAGAATTTGCATCTTTGAACAAATTCCCAAAAGACGTTGATGCTGCT  184362145

Query  421        ggttaggggactacactttgagaaccactgATCTACAGCGGGGTTCAG  468
                  |||||||||||||||||||||||||||||||||||||||||||||||
Sbjct  184362144  GGTTAGGGGACTACACTTTGAGAACCACTGATCTACAGCGGGGTTCAG  184362097
```

3)

Homo sapiens chromosome 20, GRCh38.p14 Primary Assembly

Sequence ID: NC_000020.11 **Length:** 64444167 **Number of Matches:** 1

Range 1: 4406918 to 4407324 GenBank Graphics ▼ Next Match ▲ Previous Match

Score	Expect	Identities	Gaps	Strand
732 bits(811)	0.0	406/407(99%)	0/407(0%)	Plus/Minus

Features: 157961 bp at 5' side: alpha-1d adrenergic receptor
291897 bp at 3' side: major prion protein preproprotein prp precursor

```
Query  1        CTgtggttctccaccctgtcttaacatgggaatcacctgggaagcttttaagtatcccCT  60
                ||||||||||||||||||||||||||||||||||||||||||||||||||||||||||||
Sbjct  4407324  CTGTGGTTCTCCACCCTGTCTTAACATGGGAATCACCTGGGAAGCTTTTAAGTATCCCCT  4407265

Query  61       AAGTGACTCCTTTcaarcaaacaaacaaaaacaaaacTGATACCTACATTTTATCTTCCC  120
                ||||||||||||||| ||||||||||||||||||||||||||||||||||||||||||||
Sbjct  4407264  AAGTGACTCCTTTCAAACAAACAAACAAAAACAAAACTGATACCTACATTTTATCTTCCC  4407205

Query  121      ATTCCTGGAATTCTTGATTTAATTGGTATAAGGTAAAGTCTGGACATCAAATCCAGTGGT  180
                ||||||||||||||||||||||||||||||||||||||||||||||||||||||||||||
Sbjct  4407204  ATTCCTGGAATTCTTGATTTAATTGGTATAAGGTAAAGTCTGGACATCAAATCCAGTGGT  4407145

Query  181      GTCTTCCAACCAGCCTTGTGGCCAGGTCTGACATTTACAGCCATATTGGCCACATGCTGC  240
                ||||||||||||||||||||||||||||||||||||||||||||||||||||||||||||
Sbjct  4407144  GTCTTCCAACCAGCCTTGTGGCCAGGTCTGACATTTACAGCCATATTGGCCACATGCTGC  4407085

Query  241      ACAATTCCAGAAGGCTTCATTCACATAATCTATATTGGAAATAGTTTGTTCTAAATTTGT  300
                ||||||||||||||||||||||||||||||||||||||||||||||||||||||||||||
Sbjct  4407084  ACAATTCCAGAAGGCTTCATTCACATAATCTATATTGGAAATAGTTTGTTCTAAATTTGT  4407025

Query  301      GCTGTACACAACCTTCAAAACTGTATACGGTTGGCTGATCTATCCAGCCTTATTCTGTTT  360
                ||||||||||||||||||||||||||||||||||||||||||||||||||||||||||||
Sbjct  4407024  GCTGTACACAACCTTCAAAACTGTATACGGTTGGCTGATCTATCCAGCCTTATTCTGTTT  4406965

Query  361      GCAAAATTCCTTTTTAGCTTTCTCAACACCACTCTCTCCCTCTTCCC  407
                |||||||||||||||||||||||||||||||||||||||||||||||
Sbjct  4406964  GCAAAATTCCTTTTTAGCTTTCTCAACACCACTCTCTCCCTCTTCCC  4406918
```

4)

Homo sapiens chromosome 8, GRCh38.p14 Primary Assembly

Sequence ID: NC_000008.11 **Length:** 145138636 **Number of Matches:** 1

Range 1: 110241705 to 110242033 GenBank Graphics ▼ Next Match ▲ Previous Match

Score	Expect	Identities	Gaps	Strand
578 bits(640)	9e-163	323/329(98%)	0/329(0%)	Plus/Minus

Features: 267317 bp at 5' side: potassium voltage-gated channel subfamily v member 1
1982738 bp at 3' side: cub and sushi domain-containing protein 3 isoform x6

```
Query  1          CCTTAACTTCTGATTTGGAGCTAWTGCTTTGATTCAGCCTAGATATAAKGTAAAGCCAGG  60
                  ||||||||||||||||||||||| ||||||||||||||||||||||| ||||||||||||
Sbjct  110242033  CCTTAACTTCTGATTTGGAGCTAATGCTTTGATTCAGCCTAGATATAATGTAAAGCCAGG  110241974

Query  61         AGTAATAAGAATCAKGGTAGCCATTGTTAACGTATCTTATGCTTTAAGGAAGCCAACTTT  120
                  ||||||||||||| ||||||||||||||||||||||||||||||||||||||||||||||
Sbjct  110241973  AGTAATAAGAATCATGGTAGCCATTGTTAACGTATCTTATGCTTTAAGGAAGCCAACTTT  110241914

Query  121        CTATAATTAGACTCATATAATTAAATCAGACCAATAATAGGTCAAACTTGAKTTATGTTT  180
                  |||||||||||||||||||||||||||||||||||||||||||||||||| ||||||||
Sbjct  110241913  CTATAATTAGACTCATATAATTAAATCAGACCAATAATAGGTCAAACTTGAGTTATGTTT  110241854

Query  181        AAAACAATGATATTTATTGTGTTTGACTTAAAAATATTATARGGATTTGACaaaaaaaCT  240
                  |||||||||||||||||||||||||||||||||||||||| |||||||||||||||||||
Sbjct  110241853  AAAACAATGATATTTATTGTGTTTGACTTAAAAATATTATAAGGATTTGACAAAAAAACT  110241794

Query  241        TTAATAATCATTATATATTAGTGGTGCCATTATTAARGGTTAAGTGCAAAACTACACTGG  300
                  |||||||||||||||||||||||||||||||||| ||||||||||||||||||||||||
Sbjct  110241793  TTAATAATCATTATATATTAGTGGTGCCATTATTAAAGGTTAAGTGCAAAACTACACTGG  110241734

Query  301        AAATTGACTTGTGAGAAGATTGTATGCTG  329
                  |||||||||||||||||||||||||||||
Sbjct  110241733  AAATTGACTTGTGAGAAGATTGTATGCTG  110241705
```

5)

Homo sapiens chromosome 7, GRCh38.p14 Primary Assembly

Sequence ID: NC_000007.14 **Length:** 159345973 **Number of Matches:** 1

Range 1: 137550936 to 137551276 GenBank Graphics ▼ Next Match ▲ Previous Match

Score	Expect	Identities	Gaps	Strand
613 bits(679)	5e-173	340/341(99%)	0/341(0%)	Plus/Plus

Features: diacylglycerol kinase iota isoform x3
diacylglycerol kinase iota isoform 4

```
Query  1          GATGAACCATATACAACCACTGGCATGCCACATTTTTTAACATATAACCTCAGCAATTGT  60
                  ||||||||||||||||||||||||||||||||||||||||||||||||||||||||||||
Sbjct  137550936  GATGAACCATATACAACCACTGGCATGCCACATTTTTTAACATATAACCTCAGCAATTGT  137550995

Query  61         GTATTTAACCTGATAGAAGGTAAAGGCAGGGAGGGCAGCAGGCACGGAGGACAGGAGGAA  120
                  ||||||||||||||||||||||||||||||||||||||||||||||||||||||||||||
Sbjct  137550996  GTATTTAACCTGATAGAAGGTAAAGGCAGGGAGGGCAGCAGGCACGGAGGACAGGAGGAA  137551055

Query  121        TGAGCGAGGAGTTTCACTAAATGCAAAATGTAAACAAAGAAAGACATGTAACTAAAAAAC  180
                  ||||||||||||||||||||||||||||||||||||||||||||||||||||||||||||
Sbjct  137551056  TGAGCGAGGAGTTTCACTAAATGCAAAATGTAAACAAAGAAAGACATGTAACTAAAAAAC  137551115

Query  181        ACCTCTGGAAAATGATCTAGGAAAAATTCKGGGGGAAGTCCAGATTCTGGGAGAGAAGGA  240
                  |||||||||||||||||||||||||| ||||||||||||||||||||||||||||||||
Sbjct  137551116  ACCTCTGGAAAATGATCTAGGAAAAATTCTGGGGGAAGTCCAGATTCTGGGAGAGAAGGA  137551175

Query  241        AGGAGAGGACAGACAGGATTTTTTACCCCAGCTTCAAACTGAGACCCAGATGCCAAAAGC  300
                  ||||||||||||||||||||||||||||||||||||||||||||||||||||||||||||
Sbjct  137551176  AGGAGAGGACAGACAGGATTTTTTACCCCAGCTTCAAACTGAGACCCAGATGCCAAAAGC  137551235

Query  301        TGGAACACTCTGAGAGCACTGTCTAATCCTGTTCCTCAACC  341
                  |||||||||||||||||||||||||||||||||||||||||
Sbjct  137551236  TGGAACACTCTGAGAGCACTGTCTAATCCTGTTCCTCAACC  137551276
```

6)

Homo sapiens chromosome 5, GRCh38.p14 Primary Assembly

Sequence ID: NC_000005.10 **Length:** 181538259 **Number of Matches:** 1

Range 1: 74308427 to 74308774 GenBank Graphics ▼ Next Match ▲ Previous Matc

Score	Expect	Identities	Gaps	Strand
623 bits(690)	3e-176	346/348(99%)	0/348(0%)	Plus/Minus

Features: 367414 bp at 5' side: rho guanine nucleotide exchange factor 28 isoform 3
325942 bp at 3' side: ectoderm-neural cortex protein 1 isoform 1

```
Query  1         ACTTATTTTTCAACCTGTGTTAGATTGATGTTAGTATGTTGGACCAAGTGAACATTTATT  60
                 ||||||||||||||||||||||||||||||||||||||||||||||||||||||||||||
Sbjct  74308774  ACTTATTTTTCAACCTGTGTTAGATTGATGTTAGTATGTTGGACCAAGTGAACATTTATT  74308715

Query  61        TTCAGTGTGGTTGGGTAAAGTAGGTTGGGTGTGAGCTGGAGGAAGAAGAGAGCTGGTTGG  120
                 ||||||||||||||||||||||||||||||||||||||||||||||||||||||||||||
Sbjct  74308714  TTCAGTGTGGTTGGGTAAAGTAGGTTGGGTGTGAGCTGGAGGAAGAAGAGAGCTGGTTGG  74308655

Query  121       CAACAGACCACAGATCACTAGTCATAAGGTAAAGCCTGGATCTGTATGAGGATAATTGCT  180
                 ||||||||||||||||||||||||||||||||||||||||||||||||||||||||||||
Sbjct  74308654  CAACAGACCACAGATCACTAGTCATAAGGTAAAGCCTGGATCTGTATGAGGATAATTGCT  74308595

Query  181       AGTTGACTGTATTTCACAATTTGCGGATATCTAGCTTCTTACAAATAGGTCAATGAACAT  240
                 ||||||||||||||||||||||||||||||||||||||||||||||||||||||||||||
Sbjct  74308594  AGTTGACTGTATTTCACAATTTGCGGATATCTAGCTTCTTACAAATAGGTCAATGAACAT  74308535

Query  241       ATCACATTCWTTTATTTTCAAAACACTTGAATATTTAAAWTAATACTAGATGAAAATAAC  300
                 |||||||||  ||||||||||||||||||||||||||||  ||||||||||||||||||||
Sbjct  74308534  ATCACATTCATTTATTTTCAAAACACTTGAATATTTAAATTAATACTAGATGAAAATAAC  74308475

Query  301       AGTGAGTAATCAAGCCCACATTTTTAAAAACAATTTTATTGAGTAAGA  348
                 ||||||||||||||||||||||||||||||||||||||||||||||||
Sbjct  74308474  AGTGAGTAATCAAGCCCACATTTTTAAAAACAATTTTATTGAGTAAGA  74308427
```

7)

Homo sapiens chromosome 2, GRCh38.p14 Primary Assembly

Sequence ID: NC_000002.12 **Length:** 242193529 **Number of Matches:** 1

Range 1: 12850425 to 12850721 GenBank Graphics ▼ Next Match ▲ Previous Ma

Score	Expect	Identities	Gaps	Strand
536 bits(594)	3e-150	297/297(100%)	0/297(0%)	Plus/Minus

Features: 109631 bp at 5' side: tribbles homolog 2
1783259 bp at 3' side: protein lratd1

```
Query  1         TAAAGCCAGGATTGAAATCAAGTCTGAGACCACAGTCCATGCTGCTAACTCTTGTATTAC  60
                 ||||||||||||||||||||||||||||||||||||||||||||||||||||||||||||
Sbjct  12850721  TAAAGCCAGGATTGAAATCAAGTCTGAGACCACAGTCCATGCTGCTAACTCTTGTATTAC  12850662

Query  61        ACACAGATATATGCAGTAAAAAGGATAAGGCATTTAATCAGAATGGGGAGAGAATAAAGC  120
                 ||||||||||||||||||||||||||||||||||||||||||||||||||||||||||||
Sbjct  12850661  ACACAGATATATGCAGTAAAAAGGATAAGGCATTTAATCAGAATGGGGAGAGAATAAAGC  12850602

Query  121       ATAGAAAAGAATGGCATCCCTGAGAGTCACAATGAGAAAATAAGCAAACATAGGTTTAGC  180
                 ||||||||||||||||||||||||||||||||||||||||||||||||||||||||||||
Sbjct  12850601  ATAGAAAAGAATGGCATCCCTGAGAGTCACAATGAGAAAATAAGCAAACATAGGTTTAGC  12850542

Query  181       TTTGATAATAAGTAATAAGTGGATGTGGCAGGAACTTAGGGTGTTTGGGATGTTTTGGAT  240
                 ||||||||||||||||||||||||||||||||||||||||||||||||||||||||||||
Sbjct  12850541  TTTGATAATAAGTAATAAGTGGATGTGGCAGGAACTTAGGGTGTTTGGGATGTTTTGGAT  12850482

Query  241       GTTACATAGGTGTTGTTAGGAAAATTGTCCTTAAAACAGTTGGATTCATGTCACAAA  297
                 |||||||||||||||||||||||||||||||||||||||||||||||||||||||||
Sbjct  12850481  GTTACATAGGTGTTGTTAGGAAAATTGTCCTTAAAACAGTTGGATTCATGTCACAAA  12850425
```

8)

Homo sapiens chromosome 3, GRCh38.p14 Primary Assembly

Sequence ID: NC_000003.12 **Length:** 198295559 **Number of Matches:** 1

Range 1: 139919545 to 139919691 GenBank Graphics ▼ Next Match ▲ Previous Match

Score	Expect	Identities	Gaps	Strand
266 bits(294)	3e-69	147/147(100%)	0/147(0%)	Plus/Plus

Features: 291821 bp at 5' side: nicotinamide/nicotinic acid mononucleotide adenylyltransf...
15684 bp at 3' side: calsyntenin-2 precursor

```
Query  1          ATCTGTATCCAATACCTCTTTATCCatatataggtacatttcttcatacttcattctagt  60
                  ||||||||||||||||||||||||||||||||||||||||||||||||||||||||||||
Sbjct  139919545  ATCTGTATCCAATACCTCTTTATCCATATATAGGTACATTTCTTCATACTTCATTCTAGT  139919604

Query  61         cccctggcctagttgttagtctctgaacaaatagcattctatcttaattactatagcttt  120
                  ||||||||||||||||||||||||||||||||||||||||||||||||||||||||||||
Sbjct  139919605  CCCCTGGCCTAGTTGTTAGTCTCTGAACAAATAGCATTCTATCTTAATTACTATAGCTTT  139919664

Query  121        ataataagttttgatataaggtaaAGC  147
                  |||||||||||||||||||||||||||
Sbjct  139919665  ATAATAAGTTTTGATATAAGGTAAAGC  139919691
```

9)

Homo sapiens chromosome 1, GRCh38.p14 Primary Assembly

Sequence ID: NC_000001.11 **Length:** 248956422 **Number of Matches:** 2

Range 1: 15332027 to 15332332 GenBank Graphics ▼ Next Match ▲ Previous Match

Score	Expect	Identities	Gaps	Strand
553 bits(612)	3e-155	306/306(100%)	0/306(0%)	Plus/Plus

Features: forkhead-associated domain-containing protein 1 isoform x2
forkhead-associated domain-containing protein 1 isoform x7

```
Query  1         GAATAAGAATAGAGAAGTGATTTTCAACCCTGGCACTTCAACATCTGCAGCAGGATGCTT  60
                 ||||||||||||||||||||||||||||||||||||||||||||||||||||||||||||
Sbjct  15332027  GAATAAGAATAGAGAAGTGATTTTCAACCCTGGCACTTCAACATCTGCAGCAGGATGCTT  15332086

Query  61        CCAAAGTATCCAGAAGGTGGGGTAACATTCTTAAAAAGCAAAAGCAAAACCAACATTAAT  120
                 ||||||||||||||||||||||||||||||||||||||||||||||||||||||||||||
Sbjct  15332087  CCAAAGTATCCAGAAGGTGGGGTAACATTCTTAAAAAGCAAAAGCAAAACCAACATTAAT  15332146

Query  121       TTTTATGTAGGAACCTTCCCCTCATCATATAGCAGAGAGCGTTACTGTTCTTGCAATCAA  180
                 ||||||||||||||||||||||||||||||||||||||||||||||||||||||||||||
Sbjct  15332147  TTTTATGTAGGAACCTTCCCCTCATCATATAGCAGAGAGCGTTACTGTTCTTGCAATCAA  15332206

Query  181       GGCAGAGTCGTGAGCTTACTTGAAATAAGGTAAAACATGGAGCAGAGTTCTCGTTGTTCT  240
                 ||||||||||||||||||||||||||||||||||||||||||||||||||||||||||||
Sbjct  15332207  GGCAGAGTCGTGAGCTTACTTGAAATAAGGTAAAACATGGAGCAGAGTTCTCGTTGTTCT  15332266

Query  241       TCAAGACTGGAACTAAAACAAAGACCATGATCTCCATCCTGGCAATAATAGAGCCAAGCT  300
                 ||||||||||||||||||||||||||||||||||||||||||||||||||||||||||||
Sbjct  15332267  TCAAGACTGGAACTAAAACAAAGACCATGATCTCCATCCTGGCAATAATAGAGCCAAGCT  15332326

Query  301       ACGTGT  306
                 ||||||
Sbjct  15332327  ACGTGT  15332332
```

Appendix C

Table 27. List of the commonly changed protein in patient CORD21 ROs

Protein IDs	Protein names	Gene names	FC P1/P1C	FC P2/P2C	Log P1/P1C	Log P2/P2C
A0A087X0S5;P12109	Collagen alpha-1(VI) chain	COL6A1	0.324177572	2.52020984	-1.62514381	1.333543863
A0A140G945;P02489;A0A096LPJ9;E7EWH7	Alpha-crystallin A chain;Alpha-crystallin A(1-172);Alpha-crystallin A(1-168);Alpha-crystallin A(1-162)	CRYAA	0.041011255	7.85971049	-4.60783631	2.974476173
F8W787;A0A1B0GW44;A0A1B0GVD5;A0A1B0GWE8;P07339;A0A1B0GVP3;A0A1B0GV23;C9JH19;A0A1B0GU92;A0A1B0GU03;H7C469;F8WD96;A0A1B0GVF1	Cathepsin D;Cathepsin D light chain;Cathepsin D heavy chain	CTSD	0.732653648	0.49809321	-0.44879675	-1.00551236
A0A1X7SBR3;P14136;A0A1W2PR46;A0A1X7SCE1;K7EKH9;A0A1W2PRT3;K7EJU1;K7ELP4;B4DIR1;K7EJK1;K7EKD1;A0A1W2PS58;A0A1W2PPA3;K7EPT8;K7EPI4	Glial fibrillary acidic protein	GFAP	0.013106606	2.75737723	-6.25356203	1.463296652
A0A2C9F2P4;A0A286YFF7;P50897;Q5T0S4;A0A286YFE3;A0A286YFL8;A0A286YFL6;E9PSE5;E9PK48;E9PIA8	Palmitoyl-protein thioesterase 1	PPT1	0.326231736	0.2476723	-1.61603096	-2.01349558
A0A2R8Y891;P08237;F8VZI0;F8VP00;F8VX13;F8VZQ1;F8VSF7;F8VTQ3;F8VW30;F8VUB8;F8VYK8;F8VVE3;H0YHB8	ATP-dependent 6-phosphofructokinase, muscle type	PFKM	1.249801334	0.75148439	0.321698785	-0.41218495
A0A2R8YGD1;A0A2R8YD45;O14773;A0A2R8Y7U1;A0A2R8YDY1;A0A2R8Y7I4	Tripeptidyl-peptidase 1	TPP1	0.570133416	0.30586245	-0.81062853	-1.70904511
A0A7I2V634;A0A7I2V4A4;A0A7I2YQS6;A0A7I2V612;A0A7I2V373;A0A7I2V2S1;A0A7I2V4Q3;A0A7I2V610;A0A7I2V3E3;A0A7I2V2P6;A0A7I2YQV5;A0A3B3ISG5;P14735	Insulin-degrading enzyme	IDE	3.137005925	0.27984397	1.649388254	-1.83730543
A0A494C039;Q9Y4L1;A0A087X054;E9PJ21;A0A087WWI4;K7EQK2;Q9BST8;J3QQH7;J3QLE9;J3QL06;J3KTF1;A0A087X214;A0A087WW13;A0A2R8Y358;A0A1W2PS94;Q9BXT5	Hypoxia up-regulated protein 1	HYOU1	1.323481695	0.77131402	0.404338241	-0.37460977

A0A590UJZ9;A0A590UJ76;Q9UGM3;A0A590UIX5;A0A590UJF8;A0A590UK99	Deleted in malignant brain tumors 1 protein	DMBT1	2.101710066	4.04660912	1.071563661	2.0167135
A0A669KB77;P11137;E7EV03;A8MZ31	Microtubule-associated protein 2	MAP2	1.511052593	0.47021461	0.595553875	-1.08860874
A0A6Q8PFA6;A0A6Q8PH57;A0A6Q8PGH7;A0A6Q8PG37;O00139;D6R9M0;A0A6Q8PGG1;H0Y8H2;Q8N4N8	Kinesin-like protein KIF2A	KIF2A	1.450835079	0.63719425	0.536883533	-0.65019484
A0A7I2V2R5;A0A7I2V2X8;P27487;A0A7I2V5R8;A0A7I2V2I2;A0A7I2V3F5;F8WBB6;F8WE17	Dipeptidyl peptidase 4;Dipeptidyl peptidase 4 membrane form;Dipeptidyl peptidase 4 soluble form	DPP4	5.216980714	4.79994116	2.3832151	2.26301672
A0A7P0TA76;O95573;A0A7P0TB52;A0A7P0TBB1;A0A7P0T8L6;A0A7P0T905;H7BYZ7;A0A7P0TBL9;C9JC11	Long-chain-fatty-acid--CoA ligase 3	ACSL3	1.656723304	0.55215369	0.728332672	-0.85685821
A0A7P0TAE1;H0YIV0;A0A7P0TAT8;P14625;A0A087WT78;A0A7P0T823;A0A7P0T917;A0A7P0TAY2;A0A7P0TBC2;A0A7P0T8R3;A0A7P0T885;A0A7P0Z405;Q58FF3;F8W026	Endoplasmin	HSP90B1	1.18562609	0.88925872	0.2456491	-0.16932487
A8MW49;P07148	Fatty acid-binding protein, liver	FABP1	0.562731201	2.88484789	-0.82948214	1.528495252
C9JZY3;C9J0A4;P57723;C9JTY5;C9J5V4;C9IZV9;C9J7A9;C9JSA6	Poly(rC)-binding protein 4	PCBP4	1.898596599	0.47243104	0.924933404	-1.08182433
J3KMY5;G3V3E8;E7EMS2;G3V3D1;P61916;G3V2V8;H0YIZ1	Epididymal secretory protein E1	NPC2	0.404690629	0.64216349	-1.30510865	-0.63898745
E9PCP0;P16520;F5H0S8;F5H8J8;F5H100;A0A6Q8PF84;F5GZN8	Guanine nucleotide-binding protein G(I)/G(S)/G(T) subunit beta-3	GNB3	1.75075047	0.30846567	0.807973475	-1.69681817
F5H2U8;F5H2A4;P52926;F5H6H0	High mobility group protein HMGI-C	HMGA2	0.201572575	1.90747813	-2.31062873	0.931666514
F8W1D1;H0YIJ2;P40967;F8VUB1;F8VZC6;F8VXH8	Melanocyte protein PMEL;M-alpha;M-beta	PMEL	0.090157396	0.39725046	-3.47141034	-1.33187921
F8W1R7;G3V1V0;P60660;J3KND3;G8JLA2;B7Z6Z4;G3V1Y7;F8VPF3;F8VZU9;F8W180;H0YI43;F8VXL3	Myosin light polypeptide 6	MYL6	0.730898855	2.13909312	-0.45225632	1.096999288

F8W9U4	Microtubule-associated protein	MAP4	1.764573963	0.36236063	0.819319903	-1.46450187
H0YI30;O95390	Growth/differentiation factor 11	GDF11	1.45433431	0.61688954	0.540358942	-0.69691592
O00560;B4DHN5;E9PBU7	Syntenin-1	SDCBP	0.334383795	0.50540477	-1.58042316	-0.9844888
O14531;Q5T0Q6	Dihydropyrimidinase-related protein 4	DPYSL4	1.344831909	0.78389087	0.427425861	-0.35127527
O43236;A0A5F9ZHS9;J3QLA8;J3QRS4;J3QRT6;J3KSZ7;J3KS85;J3KS26;J3QRU3;J3QLR2	Septin-4	Sep-04	4.727637243	0.46382417	2.24111934	-1.1083501
O75106	Retina-specific copper amine oxidase	AOC2	0.031147059	5.33165737	-5.00476025	2.41458407
P00352;Q5SYQ9;Q5SYQ8;Q5SYQ7	Retinal dehydrogenase 1	ALDH1A1	0.063375039	2.9845153	-3.97994146	1.577496648
Q5T9B7;P00568;H0YID2;Q9Y6K8	Adenylate kinase isoenzyme 1	AK1	1.356673042	0.72393196	0.440073073	-0.46607399
P00918;E5RID5;E5RK37	Carbonic anhydrase 2	CA2	1.381061681	0.85499436	0.465777755	-0.22601318
P02452;CON__Q862S4;I3L3H7	Collagen alpha-1(I) chain	COL1A1	0.120303905	3.52424899	-3.05524462	1.817315854
P02511;E9PJL7;E9PRA8;E9PNH7;A0A024R3B9;E9PS12	Alpha-crystallin B chain	CRYAB	0.326415871	0.57602318	-1.61521689	-0.79580122
P02751;H0Y7Z1;H0Y4K8	Fibronectin;Anastellin;Ugl-Y1;Ugl-Y2;Ugl-Y3	FN1	0.372008272	3.69876181	-1.42659339	1.887042396
P02794;G3V192;G3V1D1;E9PPQ4	Ferritin heavy chain;Ferritin heavy chain, N-terminally processed;Ferritin	FTH1	0.348822591	1.90918433	-1.51943462	0.932956397
P05783;F8VZY9;CON__H-INV:HIT000015463	Keratin, type I cytoskeletal 18	KRT18	0.054541075	2.07059625	-4.19651306	1.050046265
P06737;E9PK47	Glycogen phosphorylase, liver form;Alpha-1,4 glucan phosphorylase	PYGL	1.25824005	0.81367425	0.331407189	-0.29747677
P07585;F8VXZ8;F8VUF6;F8VWU0;F8VX58;A0A7I2PRI8;F8VNW0;F8VU58;F8VSI3;F8VNV6	Decorin	DCN	0.377449901	5.14849596	-1.40564293	2.364151036
P07900;G3V2J8;Q14568;Q58FG0	Heat shock protein HSP 90-alpha	HSP90AA1	1.326920236	0.86503891	0.40808165	-0.20916307
P08133;E5RK63;E5RJF5;E5RFF0;E5RI05;E5RJR0	Annexin A6	ANXA6	0.805588504	1.23016898	-0.311885	0.298856497
P08247;H7C4W3	Synaptophysin	SYP	1.707716123	0.38354569	0.772068173	-1.38252965
P09382;F8WEI7	Galectin-1	LGALS1	0.060554892	2.61096332	-4.04561267	1.384582192
P09874;A0A7I2V3E1;A0A7I2V625;A0A7I2V5E9;A0A7I2V384	Poly [ADP-ribose] polymerase 1	PARP1	1.229552632	0.81553406	0.298133492	-0.29418296

P11142;E9PKE3;E9PNE6;E9PN89;E9PLF4;E9PQQ4;E9PQK7;E9PK54;E9PPY6;E9PN25;E9PI65	Heat shock cognate 71 kDa protein	HSPA8	1.283688939	0.80597428	0.360295654	-0.3111943
P11216;H0Y4Z6	Glycogen phosphorylase, brain form	PYGB	1.271610259	0.67664604	0.346656561	-0.56352675
P12277;H0YJG0;G3V4N7;H0YJK0;G3V461	Creatine kinase B-type	CKB	1.677717738	0.75703646	0.746500015	-0.40156531
P13010;C9JZ81;H7C0H9	X-ray repair cross-complementing protein 5	XRCC5	1.162782987	0.85800303	0.217581868	-0.22094536
P14550;Q5T621;V9GYG2	Alcohol dehydrogenase [NADP(+)]	AKR1A1	1.180460463	0.81069377	0.239349723	-0.30277103
P14618;B4DNK4	Pyruvate kinase PKM;Pyruvate kinase	PKM	1.30807236	0.781553	0.38744235	-0.35558438
P16401	Histone H1.5	HIST1H1B	0.539495354	1.27748168	-0.89031756	0.353302598
P16402	Histone H1.3	HIST1H1D	0.489873798	1.69678207	-1.02951797	0.762801282
P17096	High mobility group protein HMG-I/HMG-Y	HMGA1	0.732954967	0.74535044	-0.44820353	-0.4240092
P17661	Desmin	DES	0.523939141	15.3565378	-0.93252885	3.94078109
P18206	Vinculin	VCL	0.52052397	1.35289076	-0.94196349	0.436045349
P19087;A0A087WZE5	Guanine nucleotide-binding protein G(t) subunit alpha-2	GNAT2	1.747069612	0.35848739	0.804937094	-1.4800057
P21333;A0A7P0NMY4;A0A087WWY3;A0A7I2V3E6;F8WE98;H0Y5C6;H0Y5F3;A0A669KBC6;H7C2E7	Filamin-A	FLNA	0.795030791	1.58809057	-0.33091736	0.667293191
P27816;H7C456	Microtubule-associated protein 4	MAP4	1.498145067	0.7511701	0.583177328	-0.41278845
P35243	Recoverin	RCVRN	1.734777995	0.53657024	0.794751048	-0.89816105
P35579;Q5BKV1;B1AH99;P12883;P13533	Myosin-9	MYH9	0.747734495	1.42708503	-0.419402	0.513071299
P36575;A0A087WWQ5;D6RCT3	Arrestin-C	ARR3	1.884038404	0.36902648	0.913828373	-1.43820375
P40126;A0A0A0MTD3	L-dopachrome tautomerase	DCT	0.015726375	0.3324954	-5.99067	-1.58859373
P41219;H7C5W5;F8W835	Peripherin	PRPH	1.968435643	11.9361574	0.977049545	3.57726656
P42166	Lamina-associated polypeptide 2, isoform alpha;Thymopoietin;Thymopentin	TMPO	0.628492476	1.1787448	-0.67003262	0.237251401
P43320	Beta-crystallin B2	CRYBB2	0.165174399	57.6817952	-2.597938	5.850044161
P46940;A0A0J9YXZ5;H0YLE8;A0A087WWP1	Ras GTPase-activating-like protein IQGAP1	IQGAP1	0.286030701	1.56212799	-1.80575809	0.643512666
P50453	Serpin B9	SERPINB9	0.085537545	2.19128279	-3.54729839	1.131775677
P52943;H0YFA4;H0YHD8	Cysteine-rich protein 2	CRIP2	0.75976038	0.70399597	-0.39638361	-0.50636092
P53674	Beta-crystallin B1	CRYBB1	0.189601823	34.7570147	-2.39895526	5.119232267

P56377;A0A5F9ZI43;H7BZG6;H0Y673;A0A5F9ZHX2;A6NH01;A0A5F9ZHW1;F6SFB5	AP-1 complex subunit sigma-2	AP1S2	1.477388503	0.647742	0.563049256	-0.6265088
P62805	Histone H4	HIST1H4A	0.48896852	0.76764665	-1.03218651	-0.3814857
P68366;C9JEV8;C9JQ00;C9JJQ8;C9JDL2	Tubulin alpha-4A chain	TUBA4A	1.970414371	0.69549102	0.978499055	-0.52389622
P98160;A0A3B3IT11	Basement membrane-specific heparan sulfate proteoglycan core protein;Endorepellin;LG3 peptide	HSPG2	5.551409348	6.26334207	2.472854078	2.646932674
Q01995;H0YCU9;E9PJ32	Transgelin	TAGLN	0.192021429	8.54820158	-2.38066077	3.09562093
Q02952	A-kinase anchor protein 12	AKAP12	0.568416002	1.44412103	-0.81498092	0.53019166
Q05707;J3QT83;Q4G0W3;A0A0A0MQT7;H0YBB2	Collagen alpha-1(XIV) chain	COL14A1	0.376302546	2.82049464	-1.41003504	1.495948195
Q06830;A0A0A0MSI0;A0A0A0MRQ5	Peroxiredoxin-1	PRDX1	1.290785945	0.88046538	0.368249774	-0.18366182
Q09666;E9PJZ0;E9PKR9;E9PJC6;E9PLK4;E9PQE3	Neuroblast differentiation-associated protein AHNAK	AHNAK	0.267508667	2.84009934	-1.90234246	1.505941391
Q13432;C9JSK0;K7EN86;K7EJU3;J3QQT8	Protein unc-119 homolog A	UNC119	1.580497631	0.46900482	0.660378873	-1.09232535
Q14194;E9PD68;Q14117	Dihydropyrimidinase-related protein 1	CRMP1	1.848264793	0.52939428	0.88617146	-0.91758549
Q14195;H0YBT4;D6RF19;H0YB87	Dihydropyrimidinase-related protein 3	DPYSL3	1.630937335	0.57644792	0.705701351	-0.79473782
Q15124;Q5JTY7	Phosphoglucomutase-like protein 5	PGM5	0.126797163	4.28843756	-2.97940563	2.100452114
Q15149;H0YDN1;E9PMV1;E9PKG0;A0A075B730;P58107;E9PQ28;E9PIA2	Plectin	PLEC	0.327020829	1.42295041	-1.61254557	0.508885383
Q16774;B1ANH0;B1ANG9;B1ANH6;B1ANH2;B1ANH5;B1ANH3	Guanylate kinase	GUK1	1.825471275	0.54618196	0.868268967	-0.87254644
Q7Z406;A0A0C4DFM8;A1L2Z2;A0A2R8Y4C3;A0A2R8Y454	Myosin-14	MYH14	0.556849531	1.39303965	-0.84464055	0.478236318
Q7Z6G3;H3BQC7;H3BPH6	N-terminal EF-hand calcium-binding protein 2	NECAB2	0.230955854	4.05146511	-2.11431098	2.018443718
Q8IUX7;H7C0W8;H7C4B5;H7C391;H7C1J5;H7C3D7;Q8N436	Adipocyte enhancer-binding protein 1	AEBP1	2.134904869	1.52330071	1.094171785	0.607200772

Q8N3J6	Cell adhesion molecule 2	CADM2	2.161555293	0.38028821	1.112069741	-1.39483489
Q8N475;Q6MZW2	Follistatin-related protein 5	FSTL5	8.316333794	0.10310412	3.055947665	-3.27782612
Q8NBS9	Thioredoxin domain-containing protein 5	TXNDC5	0.633558333	1.64784359	-0.65845064	0.720579311
Q8NFV4;H0YC52;C9J7Q4;H7BZ58	Alpha/beta hydrolase domain-containing protein 11	ABHD11	0.40331493	2.1694552	-1.31002128	1.117332794
Q8TEM1	Nuclear pore membrane glycoprotein 210	NUP210	0.317625648	0.20989208	-1.65460068	-2.25228037
Q99536;K7ERT7;K7ENX2;K7EM19;K7ESA3;K7EJM4;K7ER81	Synaptic vesicle membrane protein VAT-1 homolog	VAT1	0.61606554	1.16944383	-0.69884425	0.225822568
Q9BPU6;E7EWB4;E9PHT0;E7ESV0	Dihydropyrimidinase-related protein 5	DPYSL5	1.420760798	0.61955504	0.50666368	-0.69069564
Q9HCJ6	Synaptic vesicle membrane protein VAT-1 homolog-like	VAT1L	0.190246605	0.26250428	-2.39405738	-1.92958716
Q9NP72;A0A087X163;Q5W0J0;H0Y6T8	Ras-related protein Rab-18	RAB18	1.314901456	0.73319613	0.394954682	-0.44772893
Q9NRW1;J3KR73;C9JU14;C9JB90;C9J0I2;Q53S08;Q9H0N0	Ras-related protein Rab-6B	RAB6B	1.14890495	0.86753232	0.200259447	-0.20501059
Q9UD71;J3KSJ8;J3KT77	Protein phosphatase 1 regulatory subunit 1B	PPP1R1B	1.609356415	1.69463789	0.686483867	0.760977033
Q9UEY8	Gamma-adducin	ADD3	0.619110371	1.23035475	-0.69173147	0.299074352
Q9UI15;C9J5W6;H7C5N2;C9JCX3	Transgelin-3	TAGLN3	1.45660863	0.80960098	0.542613298	-0.30471706
Q9Y617	Phosphoserine aminotransferase	PSAT1	0.646911928	1.52635917	-0.62835878	0.610094488
Q9Y6G9;E9PHI6;C9JGM7;C9JLW1	Cytoplasmic dynein 1 light intermediate chain 1	DYNC1LI1	1.35118518	0.69328545	0.43422541	-0.52847861

Bibliography

Abad-Morales, V., Bures-Jelstrup, A., Navarro, R., Ruiz-Nogales, S., Mendez-Vendrell, P., Corcostegui, B. and Pomares, E. (2019) 'Characterization of the cone-rod dystrophy retinal phenotype caused by novel homozygous DRAM2 mutations', *Exp Eye Res*, 187, p. 107752.

Abdul-Hammed, M., Breiden, B., Adebayo, M.A., Babalola, J.O., Schwarzmann, G. and Sandhoff, K. (2010) 'Role of endosomal membrane lipids and NPC2 in cholesterol transfer and membrane fusion', *J Lipid Res*, 51(7), pp. 1747-60.

Ablonczy, Z., Dahrouj, M., Tang, P.H., Liu, Y., Sambamurti, K., Marmorstein, A.D. and Crosson, C.E. (2011) 'Human retinal pigment epithelium cells as functional models for the RPE in vivo', *Invest Ophthalmol Vis Sci*, 52(12), pp. 8614-20.

Abudayyeh, O.O., Gootenberg, J.S., Essletzbichler, P., Han, S., Joung, J., Belanto, J.J., Verdine, V., Cox, D.B.T., Kellner, M.J., Regev, A., Lander, E.S., Voytas, D.F., Ting, A.Y. and Zhang, F. (2017) 'RNA targeting with CRISPR-Cas13', *Nature*, 550(7675), pp. 280-284.

Adamis, A.P., Miller, J.W., Bernal, M.T., D'Amico, D.J., Folkman, J., Yeo, T.K. and Yeo, K.T. (1994) 'Increased vascular endothelial growth factor levels in the vitreous of eyes with proliferative diabetic retinopathy', *Am J Ophthalmol*, 118(4), pp. 445-50.

Akwa, Y., Gondard, E., Mann, A., Capetillo-Zarate, E., Alberdi, E., Matute, C., Marty, S., Vaccari, T., Lozano, A.M., Baulieu, E.E. and Tampellini, D. (2018) 'Synaptic activity protects against AD and FTD-like pathology via autophagic-lysosomal degradation', *Mol Psychiatry*, 23(6), pp. 1530-1540.

Alcalay, R.N., Levy, O.A., Waters, C.C., Fahn, S., Ford, B., Kuo, S.H., Mazzoni, P., Pauciulo, M.W., Nichols, W.C., Gan-Or, Z., Rouleau, G.A., Chung, W.K., Wolf, P., Oliva, P., Keutzer, J., Marder, K. and Zhang, X. (2015) 'Glucocerebrosidase activity in Parkinson's disease with and without GBA mutations', *Brain*, 138(Pt 9), pp. 2648-58.

Allan, B.B., Moyer, B.D. and Balch, W.E. (2000) 'Rab1 recruitment of p115 into a cis-SNARE complex: programming budding COPII vesicles for fusion', *Science*, 289(5478), pp. 444-8.

Allegranza, A., Tredici, G., Marmiroli, P., di Donato, S., Franceschetti, S. and Mariani, C. (1989) 'Sialidosis type I: pathological study in an adult', *Clin Neuropathol*, 8(6), pp. 266-71.

Altuzar, J., Notbohm, J., Stein, F., Haberkant, P., Hempelmann, P., Heybrock, S., Worsch, J., Saftig, P. and Hoglinger, D. (2023) 'Lysosome-targeted multifunctional lipid probes reveal the sterol transporter NPC1 as a sphingosine interactor', *Proc Natl Acad Sci U S A*, 120(11), p. e2213886120.

Amano, N., Yokoi, S., Akagi, M., Sakai, M., Yagishita, S. and Nakata, K. (1983) 'Neuropathological findings of an autopsy case of adult beta-galactosidase and neuraminidase deficiency', *Acta Neuropathol*, 61(3-4), pp. 283-90.

Anderson, G.W., Goebel, H.H. and Simonati, A. (2013) 'Human pathology in NCL', *Biochim Biophys Acta*, 1832(11), pp. 1807-26.

Anderson, J., Walker, G. and Pu, J. (2022) 'BORC-ARL8-HOPS ensemble is required for lysosomal cholesterol egress through NPC2', *Mol Biol Cell*, 33(9), p. ar81.

Anheuser, S., Breiden, B., Schwarzmann, G. and Sandhoff, K. (2015) 'Membrane lipids regulate ganglioside GM2 catabolism and GM2 activator protein activity', *J Lipid Res*, 56(9), pp. 1747-61.

Anitei, M. and Hoflack, B. (2011) 'Bridging membrane and cytoskeleton dynamics in the secretory and endocytic pathways', *Nat Cell Biol*, 14(1), pp. 11-9.

Anzalone, A.V., Koblan, L.W. and Liu, D.R. (2020) 'Genome editing with CRISPR-Cas nucleases, base editors, transposases and prime editors', *Nat Biotechnol*, 38(7), pp. 824-844.

Atiskova, Y., Bartsch, S., Danyukova, T., Becker, E., Hagel, C., Storch, S. and Bartsch, U. (2019) 'Mice deficient in the lysosomal enzyme palmitoyl-protein thioesterase 1 (PPT1) display a complex retinal phenotype', *Sci Rep*, 9(1), p. 14185.

Awano, T., Katz, M.L., O'Brien, D.P., Taylor, J.F., Evans, J., Khan, S., Sohar, I., Lobel, P. and Johnson, G.S. (2006) 'A mutation in the cathepsin D gene (CTSD) in American Bulldogs with neuronal ceroid lipofuscinosis', *Mol Genet Metab*, 87(4), pp. 341-8.

Axe, E.L., Walker, S.A., Manifava, M., Chandra, P., Roderick, H.L., Habermann, A., Griffiths, G. and Ktistakis, N.T. (2008) 'Autophagosome formation from membrane compartments enriched in phosphatidylinositol 3-phosphate and dynamically connected to the endoplasmic reticulum', *J Cell Biol*, 182(4), pp. 685-701.

Badilla-Porras, R., Echeverri-McCandless, A., Weimer, J.M., Ulate-Campos, A., Soto-Rodriguez, A., Gutierrez-Mata, A., Hernandez-Con, L., Bogantes-Ledezma, S., Balmaceda-Meza, A., Brudvig, J. and Sanabria-Castro, A. (2022) 'Neuronal Ceroid Lipofuscinosis Type 6 (CLN6) clinical findings and molecular diagnosis: Costa Rica's experience', *Orphanet J Rare Dis*, 17(1), p. 13.

Bagaria, J., Bagyinszky, E. and An, S.S.A. (2022) 'Genetics, Functions, and Clinical Impact of Presenilin-1 (PSEN1) Gene', *Int J Mol Sci*, 23(18).

Bagh, M.B., Peng, S., Chandra, G., Zhang, Z., Singh, S.P., Pattabiraman, N., Liu, A. and Mukherjee, A.B. (2017) 'Misrouting of v-ATPase subunit V0a1 dysregulates lysosomal acidification in a neurodegenerative lysosomal storage disease model', *Nat Commun*, 8, p. 14612.

Balboa, E., Castro, J., Pinochet, M.J., Cancino, G.I., Matias, N., Saez, P.J., Martinez, A., Alvarez, A.R., Garcia-Ruiz, C., Fernandez-Checa, J.C. and Zanlungo, S. (2017) 'MLN64 induces mitochondrial dysfunction associated with increased mitochondrial cholesterol content', *Redox Biol*, 12, pp. 274-284.

Balderhaar, H.J. and Ungermann, C. (2013) 'CORVET and HOPS tethering complexes - coordinators of endosome and lysosome fusion', *J Cell Sci*, 126(Pt 6), pp. 1307-16.

Bar-Peled, L., Schweitzer, L.D., Zoncu, R. and Sabatini, D.M. (2012) 'Ragulator is a GEF for the rag GTPases that signal amino acid levels to mTORC1', *Cell*, 150(6), pp. 1196-208.

Bartsch, U. and Storch, S. (2022) 'Experimental Therapeutic Approaches for the Treatment of Retinal Pathology in Neuronal Ceroid Lipofuscinoses', *Front Neurol*, 13, p. 866983.

Bassal, M., Liu, J., Jankowiak, W., Saftig, P. and Bartsch, U. (2021) 'Rapid and Progressive Loss of Multiple Retinal Cell Types in Cathepsin D-Deficient Mice-An Animal Model of CLN10 Disease', *Cells*, 10(3).

Baumer, N., Marquardt, T., Stoykova, A., Spieler, D., Treichel, D., Ashery-Padan, R. and Gruss, P. (2003) 'Retinal pigmented epithelium determination requires the redundant activities of Pax2 and Pax6', *Development*, 130(13), pp. 2903-15.

Bazan, N.G. (2006) 'Cell survival matters: docosahexaenoic acid signaling, neuroprotection and photoreceptors', *Trends Neurosci*, 29(5), pp. 263-71.

Belevich, I., Joensuu, M., Kumar, D., Vihinen, H. and Jokitalo, E. (2016) 'Microscopy Image Browser: A Platform for Segmentation and Analysis of Multidimensional Datasets', *PLoS Biol*, 14(1), p. e1002340.

Bellapianta, A., Cetkovic, A., Bolz, M. and Salti, A. (2022) 'Retinal Organoids and Retinal Prostheses: An Overview', *Int J Mol Sci*, 23(6).

Benador, I.Y., Veliova, M., Mahdaviani, K., Petcherski, A., Wikstrom, J.D., Assali, E.A., Acin-Perez, R., Shum, M., Oliveira, M.F., Cinti, S., Sztalryd, C., Barshop, W.D., Wohlschlegel, J.A., Corkey, B.E., Liesa, M. and Shirihai, O.S. (2018) 'Mitochondria Bound to Lipid Droplets Have Unique Bioenergetics, Composition, and Dynamics that Support Lipid Droplet Expansion', *Cell Metab*, 27(4), pp. 869-885 e6.

Benedicto, I., Lehmann, G.L., Ginsberg, M., Nolan, D.J., Bareja, R., Elemento, O., Salfati, Z., Alam, N.M., Prusky, G.T., Llanos, P., Rabbany, S.Y., Maminishkis, A., Miller, S.S., Rafii, S. and Rodriguez-Boulan, E. (2017) 'Concerted regulation of retinal pigment epithelium basement membrane and barrier function by angiocrine factors', *Nat Commun*, 8, p. 15374.

Berger, A.C., Salazar, G., Styers, M.L., Newell-Litwa, K.A., Werner, E., Maue, R.A., Corbett, A.H. and Faundez, V. (2007) 'The subcellular localization of the Niemann-Pick Type C proteins depends on the adaptor complex AP-3', *J Cell Sci*, 120(Pt 20), pp. 3640-52.

Bhardwaj, M., Lee, J.J., Versace, A.M., Harper, S.L., Goldman, A.R., Crissey, M.A.S., Jain, V., Singh, M.P., Vernon, M., Aplin, A.E., Lee, S., Morita, M., Winkler, J.D., Liu, Q., Speicher, D.W. and Amaravadi, R.K. (2023) 'Lysosomal lipid peroxidation regulates tumor immunity', *J Clin Invest*, 133(8).

Blackburn, J.B. and Lupashin, V.V. (2016) 'Creating Knockouts of Conserved Oligomeric Golgi Complex Subunits Using CRISPR-Mediated Gene Editing Paired with a Selection Strategy Based on Glycosylation Defects Associated with Impaired COG Complex Function', *Methods Mol Biol*, 1496, pp. 145-61.

Blanz, J., Zunke, F., Markmann, S., Damme, M., Braulke, T., Saftig, P. and Schwake, M. (2015) 'Mannose 6-phosphate-independent Lysosomal Sorting of LIMP-2', *Traffic*, 16(10), pp. 1127-36.

Blom, T.S., Linder, M.D., Snow, K., Pihko, H., Hess, M.W., Jokitalo, E., Veckman, V., Syvanen, A.C. and Ikonen, E. (2003) 'Defective endocytic trafficking of NPC1 and NPC2 underlying infantile Niemann-Pick type C disease', *Hum Mol Genet*, 12(3), pp. 257-72.

Bodemann, B.O., Orvedahl, A., Cheng, T., Ram, R.R., Ou, Y.H., Formstecher, E., Maiti, M., Hazelett, C.C., Wauson, E.M., Balakireva, M., Camonis, J.H., Yeaman, C., Levine, B. and White, M.A. (2011) 'RalB and the exocyst mediate the cellular starvation response by direct activation of autophagosome assembly', *Cell*, 144(2), pp. 253-67.

Bondi, M.W., Edmonds, E.C. and Salmon, D.P. (2017) 'Alzheimer's Disease: Past, Present, and Future', *J Int Neuropsychol Soc*, 23(9-10), pp. 818-831.

Bonifacino, J.S. and Traub, L.M. (2003) 'Signals for sorting of transmembrane proteins to endosomes and lysosomes', *Annu Rev Biochem*, 72, pp. 395-447.

Bonnot, O., Klunemann, H.H., Velten, C., Torres Martin, J.V. and Walterfang, M. (2019) 'Systematic review of psychiatric signs in Niemann-Pick disease type C', *World J Biol Psychiatry*, 20(4), pp. 320-332.

Bourdenx, M., Daniel, J., Genin, E., Soria, F.N., Blanchard-Desce, M., Bezard, E. and Dehay, B. (2016) 'Nanoparticles restore lysosomal acidification defects: Implications for Parkinson and other lysosomal-related diseases', *Autophagy*, 12(3), pp. 472-83.

Bowmaker, J.K. and Hunt, D.M. (2006) 'Evolution of vertebrate visual pigments', *Curr Biol*, 16(13), pp. R484-9.

Brandwine, T., Ifrah, R., Bialistoky, T., Zaguri, R., Rhodes-Mordov, E., Mizrahi-Meissonnier, L., Sharon, D., Katanaev, V.L., Gerlitz, O. and Minke, B. (2021) 'Knockdown of Dehydrodolichyl Diphosphate Synthase in the Drosophila Retina Leads to a Unique Pattern of Retinal Degeneration', *Front Mol Neurosci*, 14, p. 693967.

Breiden, B. and Sandhoff, K. (2019a) 'Emerging mechanisms of drug-induced phospholipidosis', *Biol Chem*, 401(1), pp. 31-46.

Breiden, B. and Sandhoff, K. (2019b) 'Lysosomal Glycosphingolipid Storage Diseases', *Annu Rev Biochem*, 88, pp. 461-485.

Brogden, G., Shammas, H., Walters, F., Maalouf, K., Das, A.M., Naim, H.Y. and Rizk, S. (2020) 'Different Trafficking Phenotypes of Niemann-Pick C1 Gene Mutations Correlate with Various Alterations in Lipid Storage, Membrane Composition and Miglustat Amenability', *Int J Mol Sci*, 21(6).

Brown, M.S. and Goldstein, J.L. (1999) 'A proteolytic pathway that controls the cholesterol content of membranes, cells, and blood', *Proc Natl Acad Sci U S A*, 96(20), pp. 11041-8.

Buchholz, D.E., Pennington, B.O., Croze, R.H., Hinman, C.R., Coffey, P.J. and Clegg, D.O. (2013) 'Rapid and efficient directed differentiation of human pluripotent stem cells into retinal pigmented epithelium', *Stem Cells Transl Med*, 2(5), pp. 384-93.

Buczkowska, A., Swiezewska, E. and Lefeber, D.J. (2015) 'Genetic defects in dolichol metabolism', *J Inherit Metab Dis*, 38(1), pp. 157-69.

Bunk, J., Prieto Huarcaya, S., Drobny, A., Dobert, J.P., Walther, L., Rose-John, S., Arnold, P. and Zunke, F. (2021) 'Cathepsin D Variants Associated With Neurodegenerative Diseases Show Dysregulated Functionality and Modified alpha-Synuclein Degradation Properties', *Front Cell Dev Biol*, 9, p. 581805.

Cabrera, M., Langemeyer, L., Mari, M., Rethmeier, R., Orban, I., Perz, A., Brocker, C., Griffith, J., Klose, D., Steinhoff, H.J., Reggiori, F., Engelbrecht-Vandre, S. and Ungermann, C. (2010) 'Phosphorylation of a membrane curvature-sensing motif switches function of the HOPS subunit Vps41 in membrane tethering', *J Cell Biol*, 191(4), pp. 845-59.

Cai, Y., Cheng, T., Yao, Y., Li, X., Ma, Y., Li, L., Zhao, H., Bao, J., Zhang, M., Qiu, Z. and Xue, T. (2019) 'In vivo genome editing rescues photoreceptor degeneration via a Cas9/RecA-mediated homology-directed repair pathway', *Sci Adv*, 5(4), p. eaav3335.

Calabrese, J. and Al Khalili, Y. (2023) 'Psychosis', in *StatPearls*. Treasure Island (FL).

Calcagni, A., Staiano, L., Zampelli, N., Minopoli, N., Herz, N.J., Di Tullio, G., Huynh, T., Monfregola, J., Esposito, A., Cirillo, C., Bajic, A., Zahabiyon, M., Curnock, R., Polishchuk, E., Parkitny, L., Medina, D.L., Pastore, N., Cullen, P.J., Parenti, G., De Matteis, M.A., Grumati, P. and Ballabio, A. (2023) 'Loss of the batten disease protein CLN3 leads to mis-trafficking of M6PR and defective autophagic-lysosomal reformation', *Nat Commun*, 14(1), p. 3911.

Cang, C., Zhou, Y., Navarro, B., Seo, Y.J., Aranda, K., Shi, L., Battaglia-Hsu, S., Nissim, I., Clapham, D.E. and Ren, D. (2013) 'mTOR regulates lysosomal ATP-sensitive two-pore Na(+) channels to adapt to metabolic state', *Cell*, 152(4), pp. 778-790.

Canuel, M., Korkidakis, A., Konnyu, K. and Morales, C.R. (2008) 'Sortilin mediates the lysosomal targeting of cathepsins D and H', *Biochem Biophys Res Commun*, 373(2), pp. 292-7.

Capowski, E.E., Samimi, K., Mayerl, S.J., Phillips, M.J., Pinilla, I., Howden, S.E., Saha, J., Jansen, A.D., Edwards, K.L., Jager, L.D., Barlow, K., Valiauga, R., Erlichman, Z., Hagstrom, A., Sinha, D., Sluch, V.M., Chamling, X., Zack, D.J., Skala, M.C. and Gamm, D.M. (2019) 'Reproducibility and staging of 3D human retinal organoids across multiple pluripotent stem cell lines', *Development*, 146(1).

Capowski, E.E., Samimi, K., Mayerl, S.J., Phillips, M.J., Pinilla, I., Howden, S.E., Saha, J., Jansen, A.D., Edwards, K.L., Jager, L.D., Barlow, K., Valiaμga, R., Erlichman, Z., Hagstrom, A., Sinha, D., Sluch, V.M., Chamling, X., Zack, D.J., Skala, M.C. and Gamm, D.M. (2019) 'Reproducibility and staging of 3D human retinal organoids across multiple pluripotent stem cell lines', *Development*, 146(1).

Carcel-Trullols, J., Kovacs, A.D. and Pearce, D.A. (2015) 'Cell biology of the NCL proteins: What they do and don't do', *Biochim Biophys Acta*, 1852(10 Pt B), pp. 2242-55.

Castellano, B.M., Thelen, A.M., Moldavski, O., Feltes, M., van der Welle, R.E., Mydock-McGrane, L., Jiang, X., van Eijkeren, R.J., Davis, O.B., Louie, S.M., Perera, R.M., Covey, D.F., Nomura, D.K., Ory, D.S. and Zoncu, R. (2017) 'Lysosomal cholesterol activates mTORC1 via an SLC38A9-Niemann-Pick C1 signaling complex', *Science*, 355(6331), pp. 1306-1311.

Cepko, C. (2014) 'Intrinsically different retinal progenitor cells produce specific types of progeny', *Nat Rev Neurosci*, 15(9), pp. 615-27.

Cerna-Chavez, R., Rozanska, A., Poretti, G.L., Benvenisty, N., Parulekar, M. and Lako, M. (2023) 'Retinal pigment epithelium exhibits gene expression and phagocytic activity alterations when exposed to retinoblastoma chemotherapeutics', *Exp Eye Res*, 233, p. 109542.

Chan, E.Y., Longatti, A., McKnight, N.C. and Tooze, S.A. (2009) 'Kinase-inactivated ULK proteins inhibit autophagy via their conserved C-terminal domains using an Atg13-independent mechanism', *Mol Cell Biol*, 29(1), pp. 157-71.

Chandra, G., Bagh, M.B., Peng, S., Saha, A., Sarkar, C., Moralle, M., Zhang, Z. and Mukherjee, A.B. (2015) 'Cln1 gene disruption in mice reveals a common pathogenic link between two of the most

lethal childhood neurodegenerative lysosomal storage disorders', *Hum Mol Genet*, 24(19), pp. 5416-32.

Chang, T.Y., Reid, P.C., Sµgii, S., Ohgami, N., Cruz, J.C. and Chang, C.C. (2005) 'Niemann-Pick type C disease and intracellular cholesterol trafficking', *J Biol Chem*, 280(22), pp. 20917-20.

Chattopadhyay, S. and Pearce, D.A. (2000) 'Neural and extraneural expression of the neuronal ceroid lipofuscinoses genes CLN1, CLN2, and CLN3: functional implications for CLN3', *Mol Genet Metab*, 71(1-2), pp. 207-11.

Chavrier, P., Parton, R.G., Hauri, H.P., Simons, K. and Zerial, M. (1990) 'Localization of low molecular weight GTP binding proteins to exocytic and endocytic compartments', *Cell*, 62(2), pp. 317-29.

Chen, H., Tran, J.A., Eckerd, A., Huynh, T.P., Elliott, M.H., Brush, R.S. and Mandal, N.A. (2013) 'Inhibition of de novo ceramide biosynthesis by FTY720 protects rat retina from light-induced degeneration', *J Lipid Res*, 54(6), pp. 1616-1629.

Chen, L., Perera, N.D., Karoukis, A.J., Feathers, K.L., Ali, R.R., Thompson, D.A. and Fahim, A.T. (2022) 'Oxidative stress differentially impacts apical and basolateral secretion of angiogenic factors from human iPSC-derived retinal pigment epithelium cells', *Sci Rep*, 12(1), p. 12694.

Cheng, X.T., Zhou, B., Lin, M.Y., Cai, Q. and Sheng, Z.H. (2015) 'Axonal autophagosomes recruit dynein for retrograde transport through fusion with late endosomes', *J Cell Biol*, 209(3), pp. 377-86.

Chichagova, V., Georgiou, M., Carter, M., Dorgau, B., Hilgen, G., Collin, J., Queen, R., Chung, G., Ajeian, J., Moya-Molina, M., Kustermann, S., Pognan, F., Hewitt, P., Schmitt, M., Sernagor, E., Armstrong, L. and Lako, M. (2023) 'Incorporating microglia-like cells in human induced pluripotent stem cell-derived retinal organoids', *J Cell Mol Med*, 27(3), pp. 435-445.

Choi, E.H., Suh, S., Foik, A.T., Leinonen, H., Newby, G.A., Gao, X.D., Banskota, S., Hoang, T., Du, S.W., Dong, Z., Raguram, A., Kohli, S., Blackshaw, S., Lyon, D.C., Liu, D.R. and Palczewski, K. (2022) 'In vivo base editing rescues cone photoreceptors in a mouse model of early-onset inherited retinal degeneration', *Nat Commun*, 13(1), p. 1830.

Chou, S.M. (1968) '"Megaconial" mitochondria observed in a case of chronic polymyositis', *Acta Neuropathol*, 12(1), pp. 68-89.

Choudhary, P., Booth, H., Gutteridge, A., Surmacz, B., Louca, I., Steer, J., Kerby, J. and Whiting, P.J. (2017) 'Directing Differentiation of Pluripotent Stem Cells Toward Retinal Pigment Epithelium Lineage', *Stem Cells Transl Med*, 6(2), pp. 490-501.

Citi, S. (2019) 'The mechanobiology of tight junctions', *Biophys Rev*, 11(5), pp. 783-793.

Clark, L.N., Ross, B.M., Wang, Y., Mejia-Santana, H., Harris, J., Louis, E.D., Cote, L.J., Andrews, H., Fahn, S., Waters, C., Ford, B., Frucht, S., Ottman, R. and Marder, K. (2007) 'Mutations in the glucocerebrosidase gene are associated with early-onset Parkinson disease', *Neurology*, 69(12), pp. 1270-7.

Colacurcio, D.J. and Nixon, R.A. (2016) 'Disorders of lysosomal acidification-The emerging role of v-ATPase in aging and neurodegenerative disease', *Ageing Res Rev*, 32, pp. 75-88.

Compagnucci, C., Barresi, S., Petrini, S., Bertini, E. and Zanni, G. (2015) 'Rho-kinase signaling controls nucleocytoplasmic shuttling of class IIa histone deacetylase (HDAC7) and transcriptional activation of orphan nuclear receptor NR4A1', *Biochem Biophys Res Commun*, 459(2), pp. 179-183.

Cong, L., Ran, F.A., Cox, D., Lin, S., Barretto, R., Habib, N., Hsu, P.D., Wu, X., Jiang, W., Marraffini, L.A. and Zhang, F. (2013) 'Multiplex genome engineering using CRISPR/Cas systems', *Science*, 339(6121), pp. 819-23.

Cong, L., Ran, F.A., Cox, D., Lin, S., Barretto, R., Habib, N., Hsu, P.D., Wu, X., Jiang, W., Marraffini, L.A. and Zhang, F. (2013) 'Multiplex genome engineering using CRISPR/Cas systems', *Science*, 339(6121), pp. 819-23.

Conibear, E., Cleck, J.N. and Stevens, T.H. (2003) 'Vps51p mediates the association of the GARP (Vps52/53/54) complex with the late Golgi t-SNARE Tlg1p', *Mol Biol Cell*, 14(4), pp. 1610-23.

Contreras, F.X., Sot, J., Alonso, A. and Goni, F.M. (2006) 'Sphingosine increases the permeability of model and cell membranes', *Biophys J*, 90(11), pp. 4085-92.

Costa, R.M., Martul, E.V., Reboredo, J.M. and Cigarran, S. (2013) 'Curvilinear bodies in hydroxychloroquine-induced renal phospholipidosis resembling Fabry disease', *Clin Kidney J*, 6(5), pp. 533-6.

Cowan, C.S., Renner, M., De Gennaro, M., Gross-Scherf, B., Goldblum, D., Hou, Y., Munz, M., Rodrigues, T.M., Krol, J., Szikra, T., Cuttat, R., Waldt, A., Papasaikas, P., Diggelmann, R., Patino-

Alvarez, C.P., Galliker, P., Spirig, S.E., Pavlinic, D., Gerber-Hollbach, N., Schuierer, S., Srdanovic, A., Balogh, M., Panero, R., Kusnyerik, A., Szabo, A., Stadler, M.B., Orgul, S., Picelli, S., Hasler, P.W., Hierlemann, A., Scholl, H.P.N., Roma, G., Nigsch, F. and Roska, B. (2020) 'Cell Types of the Human Retina and Its Organoids at Single-Cell Resolution', *Cell*, 182(6), pp. 1623-1640 e34.

Cowan, C.S., Renner, M., De Gennaro, M., Gross-Scherf, B., Goldblum, D., Hou, Y., Munz, M., Rodrigues, T.M., Krol, J., Szikra, T., Cuttat, R., Waldt, A., Papasaikas, P., Diggelmann, R., Patino-Alvarez, C.P., Galliker, P., Spirig, S.E., Pavlinic, D., Gerber-Hollbach, N., Schuierer, S., Srdanovic, A., Balogh, M., Panero, R., Kusnyerik, A., Szabo, A., Stadler, M.B., Orgul, S., Picelli, S., Hasler, P.W., Hierlemann, A., Scholl, H.P.N., Roma, G., Nigsch, F. and Roska, B. (2020) 'Cell Types of the Human Retina and Its Organoids at Single-Cell Resolution', *Cell*, 182(6), pp. 1623-1640 e34.

Cowan, C.S., Renner, M., De Gennaro, M., Gross-Scherf, B., Goldblum, D., Hou, Y., Munz, M., Rodrigues, T.M., Krol, J., Szikra, T., Cuttat, R., Waldt, A., Papasaikas, P., Diggelmann, R., Patino-Alvarez, C.P., Galliker, P., Spirig, S.E., Pavlinic, D., Gerber-Hollbach, N., Schuierer, S., Srdanovic, A., Balogh, M., Panero, R., Kusnyerik, A., Szabo, A., Stadler, M.B., Orgul, S., Picelli, S., Hasler, P.W., Hierlemann, A., Scholl, H.P.N., Roma, G., Nigsch, F. and Roska, B. (2020) 'Cell Types of the Human Retina and Its Organoids at Single-Cell Resolution', *Cell*, 182(6), pp. 1623-1640 e34.

Cremers, F.P.M., Boon, C.J.F., Bujakowska, K. and Zeitz, C. (2018) 'Special Issue Introduction: Inherited Retinal Disease: Novel Candidate Genes, Genotype-Phenotype Correlations, and Inheritance Models', *Genes (Basel)*, 9(4).

Crosiers, D., Verstraeten, A., Wauters, E., Engelborghs, S., Peeters, K., Mattheijssens, M., De Deyn, P.P., Theuns, J., Van Broeckhoven, C. and Cras, P. (2016) 'Mutations in glucocerebrosidase are a major genetic risk factor for Parkinson's disease and increase susceptibility to dementia in a Flanders-Belgian cohort', *Neurosci Lett*, 629, pp. 160-164.

Cuervo, A.M. and Dice, J.F. (2000) 'Regulation of lamp2a levels in the lysosomal membrane', *Traffic*, 1(7), pp. 570-83.

Cuervo, A.M. and Wong, E. (2014) 'Chaperone-mediated autophagy: roles in disease and aging', *Cell Res*, 24(1), pp. 92-104.

Cui, L., Zhao, L.P., Ye, J.Y., Yang, L., Huang, Y., Jiang, X.P., Zhang, Q., Jia, J.Z., Zhang, D.X. and Huang, Y. (2020) 'The Lysosomal Membrane Protein Lamp2 Alleviates Lysosomal Cell Death by Promoting Autophagic Flux in Ischemic Cardiomyocytes', *Front Cell Dev Biol*, 8, p. 31.

Dannhausen, K., Mohle, C. and Langmann, T. (2018) 'Immunomodulation with minocycline rescues retinal degeneration in juvenile neuronal ceroid lipofuscinosis mice highly susceptible to light damage', *Dis Model Mech*, 11(9).

Davis, L.J., Bright, N.A., Edgar, J.R., Parkinson, M.D.J., Wartosch, L., Mantell, J., Peden, A.A. and Luzio, J.P. (2021) 'Organelle tethering, pore formation and SNARE compensation in the late endocytic pathway', *J Cell Sci*, 134(10).

Dawson, D.W., Volpert, O.V., Gillis, P., Crawford, S.E., Xu, H., Benedict, W. and Bouck, N.P. (1999) 'Pigment epithelium-derived factor: a potent inhibitor of angiogenesis', *Science*, 285(5425), pp. 245-8.

Dearborn, J.T., Ramachandran, S., Shyng, C., Lu, J.Y., Thornton, J., Hofmann, S.L. and Sands, M.S. (2016) 'Histochemical localization of palmitoyl protein thioesterase-1 activity', *Mol Genet Metab*, 117(2), pp. 210-6.

Deinhardt, K., Salinas, S., Verastegui, C., Watson, R., Worth, D., Hanrahan, S., Bucci, C. and Schiavo, G. (2006) 'Rab5 and Rab7 control endocytic sorting along the axonal retrograde transport pathway', *Neuron*, 52(2), pp. 293-305.

Delevoye, C., Hurbain, I., Tenza, D., Sibarita, J.B., Uzan-Gafsou, S., Ohno, H., Geerts, W.J., Verkleij, A.J., Salamero, J., Marks, M.S. and Raposo, G. (2009) 'AP-1 and KIF13A coordinate endosomal sorting and positioning during melanosome biogenesis', *J Cell Biol*, 187(2), pp. 247-64.

Delevoye, C., Miserey-Lenkei, S., Montagnac, G., Gilles-Marsens, F., Paul-Gilloteaux, P., Giordano, F., Waharte, F., Marks, M.S., Goud, B. and Raposo, G. (2014) 'Recycling endosome tubule morphogenesis from sorting endosomes requires the kinesin motor KIF13A', *Cell Rep*, 6(3), pp. 445-54.

Demb, J.B. and Singer, J.H. (2015) 'Functional Circuitry of the Retina', *Annu Rev Vis Sci*, 1, pp. 263-289.

DeRamus, M.L., Davis, S.J., Rao, S.R., Nyankerh, C., Stacks, D., Kraft, T.W., Fliesler, S.J. and Pittler, S.J. (2020) 'Selective Ablation of Dehydrodolichyl Diphosphate Synthase in Murine Retinal Pigment Epithelium (RPE) Causes RPE Atrophy and Retinal Degeneration', *Cells*, 9(3).

Diao, A., Rahman, D., Pappin, D.J., Lucocq, J. and Lowe, M. (2003) 'The coiled-coil membrane protein golgin-84 is a novel rab effector required for Golgi ribbon formation', *J Cell Biol*, 160(2), pp. 201-12.

Do, M.T.H. (2019) 'Melanopsin and the Intrinsically Photosensitive Retinal Ganglion Cells: Biophysics to Behavior', *Neuron*, 104(2), pp. 205-226.

Doccini, S., Sartori, S., Maeser, S., Pezzini, F., Rossato, S., Moro, F., Toldo, I., Przybylski, M., Santorelli, F.M. and Simonati, A. (2016) 'Early infantile neuronal ceroid lipofuscinosis (CLN10 disease) associated with a novel mutation in CTSD', *J Neurol*, 263(5), pp. 1029-1032.

Donaldson, J.G., Honda, A. and Weigert, R. (2005) 'Multiple activities for Arf1 at the Golgi complex', *Biochim Biophys Acta*, 1744(3), pp. 364-73.

Dooley, H.C., Razi, M., Polson, H.E., Girardin, S.E., Wilson, M.I. and Tooze, S.A. (2014) 'WIPI2 links LC3 conjugation with PI3P, autophagosome formation, and pathogen clearance by recruiting Atg12-5-16L1', *Mol Cell*, 55(2), pp. 238-52.

Doray, B., Ghosh, P., Griffith, J., Geuze, H.J. and Kornfeld, S. (2002) 'Cooperation of GGAs and AP-1 in packaging MPRs at the trans-Golgi network', *Science*, 297(5587), pp. 1700-3.

Dorgau, B., Felemban, M., Hilgen, G., Kiening, M., Zerti, D., Hunt, N.C., Doherty, M., Whitfield, P., Hallam, D., White, K., Ding, Y., Krasnogor, N., Al-Aama, J., Asfour, H.Z., Sernagor, E. and Lako, M. (2019) 'Decellularised extracellular matrix-derived peptides from neural retina and retinal pigment epithelium enhance the expression of synaptic markers and light responsiveness of human pluripotent stem cell derived retinal organoids', *Biomaterials*, 199, pp. 63-75.

Dow, L.E., Fisher, J., O'Rourke, K.P., Muley, A., Kastenhuber, E.R., Livshits, G., Tschaharganeh, D.F., Socci, N.D. and Lowe, S.W. (2015) 'Inducible in vivo genome editing with CRISPR-Cas9', *Nat Biotechnol*, 33(4), pp. 390-394.

D'Souza, Z., Blackburn, J.B., Kudlyk, T., Pokrovskaya, I.D. and Lupashin, V.V. (2019) 'Defects in COG-Mediated Golgi Trafficking Alter Endo-Lysosomal System in Human Cells', *Front Cell Dev Biol*, 7, p. 118.

Duncan, M.C. (2022) 'New directions for the clathrin adaptor AP-1 in cell biology and human disease', *Curr Opin Cell Biol*, 76, p. 102079.

Dvoriashyna, M., Foss, A.J.E., Gaffney, E.A. and Repetto, R. (2020) 'Fluid and solute transport across the retinal pigment epithelium: a theoretical model', *J R Soc Interface*, 17(163), p. 20190735.

Egan, D.F., Chun, M.G., Vamos, M., Zou, H., Rong, J., Miller, C.J., Lou, H.J., Raveendra-Panickar, D., Yang, C.C., Sheffler, D.J., Teriete, P., Asara, J.M., Turk, B.E., Cosford, N.D. and Shaw, R.J. (2015) 'Small Molecule Inhibition of the Autophagy Kinase ULK1 and Identification of ULK1 Substrates', *Mol Cell*, 59(2), pp. 285-97.

Eiraku, M., Takata, N., Ishibashi, H., Kawada, M., Sakakura, E., Okuda, S., Sekiguchi, K., Adachi, T. and Sasai, Y. (2011) 'Self-organizing optic-cup morphogenesis in three-dimensional culture', *Nature*, 472(7341), pp. 51-6.

Eiraku, M., Watanabe, K., Matsuo-Takasaki, M., Kawada, M., Yonemura, S., Matsumura, M., Wataya, T., Nishiyama, A., Muguruma, K. and Sasai, Y. (2008) 'Self-organized formation of polarized cortical tissues from ESCs and its active manipulation by extrinsic signals', *Cell Stem Cell*, 3(5), pp. 519-32.

Eising, S., Thiele, L. and Frohlich, F. (2019) 'A systematic approach to identify recycling endocytic cargo depending on the GARP complex', *Elife*, 8.

El-Asrag, M.E., Sergouniotis, P.I., McKibbin, M., Plagnol, V., Sheridan, E., Waseem, N., Abdelhamed, Z., McKeefry, D., Van Schil, K., Poulter, J.A., Consortium, U.K.I.R.D., Johnson, C.A., Carr, I.M., Leroy, B.P., De Baere, E., Inglehearn, C.F., Webster, A.R., Toomes, C. and Ali, M. (2015) 'Biallelic mutations in the autophagy regulator DRAM2 cause retinal dystrophy with early macular involvement', *Am J Hum Genet*, 96(6), pp. 948-54.

Eldred, K.C., Hadyniak, S.E., Hussey, K.A., Brenerman, B., Zhang, P.W., Chamling, X., Sluch, V.M., Welsbie, D.S., Hattar, S., Taylor, J., Wahlin, K., Zack, D.J. and Johnston, R.J., Jr. (2018) 'Thyroid hormone signaling specifies cone subtypes in human retinal organoids', *Science*, 362(6411).

Encarnacao, M., Espada, L., Escrevente, C., Mateus, D., Ramalho, J., Michelet, X., Santarino, I., Hsu, V.W., Brenner, M.B., Barral, D.C. and Vieira, O.V. (2016) 'A Rab3a-dependent complex essential for lysosome positioning and plasma membrane repair', *J Cell Biol*, 213(6), pp. 631-40.

Evans, W.R. and Hendriksz, C.J. (2017) 'Niemann-Pick type C disease - the tip of the iceberg? A review of neuropsychiatric presentation, diagnosis and treatment', *BJPsych Bull*, 41(2), pp. 109-114.

Faitg, J., Davey, T., Turnbull, D.M., White, K. and Vincent, A.E. (2020) 'Mitochondrial morphology and function: two for the price of one!', *J Microsc*, 278(2), pp. 89-106.

Fan, J., Liu, J., Liu, J., Chen, C., Koutalos, Y. and Crosson, C.E. (2021) 'Evidence for ceramide induced cytotoxicity in retinal ganglion cells', *Exp Eye Res*, 211, p. 108762.

Fei, W., Shui, G., Gaeta, B., Du, X., Kuerschner, L., Li, P., Brown, A.J., Wenk, M.R., Parton, R.G. and Yang, H. (2008) 'Fld1p, a functional homologue of human seipin, regulates the size of lipid droplets in yeast', *J Cell Biol*, 180(3), pp. 473-82.

Feinstein, M., Flusser, H., Lerman-Sagie, T., Ben-Zeev, B., Lev, D., Agamy, O., Cohen, I., Kadir, R., Sivan, S., Leshinsky-Silver, E., Markus, B. and Birk, O.S. (2014) 'VPS53 mutations cause progressive cerebello-cerebral atrophy type 2 (PCCA2)', *J Med Genet*, 51(5), pp. 303-8.

Feng, Q.N., Song, S.J., Yu, S.X., Wang, J.G., Li, S. and Zhang, Y. (2017) 'Adaptor Protein-3-Dependent Vacuolar Trafficking Involves a Subpopulation of COPII and HOPS Tethering Proteins', *Plant Physiol*, 174(3), pp. 1609-1620.

Feng, Y., He, D., Yao, Z. and Klionsky, D.J. (2014) 'The machinery of macroautophagy', *Cell Res*, 24(1), pp. 24-41.

Fernandes, T., Domingues, M.R., Moreira, P.I. and Pereira, C.F. (2023) 'A Perspective on the Link between Mitochondria-Associated Membranes (MAMs) and Lipid Droplets Metabolism in Neurodegenerative Diseases', *Biology (Basel)*, 12(3).

Ferruzza, S., Rossi, C., Sambuy, Y. and Scarino, M.L. (2013) 'Serum-reduced and serum-free media for differentiation of Caco-2 cells', *ALTEX*, 30(2), pp. 159-68.

Fields, M.A., Del Priore, L.V., Adelman, R.A. and Rizzolo, L.J. (2020) 'Interactions of the choroid, Bruch's membrane, retinal pigment epithelium, and neurosensory retina collaborate to form the outer blood-retinal-barrier', *Prog Retin Eye Res*, 76, p. 100803.

Filipek, P.A., de Araujo, M.E.G., Vogel, G.F., De Smet, C.H., Eberharter, D., Rebsamen, M., Rudashevskaya, E.L., Kremser, L., Yordanov, T., Tschaikner, P., Furnrohr, B.G., Lechner, S., Dunzendorfer-Matt, T., Scheffzek, K., Bennett, K.L., Superti-Furga, G., Lindner, H.H., Stasyk, T. and Huber, L.A. (2017) 'LAMTOR/Ragulator is a negative regulator of Arl8b- and BORC-dependent late endosomal positioning', *J Cell Biol*, 216(12), pp. 4199-4215.

Fischer, E.G., Moore, M.J. and Lager, D.J. (2006) 'Fabry disease: a morphologic study of 11 cases', *Mod Pathol*, 19(10), pp. 1295-301.

Flaxman, S.R., Bourne, R.R.A., Resnikoff, S., Ackland, P., Braithwaite, T., Cicinelli, M.V., Das, A., Jonas, J.B., Keeffe, J., Kempen, J.H., Leasher, J., Limburg, H., Naidoo, K., Pesudovs, K., Silvester, A., Stevens, G.A., Tahhan, N., Wong, T.Y., Taylor, H.R. and Vision Loss Expert Group of the Global Burden of Disease, S. (2017) 'Global causes of blindness and distance vision impairment 1990-2020: a systematic review and meta-analysis', *Lancet Glob Health*, 5(12), pp. e1221-e1234.

Foltz, L.P. and Clegg, D.O. (2017) 'Rapid, Directed Differentiation of Retinal Pigment Epithelial Cells from Human Embryonic or Induced Pluripotent Stem Cells', *J Vis Exp*, (128).

Foulquier, F. (2009) 'COG defects, birth and rise!', *Biochim Biophys Acta*, 1792(9), pp. 896-902.

Fraldi, A., Klein, A.D., Medina, D.L. and Settembre, C. (2016) 'Brain Disorders Due to Lysosomal Dysfunction', *Annu Rev Neurosci*, 39, pp. 277-95.

Fritchie, K., Siintola, E., Armao, D., Lehesjoki, A.E., Marino, T., Powell, C., Tennison, M., Booker, J.M., Koch, S., Partanen, S., Suzuki, K., Tyynela, J. and Thorne, L.B. (2009) 'Novel mutation and the first prenatal screening of cathepsin D deficiency (CLN10)', *Acta Neuropathol*, 117(2), pp. 201-8.

Fritchie, K., Siintola, E., Armao, D., Lehesjoki, A.E., Marino, T., Powell, C., Tennison, M., Booker, J.M., Koch, S., Partanen, S., Suzuki, K., Tyynela, J. and Thorne, L.B. (2009) 'Novel mutation and the first prenatal screening of cathepsin D deficiency (CLN10)', *Acta Neuropathol*, 117(2), pp. 201-8.

Frohlich, F., Petit, C., Kory, N., Christiano, R., Hannibal-Bach, H.K., Graham, M., Liu, X., Ejsing, C.S., Farese, R.V. and Walther, T.C. (2015) 'The GARP complex is required for cellular sphingolipid homeostasis', *Elife*, 4.

Frolov, A., Zielinski, S.E., Crowley, J.R., Dudley-Rucker, N., Schaffer, J.E. and Ory, D.S. (2003) 'NPC1 and NPC2 regulate cellular cholesterol homeostasis through generation of low density lipoprotein cholesterol-derived oxysterols', *J Biol Chem*, 278(28), pp. 25517-25.

Fu, X., Menke, J.G., Chen, Y., Zhou, G., MacNaul, K.L., Wright, S.D., Sparrow, C.P. and Lund, E.G. (2001) '27-hydroxycholesterol is an endogenous ligand for liver X receptor in cholesterol-loaded cells', *J Biol Chem*, 276(42), pp. 38378-87.

Fuhrmann, S., Zou, C. and Levine, E.M. (2014) 'Retinal pigment epithelium development, plasticity, and tissue homeostasis', *Exp Eye Res*, 123, pp. 141-50.

Fujita, H., Saeki, M., Yasunaga, K., Ueda, T., Imoto, T. and Himeno, M. (1999) 'In vitro binding study of adaptor protein complex (AP-1) to lysosomal targeting motif (LI-motif)', *Biochem Biophys Res Commun*, 255(1), pp. 54-8.

Fujita, N., Itoh, T., Omori, H., Fukuda, M., Noda, T. and Yoshimori, T. (2008) 'The Atg16L complex specifies the site of LC3 lipidation for membrane biogenesis in autophagy', *Mol Biol Cell*, 19(5), pp. 2092-100.

Fukui, K., Yang, Q., Cao, Y., Takahashi, N., Hatakeyama, H., Wang, H., Wada, J., Zhang, Y., Marselli, L., Nammo, T., Yoneda, K., Onishi, M., Higashiyama, S., Matsuzawa, Y., Gonzalez, F.J., Weir, G.C., Kasai, H., Shimomura, I., Miyagawa, J., Wollheim, C.B. and Yamagata, K. (2005) 'The HNF-1 target collectrin controls insulin exocytosis by SNARE complex formation', *Cell Metab*, 2(6), pp. 373-84.

Galindo, A. and Munro, S. (2023) 'The TRAPP complexes: oligomeric exchange factors that activate the small GTPases Rab1 and Rab11', *FEBS Lett*, 597(6), pp. 734-749.

Ganasen, M., Togashi, H., Takeda, H., Asakura, H., Tosha, T., Yamashita, K., Hirata, K., Nariai, Y., Urano, T., Yuan, X., Hamza, I., Mauk, A.G., Shiro, Y., Sμgimoto, H. and Sawai, H. (2018) 'Structural basis for promotion of duodenal iron absorption by enteric ferric reductase with ascorbate', *Commun Biol*, 1, p. 120.

Gao, J., Nicastro, R., Peli-Gulli, M.P., Grziwa, S., Chen, Z., Kurre, R., Piehler, J., De Virgilio, C., Frohlich, F. and Ungermann, C. (2022) 'The HOPS tethering complex is required to maintain signaling endosome identity and TORC1 activity', *J Cell Biol*, 221(5).

Garcia-Sanz, P., Orgaz, L., Bueno-Gil, G., Espadas, I., Rodriguez-Traver, E., Kulisevsky, J., Gutierrez, A., Davila, J.C., Gonzalez-Polo, R.A., Fuentes, J.M., Mir, P., Vicario, C. and Moratalla, R. (2017) 'N370S-GBA1 mutation causes lysosomal cholesterol accumulation in Parkinson's disease', *Mov Disord*, 32(10), pp. 1409-1422.

Garita-Hernandez, M., Lampic, M., Chaffiol, A., Guibbal, L., Routet, F., Santos-Ferreira, T., Gasparini, S., Borsch, O., Gagliardi, G., Reichman, S., Picaud, S., Sahel, J.A., Goureau, O., Ader, M., Dalkara, D. and Duebel, J. (2019) 'Restoration of visual function by transplantation of optogenetically engineered photoreceptors', *Nat Commun*, 10(1), p. 4524.

Gaudelli, N.M., Komor, A.C., Rees, H.A., Packer, M.S., Badran, A.H., Bryson, D.I. and Liu, D.R. (2017) 'Programmable base editing of A*T to G*C in genomic DNA without DNA cleavage', *Nature*, 551(7681), pp. 464-471.

Georgiou, M., Fujinami, K. and Michaelides, M. (2021) 'Inherited retinal diseases: Therapeutics, clinical trials and end points-A review', *Clin Exp Ophthalmol*, 49(3), pp. 270-288.

German, O.L., Miranda, G.E., Abrahan, C.E. and Rotstein, N.P. (2006) 'Ceramide is a mediator of apoptosis in retina photoreceptors', *Invest Ophthalmol Vis Sci*, 47(4), pp. 1658-68.

Gershlick, D.C., Ishida, M., Jones, J.R., Bellomo, A., Bonifacino, J.S. and Everman, D.B. (2019) 'A neurodevelopmental disorder caused by mutations in the VPS51 subunit of the GARP and EARP complexes', *Hum Mol Genet*, 28(9), pp. 1548-1560.

Giannelli, S.G., Luoni, M., Castoldi, V., Massimino, L., Cabassi, T., Angeloni, D., Demontis, G.C., Leocani, L., Andreazzoli, M. and Broccoli, V. (2018) 'Cas9/sgRNA selective targeting of the P23H Rhodopsin mutant allele for treating retinitis pigmentosa by intravitreal AAV9.PHP.B-based delivery', *Hum Mol Genet*, 27(5), pp. 761-779.

Gilissen, E.P. and Staneva-Dobrovski, L. (2013) 'Distinct types of lipofuscin pigment in the hippocampus and cerebellum of aged cheirogaleid primates', *Anat Rec (Hoboken)*, 296(12), pp. 1895-906.

Gillingham, A.K., Sinka, R., Torres, I.L., Lilley, K.S. and Munro, S. (2014) 'Toward a comprehensive map of the effectors of rab GTPases', *Dev Cell*, 31(3), pp. 358-373.

Goldberg, A.F., Moritz, O.L. and Williams, D.S. (2016) 'Molecular basis for photoreceptor outer segment architecture', *Prog Retin Eye Res*, 55, pp. 52-81.

Gonzalez-Cordero, A., Kruczek, K., Naeem, A., Fernando, M., Kloc, M., Ribeiro, J., Goh, D., Duran, Y., Blackford, S.J.I., Abelleira-Hervas, L., Sampson, R.D., Shum, I.O., Branch, M.J., Gardner, P.J., Sowden, J.C., Bainbridge, J.W.B., Smith, A.J., West, E.L., Pearson, R.A. and Ali, R.R. (2017) 'Recapitulation of Human Retinal Development from Human Pluripotent Stem Cells Generates Transplantable Populations of Cone Photoreceptors', *Stem Cell Reports*, 9(3), pp. 820-837.

Goo, M.S., Sancho, L., Slepak, N., Boassa, D., Deerinck, T.J., Ellisman, M.H., Bloodgood, B.L. and Patrick, G.N. (2017) 'Activity-dependent trafficking of lysosomes in dendrites and dendritic spines', *J Cell Biol*, 216(8), pp. 2499-2513.

Gowrishankar, S., Yuan, P., Wu, Y., Schrag, M., Paradise, S., Grutzendler, J., De Camilli, P. and Ferguson, S.M. (2015) 'Massive accumulation of luminal protease-deficient axonal lysosomes at Alzheimer's disease amyloid plaques', *Proc Natl Acad Sci U S A*, 112(28), pp. E3699-708.

Graf, R., Li, X., Chu, V.T. and Rajewsky, K. (2019) 'sgRNA Sequence Motifs Blocking Efficient CRISPR/Cas9-Mediated Gene Editing', *Cell Rep*, 26(5), pp. 1098-1103 e3.

Greenberg, A.S., Coleman, R.A., Kraemer, F.B., McManaman, J.L., Obin, M.S., Puri, V., Yan, Q.W., Miyoshi, H. and Mashek, D.G. (2011) 'The role of lipid droplets in metabolic disease in rodents and humans', *J Clin Invest*, 121(6), pp. 2102-10.

Griffey, M., Macauley, S.L., Ogilvie, J.M. and Sands, M.S. (2005) 'AAV2-mediated ocular gene therapy for infantile neuronal ceroid lipofuscinosis', *Mol Ther*, 12(3), pp. 413-21.

Groh, J., Berve, K. and Martini, R. (2017) 'Fingolimod and Teriflunomide Attenuate Neurodegeneration in Mouse Models of Neuronal Ceroid Lipofuscinosis', *Mol Ther*, 25(8), pp. 1889-1899.

Groh, J., Kuhl, T.G., Ip, C.W., Nelvagal, H.R., Sri, S., Duckett, S., Mirza, M., Langmann, T., Cooper, J.D. and Martini, R. (2013) 'Immune cells perturb axons and impair neuronal survival in a mouse model of infantile neuronal ceroid lipofuscinosis', *Brain*, 136(Pt 4), pp. 1083-101.

Groh, J., Ribechini, E., Stadler, D., Schilling, T., Lutz, M.B. and Martini, R. (2016) 'Sialoadhesin promotes neuroinflammation-related disease progression in two mouse models of CLN disease', *Glia*, 64(5), pp. 792-809.

Guan, Z., Li, W., L., Byron, L.W., ; Wen., R. (2015). 'Significant age-related accumulation and shortening of dolichol in the normal retina.' *ARVO Annual meeting abstract.*

Guo, H., Zhao, M., Qiu, X., Deis, J.A., Huang, H., Tang, Q.Q. and Chen, X. (2016) 'Niemann-Pick type C2 deficiency impairs autophagy-lysosomal activity, mitochondrial function, and TLR signaling in adipocytes', *J Lipid Res*, 57(9), pp. 1644-58.

Guo, Y., Sirkis, D.W. and Schekman, R. (2014) 'Protein sorting at the trans-Golgi network', *Annu Rev Cell Dev Biol*, 30, pp. 169-206.

Gurdon, J.B. (1962) 'The developmental capacity of nuclei taken from intestinal epithelium cells of feeding tadpoles', *J Embryol Exp Morphol*, 10, pp. 622-40.

Hachiro, T., Yamamoto, T., Nakano, K. and Tanaka, K. (2013) 'Phospholipid flippases Lem3p-Dnf1p and Lem3p-Dnf2p are involved in the sorting of the tryptophan permease Tat2p in yeast', *J Biol Chem*, 288(5), pp. 3594-608.

Hady-Cohen, R., Ben-Pazi, H., Adir, V., Yosovich, K., Blumkin, L., Lerman-Sagie, T. and Lev, D. (2018) 'Progressive cerebello-cerebral atrophy and progressive encephalopathy with edema, hypsarrhythmia and optic atrophy may be allelic syndromes', *Eur J Paediatr Neurol*, 22(6), pp. 1133-1138.

Hall, M.O., Burgess, B.L., Arakawa, H. and Fliesler, S.J. (1990) 'The effect of inhibitors of glycoprotein synthesis and processing on the phagocytosis of rod outer segments by cultured retinal pigment epithelial cells', *Glycobiology*, 1(1), pp. 51-61.

Hallam, D., Hilgen, G., Dorgau, B., Zhu, L., Yu, M., Bojic, S., Hewitt, P., Schmitt, M., Uteng, M., Kustermann, S., Steel, D., Nicholds, M., Thomas, R., Treumann, A., Porter, A., Sernagor, E., Armstrong, L. and Lako, M. (2018) 'Human-Induced Pluripotent Stem Cells Generate Light Responsive Retinal Organoids with Variable and Nutrient-Dependent Efficiency', *Stem Cells*, 36(10), pp. 1535-1551.

Hallam, D., Hilgen, G., Dorgau, B., Zhu, L., Yu, M., Bojic, S., Hewitt, P., Schmitt, M., Uteng, M., Kustermann, S., Steel, D., Nicholds, M., Thomas, R., Treumann, A., Porter, A., Sernagor, E., Armstrong, L. and Lako, M. (2018) 'Human-Induced Pluripotent Stem Cells Generate Light Responsive Retinal Organoids with Variable and Nutrient-Dependent Efficiency', *Stem Cells*, 36(10), pp. 1535-1551.

Haltia, M., Rapola, J. and Santavuori, P. (1973) 'Infantile type of so-called neuronal ceroid-lipofuscinosis. Histological and electron microscopic studies', *Acta Neuropathol*, 26(2), pp. 157-70.

Handa, J.T. (2012) 'How does the macula protect itself from oxidative stress?', *Mol Aspects Med*, 33(4), pp. 418-35.

Harada, A., Takei, Y., Kanai, Y., Tanaka, Y., Nonaka, S. and Hirokawa, N. (1998) 'Golgi vesiculation and lysosome dispersion in cells lacking cytoplasmic dynein', *J Cell Biol*, 141(1), pp. 51-9.

Hariri, M., Millane, G., Guimond, M.P., Guay, G., Dennis, J.W. and Nabi, I.R. (2000) 'Biogenesis of multilamellar bodies via autophagy', *Mol Biol Cell*, 11(1), pp. 255-68.

Hatakeyama, R., Peli-Gulli, M.P., Hu, Z., Jaquenoud, M., Garcia Osuna, G.M., Sardu, A., Dengjel, J. and De Virgilio, C. (2019) 'Spatially Distinct Pools of TORC1 Balance Protein Homeostasis', *Mol Cell*, 73(2), pp. 325-338 e8.

Haynes, T., Gutierrez, C., Aycinena, J.C., Tsonis, P.A. and Del Rio-Tsonis, K. (2007) 'BMP signaling mediates stem/progenitor cell-induced retina regeneration', *Proc Natl Acad Sci U S A*, 104(51), pp. 20380-5.

Henry, O.Y.F., Villenave, R., Cronce, M.J., Leineweber, W.D., Benz, M.A. and Ingber, D.E. (2017) 'Organs-on-chips with integrated electrodes for trans-epithelial electrical resistance (TEER) measurements of human epithelial barrier function', *Lab Chip*, 17(13), pp. 2264-2271.

Hernandez-Juarez, J., Rodriguez-Uribe, G. and Borooah, S. (2021) 'Toward the Treatment of Inherited Diseases of the Retina Using CRISPR-Based Gene Editing', *Front Med (Lausanne)*, 8, p. 698521.

Hersheson, J., Burke, D., Clayton, R., Anderson, G., Jacques, T.S., Mills, P., Wood, N.W., Gissen, P., Clayton, P., Fearnley, J., Mole, S.E. and Houlden, H. (2014) 'Cathepsin D deficiency causes juvenile-onset ataxia and distinctive muscle pathology', *Neurology*, 83(20), pp. 1873-5.

Heyer, W.D., Ehmsen, K.T. and Liu, J. (2010) 'Regulation of homologous recombination in eukaryotes', *Annu Rev Genet*, 44, pp. 113-39.

Hirata, T., Fujita, M., Nakamura, S., Gotoh, K., Motooka, D., Murakami, Y., Maeda, Y. and Kinoshita, T. (2015) 'Post-Golgi anterograde transport requires GARP-dependent endosome-to-TGN retrograde transport', *Mol Biol Cell*, 26(17), pp. 3071-84.

Hirst, J., Borner, G.H., Antrobus, R., Peden, A.A., Hodson, N.A., Sahlender, D.A. and Robinson, M.S. (2012) 'Distinct and overlapping roles for AP-1 and GGAs revealed by the "knocksideways" system', *Curr Biol*, 22(18), pp. 1711-6.

Hirst, J., Miller, S.E., Taylor, M.J., von Mollard, G.F. and Robinson, M.S. (2004) 'EpsinR is an adaptor for the SNARE protein Vti1b', *Mol Biol Cell*, 15(12), pp. 5593-602.

Hoglinger, D., Burgoyne, T., Sanchez-Heras, E., Hartwig, P., Colaco, A., Newton, J., Futter, C.E., Spiegel, S., Platt, F.M. and Eden, E.R. (2019) 'NPC1 regulates ER contacts with endocytic organelles to mediate cholesterol egress', *Nat Commun*, 10(1), p. 4276.

Hollenbeck, P.J. and Swanson, J.A. (1990) 'Radial extension of macrophage tubular lysosomes supported by kinesin', *Nature*, 346(6287), pp. 864-6.

Homma, Y., Hiragi, S. and Fukuda, M. (2021) 'Rab family of small GTPases: an updated view on their regulation and functions', *FEBS J*, 288(1), pp. 36-55.

Hong, Z., Pedersen, N.M., Wang, L., Torgersen, M.L., Stenmark, H. and Raiborg, C. (2017) 'PtdIns3P controls mTORC1 signaling through lysosomal positioning', *J Cell Biol*, 216(12), pp. 4217-4233.

Honing, S., Griffith, J., Geuze, H.J. and Hunziker, W. (1996) 'The tyrosine-based lysosomal targeting signal in lamp-1 mediates sorting into Golgi-derived clathrin-coated vesicles', *EMBO J*, 15(19), pp. 5230-9.

Honing, S., Sandoval, I.V. and von Figura, K. (1998) 'A di-leucine-based motif in the cytoplasmic tail of LIMP-II and tyrosinase mediates selective binding of AP-3', *EMBO J*, 17(5), pp. 1304-14.

Hu, Y.B., Dammer, E.B., Ren, R.J. and Wang, G. (2015) 'The endosomal-lysosomal system: from acidification and cargo sorting to neurodegeneration', *Transl Neurodegener*, 4, p. 18.

Huang, Z. and Liu, G. (2023) 'Current advancement in the application of prime editing', *Front Bioeng Biotechnol*, 11, p. 1039315.

Ibuchi, K., Fukaya, M., Shinohara, T., Hara, Y., Shiroshima, T., Sμgawara, T. and Sakagami, H. (2020) 'The Vps52 subunit of the GARP and EARP complexes is a novel Arf6-interacting protein that negatively regulates neurite outgrowth of hippocampal neurons', *Brain Res*, 1745, p. 146905.

Idelson, M., Alper, R., Obolensky, A., Ben-Shushan, E., Hemo, I., Yachimovich-Cohen, N., Khaner, H., Smith, Y., Wiser, O., Gropp, M., Cohen, M.A., Even-Ram, S., Berman-Zaken, Y., Matzrafi, L., Rechavi, G., Banin, E. and Reubinoff, B. (2009) 'Directed differentiation of human embryonic stem cells into functional retinal pigment epithelium cells', *Cell Stem Cell*, 5(4), pp. 396-408.

Infante, R.E., Wang, M.L., Radhakrishnan, A., Kwon, H.J., Brown, M.S. and Goldstein, J.L. (2008) 'NPC2 facilitates bidirectional transfer of cholesterol between NPC1 and lipid bilayers, a step in cholesterol egress from lysosomes', *Proc Natl Acad Sci U S A*, 105(40), pp. 15287-92.

Introne, W.J., Huizing, M., Malicdan, M.C.V., O'Brien, K.J. and Gahl, W.A. (1993) 'Hermansky-Pudlak Syndrome', in Adam, M.P., Mirzaa, G.M., Pagon, R.A., Wallace, S.E., Bean, L.J.H., Gripp, K.W. and Amemiya, A. (eds.) *GeneReviews((R))*. Seattle (WA).

Inui, M., Miyado, M., Igarashi, M., Tamano, M., Kubo, A., Yamashita, S., Asahara, H., Fukami, M. and Takada, S. (2014) 'Rapid generation of mouse models with defined point mutations by the CRISPR/Cas9 system', *Sci Rep*, 4, p. 5396.

Iqbal, K., Liu, F., Gong, C.X. and Grundke-Iqbal, I. (2010) 'Tau in Alzheimer disease and related tauopathies', *Curr Alzheimer Res*, 7(8), pp. 656-64.

Itakura, E., Kishi-Itakura, C. and Mizushima, N. (2012) 'The hairpin-type tail-anchored SNARE syntaxin 17 targets to autophagosomes for fusion with endosomes/lysosomes', *Cell*, 151(6), pp. 1256-69.

Iwasaki, Y., Sugita, S., Mandai, M., Yonemura, S., Onishi, A., Ito, S., Mochizuki, M., Ohno-Matsui, K. and Takahashi, M. (2016) 'Differentiation/Purification Protocol for Retinal Pigment Epithelium from Mouse Induced Pluripotent Stem Cells as a Research Tool', *PLoS One*, 11(7), p. e0158282.

Jahani-Asl, A., Cheung, E.C., Neuspiel, M., MacLaurin, J.G., Fortin, A., Park, D.S., McBride, H.M. and Slack, R.S. (2007) 'Mitofusin 2 protects cerebellar granule neurons against injury-induced cell death', *J Biol Chem*, 282(33), pp. 23788-98.

Jain, A., Zode, G., Kasetti, R.B., Ran, F.A., Yan, W., Sharma, T.P., Bugge, K., Searby, C.C., Fingert, J.H., Zhang, F., Clark, A.F. and Sheffield, V.C. (2017) 'CRISPR-Cas9-based treatment of myocilin-associated glaucoma', *Proc Natl Acad Sci U S A*, 114(42), pp. 11199-11204.

Jalanko, A. and Braulke, T. (2009) 'Neuronal ceroid lipofuscinoses', *Biochim Biophys Acta*, 1793(4), pp. 697-709.

Jankowiak, W., Brandenstein, L., Dulz, S., Hagel, C., Storch, S. and Bartsch, U. (2016) 'Retinal Degeneration in Mice Deficient in the Lysosomal Membrane Protein CLN7', *Invest Ophthalmol Vis Sci*, 57(11), pp. 4989-4998.

Janvier, K., Kato, Y., Boehm, M., Rose, J.R., Martina, J.A., Kim, B.Y., Venkatesan, S. and Bonifacino, J.S. (2003) 'Recognition of dileucine-based sorting signals from HIV-1 Nef and LIMP-II by the AP-1 gamma-sigma1 and AP-3 delta-sigma3 hemicomplexes', *J Cell Biol*, 163(6), pp. 1281-90.

Jazvinscak Jembrek, M., Slade, N., Hof, P.R. and Simic, G. (2018) 'The interactions of p53 with tau and Ass as potential therapeutic targets for Alzheimer's disease', *Prog Neurobiol*, 168, pp. 104-127.

Jeong, Y.K., Song, B. and Bae, S. (2020) 'Current Status and Challenges of DNA Base Editing Tools', *Mol Ther*, 28(9), pp. 1938-1952.

Jo, D.H., Song, D.W., Cho, C.S., Kim, U.G., Lee, K.J., Lee, K., Park, S.W., Kim, D., Kim, J.H., Kim, J.S., Kim, S., Kim, J.H. and Lee, J.M. (2019) 'CRISPR-Cas9-mediated therapeutic editing of Rpe65 ameliorates the disease phenotypes in a mouse model of Leber congenital amaurosis', *Sci Adv*, 5(10), p. eaax1210.

Johnson, D.E., Ostrowski, P., Jaumouille, V. and Grinstein, S. (2016) 'The position of lysosomes within the cell determines their luminal pH', *J Cell Biol*, 212(6), pp. 677-92.

Johnson, T.B., Cain, J.T., White, K.A., Ramirez-Montealegre, D., Pearce, D.A. and Weimer, J.M. (2019) 'Therapeutic landscape for Batten disease: current treatments and future prospects', *Nat Rev Neurol*, 15(3), pp. 161-178.

Jones, M.K., Orozco, L.D., Qin, H., Truong, T., Caplazi, P., Elstrott, J., Modrusan, Z., Chaney, S.Y. and Jeanne, M. (2023) 'Integration of human stem cell-derived in vitro systems and mouse preclinical models identifies complex pathophysiologic mechanisms in retinal dystrophy', *Front Cell Dev Biol*, 11, p. 1252547.

Jongsma, M.L., Berlin, I., Wijdeven, R.H., Janssen, L., Janssen, G.M., Garstka, M.A., Janssen, H., Mensink, M., van Veelen, P.A., Spaapen, R.M. and Neefjes, J. (2016) 'An ER-Associated Pathway Defines Endosomal Architecture for Controlled Cargo Transport', *Cell*, 166(1), pp. 152-66.

Kabeya, Y., Mizushima, N., Yamamoto, A., Oshitani-Okamoto, S., Ohsumi, Y. and Yoshimori, T. (2004) 'LC3, GABARAP and GATE16 localize to autophagosomal membrane depending on form-II formation', *J Cell Sci*, 117(Pt 13), pp. 2805-12.

Kalviainen, R., Eriksson, K., Losekoot, M., Sorri, I., Harvima, I., Santavuori, P., Jarvela, I., Autti, T., Vanninen, R., Salmenpera, T. and van Diggelen, O.P. (2007) 'Juvenile-onset neuronal ceroid lipofuscinosis with infantile CLN1 mutation and palmitoyl-protein thioesterase deficiency', *Eur J Neurol*, 14(4), pp. 369-72.

Karakocak, B.B., Keshavan, S., Gunasingam, G., Angeloni, S., Auderset, A., Petri-Fink, A. and Rothen-Rutishauser, B. (2023) 'Rethinking of TEER measurement reporting for epithelial cells grown on permeable inserts', *Eur J Pharm Sci*, 188, p. 106511.

Karlsson, P., Droce, A., Moser, J.M., Cuhlmann, S., Padilla, C.O., Heimann, P., Bartsch, J.W., Fuchtbauer, A., Fuchtbauer, E.M. and Schmitt-John, T. (2013) 'Loss of vps54 function leads to vesicle traffic impairment, protein mis-sorting and embryonic lethality', *Int J Mol Sci*, 14(6), pp. 10908-25.

Kaya, I., Brinet, D., Michno, W., Syvanen, S., Sehlin, D., Zetterberg, H., Blennow, K. and Hanrieder, J. (2017) 'Delineating Amyloid Plaque Associated Neuronal Sphingolipids in Transgenic Alzheimer's Disease Mice (tgArcSwe) Using MALDI Imaging Mass Spectrometry', *ACS Chem Neurosci*, 8(2), pp. 347-355.

Kaya, K.D., Chen, H.Y., Brooks, M.J., Kelley, R.A., Shimada, H., Nagashima, K., de Val, N., Drinnan, C.T., Gieser, L., Kruczek, K., Erceg, S., Li, T., Lukovic, D., Adlakha, Y.K., Welby, E. and Swaroop, A. (2019) 'Transcriptome-based molecular staging of human stem cell-derived retinal organoids uncovers accelerated photoreceptor differentiation by 9-cis retinal', *Mol Vis*, 25, pp. 663-678.

Kaylor, J.J., Yuan, Q., Cook, J., Sarfare, S., Makshanoff, J., Miu, A., Kim, A., Kim, P., Habib, S., Roybal, C.N., Xu, T., Nusinowitz, S. and Travis, G.H. (2013) 'Identification of DES1 as a vitamin A isomerase in Muller glial cells of the retina', *Nat Chem Biol*, 9(1), pp. 30-6.

Kean, E.L. (1980) 'The lipid intermediate pathway in the retina for the activation of carbohydrates involved in the glycosylation of rhodopsin', *Neurochem Int*, 1C, pp. 59-68.

Kean, E.L. (1999) 'The dolichol pathway in the retina and its involvement in the glycosylation of rhodopsin', *Biochim Biophys Acta*, 1473(2-3), pp. 272-85.

Kegeles, E., Perepelkina, T. and Baranov, P. (2020) 'Semi-Automated Approach for Retinal Tissue Differentiation', *Transl Vis Sci Technol*, 9(10), p. 24.

Kennedy, B.E., Charman, M. and Karten, B. (2012) 'Niemann-Pick Type C2 protein contributes to the transport of endosomal cholesterol to mitochondria without interacting with NPC1', *J Lipid Res*, 53(12), pp. 2632-42.

Kennedy, C.J., Rakoczy, P.E. and Constable, I.J. (1995) 'Lipofuscin of the retinal pigment epithelium: a review', *Eye (Lond)*, 9 (Pt 6), pp. 763-71.

Khakurel, A. and Lupashin, V.V. (2023) 'Role of GARP Vesicle Tethering Complex in Golgi Physiology', *Int J Mol Sci*, 24(7).

Khakurel, A., Kudlyk, T., Bonifacino, J.S. and Lupashin, V.V. (2021) 'The Golgi-associated retrograde protein (GARP) complex plays an essential role in the maintenance of the Golgi glycosylation machinery', *Mol Biol Cell*, 32(17), pp. 1594-1610.

Khakurel, A., Kudlyk, T., Pokrovskaya, I., D'Souza, Z. and Lupashin, V.V. (2022) 'GARP dysfunction results in COPI displacement, depletion of Golgi v-SNAREs and calcium homeostasis proteins', *Front Cell Dev Biol*, 10, p. 1066504.

Kiamehr, M., Klettner, A., Richert, E., Koskela, A., Koistinen, A., Skottman, H., Kaarniranta, K., Aalto-Setala, K. and Juuti-Uusitalo, K. (2019) 'Compromised Barrier Function in Human Induced Pluripotent Stem-Cell-Derived Retinal Pigment Epithelial Cells from Type 2 Diabetic Patients', *Int J Mol Sci*, 20(15).

Kim, J.K., Lee, H.M., Park, K.S., Shin, D.M., Kim, T.S., Kim, Y.S., Suh, H.W., Kim, S.Y., Kim, I.S., Kim, J.M., Son, J.W., Sohn, K.M., Jung, S.S., Chung, C., Han, S.B., Yang, C.S. and Jo, E.K. (2017) 'MIR144* inhibits antimicrobial responses against Mycobacterium tuberculosis in human monocytes and macrophages by targeting the autophagy protein DRAM2', *Autophagy*, 13(2), pp. 423-441.

Kim, K., Park, S.W., Kim, J.H., Lee, S.H., Kim, D., Koo, T., Kim, K.E., Kim, J.H. and Kim, J.S. (2017) 'Genome surgery using Cas9 ribonucleoproteins for the treatment of age-related macular degeneration', *Genome Res*, 27(3), pp. 419-426.

Kim, S., Ochoa, K., Melli, S.E., Yousufzai, F.A.K., Barrera, Z.D., Williams, A.A., McIntyre, G., Delgado, E., Bolish, J.N., Macleod, C.M., Boghos, M., Lens, H.P., Ramos, A.G., Wilson, V.B., Maloney, K., Padron, Z.M., Khan, A.H., Blanco, R.E. and Soto, I. (2023) 'Disruptive lysosomal-metabolic signaling and neurodevelopmental deficits that precede Purkinje cell loss in a mouse model of Niemann-Pick Type-C disease', *Sci Rep*, 13(1), p. 5665.

Kim, S.J., Zhang, Z., Sarkar, C., Tsai, P.C., Lee, Y.C., Dye, L. and Mukherjee, A.B. (2008) 'Palmitoyl protein thioesterase-1 deficiency impairs synaptic vesicle recycling at nerve terminals, contributing to neuropathology in humans and mice', *J Clin Invest*, 118(9), pp. 3075-86.

Klein, A.M. and Simons, B.D. (2011) 'Universal patterns of stem cell fate in cycling adult tissues', *Development*, 138(15), pp. 3103-11.

Klettner, A.K., Dithmar, S., (2020) Retinal Pigment Epithelium in Health and Disease. *Springer Cham*. 1,pp. XI, 357.

Klimanskaya, I., Hipp, J., Rezai, K.A., West, M., Atala, A. and Lanza, R. (2004) 'Derivation and comparative assessment of retinal pigment epithelium from human embryonic stem cells using transcriptomics', *Cloning Stem Cells*, 6(3), pp. 217-45.

Klionsky, D.J., Abeliovich, H., Agostinis, P., Agrawal, D.K., Aliev, G., Askew, D.S., Baba, M., Baehrecke, E.H., Bahr, B.A., Ballabio, A., Bamber, B.A., Bassham, D.C., Bergamini, E., Bi, X., Biard-Piechaczyk, M., Blum, J.S., Bredesen, D.E., Brodsky, J.L., Brumell, J.H., Brunk, U.T., Bursch, W., Camougrand, N., Cebollero, E., Cecconi, F., Chen, Y., Chin, L.S., Choi, A., Chu, C.T., Chung, J., Clarke, P.G., Clark, R.S., Clarke, S.G., Clave, C., Cleveland, J.L., Codogno, P., Colombo, M.I., Coto-Montes, A., Cregg, J.M., Cuervo, A.M., Debnath, J., Demarchi, F., Dennis, P.B., Dennis, P.A., Deretic, V., Devenish, R.J., Di Sano, F., Dice, J.F., Difiglia, M., Dinesh-Kumar, S., Distelhorst, C.W., Djavaheri-Mergny, M., Dorsey, F.C., Droge, W., Dron, M., Dunn, W.A., Jr., Duszenko, M., Eissa, N.T., Elazar, Z., Esclatine, A., Eskelinen, E.L., Fesus, L., Finley, K.D., Fuentes, J.M., Fueyo, J., Fujisaki, K., Galliot, B., Gao, F.B., Gewirtz, D.A., Gibson, S.B., Gohla, A., Goldberg, A.L., Gonzalez, R., Gonzalez-Estevez, C., Gorski, S., Gottlieb, R.A., Haussinger, D., He, Y.W., Heidenreich, K., Hill, J.A., Hoyer-Hansen, M., Hu, X., Huang, W.P., Iwasaki, A., Jaattela, M., Jackson, W.T., Jiang, X., Jin, S., Johansen, T., Jung, J.U., Kadowaki, M., Kang, C., Kelekar, A., Kessel, D.H., Kiel, J.A., Kim, H.P., Kimchi, A., Kinsella, T.J., Kiselyov, K., Kitamoto, K., Knecht, E., et al. (2008) 'Guidelines for the use and interpretation of assays for monitoring autophagy in higher eukaryotes', *Autophagy*, 4(2), pp. 151-75.

Kollmann, K., Uusi-Rauva, K., Scifo, E., Tyynela, J., Jalanko, A. and Braulke, T. (2013) 'Cell biology and function of neuronal ceroid lipofuscinosis-related proteins', *Biochim Biophys Acta*, 1832(11), pp. 1866-81.

Komor, A.C., Kim, Y.B., Packer, M.S., Zuris, J.A. and Liu, D.R. (2016) 'Programmable editing of a target base in genomic DNA without double-stranded DNA cleavage', *Nature*, 533(7603), pp. 420-4.

Korolchuk, V.I., Saiki, S., Lichtenberg, M., Siddiqi, F.H., Roberts, E.A., Imarisio, S., Jahreiss, L., Sarkar, S., Futter, M., Menzies, F.M., O'Kane, C.J., Deretic, V. and Rubinsztein, D.C. (2011) 'Lysosomal positioning coordinates cellular nutrient responses', *Nat Cell Biol*, 13(4), pp. 453-60.

Krasovec, T., Volk, M., Sustar Habjan, M., Hawlina, M., Vidovic Valentincic, N. and Fakin, A. (2022) 'The Clinical Spectrum and Disease Course of DRAM2 Retinopathy', *Int J Mol Sci*, 23(13).

Kuniyoshi, K., Hayashi, T., Kameya, S., Katagiri, S., Mizobuchi, K., Tachibana, T., Kubota, D., Sakuramoto, H., Tsunoda, K., Fujinami, K., Yoshitake, K., Iwata, T., Nakano, T. and Kusaka, S. (2020)

'Clinical Course and Electron Microscopic Findings in Lymphocytes of Patients with DRAM2-Associated Retinopathy', *Int J Mol Sci*, 21(4).

Kurzawa-Akanbi, M., Whitfield, P., Burte, F., Bertelli, P.M., Pathak, V., Doherty, M., Hilgen, B., Gliaudelyte, L., Platt, M., Queen, R., Coxhead, J., Porter, A., Oberg, M., Fabrikova, D., Davey, T., Beh, C.S., Georgiou, M., Collin, J., Boczonadi, V., Hartlova, A., Taggart, M., Al-Aama, J., Korolchuk, V.I., Morris, C.M., Guduric-Fuchs, J., Steel, D.H., Medina, R.J., Armstrong, L. and Lako, M. (2022) 'Retinal pigment epithelium extracellular vesicles are potent inducers of age-related macular degeneration disease phenotype in the outer retina', *J Extracell Vesicles*, 11(12), p. e12295.

Kuwahara, A., Ozone, C., Nakano, T., Saito, K., Eiraku, M. and Sasai, Y. (2015) 'Generation of a ciliary margin-like stem cell niche from self-organizing human retinal tissue', *Nat Commun*, 6, p. 6286.

Kwon, H.J., Abi-Mosleh, L., Wang, M.L., Deisenhofer, J., Goldstein, J.L., Brown, M.S. and Infante, R.E. (2009) 'Structure of N-terminal domain of NPC1 reveals distinct subdomains for binding and transfer of cholesterol', *Cell*, 137(7), pp. 1213-24.

Kwon, S.E. and Chapman, E.R. (2011) 'Synaptophysin regulates the kinetics of synaptic vesicle endocytosis in central neurons', *Neuron*, 70(5), pp. 847-54.

Lamb, C.A., Yoshimori, T. and Tooze, S.A. (2013) 'The autophagosome: origins unknown, biogenesis complex', *Nat Rev Mol Cell Biol*, 14(12), pp. 759-74.

Lamb, C.A., Yoshimori, T. and Tooze, S.A. (2013) 'The autophagosome: origins unknown, biogenesis complex', *Nat Rev Mol Cell Biol*, 14(12), pp. 759-74.

Lamba, D.A., Gust, J. and Reh, T.A. (2009) 'Transplantation of human embryonic stem cell-derived photoreceptors restores some visual function in Crx-deficient mice', *Cell Stem Cell*, 4(1), pp. 73-9.

Lamba, D.A., Karl, M.O., Ware, C.B. and Reh, T.A. (2006) 'Efficient generation of retinal progenitor cells from human embryonic stem cells', *Proc Natl Acad Sci U S A*, 103(34), pp. 12769-74.

Lambert, E., Saha, O., Soares Landeira, B., Melo de Farias, A.R., Hermant, X., Carrier, A., Pelletier, A., Gadaut, J., Davoine, L., Dupont, C., Amouyel, P., Bonnefond, A., Lafont, F., Abdelfettah, F., Verstreken, P., Chapuis, J., Barois, N., Delahaye, F., Dermaut, B., Lambert, J.C., Costa, M.R. and Dourlen, P. (2022) 'The Alzheimer susceptibility gene BIN1 induces isoform-dependent neurotoxicity through early endosome defects', *Acta Neuropathol Commun*, 10(1), p. 4.

Latunde-Dada, G.O., Simpson, R.J. and McKie, A.T. (2008) 'Duodenal cytochrome B expression stimulates iron uptake by human intestinal epithelial cells', *J Nutr*, 138(6), pp. 991-5.

Law, C.Y., Siu, C.W., Fan, K., Lai, W.H., Au, K.W., Lau, Y.M., Wong, L.Y., Ho, J.C.Y., Lee, Y.K., Tse, H.F. and Ng, K.M. (2016) 'Lysosomal membrane permeabilization is involved in oxidative stress-induced apoptotic cell death in LAMP2-deficient iPSCs-derived cerebral cortical neurons', *Biochem Biophys Rep*, 5, pp. 335-345.

Le Borgne, R. and Hoflack, B. (1997) 'Mannose 6-phosphate receptors regulate the formation of clathrin-coated vesicles in the TGN', *J Cell Biol*, 137(2), pp. 335-45.

Lee, J.H., Yu, W.H., Kumar, A., Lee, S., Mohan, P.S., Peterhoff, C.M., Wolfe, D.M., Martinez-Vicente, M., Massey, A.C., Sovak, G., Uchiyama, Y., Westaway, D., Cuervo, A.M. and Nixon, R.A. (2010) 'Lysosomal proteolysis and autophagy require presenilin 1 and are disrupted by Alzheimer-related PS1 mutations', *Cell*, 141(7), pp. 1146-58.

Lee, S., Sato, Y. and Nixon, R.A. (2011) 'Lysosomal proteolysis inhibition selectively disrupts axonal transport of degradative organelles and causes an Alzheimer's-like axonal dystrophy', *J Neurosci*, 31(21), pp. 7817-30.

Lee, S.J., Zhang, J., Choi, A.M. and Kim, H.P. (2013) 'Mitochondrial dysfunction induces formation of lipid droplets as a generalized response to stress', *Oxid Med Cell Longev*, 2013, p. 327167.

Leinonen, H., Keksa-Goldsteine, V., Ragauskas, S., Kohlmann, P., Singh, Y., Savchenko, E., Puranen, J., Malm, T., Kalesnykas, G., Koistinaho, J., Tanila, H. and Kanninen, K.M. (2017) 'Retinal Degeneration In A Mouse Model Of CLN5 Disease Is Associated With Compromised Autophagy', *Sci Rep*, 7(1), p. 1597.

Levine, B. and Klionsky, D.J. (2004) 'Development by self-digestion: molecular mechanisms and biological functions of autophagy', *Dev Cell*, 6(4), pp. 463-77.

Levitsky, Y., Hammer, S.S., Fisher, K.P., Huang, C., Gentles, T.L., Pegouske, D.J., Xi, C., Lydic, T.A., Busik, J.V. and Proshlyakov, D.A. (2020) 'Mitochondrial Ceramide Effects on the Retinal Pigment Epithelium in Diabetes', *Int J Mol Sci*, 21(11).

Lewandowska, E., Dziewulska, D., Parys, M. and Pasennik, E. (2011) 'Ultrastructure of granular osmiophilic material deposits (GOM) in arterioles of CADASIL patients', *Folia Neuropathol*, 49(3), pp. 174-80.

Li, C., Luo, X., Zhao, S., Siu, G.K., Liang, Y., Chan, H.C., Satoh, A. and Yu, S.S. (2017) 'COPI-TRAPPII activates Rab18 and regulates its lipid droplet association', *EMBO J*, 36(4), pp. 441-457.

Li, F., Jiang, D. and Samuel, M.A. (2019) 'Microglia in the developing retina', *Neural Dev*, 14(1), p. 12.

Li, T., Yang, Y., Qi, H., Cui, W., Zhang, L., Fu, X., He, X., Liu, M., Li, P.F. and Yu, T. (2023) 'CRISPR/Cas9 therapeutics: progress and prospects', *Signal Transduct Target Ther*, 8(1), p. 36.

Li, X., Rydzewski, N., Hider, A., Zhang, X., Yang, J., Wang, W., Gao, Q., Cheng, X. and Xu, H. (2016) 'A molecular mechanism to regulate lysosome motility for lysosome positioning and tubulation', *Nat Cell Biol*, 18(4), pp. 404-17.

Liang, X., Potter, J., Kumar, S., Ravinder, N. and Chesnut, J.D. (2017) 'Enhanced CRISPR/Cas9-mediated precise genome editing by improved design and delivery of gRNA, Cas9 nuclease, and donor DNA', *J Biotechnol*, 241, pp. 136-146.

Lie, P.P.Y. and Nixon, R.A. (2019) 'Lysosome trafficking and signaling in health and neurodegenerative diseases', *Neurobiol Dis*, 122, pp. 94-105.

Liewen, H., Meinhold-Heerlein, I., Oliveira, V., Schwarzenbacher, R., Luo, G., Wadle, A., Jung, M., Pfreundschuh, M. and Stenner-Liewen, F. (2005) 'Characterization of the human GARP (Golgi associated retrograde protein) complex', *Exp Cell Res*, 306(1), pp. 24-34.

Lin, S., Staahl, B.T., Alla, R.K. and Doudna, J.A. (2014) 'Enhanced homology-directed human genome engineering by controlled timing of CRISPR/Cas9 delivery', *Elife*, 3, p. e04766.

Liou, H.L., Dixit, S.S., Xu, S., Tint, G.S., Stock, A.M. and Lobel, P. (2006) 'NPC2, the protein deficient in Niemann-Pick C2 disease, consists of multiple glycoforms that bind a variety of sterols', *J Biol Chem*, 281(48), pp. 36710-23.

Lipatova, Z., Belogortseva, N., Zhang, X.Q., Kim, J., Taussig, D. and Segev, N. (2012) 'Regulation of selective autophagy onset by a Ypt/Rab GTPase module', *Proc Natl Acad Sci U S A*, 109(18), pp. 6981-6.

Liu, J., Bassal, M., Schlichting, S., Braren, I., Di Spiezio, A., Saftig, P. and Bartsch, U. (2022) 'Intravitreal gene therapy restores the autophagy-lysosomal pathway and attenuates retinal degeneration in cathepsin D-deficient mice', *Neurobiol Dis*, 164, p. 105628.

Liu, K., Surendhran, K., Nothwehr, S.F. and Graham, T.R. (2008) 'P4-ATPase requirement for AP-1/clathrin function in protein transport from the trans-Golgi network and early endosomes', *Mol Biol Cell*, 19(8), pp. 3526-35.

Liu, K.I., Sutrisnoh, N.B., Wang, Y. and Tan, M.H. (2019) 'Genome Editing in Mammalian Cell Lines using CRISPR-Cas', *J Vis Exp*, (146).

Llonch, S., Carido, M. and Ader, M. (2018) 'Organoid technology for retinal repair', *Dev Biol*, 433(2), pp. 132-143.

Lloyd-Evans, E. and Haslett, L.J. (2016) 'The lysosomal storage disease continuum with ageing-related neurodegenerative disease', *Ageing Res Rev*, 32, pp. 104-121.

Lloyd-Evans, E., Morgan, A.J., He, X., Smith, D.A., Elliot-Smith, E., Sillence, D.J., Churchill, G.C., Schuchman, E.H., Galione, A. and Platt, F.M. (2008) 'Niemann-Pick disease type C1 is a sphingosine storage disease that causes deregulation of lysosomal calcium', *Nat Med*, 14(11), pp. 1247-55.

Lobo, G.P., Fulmer, D., Guo, L., Zuo, X., Dang, Y., Kim, S.H., Su, Y., George, K., Obert, E., Fogelgren, B., Nihalani, D., Norris, R.A., Rohrer, B. and Lipschutz, J.H. (2017) 'The exocyst is required for photoreceptor ciliogenesis and retinal development', *J Biol Chem*, 292(36), pp. 14814-14826.

Locatelli-Hoops, S., Remmel, N., Klingenstein, R., Breiden, B., Rossocha, M., Schoeniger, M., Koenigs, C., Saenger, W. and Sandhoff, K. (2006) 'Saposin A mobilizes lipids from low cholesterol and high bis(monoacylglycerol)phosphate-containing membranes: patient variant Saposin A lacks lipid extraction capacity', *J Biol Chem*, 281(43), pp. 32451-60.

Long, X., Lin, Y., Ortiz-Vega, S., Yonezawa, K. and Avruch, J. (2005) 'Rheb binds and regulates the mTOR kinase', *Curr Biol*, 15(8), pp. 702-13.

Lowe, A., Harris, R., Bhansali, P., Cvekl, A. and Liu, W. (2016) 'Intercellular Adhesion-Dependent Cell Survival and ROCK-Regulated Actomyosin-Driven Forces Mediate Self-Formation of a Retinal Organoid', *Stem Cell Reports*, 6(5), pp. 743-756.

Lu, S., Goμgh, A.W., Bobrowski, W.F. and Stewart, B.H. (1996) 'Transport properties are not altered across Caco-2 cells with heightened TEER despite underlying physiological and ultrastructural changes', *J Pharm Sci*, 85(3), pp. 270-3.

Lubbehusen, J., Thiel, C., Rind, N., Ungar, D., Prinsen, B.H., de Koning, T.J., van Hasselt, P.M. and Korner, C. (2010) 'Fatal outcome due to deficiency of subunit 6 of the conserved oligomeric Golgi complex leading to a new type of congenital disorders of glycosylation', *Hum Mol Genet*, 19(18), pp. 3623-33.

Ludwig, A.L., Mayerl, S.J., Gao, Y., Banghart, M., Bacig, C., Fernandez Zepeda, M.A., Zhao, X. and Gamm, D.M. (2023) 'Re-formation of synaptic connectivity in dissociated human stem cell-derived retinal organoid cultures', *Proc Natl Acad Sci U S A*, 120(2), p. e2213418120.

Lund, R.D., Wang, S., Klimanskaya, I., Holmes, T., Ramos-Kelsey, R., Lu, B., Girman, S., Bischoff, N., Sauve, Y. and Lanza, R. (2006) 'Human embryonic stem cell-derived cells rescue visual function in dystrophic RCS rats', *Cloning Stem Cells*, 8(3), pp. 189-99.

Luo, Y., Fukuhara, M., Weitzman, M. and Rizzolo, L.J. (2006) 'Expression of JAM-A, AF-6, PAR-3 and PAR-6 during the assembly and remodeling of RPE tight junctions', *Brain Res*, 1110(1), pp. 55-63.

Lyu, Y., Tschulakow, A.V., Wang, K., Brash, D.E. and Schraermeyer, U. (2023) 'Chemiexcitation and melanin in photoreceptor disc turnover and prevention of macular degeneration', *Proc Natl Acad Sci U S A*, 120(20), p. e2216935120.

Ma, L., Gholam Azad, M., Dharmasivam, M., Richardson, V., Quinn, R.J., Feng, Y., Pountney, D.L., Tonissen, K.F., Mellick, G.D., Yanatori, I. and Richardson, D.R. (2021) 'Parkinson's disease: Alterations in iron and redox biology as a key to unlock therapeutic strategies', *Redox Biol*, 41, p. 101896.

Maday, S., Wallace, K.E. and Holzbaur, E.L. (2012) 'Autophagosomes initiate distally and mature during transport toward the cell soma in primary neurons', *J Cell Biol*, 196(4), pp. 407-17.

Maib, H. and Murray, D.H. (2022) 'A mechanism for exocyst-mediated tethering via Arf6 and PIP5K1C-driven phosphoinositide conversion', *Curr Biol*, 32(13), pp. 2821-2833 e6.

Mali, P., Yang, L., Esvelt, K.M., Aach, J., Guell, M., DiCarlo, J.E., Norville, J.E. and Church, G.M. (2013) 'RNA-guided human genome engineering via Cas9', *Science*, 339(6121), pp. 823-6.

Mardones, G.A., Burgos, P.V., Brooks, D.A., Parkinson-Lawrence, E., Mattera, R. and Bonifacino, J.S. (2007) 'The trans-Golgi network accessory protein p56 promotes long-range movement of GGA/clathrin-containing transport carriers and lysosomal enzyme sorting', *Mol Biol Cell*, 18(9), pp. 3486-501.

Marquer, C., Tian, H., Yi, J., Bastien, J., Dall'Armi, C., Yang-Klingler, Y., Zhou, B., Chan, R.B. and Di Paolo, G. (2016) 'Arf6 controls retromer traffic and intracellular cholesterol distribution via a phosphoinositide-based mechanism', *Nat Commun*, 7, p. 11919.

Marques, A.R.A., Di Spiezio, A., Thiessen, N., Schmidt, L., Grotzinger, J., Lullmann-Rauch, R., Damme, M., Storck, S.E., Pietrzik, C.U., Fogh, J., Bar, J., Mikhaylova, M., Glatzel, M., Bassal, M., Bartsch, U. and Saftig, P. (2020) 'Enzyme replacement therapy with recombinant pro-CTSD (cathepsin D) corrects defective proteolysis and autophagy in neuronal ceroid lipofuscinosis', *Autophagy*, 16(5), pp. 811-825.

Maruyama, T., Doμgan, S.K., Truttmann, M.C., Bilate, A.M., Ingram, J.R. and Ploegh, H.L. (2015) 'Increasing the efficiency of precise genome editing with CRISPR-Cas9 by inhibition of nonhomologous end joining', *Nat Biotechnol*, 33(5), pp. 538-42.

Maruyama, T., Dougan, S.K., Truttmann, M.C., Bilate, A.M., Ingram, J.R. and Ploegh, H.L. (2015) 'Increasing the efficiency of precise genome editing with CRISPR-Cas9 by inhibition of nonhomologous end joining', *Nat Biotechnol*, 33(5), pp. 538-42.

Matsumoto, E., Koide, N., Hanzawa, H., Kiyama, M., Ohta, M., Kuwabara, J., Takeda, S. and Takahashi, M. (2019) 'Fabricating retinal pigment epithelial cell sheets derived from human induced pluripotent stem cells in an automated closed culture system for regenerative medicine', *PLoS One*, 14(3), p. e0212369.

Matter, K. and Balda, M.S. (2003) 'Functional analysis of tight junctions', *Methods*, 30(3), pp. 228-34.

Mazzei, R., Conforti, F.L., Magariello, A., Bravaccio, C., Militerni, R., Gabriele, A.L., Sampaolo, S., Patitucci, A., Di Iorio, G., Mμglia, M. and Quattrone, A. (2002) 'A novel mutation in the CLN1 gene in a patient with juvenile neuronal ceroid lipofuscinosis', *J Neurol*, 249(10), pp. 1398-400.

Mazzei, R., Conforti, F.L., Magariello, A., Bravaccio, C., Militerni, R., Gabriele, A.L., Sampaolo, S., Patitucci, A., Di Iorio, G., Mμglia, M. and Quattrone, A. (2002) 'A novel mutation in the CLN1 gene in a patient with juvenile neuronal ceroid lipofuscinosis', *J Neurol*, 249(10), pp. 1398-400.

McCauliff, L.A., Langan, A., Li, R., Ilnytska, O., Bose, D., Waghalter, M., Lai, K., Kahn, P.C. and Storch, J. (2019) 'Intracellular cholesterol trafficking is dependent upon NPC2 interaction with lysobisphosphatidic acid', *Elife*, 8.

McKenney, R.J., Huynh, W., Tanenbaum, M.E., Bhabha, G. and Vale, R.D. (2014) 'Activation of cytoplasmic dynein motility by dynactin-cargo adapter complexes', *Science*, 345(6194), pp. 337-41.

Medina, D.L., Di Paola, S., Peluso, I., Armani, A., De Stefani, D., Venditti, R., Montefusco, S., Scotto-Rosato, A., Prezioso, C., Forrester, A., Settembre, C., Wang, W., Gao, Q., Xu, H., Sandri, M., Rizzuto, R., De Matteis, M.A. and Ballabio, A. (2015) 'Lysosomal calcium signalling regulates autophagy through calcineurin and TFEB', *Nat Cell Biol*, 17(3), pp. 288-99.

Mellough, C.B., Collin, J., Khazim, M., White, K., Sernagor, E., Steel, D.H. and Lako, M. (2015) 'IGF-1 Signaling Plays an Important Role in the Formation of Three-Dimensional Laminated Neural Retina and Other Ocular Structures From Human Embryonic Stem Cells', *Stem Cells*, 33(8), pp. 2416-30.

Mellough, C.B., Collin, J., Queen, R., Hilgen, G., Dorgau, B., Zerti, D., Felemban, M., White, K., Sernagor, E. and Lako, M. (2019) 'Systematic Comparison of Retinal Organoid Differentiation from Human Pluripotent Stem Cells Reveals Stage Specific, Cell Line, and Methodological Differences', *Stem Cells Transl Med*, 8(7), pp. 694-706.

Meyer, C., Zizioli, D., Lausmann, S., Eskelinen, E.L., Hamann, J., Saftig, P., von Figura, K. and Schu, P. (2000) 'mu1A-adaptin-deficient mice: lethality, loss of AP-1 binding and rerouting of mannose 6-phosphate receptors', *EMBO J*, 19(10), pp. 2193-203.

Meyer, J.S., Howden, S.E., Wallace, K.A., Verhoeven, A.D., Wright, L.S., Capowski, E.E., Pinilla, I., Martin, J.M., Tian, S., Stewart, R., Pattnaik, B., Thomson, J.A. and Gamm, D.M. (2011) 'Optic vesicle-like structures derived from human pluripotent stem cells facilitate a customized approach to retinal disease treatment', *Stem Cells*, 29(8), pp. 1206-18.

Meyer, J.S., Shearer, R.L., Capowski, E.E., Wright, L.S., Wallace, K.A., McMillan, E.L., Zhang, S.C. and Gamm, D.M. (2009) 'Modeling early retinal development with human embryonic and induced pluripotent stem cells', *Proc Natl Acad Sci U S A*, 106(39), pp. 16698-703.

Meyer, J.S., Shearer, R.L., Capowski, E.E., Wright, L.S., Wallace, K.A., McMillan, E.L., Zhang, S.C. and Gamm, D.M. (2009) 'Modeling early retinal development with human embryonic and induced pluripotent stem cells', *Proc Natl Acad Sci U S A*, 106(39), pp. 16698-703.

Millarte, V. and Spiess, M. (2022) 'RABEP1/Rabaptin5: a link between autophagy and early endosome homeostasis', *Autophagy*, 18(3), pp. 698-699.

Mirza, M., Volz, C., Karlstetter, M., Langiu, M., Somogyi, A., Ruonala, M.O., Tamm, E.R., Jagle, H. and Langmann, T. (2013) 'Progressive retinal degeneration and glial activation in the CLN6 (nclf) mouse model of neuronal ceroid lipofuscinosis: a beneficial effect of DHA and curcumin supplementation', *PLoS One*, 8(10), p. e75963.

Mitter, S.K., Song, C., Qi, X., Mao, H., Rao, H., Akin, D., Lewin, A., Grant, M., Dunn, W., Jr., Ding, J., Bowes Rickman, C. and Boulton, M. (2014) 'Dysregulated autophagy in the RPE is associated with increased susceptibility to oxidative stress and AMD', *Autophagy*, 10(11), pp. 1989-2005.

Mondal, A., Appu, A.P., Sadhukhan, T., Bagh, M.B., Previde, R.M., Sadhukhan, S., Stojilkovic, S., Liu, A. and Mukherjee, A.B. (2022) 'Ppt1-deficiency dysregulates lysosomal Ca(++) homeostasis contributing to pathogenesis in a mouse model of CLN1 disease', *J Inherit Metab Dis*, 45(3), pp. 635-656.

Montilla-Rojo, J., Bialecka, M., Wever, K.E., Mummery, C.L., Looijenga, L.H.J., Roelen, B.A.J. and Salvatori, D.C.F. (2023) 'Teratoma Assay for Testing Pluripotency and Malignancy of Stem Cells: Insufficient Reporting and Uptake of Animal-Free Methods-A Systematic Review', *Int J Mol Sci*, 24(4).

Morgan, A.J., Platt, F.M., Lloyd-Evans, E. and Galione, A. (2011) 'Molecular mechanisms of endolysosomal Ca2+ signalling in health and disease', *Biochem J*, 439(3), pp. 349-74.

Moser, J.M., Bigini, P. and Schmitt-John, T. (2013) 'The wobbler mouse, an ALS animal model', *Mol Genet Genomics*, 288(5-6), pp. 207-29.

Moyer, B.D., Allan, B.B. and Balch, W.E. (2001) 'Rab1 interaction with a GM130 effector complex regulates COPII vesicle cis--Golgi tethering', *Traffic*, 2(4), pp. 268-76.

Murphy, K.E., Gysbers, A.M., Abbott, S.K., Tayebi, N., Kim, W.S., Sidransky, E., Cooper, A., Garner, B. and Halliday, G.M. (2014) 'Reduced glucocerebrosidase is associated with increased alpha-synuclein in sporadic Parkinson's disease', *Brain*, 137(Pt 3), pp. 834-48.

Murray, A.R., Fliesler, S.J. and Al-Ubaidi, M.R. (2009) 'Rhodopsin: the functional significance of asn-linked glycosylation and other post-translational modifications', *Ophthalmic Genet*, 30(3), pp. 109-20.

Mustafi, D., Engel, A.H. and Palczewski, K. (2009) 'Structure of cone photoreceptors', *Prog Retin Eye Res*, 28(4), pp. 289-302.

Nabi, I.R. and Rodriguez-Boulan, E. (1993) 'Increased LAMP-2 polylactosamine glycosylation is associated with its slower Golgi transit during establishment of a polarized MDCK epithelial monolayer', *Mol Biol Cell*, 4(6), pp. 627-35.

Nakano, K., Yamamoto, T., Kishimoto, T., Noji, T. and Tanaka, K. (2008) 'Protein kinases Fpk1p and Fpk2p are novel regulators of phospholipid asymmetry', *Mol Biol Cell*, 19(4), pp. 1783-97.

Nakano, T., Ando, S., Takata, N., Kawada, M., Muguruma, K., Sekiguchi, K., Saito, K., Yonemura, S., Eiraku, M. and Sasai, Y. (2012) 'Self-formation of optic cups and storable stratified neural retina from human ESCs', *Cell Stem Cell*, 10(6), pp. 771-785.

Napoli, D. and Strettoi, E. (2023) 'Structural abnormalities of retinal pigment epithelial cells in a light-inducible, rhodopsin mutant mouse', *J Anat*, 243(2), pp. 223-234.

Napolitano, G. and Ballabio, A. (2016) 'TFEB at a glance', *J Cell Sci*, 129(13), pp. 2475-81.

Navneet, S. and Rohrer, B. (2022) 'Elastin turnover in ocular diseases: A special focus on age-related macular degeneration', *Exp Eye Res*, 222, p. 109164.

Naylor, A., Hopkins, A., Hudson, N. and Campbell, M. (2019) 'Tight Junctions of the Outer Blood Retina Barrier', *Int J Mol Sci*, 21(1).

Neu-Yilik, G., Amthor, B., Gehring, N.H., Bahri, S., Paidassi, H., Hentze, M.W. and Kulozik, A.E. (2011) 'Mechanism of escape from nonsense-mediated mRNA decay of human beta-globin transcripts with nonsense mutations in the first exon', *RNA*, 17(5), pp. 843-54.

Newton, J., Hait, N.C., Maceyka, M., Colaco, A., Maczis, M., Wassif, C.A., Coμgnoux, A., Porter, F.D., Milstien, S., Platt, N., Platt, F.M. and Spiegel, S. (2017) 'FTY720/fingolimod increases NPC1 and NPC2 expression and reduces cholesterol and sphingolipid accumulation in Niemann-Pick type C mutant fibroblasts', *FASEB J*, 31(4), pp. 1719-1730.

Newton, J., Milstien, S. and Spiegel, S. (2018) 'Niemann-Pick type C disease: The atypical sphingolipidosis', *Adv Biol Regul*, 70, pp. 82-88.

Nixon, R.A., Yang, D.S. and Lee, J.H. (2008) 'Neurodegenerative lysosomal disorders: a continuum from development to late age', *Autophagy*, 4(5), pp. 590-9.

Nosi, U., Lanner, F., Huang, T. and Cox, B. (2017) 'Overexpression of Trophoblast Stem Cell-Enriched MicroRNAs Promotes Trophoblast Fate in Embryonic Stem Cells', *Cell Rep*, 19(6), pp. 1101-1109.

Notomi, S., Ishihara, K., Efstathiou, N.E., Lee, J.J., Hisatomi, T., Tachibana, T., Konstantinou, E.K., Ueta, T., Murakami, Y., Maidana, D.E., Ikeda, Y., Kume, S., Terasaki, H., Sonoda, S., Blanz, J., Young, L., Sakamoto, T., Sonoda, K.H., Saftig, P., Ishibashi, T., Miller, J.W., Kroemer, G. and Vavvas, D.G. (2019) 'Genetic LAMP2 deficiency accelerates the age-associated formation of basal laminar deposits in the retina', *Proc Natl Acad Sci U S A*, 116(47), pp. 23724-23734.

O'Brien, C.E., Younger, S.H., Jan, L.Y. and Jan, Y.N. (2023) 'The GARP complex prevents sterol accumulation at the trans-Golgi network during dendrite remodeling', *J Cell Biol*, 222(1).

Ohlemacher, S.K., Iglesias, C.L., Sridhar, A., Gamm, D.M. and Meyer, J.S. (2015) 'Generation of highly enriched populations of optic vesicle-like retinal cells from human pluripotent stem cells', *Curr Protoc Stem Cell Biol*, 32, pp. 1H 8 1-1H 8 20.

Ohshima, T., Murray, G.J., Swaim, W.D., Longenecker, G., Quirk, J.M., Cardarelli, C.O., Sμgimoto, Y., Pastan, I., Gottesman, M.M., Brady, R.O. and Kulkarni, A.B. (1997) 'alpha-Galactosidase A deficient mice: a model of Fabry disease', *Proc Natl Acad Sci U S A*, 94(6), pp. 2540-4.

Ohsumi, Y. (2001) 'Molecular dissection of autophagy: two ubiquitin-like systems', *Nat Rev Mol Cell Biol*, 2(3), pp. 211-6.

Okamoto, S., Amaishi, Y., Maki, I., Enoki, T. and Mineno, J. (2019) 'Highly efficient genome editing for single-base substitutions using optimized ssODNs with Cas9-RNPs', *Sci Rep*, 9(1), p. 4811.

Oninla, V.O., Breiden, B., Babalola, J.O. and Sandhoff, K. (2014) 'Acid sphingomyelinase activity is regulated by membrane lipids and facilitates cholesterol transfer by NPC2', *J Lipid Res*, 55(12), pp. 2606-19.

O'Prey, J., Skommer, J., Wilkinson, S. and Ryan, K.M. (2009) 'Analysis of DRAM-related proteins reveals evolutionarily conserved and divergent roles in the control of autophagy', *Cell Cycle*, 8(14), pp. 2260-5.

Oriola, D., Roth, S., Dogterom, M. and Casademunt, J. (2015) 'Formation of helical membrane tubes around microtubules by single-headed kinesin KIF1A', *Nat Commun*, 6, p. 8025.

Osakada, F., Ikeda, H., Mandai, M., Wataya, T., Watanabe, K., Yoshimura, N., Akaike, A., Sasai, Y. and Takahashi, M. (2008) 'Toward the generation of rod and cone photoreceptors from mouse, monkey and human embryonic stem cells', *Nat Biotechnol*, 26(2), pp. 215-24.

Osakada, F., Ikeda, H., Sasai, Y. and Takahashi, M. (2009) 'Stepwise differentiation of pluripotent stem cells into retinal cells', *Nat Protoc*, 4(6), pp. 811-24.

Osakada, F., Ikeda, H., Sasai, Y. and Takahashi, M. (2009) 'Stepwise differentiation of pluripotent stem cells into retinal cells', *Nat Protoc*, 4(6), pp. 811-24.

Overly, C.C. and Hollenbeck, P.J. (1996) 'Dynamic organization of endocytic pathways in axons of cultured sympathetic neurons', *J Neurosci*, 16(19), pp. 6056-64.

Overly, C.C., Lee, K.D., Berthiaume, E. and Hollenbeck, P.J. (1995) 'Quantitative measurement of intraorganelle pH in the endosomal-lysosomal pathway in neurons by using ratiometric imaging with pyranine', *Proc Natl Acad Sci U S A*, 92(8), pp. 3156-60.

Paniagua, A.E., Herranz-Martin, S., Jimeno, D., Jimeno, A.M., Lopez-Benito, S., Carlos Arevalo, J., Velasco, A., Aijon, J. and Lillo, C. (2015) 'CRB2 completes a fully expressed Crumbs complex in the Retinal Pigment Epithelium', *Sci Rep*, 5, p. 14504.

Paniagua, A.E., Segurado, A., Dolon, J.F., Esteve-Rudd, J., Velasco, A., Williams, D.S. and Lillo, C. (2021) 'Key Role for CRB2 in the Maintenance of Apicobasal Polarity in Retinal Pigment Epithelial Cells', *Front Cell Dev Biol*, 9, p. 701853.

Pankiv, S., Clausen, T.H., Lamark, T., Brech, A., Bruun, J.A., Outzen, H., Overvatn, A., Bjorkoy, G. and Johansen, T. (2007) 'p62/SQSTM1 binds directly to Atg8/LC3 to facilitate degradation of ubiquitinated protein aggregates by autophagy', *J Biol Chem*, 282(33), pp. 24131-45.

Paquet, D., Kwart, D., Chen, A., Sproul, A., Jacob, S., Teo, S., Olsen, K.M., Gregg, A., Noggle, S. and Tessier-Lavigne, M. (2016) 'Efficient introduction of specific homozygous and heterozygous mutations using CRISPR/Cas9', *Nature*, 533(7601), pp. 125-9.

Park, B., Alves, C.H., Lundvig, D.M., Tanimoto, N., Beck, S.C., Huber, G., Richard, F., Klooster, J., Andlauer, T.F., Swindell, E.C., Jamrich, M., Le Bivic, A., Seeliger, M.W. and Wijnholds, J. (2011) 'PALS1 is essential for retinal pigment epithelium structure and neural retina stratification', *J Neurosci*, 31(47), pp. 17230-41.

Park, E.J., Grabinska, K.A., Guan, Z., Stranecky, V., Hartmannova, H., Hodanova, K., Baresova, V., Sovova, J., Jozsef, L., Ondruskova, N., Hansikova, H., Honzik, T., Zeman, J., Hulkova, H., Wen, R., Kmoch, S. and Sessa, W.C. (2014) 'Mutation of Nogo-B receptor, a subunit of cis-prenyltransferase, causes a congenital disorder of glycosylation', *Cell Metab*, 20(3), pp. 448-57.

Park, S.M., Kim, K., Lee, E.J., Kim, B.K., Lee, T.J., Seo, T., Jang, I.S., Lee, S.H., Kim, S., Lee, J.H. and Park, J. (2009) 'Reduced expression of DRAM2/TMEM77 in tumor cells interferes with cell death', *Biochem Biophys Res Commun*, 390(4), pp. 1340-4.

Park, W.D., O'Brien, J.F., Lundquist, P.A., Kraft, D.L., Vockley, C.W., Karnes, P.S., Patterson, M.C. and Snow, K. (2003) 'Identification of 58 novel mutations in Niemann-Pick disease type C: correlation with biochemical phenotype and importance of PTC1-like domains in NPC1', *Hum Mutat*, 22(4), pp. 313-25.

Patel, S. and Cai, X. (2015) 'Evolution of acidic Ca(2)(+) stores and their resident Ca(2)(+)-permeable channels', *Cell Calcium*, 57(3), pp. 222-30.

Patrizi, C., Llado, M., Benati, D., Iodice, C., Marrocco, E., Guarascio, R., Surace, E.M., Cheetham, M.E., Auricchio, A. and Recchia, A. (2021) 'Allele-specific editing ameliorates dominant retinitis pigmentosa in a transgenic mouse model', *Am J Hum Genet*, 108(2), pp. 295-308.

Patterson, M.C., Hendriksz, C.J., Walterfang, M., Sedel, F., Vanier, M.T., Wijburg, F. and Group, N.-C.G.W. (2012) 'Recommendations for the diagnosis and management of Niemann-Pick disease type C: an update', *Mol Genet Metab*, 106(3), pp. 330-44.

Pechincha, C., Groessl, S., Kalis, R., de Almeida, M., Zanotti, A., Wittmann, M., Schneider, M., de Campos, R.P., Rieser, S., Brandstetter, M., Schleiffer, A., Müller-Decker, K., Helm, D., Jabs, S., Haselbach, D., Lemberg, M.K., Zuber, J. and Palm, W. (2022) 'Lysosomal enzyme trafficking factor LYSET enables nutritional usage of extracellular proteins', *Science*, 378(6615), p. eabn5637.

Peden, A.A., Oorschot, V., Hesser, B.A., Austin, C.D., Scheller, R.H. and Klumperman, J. (2004) 'Localization of the AP-3 adaptor complex defines a novel endosomal exit site for lysosomal membrane proteins', *J Cell Biol*, 164(7), pp. 1065-76.

Pentchev, P.G. (2004) 'Niemann-Pick C research from mouse to gene', *Biochim Biophys Acta*, 1685(1-3), pp. 3-7.

Pentchev, P.G., Boothe, A.D., Kruth, H.S., Weintroub, H., Stivers, J. and Brady, R.O. (1984) 'A genetic storage disorder in BALB/C mice with a metabolic block in esterification of exogenous cholesterol', *J Biol Chem*, 259(9), pp. 5784-91.

Perez-Victoria, F.J. and Bonifacino, J.S. (2009) 'Dual roles of the mammalian GARP complex in tethering and SNARE complex assembly at the trans-golgi network', *Mol Cell Biol*, 29(19), pp. 5251-63.

Perez-Victoria, F.J., Mardones, G.A. and Bonifacino, J.S. (2008) 'Requirement of the human GARP complex for mannose 6-phosphate-receptor-dependent sorting of cathepsin D to lysosomes', *Mol Biol Cell*, 19(6), pp. 2350-62.

Perez-Victoria, F.J., Schindler, C., Magadan, J.G., Mardones, G.A., Delevoye, C., Romao, M., Raposo, G. and Bonifacino, J.S. (2010) 'Ang2/fat-free is a conserved subunit of the Golgi-associated retrograde protein complex', *Mol Biol Cell*, 21(19), pp. 3386-95.

Petit, C.S., Lee, J.J., Boland, S., Swarup, S., Christiano, R., Lai, Z.W., Mejhert, N., Elliott, S.D., McFall, D., Haque, S., Huang, E.J., Bronson, R.T., Harper, J.W., Farese, R.V., Jr. and Walther, T.C. (2020) 'Inhibition of sphingolipid synthesis improves outcomes and survival in GARP mutant wobbler mice, a model of motor neuron degeneration', *Proc Natl Acad Sci U S A*, 117(19), pp. 10565-10574.

Pike, L.S., Tannous, B.A., Deliolanis, N.C., Hsich, G., Morse, D., Tung, C.H., Sena-Esteves, M. and Breakefield, X.O. (2011) 'Imaging gene delivery in a mouse model of congenital neuronal ceroid lipofuscinosis', *Gene Ther*, 18(12), pp. 1173-8.

Piret, J., Schanck, A., Delfosse, S., Van Bambeke, F., Kishore, B.K., Tulkens, P.M. and Mingeot-Leclercq, M.P. (2005) 'Modulation of the in vitro activity of lysosomal phospholipase A1 by membrane lipids', *Chem Phys Lipids*, 133(1), pp. 1-15.

Platt, R.J., Chen, S., Zhou, Y., Yim, M.J., Swiech, L., Kempton, H.R., Dahlman, J.E., Parnas, O., Eisenhaure, T.M., Jovanovic, M., Graham, D.B., Jhunjhunwala, S., Heidenreich, M., Xavier, R.J., Langer, R., Anderson, D.G., Hacohen, N., Regev, A., Feng, G., Sharp, P.A. and Zhang, F. (2014) 'CRISPR-Cas9 knockin mice for genome editing and cancer modeling', *Cell*, 159(2), pp. 440-55.

Plavelil, N. (2023). 'Misrouting of Niemann-Pick C1 protein mediates cholesterol induced mTORC1-activation contributing to pathogenesis of CLN1-disease'. *Journal of Biological Chemistry.*

Pokrovskaya, I.D., Willett, R., Smith, R.D., Morelle, W., Kudlyk, T. and Lupashin, V.V. (2011) 'Conserved oligomeric Golgi complex specifically regulates the maintenance of Golgi glycosylation machinery', *Glycobiology*, 21(12), pp. 1554-69.

Porto, E.M., Komor, A.C., Slaymaker, I.M. and Yeo, G.W. (2020) 'Base editing: advances and therapeutic opportunities', *Nat Rev Drug Discov*, 19(12), pp. 839-859.

Prinetti, A., Loberto, N., Chigorno, V. and Sonnino, S. (2009) 'Glycosphingolipid behaviour in complex membranes', *Biochim Biophys Acta*, 1788(1), pp. 184-93.

Pryor, P.R., Mullock, B.M., Bright, N.A., Lindsay, M.R., Gray, S.R., Richardson, S.C., Stewart, A., James, D.E., Piper, R.C. and Luzio, J.P. (2004) 'Combinatorial SNARE complexes with VAMP7 or VAMP8 define different late endocytic fusion events', *EMBO Rep*, 5(6), pp. 590-5.

Pu, J., Guardia, C.M., Keren-Kaplan, T. and Bonifacino, J.S. (2016) 'Mechanisms and functions of lysosome positioning', *J Cell Sci*, 129(23), pp. 4329-4339.

Pu, J., Keren-Kaplan, T. and Bonifacino, J.S. (2017) 'A Ragulator-BORC interaction controls lysosome positioning in response to amino acid availability', *J Cell Biol*, 216(12), pp. 4183-4197.

Puri, V., Watanabe, R., Dominguez, M., Sun, X., Wheatley, C.L., Marks, D.L. and Pagano, R.E. (1999) 'Cholesterol modulates membrane traffic along the endocytic pathway in sphingolipid-storage diseases', *Nat Cell Biol*, 1(6), pp. 386-8.

Qi, L.S., Larson, M.H., Gilbert, L.A., Doudna, J.A., Weissman, J.S., Arkin, A.P. and Lim, W.A. (2013) 'Repurposing CRISPR as an RNA-guided platform for sequence-specific control of gene expression', *Cell*, 152(5), pp. 1173-83.

Qian, H., Wu, X., Du, X., Yao, X., Zhao, X., Lee, J., Yang, H. and Yan, N. (2020) 'Structural Basis of Low-pH-Dependent Lysosomal Cholesterol Egress by NPC1 and NPC2', *Cell*, 182(1), pp. 98-111 e18.

Qin, Q., Liao, G., Baudry, M. and Bi, X. (2010) 'Cholesterol Perturbation in Mice Results in p53 Degradation and Axonal Pathology through p38 MAPK and Mdm2 Activation', *PLoS One*, 5(4), p. e9999.

Quadros, R.M., Miura, H., Harms, D.W., Akatsuka, H., Sato, T., Aida, T., Redder, R., Richardson, G.P., Inagaki, Y., Sakai, D., Buckley, S.M., Seshacharyulu, P., Batra, S.K., Behlke, M.A., Zeiner, S.A., Jacobi, A.M., Izu, Y., Thoreson, W.B., Urness, L.D., Mansour, S.L., Ohtsuka, M. and Gurumurthy, C.B. (2017) 'Easi-CRISPR: a robust method for one-step generation of mice carrying conditional and insertion alleles using long ssDNA donors and CRISPR ribonucleoproteins', *Genome Biol*, 18(1), p. 92.

Radhakrishnan, A., Goldstein, J.L., McDonald, J.G. and Brown, M.S. (2008) 'Switch-like control of SREBP-2 transport triggered by small changes in ER cholesterol: a delicate balance', *Cell Metab*, 8(6), pp. 512-21.

Radisic, M., Malda, J., Epping, E., Geng, W., Langer, R. and Vunjak-Novakovic, G. (2006) 'Oxygen gradients correlate with cell density and cell viability in engineered cardiac tissue', *Biotechnol Bioeng*, 93(2), pp. 332-43.

Rahman, N., Georgiou, M., Khan, K.N. and Michaelides, M. (2020) 'Macular dystrophies: clinical and imaging features, molecular genetics and therapeutic options', *Br J Ophthalmol*, 104(4), pp. 451-460.

Rakoczy, P.E., Lai, C.M., Baines, M., Di Grandi, S., Fitton, J.H. and ConsTable, I.J. (1997) 'Modulation of cathepsin D activity in retinal pigment epithelial cells', *Biochem J*, 324 (Pt 3)(Pt 3), pp. 935-40.

Rakoczy, P.E., Zhang, D., Robertson, T., Barnett, N.L., Papadimitriou, J., ConsTable, I.J. and Lai, C.M. (2002) 'Progressive age-related changes similar to age-related macular degeneration in a transgenic mouse model', *Am J Pathol*, 161(4), pp. 1515-24.

Ram, R.J., Li, B. and Kaiser, C.A. (2002) 'Identification of Sec36p, Sec37p, and Sec38p: components of yeast complex that contains Sec34p and Sec35p', *Mol Biol Cell*, 13(5), pp. 1484-500.

Ramadan, H., Al-Din, A.S., Ismail, A., Balen, F., Varma, A., Twomey, A., Watts, R., Jackson, M., Anderson, G., Green, E. and Mole, S.E. (2007) 'Adult neuronal ceroid lipofuscinosis caused by deficiency in palmitoyl protein thioesterase 1', *Neurology*, 68(5), pp. 387-8.

Ran, F.A., Hsu, P.D., Wright, J., Agarwala, V., Scott, D.A. and Zhang, F. (2013) 'Genome engineering using the CRISPR-Cas9 system', *Nat Protoc*, 8(11), pp. 2281-2308.

Raouf, J., Idborg, H., Englund, P., Alexanderson, H., Dastmalchi, M., Jakobsson, P.J., Lundberg, I.E. and Korotkova, M. (2018) 'Targeted lipidomics analysis identified altered serum lipid profiles in patients with polymyositis and dermatomyositis', *Arthritis Res Ther*, 20(1), p. 83.

Raposo, G. and Marks, M.S. (2007) 'Melanosomes--dark organelles enlighten endosomal membrane transport', *Nat Rev Mol Cell Biol*, 8(10), pp. 786-97.

Raychowdhury, M.K., Gonzalez-Perrett, S., Montalbetti, N., Timpanaro, G.A., Chasan, B., Goldmann, W.H., Stahl, S., Cooney, A., Goldin, E. and Cantiello, H.F. (2004) 'Molecular pathophysiology of

mucolipidosis type IV: pH dysregulation of the mucolipin-1 cation channel', *Hum Mol Genet*, 13(6), pp. 617-27.

Raymond, S.M. and Jackson, I.J. (1995) 'The retinal pigmented epithelium is required for development and maintenance of the mouse neural retina', *Curr Biol*, 5(11), pp. 1286-95.

Reczek, D., Schwake, M., Schroder, J., Hμghes, H., Blanz, J., Jin, X., Brondyk, W., Van Patten, S., Edmunds, T. and Saftig, P. (2007) 'LIMP-2 is a receptor for lysosomal mannose-6-phosphate-independent targeting of beta-glucocerebrosidase', *Cell*, 131(4), pp. 770-83.

Regent, F., Morizur, L., Lesueur, L., Habeler, W., Plancheron, A., Ben M'Barek, K. and Monville, C. (2019) 'Automation of human pluripotent stem cell differentiation toward retinal pigment epithelial cells for large-scale productions', *Sci Rep*, 9(1), p. 10646.

Reggiori, F. and Klionsky, D.J. (2006) 'Atg9 sorting from mitochondria is impaired in early secretion and VFT-complex mutants in Saccharomyces cerevisiae', *J Cell Sci*, 119(Pt 14), pp. 2903-11.

Reggiori, F., Tucker, K.A., Stromhaug, P.E. and Klionsky, D.J. (2004) 'The Atg1-Atg13 complex regulates Atg9 and Atg23 retrieval transport from the pre-autophagosomal structure', *Dev Cell*, 6(1), pp. 79-90.

Reggiori, F., Wang, C.W., Stromhaμg, P.E., Shintani, T. and Klionsky, D.J. (2003) 'Vps51 is part of the yeast Vps fifty-three tethering complex essential for retrograde traffic from the early endosome and Cvt vesicle completion', *J Biol Chem*, 278(7), pp. 5009-20.

Reichman, S., Terray, A., Slembrouck, A., Nanteau, C., Orieux, G., Habeler, W., Nandrot, E.F., Sahel, J.A., Monville, C. and Goureau, O. (2014) 'From confluent human iPS cells to self-forming neural retina and retinal pigmented epithelium', *Proc Natl Acad Sci U S A*, 111(23), pp. 8518-23.

Reichman, S., Terray, A., Slembrouck, A., Nanteau, C., Orieux, G., Habeler, W., Nandrot, E.F., Sahel, J.A., Monville, C. and Goureau, O. (2014) 'From confluent human iPS cells to self-forming neural retina and retinal pigmented epithelium', *Proc Natl Acad Sci U S A*, 111(23), pp. 8518-23.

Rein, D.B., Zhang, P., Wirth, K.E., Lee, P.P., Hoerger, T.J., McCall, N., Klein, R., Tielsch, J.M., Vijan, S. and Saaddine, J. (2006) 'The economic burden of major adult visual disorders in the United States', *Arch Ophthalmol*, 124(12), pp. 1754-60.

Remmel, N., Locatelli-Hoops, S., Breiden, B., Schwarzmann, G. and Sandhoff, K. (2007) 'Saposin B mobilizes lipids from cholesterol-poor and bis(monoacylglycero)phosphate-rich membranes at acidic pH. Unglycosylated patient variant saposin B lacks lipid-extraction capacity', *FEBS J*, 274(13), pp. 3405-20.

Ren, X., Farias, G.G., Canagarajah, B.J., Bonifacino, J.S. and Hurley, J.H. (2013) 'Structural basis for recruitment and activation of the AP-1 clathrin adaptor complex by Arf1', *Cell*, 152(4), pp. 755-67.

Ribeiro, I., Marcao, A., Amaral, O., Sa Miranda, M.C., Vanier, M.T. and Millat, G. (2001) 'Niemann-Pick type C disease: NPC1 mutations associated with severe and mild cellular cholesterol trafficking alterations', *Hum Genet*, 109(1), pp. 24-32.

Riboldi, G.M. and Di Fonzo, A.B. (2019) 'GBA, Gaucher Disease, and Parkinson's Disease: From Genetic to Clinic to New Therapeutic Approaches', *Cells*, 8(4).

Richards, C.M., Jabs, S., Qiao, W., Varanese, L.D., Schweizer, M., Mosen, P.R., Riley, N.M., Klussendorf, M., Zengel, J.R., Flynn, R.A., Rustagi, A., Widen, J.C., Peters, C.E., Ooi, Y.S., Xie, X., Shi, P.Y., Bartenschlager, R., Puschnik, A.S., Bogyo, M., Bertozzi, C.R., Blish, C.A., Winter, D., Nagamine, C.M., Braulke, T. and Carette, J.E. (2022) 'The human disease gene LYSET is essential for lysosomal enzyme transport and viral infection', *Science*, 378(6615), p. eabn5648.

Richardson, C.D., Ray, G.J., DeWitt, M.A., Curie, G.L. and Corn, J.E. (2016) 'Enhancing homology-directed genome editing by catalytically active and inactive CRISPR-Cas9 using asymmetric donor DNA', *Nat Biotechnol*, 34(3), pp. 339-44.

Rivera-Molina, F.E., Xi, Z., Reales, E., Wang, B. and Toomre, D. (2021) 'Exocyst complex mediates recycling of internal cilia', *Curr Biol*, 31(24), pp. 5580-5589 e5.

Rocha, E.M., Smith, G.A., Park, E., Cao, H., Brown, E., Hallett, P. and Isacson, O. (2015) 'Progressive decline of glucocerebrosidase in aging and Parkinson's disease', *Ann Clin Transl Neurol*, 2(4), pp. 433-8.

Roelants, F.M., Baltz, A.G., Trott, A.E., Fereres, S. and Thorner, J. (2010) 'A protein kinase network regulates the function of aminophospholipid flippases', *Proc Natl Acad Sci U S A*, 107(1), pp. 34-9.

Rogov, V., Dotsch, V., Johansen, T. and Kirkin, V. (2014) 'Interactions between autophagy receptors and ubiquitin-like proteins form the molecular basis for selective autophagy', *Mol Cell*, 53(2), pp. 167-78.

Rohrer, B., Biswal, M.R., Obert, E., Dang, Y., Su, Y., Zuo, X., Fogelgren, B., Kondkar, A.A., Lobo, G.P. and Lipschutz, J.H. (2021) 'Conditional Loss of the Exocyst Component Exoc5 in Retinal Pigment Epithelium (RPE) Results in RPE Dysfunction, Photoreceptor Cell Degeneration, and Decreased Visual Function', *Int J Mol Sci*, 22(10).

Romanov, J., Walczak, M., Ibiricu, I., Schuchner, S., Ogris, E., Kraft, C. and Martens, S. (2012) 'Mechanism and functions of membrane binding by the Atg5-Atg12/Atg16 complex during autophagosome formation', *EMBO J*, 31(22), pp. 4304-17.

Rowland, T.J., Blaschke, A.J., Buchholz, D.E., Hikita, S.T., Johnson, L.V. and Clegg, D.O. (2013) 'Differentiation of human pluripotent stem cells to retinal pigmented epithelium in defined conditions using purified extracellular matrix proteins', *J Tissue Eng Regen Med*, 7(8), pp. 642-53.

Rowland, T.J., Buchholz, D.E. and Clegg, D.O. (2012) 'Pluripotent human stem cells for the treatment of retinal disease', *J Cell Physiol*, 227(2), pp. 457-66.

Ruan, G.X., Barry, E., Yu, D., Lukason, M., Cheng, S.H. and Scaria, A. (2017) 'CRISPR/Cas9-Mediated Genome Editing as a Therapeutic Approach for Leber Congenital Amaurosis 10', *Mol Ther*, 25(2), pp. 331-341.

Russell, R.C., Tian, Y., Yuan, H., Park, H.W., Chang, Y.Y., Kim, J., Kim, H., Neufeld, T.P., Dillin, A. and Guan, K.L. (2013) 'ULK1 induces autophagy by phosphorylating Beclin-1 and activating VPS34 lipid kinase', *Nat Cell Biol*, 15(7), pp. 741-50.

Sμgimoto, M., Kondo, M., Hirose, M., Suzuki, M., Mekada, K., Abe, T., Kiyonari, H., Ogura, A., Takagi, N., Artzt, K. and Abe, K. (2012) 'Molecular identification of t(w5): Vps52 promotes pluripotential cell differentiation through cell-cell interactions', *Cell Rep*, 2(5), pp. 1363-74.

Saftig, P. and Klumperman, J. (2009) 'Lysosome biogenesis and lysosomal membrane proteins: trafficking meets function', *Nat Rev Mol Cell Biol*, 10(9), pp. 623-35.

Saftig, P. and Klumperman, J. (2009) 'Lysosome biogenesis and lysosomal membrane proteins: trafficking meets function', *Nat Rev Mol Cell Biol*, 10(9), pp. 623-35.

Saftig, P., Hetman, M., Schmahl, W., Weber, K., Heine, L., Mossmann, H., Koster, A., Hess, B., Evers, M., von Figura, K. and et al. (1995) 'Mice deficient for the lysosomal proteinase cathepsin D exhibit progressive atrophy of the intestinal mucosa and profound destruction of lymphoid cells', *EMBO J*, 14(15), pp. 3599-608.

Saha, A., Capowski, E., Fernandez Zepeda, M.A., Nelson, E.C., Gamm, D.M. and Sinha, R. (2022) 'Cone photoreceptors in human stem cell-derived retinal organoids demonstrate intrinsic light responses that mimic those of primate fovea', *Cell Stem Cell*, 29(3), pp. 487-489.

Saint-Geniez, M., Kurihara, T., Sekiyama, E., Maldonado, A.E. and D'Amore, P.A. (2009) 'An essential role for RPE-derived soluble VEGF in the maintenance of the choriocapillaris', *Proc Natl Acad Sci U S A*, 106(44), pp. 18751-6.

Saito, Y., Suzuki, K., Hulette, C.M. and Murayama, S. (2004) 'Aberrant phosphorylation of alpha-synuclein in human Niemann-Pick type C1 disease', *J Neuropathol Exp Neurol*, 63(4), pp. 323-8.

Salazar, G., Craige, B., Styers, M.L., Newell-Litwa, K.A., Doucette, M.M., Wainer, B.H., Falcon-Perez, J.M., Dell'Angelica, E.C., Peden, A.A., Werner, E. and Faundez, V. (2006) 'BLOC-1 complex deficiency alters the targeting of adaptor protein complex-3 cargoes', *Mol Biol Cell*, 17(9), pp. 4014-26.

Salo, P.P., Vaara, S., Kettunen, J., Pirinen, M., Sarin, A.P., Huikuri, H., Karhunen, P.J., Eskola, M., Nikus, K., Lokki, M.L., Ripatti, S., Havulinna, A.S., Salomaa, V., Palotie, A., Nieminen, M.S., Sinisalo, J. and Perola, M. (2015) 'Genetic Variants on Chromosome 1p13.3 Are Associated with Non-ST Elevation Myocardial Infarction and the Expression of DRAM2 in the Finnish Population', *PLoS One*, 10(10), p. e0140576.

Salman, A., McClements, M.E., MacLaren, R.E. (2021).'Insights on the Regeneration Potential of Müller Glia in the Mammalian Retina'. *Cells*. 10 (8), 1957.

Sambri, I., D'Alessio, R., Ezhova, Y., Giuliano, T., Sorrentino, N.C., Cacace, V., De Risi, M., Cataldi, M., Annunziato, L., De Leonibus, E. and Fraldi, A. (2017) 'Lysosomal dysfunction disrupts presynaptic maintenance and restoration of presynaptic function prevents neurodegeneration in lysosomal storage diseases', *EMBO Mol Med*, 9(1), pp. 112-132.

Sandhoff, R. and Sandhoff, K. (2018) 'Emerging concepts of ganglioside metabolism', *FEBS Lett*, 592(23), pp. 3835-3864.

Santavuori, P. (1988) 'Neuronal ceroid-lipofuscinoses in childhood', *Brain Dev*, 10(2), pp. 80-3.

Santavuori, P., Haltia, M., Rapola, J. and Raitta, C. (1973) 'Infantile type of so-called neuronal ceroid-lipofuscinosis. 1. A clinical study of 15 patients', *J Neurol Sci*, 18(3), pp. 257-67.

Santavuori, P., Lauronen, L., Kirveskari, E., Aberg, L., Sainio, K. and Autti, T. (2000) 'Neuronal ceroid lipofuscinoses in childhood', *Neurol Sci*, 21(3 Suppl), pp. S35-41.

Santavuori, P., Rapola, J., Raininko, R., Autti, T., Lappi, M., Nuutila, A., Launes, J. and Sainio, K. (1993) 'Early juvenile neuronal ceroid-lipofuscinosis or variant Jansky-Bielschowsky disease: diagnostic criteria and nomenclature', *J Inherit Metab Dis*, 16(2), pp. 230-2.

Sapir, T., Segal, M., Grigoryan, G., Hansson, K.M., James, P., Segal, M. and Reiner, O. (2019) 'The Interactome of Palmitoyl-Protein Thioesterase 1 (PPT1) Affects Neuronal Morphology and Function', *Front Cell Neurosci*, 13, p. 92.

Sato, H. and Singer, R.H. (2021) 'Cellular variability of nonsense-mediated mRNA decay', *Nat Commun*, 12(1), p. 7203.

Schindler, C., Chen, Y., Pu, J., Guo, X. and Bonifacino, J.S. (2015) 'EARP is a multisubunit tethering complex involved in endocytic recycling', *Nat Cell Biol*, 17(5), pp. 639-50.

Schleinitz, A., Pottgen, L.A., Keren-Kaplan, T., Pu, J., Saftig, P., Bonifacino, J.S., Haas, A. and Jeschke, A. (2023) 'Consecutive functions of small GTPases guide HOPS-mediated tethering of late endosomes and lysosomes', *Cell Rep*, 42(1), p. 111969.

Schmitt-John, T., Drepper, C., Mussmann, A., Hahn, P., Kuhlmann, M., Thiel, C., Hafner, M., Lengeling, A., Heimann, P., Jones, J.M., Meisler, M.H. and Jockusch, H. (2005) 'Mutation of Vps54 causes motor neuron disease and defective spermiogenesis in the wobbler mouse', *Nat Genet*, 37(11), pp. 1213-5.

Schmitz, F., Tabares, L., Khimich, D., Strenzke, N., de la Villa-Polo, P., Castellano-Munoz, M., Bulankina, A., Moser, T., Fernandez-Chacon, R. and Sudhof, T.C. (2006) 'CSPalpha-deficiency causes massive and rapid photoreceptor degeneration', *Proc Natl Acad Sci U S A*, 103(8), pp. 2926-31.

Scholl, H.P., Strauss, R.W., Singh, M.S., Dalkara, D., Roska, B., Picaud, S. and Sahel, J.A. (2016) 'Emerging therapies for inherited retinal degeneration', *Sci Transl Med*, 8(368), p. 368rv6.

Schoppe, J., Mari, M., Yavavli, E., Auffarth, K., Cabrera, M., Walter, S., Frohlich, F. and Ungermann, C. (2020) 'AP-3 vesicle uncoating occurs after HOPS-dependent vacuole tethering', *EMBO J*, 39(20), p. e105117.

Schroder, J., Lullmann-Rauch, R., Himmerkus, N., Pleines, I., Nieswandt, B., Orinska, Z., Koch-Nolte, F., Schroder, B., Bleich, M. and Saftig, P. (2009) 'Deficiency of the tetraspanin CD63 associated with kidney pathology but normal lysosomal function', *Mol Cell Biol*, 29(4), pp. 1083-94.

Schulz, A., Kohlschutter, A., Mink, J., Simonati, A. and Williams, R. (2013) 'NCL diseases - clinical perspectives', *Biochim Biophys Acta*, 1832(11), pp. 1801-6.

Seehafer, S.S. and Pearce, D.A. (2006) 'You say lipofuscin, we say ceroid: defining autofluorescent storage material', *Neurobiol Aging*, 27(4), pp. 576-88.

Segal-Salto, M., Hansson, K., Sapir, T., Kaplan, A., Levy, T., Schweizer, M., Frotscher, M., James, P. and Reiner, O. (2017) 'Proteomics insights into infantile neuronal ceroid lipofuscinosis (CLN1) point to the involvement of cilia pathology in the disease', *Hum Mol Genet*, 26(9), p. 1678.

Segal-Salto, M., Sapir, T. and Reiner, O. (2016) 'Reversible Cysteine Acylation Regulates the Activity of Human Palmitoyl-Protein Thioesterase 1 (PPT1)', *PLoS One*, 11(1), p. e0146466.

Segurado, A., Rodriguez-Carrillo, A., Castellanos, B., Hernandez-Galilea, E., Velasco, A. and Lillo, C. (2022) 'Scribble basal polarity acquisition in RPE cells and its mislocalization in a pathological AMD-like model', *Front Neuroanat*, 16, p. 983151.

Sekiya, M., Hiraishi, A., Touyama, M. and Sakamoto, K. (2008) 'Oxidative stress induced lipid accumulation via SREBP1c activation in HepG2 cells', *Biochem Biophys Res Commun*, 375(4), pp. 602-7.

Sen, D., Sarkar, S. and Mukhopadhyay, P. (2023) 'Prime Editing: An Emerging Tool in Cancer Treatment', *Mol Biotechnol*, 65(4), pp. 509-520.

Sergouniotis, P.I., McKibbin, M., Robson, A.G., Bolz, H.J., De Baere, E., Müller, P.L., Heller, R., El-Asrag, M.E., Van Schil, K., Plagnol, V., Toomes, C., Uk Inherited Retinal Disease, C., Ali, M., Holder, G.E., Charbel Issa, P., Leroy, B.P., Inglehearn, C.F. and Webster, A.R. (2015) 'Disease Expression in Autosomal Recessive Retinal Dystrophy Associated With Mutations in the DRAM2 Gene', *Invest Ophthalmol Vis Sci*, 56(13), pp. 8083-90.

Sharifi, A., Kousi, M., Sagne, C., Bellenchi, G.C., Morel, L., Darmon, M., Hulkova, H., Ruivo, R., Debacker, C., El Mestikawy, S., Elleder, M., Lehesjoki, A.E., Jalanko, A., Gasnier, B. and Kyttala, A. (2010) 'Expression and lysosomal targeting of CLN7, a major facilitator superfamily transporter

associated with variant late-infantile neuronal ceroid lipofuscinosis', *Hum Mol Genet*, 19(22), pp. 4497-514.

Shevtsova, Z., Garrido, M., Weishaupt, J., Saftig, P., Bahr, M., Luhder, F. and Kμgler, S. (2010) 'CNS-expressed cathepsin D prevents lymphopenia in a murine model of congenital neuronal ceroid lipofuscinosis', *Am J Pathol*, 177(1), pp. 271-9.

Shi, Z., Chen, S., Han, X., Peng, R., Luo, J., Yang, L., Zheng, Y. and Wang, H. (2019) 'The rare mutation in the endosome-associated recycling protein gene VPS50 is associated with human neural tube defects', *Mol Cytogenet*, 12, p. 8.

Shirai, H., Mandai, M., Matsushita, K., Kuwahara, A., Yonemura, S., Nakano, T., Assawachananont, J., Kimura, T., Saito, K., Terasaki, H., Eiraku, M., Sasai, Y. and Takahashi, M. (2016) 'Transplantation of human embryonic stem cell-derived retinal tissue in two primate models of retinal degeneration', *Proc Natl Acad Sci U S A*, 113(1), pp. E81-90.

Shweiki, D., Itin, A., Soffer, D. and Keshet, E. (1992) 'Vascular endothelial growth factor induced by hypoxia may mediate hypoxia-initiated angiogenesis', *Nature*, 359(6398), pp. 843-5.

Sidransky, E., Nalls, M.A., Aasly, J.O., Aharon-Peretz, J., Annesi, G., Barbosa, E.R., Bar-Shira, A., Berg, D., Bras, J., Brice, A., Chen, C.M., Clark, L.N., Condroyer, C., De Marco, E.V., Durr, A., Eblan, M.J., Fahn, S., Farrer, M.J., Fung, H.C., Gan-Or, Z., Gasser, T., Gershoni-Baruch, R., Giladi, N., Griffith, A., Gurevich, T., Januario, C., Kropp, P., Lang, A.E., Lee-Chen, G.J., Lesage, S., Marder, K., Mata, I.F., Mirelman, A., Mitsui, J., Mizuta, I., Nicoletti, G., Oliveira, C., Ottman, R., Orr-Urtreger, A., Pereira, L.V., Quattrone, A., Rogaeva, E., Rolfs, A., Rosenbaum, H., Rozenberg, R., Samii, A., Samaddar, T., Schulte, C., Sharma, M., Singleton, A., Spitz, M., Tan, E.K., Tayebi, N., Toda, T., Troiano, A.R., Tsuji, S., Wittstock, M., Wolfsberg, T.G., Wu, Y.R., Zabetian, C.P., Zhao, Y. and Ziegler, S.G. (2009) 'Multicenter analysis of glucocerebrosidase mutations in Parkinson's disease', *N Engl J Med*, 361(17), pp. 1651-61.

Siintola, E., Partanen, S., Stromme, P., Haapanen, A., Haltia, M., Maehlen, J., Lehesjoki, A.E. and Tyynela, J. (2006) 'Cathepsin D deficiency underlies congenital human neuronal ceroid-lipofuscinosis', *Brain*, 129(Pt 6), pp. 1438-45.

Simo, R., Villarroel, M., Corraliza, L., Hernandez, C. and Garcia-Ramirez, M. (2010) 'The retinal pigment epithelium: something more than a constituent of the blood-retinal barrier--implications for the pathogenesis of diabetic retinopathy', *J Biomed Biotechnol*, 2010, p. 190724.

Simon, M.V., Basu, S.K., Qaladize, B., Grambergs, R., Rotstein, N.P. and Mandal, N. (2021) 'Sphingolipids as critical players in retinal physiology and pathology', *J Lipid Res*, 62, p. 100037.

Sohocki, M.M., Daiger, S.P., Bowne, S.J., Rodriquez, J.A., Northrup, H., Heckenlively, J.R., Birch, D.G., Mintz-Hittner, H., Ruiz, R.S., Lewis, R.A., Saperstein, D.A. and Sullivan, L.S. (2001) 'Prevalence of mutations causing retinitis pigmentosa and other inherited retinopathies', *Hum Mutat*, 17(1), pp. 42-51.

Sou, Y.S., Tanida, I., Komatsu, M., Ueno, T. and Kominami, E. (2006) 'Phosphatidylserine in addition to phosphatidylethanolamine is an in vitro target of the mammalian Atg8 modifiers, LC3, GABARAP, and GATE-16', *J Biol Chem*, 281(6), pp. 3017-24.

Spang, A. (2016) 'Membrane Tethering Complexes in the Endosomal System', *Front Cell Dev Biol*, 4, p. 35.

Spelbrink, R.G. and Nothwehr, S.F. (1999) 'The yeast GRD20 gene is required for protein sorting in the trans-Golgi network/endosomal system and for polarization of the actin cytoskeleton', *Mol Biol Cell*, 10(12), pp. 4263-81.

Srinivasan, B., Kolli, A.R., Esch, M.B., Abaci, H.E., Shuler, M.L. and Hickman, J.J. (2015) 'TEER measurement techniques for in vitro barrier model systems', *J Lab Autom*, 20(2), pp. 107-26.

Srivastava, G.K., Martin, L., Singh, A.K., Fernandez-Bueno, I., Gayoso, M.J., Garcia-Gutierrez, M.T., Girotti, A., Alonso, M., Rodriguez-Cabello, J.C. and Pastor, J.C. (2011) 'Elastin-like recombinamers as substrates for retinal pigment epithelial cell growth', *J Biomed Mater Res A*, 97(3), pp. 243-50.

Steinberg, S.J., Mondal, D. and Fensom, A.H. (1996) 'Co-cultivation of Niemann-Pick disease type C fibroblasts belonging to complementation groups alpha and beta stimulates LDL-derived cholesterol esterification', *J Inherit Metab Dis*, 19(6), pp. 769-74.

Steinfeld, R., Reinhardt, K., Schreiber, K., Hillebrand, M., Kraetzner, R., Bruck, W., Saftig, P. and Gartner, J. (2006) 'Cathepsin D deficiency is associated with a human neurodegenerative disorder', *Am J Hum Genet*, 78(6), pp. 988-98.

Su, D. and Asard, H. (2006) 'Three mammalian cytochromes b561 are ascorbate-dependent ferrireductases', *FEBS J*, 273(16), pp. 3722-34.

Su, D., May, J.M., Koury, M.J. and Asard, H. (2006) 'Human erythrocyte membranes contain a cytochrome b561 that may be involved in extracellular ascorbate recycling', *J Biol Chem*, 281(52), pp. 39852-9.

Sundaresan, Y., Yacoub, S., Kodati, B., Amankwa, C.E., Raola, A. and Zode, G. (2023) 'Therapeutic applications of CRISPR/Cas9 gene editing technology for the treatment of ocular diseases', *FEBS J*.

Suvorova, E.S., Duden, R. and Lupashin, V.V. (2002) 'The Sec34/Sec35p complex, a Ypt1p effector required for retrograde intra-Golgi trafficking, interacts with Golgi SNAREs and COPI vesicle coat proteins', *J Cell Biol*, 157(4), pp. 631-43.

Suzuki, K., Kirisako, T., Kamada, Y., Mizushima, N., Noda, T. and Ohsumi, Y. (2001) 'The pre-autophagosomal structure organized by concerted functions of APG genes is essential for autophagosome formation', *EMBO J*, 20(21), pp. 5971-81.

Szymanski, K.M., Binns, D., Bartz, R., Grishin, N.V., Li, W.P., Agarwal, A.K., Garg, A., Anderson, R.G. and Goodman, J.M. (2007) 'The lipodystrophy protein seipin is found at endoplasmic reticulum lipid droplet junctions and is important for droplet morphology', *Proc Natl Acad Sci U S A*, 104(52), pp. 20890-5.

Takagi, K., Iwamoto, K., Kobayashi, S., Horiuchi, H., Fukuda, R. and Ohta, A. (2012) 'Involvement of Golgi-associated retrograde protein complex in the recycling of the putative Dnf aminophospholipid flippases in yeast', *Biochem Biophys Res Commun*, 417(1), pp. 490-4.

Takahashi, K. and Yamanaka, S. (2006) 'Induction of pluripotent stem cells from mouse embryonic and adult fibroblast cultures by defined factors', *Cell*, 126(4), pp. 663-76.

Takahashi, K., Tanabe, K., Ohnuki, M., Narita, M., Ichisaka, T., Tomoda, K. and Yamanaka, S. (2007) 'Induction of pluripotent stem cells from adult human fibroblasts by defined factors', *Cell*, 131(5), pp. 861-72.

Takano, T., Xu, C., Funahashi, Y., Namba, T. and Kaibuchi, K. (2015) 'Neuronal polarization', *Development*, 142(12), pp. 2088-93.

Talari, N.K., Mattam, U., Meher, N.K., Paripati, A.K., Mahadev, K., Krishnamoorthy, T. and Sepuri, N.B.V. (2023) 'Lipid-droplet associated mitochondria promote fatty-acid oxidation through a distinct bioenergetic pattern in male Wistar rats', *Nat Commun*, 14(1), p. 766.

Tanida, I., Tanida-Miyake, E., Komatsu, M., Ueno, T. and Kominami, E. (2002) 'Human Apg3p/Aut1p homologue is an authentic E2 enzyme for multiple substrates, GATE-16, GABARAP, and MAP-LC3, and facilitates the conjugation of hApg12p to hApg5p', *J Biol Chem*, 277(16), pp. 13739-44.

Tanida, I., Tanida-Miyake, E., Ueno, T. and Kominami, E. (2001) 'The human homolog of Saccharomyces cerevisiae Apg7p is a Protein-activating enzyme for multiple substrates including human Apg12p, GATE-16, GABARAP, and MAP-LC3', *J Biol Chem*, 276(3), pp. 1701-6.

Tanida, I., Ueno, T. and Kominami, E. (2008) 'LC3 and Autophagy', *Methods Mol Biol*, 445, pp. 77-88.

Thaler, A., Gurevich, T., Bar Shira, A., Gana Weisz, M., Ash, E., Shiner, T., Orr-Urtreger, A., Giladi, N. and Mirelman, A. (2017) 'A "dose" effect of mutations in the GBA gene on Parkinson's disease phenotype', *Parkinsonism Relat Disord*, 36, pp. 47-51.

Thomas, R., Moloney, E.B., Macbain, Z.K., Hallett, P.J. and Isacson, O. (2021) 'Fibroblasts from idiopathic Parkinson's disease exhibit deficiency of lysosomal glucocerebrosidase activity associated with reduced levels of the trafficking receptor LIMP2', *Mol Brain*, 14(1), p. 16.

Thwaites, D.T., Hirst, B.H. and Simmons, N.L. (1993) 'Passive transepithelial absorption of thyrotropin-releasing hormone (TRH) via a paracellular route in cultured intestinal and renal epithelial cell lines', *Pharm Res*, 10(5), pp. 674-81.

Tognoli, M.L., Dancourt, J., Bonsergent, E., Palmulli, R., de Jong, O.G., Van Niel, G., Rubinstein, E., Vader, P. and Lavieu, G. (2023) 'Lack of involvement of CD63 and CD9 tetraspanins in the extracellular vesicle content delivery process', *Commun Biol*, 6(1), p. 532.

Tombran-Tink, J., Chader, G.G. and Johnson, L.V. (1991) 'PEDF: a pigment epithelium-derived factor with potent neuronal differentiative activity', *Exp Eye Res*, 53(3), pp. 411-4.

Topalidou, I., Cattin-Ortola, J., Hummer, B., Asensio, C.S. and Ailion, M. (2020) 'EIPR1 controls dense-core vesicle cargo retention and EARP complex localization in insulin-secreting cells', *Mol Biol Cell*, 31(1), pp. 59-79.

Topalidou, I., Cattin-Ortola, J., Pappas, A.L., Cooper, K., Merrihew, G.E., MacCoss, M.J. and Ailion, M. (2016) 'The EARP Complex and Its Interactor EIPR-1 Are Required for Cargo Sorting to Dense-Core Vesicles', *PLoS Genet*, 12(5), p. e1006074.

Tremel, S., Ohashi, Y., Morado, D.R., Bertram, J., Perisic, O., Brandt, L.T.L., von Wrisberg, M.K., Chen, Z.A., Maslen, S.L., Kovtun, O., Skehel, M., Rappsilber, J., Lang, K., Munro, S., Briggs, J.A.G. and Williams, R.L. (2021) 'Structural basis for VPS34 kinase activation by Rab1 and Rab5 on membranes', *Nat Commun*, 12(1), p. 1564.

Truong, V., Viken, K., Geng, Z., Barkan, S., Johnson, B., Ebeling, M.C., Montezuma, S.R., Ferrington, D.A. and Dutton, J.R. (2021) 'Automating Human Induced Pluripotent Stem Cell Culture and Differentiation of iPSC-Derived Retinal Pigment Epithelium for Personalized Drug Testing', *SLAS Technol*, 26(3), pp. 287-299.

Tsin, A., Betts-Obregon, B. and Grigsby, J. (2018) 'Visual cycle proteins: Structure, function, and roles in human retinal disease', *J Biol Chem*, 293(34), pp. 13016-13021.

Tsin, A., Betts-Obregon, B. and Grigsby, J. (2018) 'Visual cycle proteins: Structure, function, and roles in human retinal disease', *J Biol Chem*, 293(34), pp. 13016-13021.

Tsukita, S., Furuse, M. and Itoh, M. (2001) 'Multifunctional strands in tight junctions', *Nat Rev Mol Cell Biol*, 2(4), pp. 285-93.

Tyynela, J., Sohar, I., Sleat, D.E., Gin, R.M., Donnelly, R.J., Baumann, M., Haltia, M. and Lobel, P. (2001) 'Congenital ovine neuronal ceroid lipofuscinosis--a cathepsin D deficiency with increased levels of the inactive enzyme', *Eur J Paediatr Neurol*, 5 Suppl A, pp. 43-5.

Urano, Y., Watanabe, H., Murphy, S.R., Shibuya, Y., Geng, Y., Peden, A.A., Chang, C.C. and Chang, T.Y. (2008) 'Transport of LDL-derived cholesterol from the NPC1 compartment to the ER involves the trans-Golgi network and the SNARE protein complex', *Proc Natl Acad Sci U S A*, 105(43), pp. 16513-8.

Valapala, M., Wilson, C., Hose, S., Bhutto, I.A., Grebe, R., Dong, A., Greenbaum, S., Gu, L., Sengupta, S., Cano, M., Hackett, S., Xu, G., Lutty, G.A., Dong, L., Sergeev, Y., Handa, J.T., Campochiaro, P., Wawrousek, E., Zigler, J.S., Jr. and Sinha, D. (2014) 'Lysosomal-mediated waste clearance in retinal pigment epithelial cells is regulated by CRYBA1/betaA3/A1-crystallin via V-ATPase-MTORC1 signaling', *Autophagy*, 10(3), pp. 480-96.

van de Pavert, S.A., Kantardzhieva, A., Malysheva, A., Meuleman, J., Versteeg, I., Levelt, C., Klooster, J., Geiger, S., Seeliger, M.W., Rashbass, P., Le Bivic, A. and Wijnholds, J. (2004) 'Crumbs homologue 1 is required for maintenance of photoreceptor cell polarization and adhesion during light exposure', *J Cell Sci*, 117(Pt 18), pp. 4169-77.

van Niel, G., Charrin, S., Simoes, S., Romao, M., Rochin, L., Saftig, P., Marks, M.S., Rubinstein, E. and Raposo, G. (2011) 'The tetraspanin CD63 regulates ESCRT-independent and -dependent endosomal sorting during melanogenesis', *Dev Cell*, 21(4), pp. 708-21.

Vanier, M.T. (1983) 'Biochemical studies in Niemann-Pick disease. I. Major sphingolipids of liver and spleen', *Biochim Biophys Acta*, 750(1), pp. 178-84.

Vanier, M.T. (1999) 'Lipid changes in Niemann-Pick disease type C brain: personal experience and review of the literature', *Neurochem Res*, 24(4), pp. 481-9.

Vanier, M.T. and Millat, G. (2003) 'Niemann-Pick disease type C', *Clin Genet*, 64(4), pp. 269-81.

Vanier, M.T., Duthel, S., Rodriguez-Lafrasse, C., Pentchev, P. and Carstea, E.D. (1996) 'Genetic heterogeneity in Niemann-Pick C disease: a study using somatic cell hybridization and linkage analysis', *Am J Hum Genet*, 58(1), pp. 118-25.

Varvagiannis, K., Hanquinet, S., Billieux, M.H., De Luca, R., Rimensberger, P., Lidgren, M., Guipponi, M., Makrythanasis, P., Blouin, J.L., Antonarakis, S.E., Steinfeld, R., Kern, I., Poretti, A., Fluss, J. and Fokstuen, S. (2018) 'Congenital Neuronal Ceroid Lipofuscinosis with a Novel CTSD Gene Mutation: A Rare Cause of Neonatal-Onset Neurodegenerative Disorder', *Neuropediatrics*, 49(2), pp. 150-153.

Velazquez-Diaz, P., Nakajima, E., Sorkhdini, P., Hernandez-Gutierrez, A., Eberle, A., Yang, D. and Zhou, Y. (2021) 'Hermansky-Pudlak Syndrome and Lung Disease: Pathogenesis and Therapeutics', *Front Pharmacol*, 12, p. 644671.

Vicario-Orri, E., Opazo, C.M. and Munoz, F.J. (2015) 'The pathophysiology of axonal transport in Alzheimer's disease', *J Alzheimers Dis*, 43(4), pp. 1097-113.

Vitner, E.B., Dekel, H., Zigdon, H., Shachar, T., Farfel-Becker, T., Eilam, R., Karlsson, S. and Futerman, A.H. (2010) 'Altered expression and distribution of cathepsins in neuronopathic forms of Gaucher disease and in other sphingolipidoses', *Hum Mol Genet*, 19(18), pp. 3583-90.

Volkner, M., Zschatzsch, M., Rostovskaya, M., Overall, R.W., Busskamp, V., Anastassiadis, K. and Karl, M.O. (2016) 'Retinal Organoids from Pluripotent Stem Cells Efficiently Recapitulate Retinogenesis', *Stem Cell Reports*, 6(4), pp. 525-538.

Volland, S., Esteve-Rudd, J., Hoo, J., Yee, C. and Williams, D.S. (2015) 'A comparison of some organizational characteristics of the mouse central retina and the human macula', *PLoS One*, 10(4), p. e0125631.

Wagstaff, E.L., Ten Asbroek, A., Ten Brink, J.B., Jansonius, N.M. and Bergen, A.A.B. (2021) 'An alternative approach to produce versatile retinal organoids with accelerated ganglion cell development', *Sci Rep*, 11(1), p. 1101.

Wahlin, K.J., Maruotti, J.A., Sripathi, S.R., Ball, J., Angueyra, J.M., Kim, C., Grebe, R., Li, W., Jones, B.W. and Zack, D.J. (2017) 'Photoreceptor Outer Segment-like Structures in Long-Term 3D Retinas from Human Pluripotent Stem Cells', *Sci Rep*, 7(1), p. 766.

Walkley, S.U. and Suzuki, K. (2004) 'Consequences of NPC1 and NPC2 loss of function in mammalian neurons', *Biochim Biophys Acta*, 1685(1-3), pp. 48-62.

Waller-Evans, H. and Lloyd-Evans, E. (2015) 'Regulation of TRPML1 function', *Biochem Soc Trans*, 43(3), pp. 442-6.

Wang, H., Cai, Y., Cai, L., Hu, Y., Chen, X. and Deng, J. (2014) 'Altered lipid levels in untreated patients with early polymyositis', *PLoS One*, 9(2), p. e89827.

Wang, H., Yang, H., Shivalila, C.S., Dawlaty, M.M., Cheng, A.W., Zhang, F. and Jaenisch, R. (2013) 'One-step generation of mice carrying mutations in multiple genes by CRISPR/Cas-mediated genome engineering', *Cell*, 153(4), pp. 910-8.

Wang, J., Davis, S., Menon, S., Zhang, J., Ding, J., Cervantes, S., Miller, E., Jiang, Y. and Ferro-Novick, S. (2015) 'Ypt1/Rab1 regulates Hrr25/CK1delta kinase activity in ER-Golgi traffic and macroautophagy', *J Cell Biol*, 210(2), pp. 273-85.

Wang, J., Menon, S., Yamasaki, A., Chou, H.T., Walz, T., Jiang, Y. and Ferro-Novick, S. (2013) 'Ypt1 recruits the Atg1 kinase to the preautophagosomal structure', *Proc Natl Acad Sci U S A*, 110(24), pp. 9800-5.

Wang, J.S. and Kefalov, V.J. (2011) 'The cone-specific visual cycle', *Prog Retin Eye Res*, 30(2), pp. 115-28.

Wang, M., Li, H. and Wang, F. (2022) 'Roles of Transepithelial Electrical Resistance in Mechanisms of Retinal Pigment Epithelial Barrier and Retinal Disorders', *Discov Med*, 34(171), pp. 19-24.

Wang, M.L., Motamed, M., Infante, R.E., Abi-Mosleh, L., Kwon, H.J., Brown, M.S. and Goldstein, J.L. (2010) 'Identification of surface residues on Niemann-Pick C2 essential for hydrophobic handoff of cholesterol to NPC1 in lysosomes', *Cell Metab*, 12(2), pp. 166-73.

Wang, S., Tsun, Z.Y., Wolfson, R.L., Shen, K., Wyant, G.A., Plovanich, M.E., Yuan, E.D., Jones, T.D., Chantranupong, L., Comb, W., Wang, T., Bar-Peled, L., Zoncu, R., Straub, C., Kim, C., Park, J., Sabatini, B.L. and Sabatini, D.M. (2015a) 'Metabolism. Lysosomal amino acid transporter SLC38A9 signals arginine sufficiency to mTORC1', *Science*, 347(6218), pp. 188-94.

Wang, X., Xiong, K., Lin, C., Lv, L., Chen, J., Xu, C., Wang, S., Gu, D., Zheng, H., Yu, H., Li, Y., Xiao, H. and Zhou, G. (2015b) 'New medium used in the differentiation of human pluripotent stem cells to retinal cells is comparable to fetal human eye tissue', *Biomaterials*, 53, pp. 40-9.

Wang, Z., Guo, R., Trudeau, S.J., Wolinsky, E., Ast, T., Liang, J.H., Jiang, C., Ma, Y., Teng, M., Mootha, V.K. and Gewurz, B.E. (2021) 'CYB561A3 is the key lysosomal iron reductase required for Burkitt B-cell growth and survival', *Blood*, 138(22), pp. 2216-2230.

Ward, M.E., Chen, R., Huang, H.Y., Ludwig, C., Telpoukhovskaia, M., Taubes, A., Boudin, H., Minami, S.S., Reichert, M., Albrecht, P., Gelfand, J.M., Cruz-Herranz, A., Cordano, C., Alavi, M.V., Leslie, S., Seeley, W.W., Miller, B.L., Bigio, E., Mesulam, M.M., Bogyo, M.S., Mackenzie, I.R., Staropoli, J.F., Cotman, S.L., Huang, E.J., Gan, L. and Green, A.J. (2017) 'Individuals with progranulin haploinsufficiency exhibit features of neuronal ceroid lipofuscinosis', *Sci Transl Med*, 9(385).

Watanabe, K., Kamiya, D., Nishiyama, A., Katayama, T., Nozaki, S., Kawasaki, H., Watanabe, Y., Mizuseki, K. and Sasai, Y. (2005) 'Directed differentiation of telencephalic precursors from embryonic stem cells', *Nat Neurosci*, 8(3), pp. 288-96.

Weber, R.A., Yen, F.S., Nicholson, S.P.V., Alwaseem, H., Bayraktar, E.C., Alam, M., Timson, R.C., La, K., Abu-Remaileh, M., Molina, H. and Birsoy, K. (2020) 'Maintaining Iron Homeostasis Is the Key Role of Lysosomal Acidity for Cell Proliferation', *Mol Cell*, 77(3), pp. 645-655 e7.

Wei, J., Zhang, Y.Y., Luo, J., Wang, J.Q., Zhou, Y.X., Miao, H.H., Shi, X.J., Qu, Y.X., Xu, J., Li, B.L. and Song, B.L. (2017) 'The GARP Complex Is Involved in Intracellular Cholesterol Transport via Targeting NPC2 to Lysosomes', *Cell Rep*, 19(13), pp. 2823-2835.

Wei, M.L. (2006) 'Hermansky-Pudlak syndrome: a disease of protein trafficking and organelle function', *Pigment Cell Res*, 19(1), pp. 19-42.

Weide, T., Bayer, M., Koster, M., Siebrasse, J.P., Peters, R. and Barnekow, A. (2001) 'The Golgi matrix protein GM130: a specific interacting partner of the small GTPase rab1b', *EMBO Rep*, 2(4), pp. 336-41.

Weleber, R.G. (1998) 'The dystrophic retina in multisystem disorders: the electroretinogram in neuronal ceroid lipofuscinoses', *Eye (Lond)*, 12 (Pt 3b), pp. 580-90.

Weleber, R.G., Gupta, N., Trzupek, K.M., Wepner, M.S., Kurz, D.E. and Milam, A.H. (2004) 'Electroretinographic and clinicopathologic correlations of retinal dysfunction in infantile neuronal ceroid lipofuscinosis (infantile Batten disease)', *Mol Genet Metab*, 83(1-2), pp. 128-37.

Welz, T., Wellbourne-Wood, J. and Kerkhoff, E. (2014) 'Orchestration of cell surface proteins by Rab11', *Trends Cell Biol*, 24(7), pp. 407-15.

Wen, R., Dallman, J.E., Li, Y., Zuchner, S.L., Vance, J.M., Pericak-Vance, M.A. and Lam, B.L. (2014) 'Knock-down DHDDS expression induces photoreceptor degeneration in zebrafish', *Adv Exp Med Biol*, 801, pp. 543-50.

Wen, R., Lam, B.L. and Guan, Z. (2013) 'Aberrant dolichol chain lengths as biomarkers for retinitis pigmentosa caused by impaired dolichol biosynthesis', *J Lipid Res*, 54(12), pp. 3516-22.

West, E.L., Majumder, P., Naeem, A., Fernando, M., O'Hara-Wright, M., Lanning, E., Kloc, M., Ribeiro, J., Ovando-Roche, P., Shum, I.O., Jumbu, N., Sampson, R., Hayes, M., Bainbridge, J.W.B., Georgiadis, A., Smith, A.J., Gonzalez-Cordero, A. and Ali, R.R. (2022) 'Antioxidant and lipid supplementation improve the development of photoreceptor outer segments in pluripotent stem cell-derived retinal organoids', *Stem Cell Reports*, 17(4), pp. 775-788.

White, D.A., Fritz, J.J., Hauswirth, W.W., Kaushal, S. and Lewin, A.S. (2007) 'Increased sensitivity to light-induced damage in a mouse model of autosomal dominant retinal disease', *Invest Ophthalmol Vis Sci*, 48(5), pp. 1942-51.

Wiedenmann, B., Franke, W.W., Kuhn, C., Moll, R. and Gould, V.E. (1986) 'Synaptophysin: a marker protein for neuroendocrine cells and neoplasms', *Proc Natl Acad Sci U S A*, 83(10), pp. 3500-4.

Willenborg, M., Schmidt, C.K., Braun, P., Landgrebe, J., von Figura, K., Saftig, P. and Eskelinen, E.L. (2005) 'Mannose 6-phosphate receptors, Niemann-Pick C2 protein, and lysosomal cholesterol accumulation', *J Lipid Res*, 46(12), pp. 2559-69.

Willett, R., Blackburn, J.B., Climer, L., Pokrovskaya, I., Kudlyk, T., Wang, W. and Lupashin, V. (2016) 'COG lobe B sub-complex engages v-SNARE GS15 and functions via regulated interaction with lobe A sub-complex', *Sci Rep*, 6, p. 29139.

Willett, R., Martina, J.A., Zewe, J.P., Wills, R., Hammond, G.R.V. and Puertollano, R. (2017) 'TFEB regulates lysosomal positioning by modulating TMEM55B expression and JIP4 recruitment to lysosomes', *Nat Commun*, 8(1), p. 1580.

Williams, R.E. and Mole, S.E. (2012) 'New nomenclature and classification scheme for the neuronal ceroid lipofuscinoses', *Neurology*, 79(2), pp. 183-91.

Willy, P.J., Umesono, K., Ong, E.S., Evans, R.M., Heyman, R.A. and Mangelsdorf, D.J. (1995) 'LXR, a nuclear receptor that defines a distinct retinoid response pathway', *Genes Dev*, 9(9), pp. 1033-45.

Wilmut, I., Schnieke, A.E., McWhir, J., Kind, A.J. and Campbell, K.H. (1997) 'Viable offspring derived from fetal and adult mammalian cells', *Nature*, 385(6619), pp. 810-3.

Wisniewski, K., Rudelli, R., Laure-Kamionowska, M., Sklower, S., Houck, G.E., Jr., Kieras, F., Ramos, P., Wisniewski, H.M. and Braak, H. (1985) 'Sanfilippo disease, type A with some features of ceroid lipofuscinosis', *Neuropediatrics*, 16(2), pp. 98-105.

Wu, J., Bell, O.H., Copland, D.A., Young, A., Pooley, J.R., Maswood, R., Evans, R.S., Khaw, P.T., Ali, R.R., Dick, A.D. and Chu, C.J. (2020) 'Gene Therapy for Glaucoma by Ciliary Body Aquaporin 1 Disruption Using CRISPR-Cas9', *Mol Ther*, 28(3), pp. 820-829.

Wu, Q., Shang, Y., Bai, Y., Wu, Y., Wang, H. and Shen, T. (2021) 'Sufentanil preconditioning protects against myocardial ischemia/reperfusion injury via miR-125a/DRAM2 axis', *Cell Cycle*, 20(4), pp. 383-391.

Wu, W.H., Tsai, Y.T., Justus, S., Lee, T.T., Zhang, L., Lin, C.S., Bassuk, A.G., Mahajan, V.B. and Tsang, S.H. (2016) 'CRISPR Repair Reveals Causative Mutation in a Preclinical Model of Retinitis Pigmentosa', *Mol Ther*, 24(8), pp. 1388-94.

Wu, W.I., Lin, Y.P., Wang, E., Merrill, A.H., Jr. and Carman, G.M. (1993) 'Regulation of phosphatidate phosphatase activity from the yeast Saccharomyces cerevisiae by sphingoid bases', *J Biol Chem*, 268(19), pp. 13830-7.

Wu, X., Steet, R.A., Bohorov, O., Bakker, J., Newell, J., Krieger, M., Spaapen, L., Kornfeld, S. and Freeze, H.H. (2004) 'Mutation of the COG complex subunit gene COG7 causes a lethal congenital disorder', *Nat Med*, 10(5), pp. 518-23.

Xu, D., Li, Y., Wu, L., Li, Y., Zhao, D., Yu, J., Huang, T., Ferguson, C., Parton, R.G., Yang, H. and Li, P. (2018) 'Rab18 promotes lipid droplet (LD) growth by tethering the ER to LDs through SNARE and NRZ interactions', *J Cell Biol*, 217(3), pp. 975-995.

Yambire, K.F., Rostosky, C., Watanabe, T., Pacheu-Grau, D., Torres-Odio, S., Sanchez-Guerrero, A., Senderovich, O., Meyron-Holtz, E.G., Milosevic, I., Frahm, J., West, A.P. and Raimundo, N. (2019) 'Impaired lysosomal acidification triggers iron deficiency and inflammation in vivo', *Elife*, 8.

Yan, C., Jiang, J., Yang, Y., Geng, X. and Dong, W. (2022) 'The function of VAMP2 in mediating membrane fusion: An overview', *Front Mol Neurosci*, 15, p. 948160.

Yang, M., Luo, S., Yang, J., Chen, W., He, L., Liu, D., Zhao, L. and Wang, X. (2022) 'Lipid droplet - mitochondria coupling: A novel lipid metabolism regulatory hub in diabetic nephropathy', *Front Endocrinol (Lausanne)*, 13, p. 1017387.

Yang, S., Zhou, J. and Li, D. (2021) 'Functions and Diseases of the Retinal Pigment Epithelium', *Front Pharmacol*, 12, p. 727870.

Yang, X., Yu, X.W., Zhang, D.D. and Fan, Z.G. (2020) 'Blood-retinal barrier as a converging pivot in understanding the initiation and development of retinal diseases', *Chin Med J (Engl)*, 133(21), pp. 2586-2594.

Yau, K.W. (1994) 'Phototransduction mechanism in retinal rods and cones. The Friedenwald Lecture', *Invest Ophthalmol Vis Sci*, 35(1), pp. 9-32.

Yen, W.L., Legakis, J.E., Nair, U. and Klionsky, D.J. (2007) 'Atg27 is required for autophagy-dependent cycling of Atg9', *Mol Biol Cell*, 18(2), pp. 581-93.

Yoon, J.H., Her, S., Kim, M., Jang, I.S. and Park, J. (2012) 'The expression of damage-regulated autophagy modulator 2 (DRAM2) contributes to autophagy induction', *Mol Biol Rep*, 39(2), pp. 1087-93.

Young, R.W. and Bok, D. (1969) 'Participation of the retinal pigment epithelium in the rod outer segment renewal process', *J Cell Biol*, 42(2), pp. 392-403.

Yu, I.M. and Hμghson, F.M. (2010) 'Tethering factors as organizers of intracellular vesicular traffic', *Annu Rev Cell Dev Biol*, 26, pp. 137-56.

Zahabi, A., Shahbazi, E., Ahmadieh, H., Hassani, S.N., Totonchi, M., Taei, A., Masoudi, N., Ebrahimi, M., Aghdami, N., Seifinejad, A., Mehrnejad, F., Daftarian, N., Salekdeh, G.H. and Baharvand, H. (2012) 'A new efficient protocol for directed differentiation of retinal pigmented epithelial cells from normal and retinal disease induced pluripotent stem cells', *Stem Cells Dev*, 21(12), pp. 2262-72.

Zakrzewski, W., Dobrzynski, M., Szymonowicz, M. and Rybak, Z. (2019) 'Stem cells: past, present, and future', *Stem Cell Res Ther*, 10(1), p. 68.

Zappa, F., Venditti, R. and De Matteis, M.A. (2017) 'TRAPPing Rab18 in lipid droplets', *EMBO J*, 36(4), pp. 394-396.

Zeng, C.W., Chen, Z.H., Zhang, X.J., Han, B.W., Lin, K.Y., Li, X.J., Wei, P.P., Zhang, H., Li, Y. and Chen, Y.Q. (2014) 'MIR125B1 represses the degradation of the PML-RARA oncoprotein by an autophagy-lysosomal pathway in acute promyelocytic leukemia', *Autophagy*, 10(10), pp. 1726-37.

Zeng, C.W., Chen, Z.H., Zhang, X.J., Han, B.W., Lin, K.Y., Li, X.J., Wei, P.P., Zhang, H., Li, Y. and Chen, Y.Q. (2014) 'MIR125B1 represses the degradation of the PML-RARA oncoprotein by an autophagy-lysosomal pathway in acute promyelocytic leukemia', *Autophagy*, 10(10), pp. 1726-37.

Zerti, D., Molina, M.M., Dorgau, B., Mearns, S., Bauer, R., Al-Aama, J. and Lako, M. (2021) 'IGFBPs mediate IGF-1's functions in retinal lamination and photoreceptor development during pluripotent stem cell differentiation to retinal organoids', *Stem Cells*, 39(4), pp. 458-466.

Zetsche, B., Gootenberg, J.S., Abudayyeh, O.O., Slaymaker, I.M., Makarova, K.S., Essletzbichler, P., Volz, S.E., Joung, J., van der Oost, J., Regev, A., Koonin, E.V. and Zhang, F. (2015) 'Cpf1 is a single RNA-guided endonuclease of a class 2 CRISPR-Cas system', *Cell*, 163(3), pp. 759-71.

Zhang, C., Wu, B., Beglopoulos, V., Wines-Samuelson, M., Zhang, D., Dragatsis, I., Sudhof, T.C. and Shen, J. (2009) 'Presenilins are essential for regulating neurotransmitter release', *Nature*, 460(7255), pp. 632-6.

Zhang, C.S., Jiang, B., Li, M., Zhu, M., Peng, Y., Zhang, Y.L., Wu, Y.Q., Li, T.Y., Liang, Y., Lu, Z., Lian, G., Liu, Q., Guo, H., Yin, Z., Ye, Z., Han, J., Wu, J.W., Yin, H., Lin, S.Y. and Lin, S.C. (2014) 'The lysosomal v-ATPase-Ragulator complex is a common activator for AMPK and mTORC1, acting as a switch between catabolism and anabolism', *Cell Metab*, 20(3), pp. 526-40.

Zhang, D.L., Su, D., Berczi, A., Vargas, A. and Asard, H. (2006) 'An ascorbate-reducible cytochrome b561 is localized in macrophage lysosomes', *Biochim Biophys Acta*, 1760(12), pp. 1903-13.

Zhang, W., Yang, X., Li, Y., Yu, L., Zhang, B., Zhang, J., Cho, W.J., Venkatarangan, V., Chen, L., Burµgula, B.B., Bui, S., Wang, Y., Duan, C., Kitzman, J.O. and Li, M. (2022) 'GCAF(TMEM251) regulates lysosome biogenesis by activating the mannose-6-phosphate pathway', *Nat Commun*, 13(1), p. 5351.

Zhao, X., Xu, Z., Xiao, L., Shi, T., Xiao, H., Wang, Y., Li, Y., Xue, F. and Zeng, W. (2021) 'Review on the Vascularization of Organoids and Organoids-on-a-Chip', *Front Bioeng Biotechnol*, 9, p. 637048.

Zheng, Y.L. (2016) 'Some Ethical Concerns About Human Induced Pluripotent Stem Cells', *Sci Eng Ethics*, 22(5), pp. 1277-1284.

Zhong, X., Gutierrez, C., Xue, T., Hampton, C., Vergara, M.N., Cao, L.H., Peters, A., Park, T.S., Zambidis, E.T., Meyer, J.S., Gamm, D.M., Yau, K.W. and Canto-Soler, M.V. (2014) 'Generation of three-dimensional retinal tissue with functional photoreceptors from human iPSCs', *Nat Commun*, 5, p. 4047.

Zhong, X., Gutierrez, C., Xue, T., Hampton, C., Vergara, M.N., Cao, L.H., Peters, A., Park, T.S., Zambidis, E.T., Meyer, J.S., Gamm, D.M., Yau, K.W. and Canto-Soler, M.V. (2014) 'Generation of three-dimensional retinal tissue with functional photoreceptors from human iPSCs', *Nat Commun*, 5, p. 4047.

Zhong, X., Gutierrez, C., Xue, T., Hampton, C., Vergara, M.N., Cao, L.H., Peters, A., Park, T.S., Zambidis, E.T., Meyer, J.S., Gamm, D.M., Yau, K.W. and Canto-Soler, M.V. (2014) 'Generation of three-dimensional retinal tissue with functional photoreceptors from human iPSCs', *Nat Commun*, 5, p. 4047.

Zhou, R., Lu, Y., Han, Y., Li, X., Lou, H., Zhu, L., Zhen, X. and Duan, S. (2015) 'Mice heterozygous for cathepsin D deficiency exhibit mania-related behavior and stress-induced depression', *Prog Neuropsychopharmacol Biol Psychiatry*, 63, pp. 110-8.

Zhou, S., Flamier, A., Abdouh, M., Tetreault, N., Barabino, A., Wadhwa, S. and Bernier, G. (2015) 'Differentiation of human embryonic stem cells into cone photoreceptors through simultaneous inhibition of BMP, TGFbeta and Wnt signaling', *Development*, 142(19), pp. 3294-306.

Zhu, Y., Carido, M., Meinhardt, A., Kurth, T., Karl, M.O., Ader, M. and Tanaka, E.M. (2013) 'Three-dimensional neuroepithelial culture from human embryonic stem cells and its use for quantitative conversion to retinal pigment epithelium', *PLoS One*, 8(1), p. e54552.

Zlatic, S.A., Tornieri, K., L'Hernault, S.W. and Faundez, V. (2011) 'Clathrin-dependent mechanisms modulate the subcellular distribution of class C Vps/HOPS tether subunits in polarized and nonpolarized cells', *Mol Biol Cell*, 22(10), pp. 1699-715.

Zolov, S.N. and Lupashin, V.V. (2005) 'Cog3p depletion blocks vesicle-mediated Golgi retrograde trafficking in HeLa cells', *J Cell Biol*, 168(5), pp. 747-59.

Zoncu, R., Bar-Peled, L., Efeyan, A., Wang, S., Sancak, Y. and Sabatini, D.M. (2011) 'mTORC1 senses lysosomal amino acids through an inside-out mechanism that requires the vacuolar H(+)-ATPase', *Science*, 334(6056), pp. 678-83.

Zunke, F., Andresen, L., Wesseler, S., Groth, J., Arnold, P., Rothaμg, M., Mazzulli, J.R., Krainc, D., Blanz, J., Saftig, P. and Schwake, M. (2016) 'Characterization of the complex formed by beta-glucocerebrosidase and the lysosomal integral membrane protein type-2', *Proc Natl Acad Sci U S A*, 113(14), pp. 3791-6.